Eley-Rideal type mechanism of CO_2 hydrogenation to formate on Cu catalysts

Jiamei Quan
Doctoral Program in
Nano-Science and Nano-Technology

Submitted to the Graduate School of
Pure and Applied Sciences
in Partial Fulfillment of the Requirements
for the Degree of Doctor of Philosophy in
Engineering

at the
University of Tsukuba

Abstract

Catalytic conversion of CO_2 into valuable fuel, especially if activated by a precise energetic control, represents a potentially economic strategy for utilization of fossil feedstock and reducing CO_2 emissions as well as their contributions to climate changes. Among the various catalytic reactions related to CO_2, methanol synthesis from CO_2 hydrogenation (i.e. $CO_2 + 3H_2 \rightarrow CH_3OH + H_2O$) over Cu-based catalysts is considered to be the most promising catalytic process for this purpose. In order to realize highly efficient CO_2 conversion, the elementary steps of methanol synthesis on Cu catalysts should be well-understood in terms of kinetics and dynamics. In particular, the hydrogenation of CO_2 into formate intermediates (i.e. $CO_2 + H_a \rightarrow HCOO_a$) is an important reaction step for methanol synthesis insofar as it represents the initial activation process of CO_2 on Cu surfaces and limits the efficiency of CO_2 further hydrogenations; this is because the reaction probability of the formation of formate is very low (i.e. $\sim 10^{-12}$) at 340 K, it is comparable to the reaction probability of methanol synthesis as 3×10^{-12} at 523 K. In this thesis, extensive experimental and theoretical studies have shown the formation of formate intermediates on Cu catalysts to occur predominantly through an Eley-Rideal (ER)-type mechanism: the energetic CO_2 molecule directly attacks an adsorbed hydrogen atom under the thermal non-equilibrium reaction system.

Firstly, I carried out supersonic molecular beam experiments. Temperature programmed desorption (TPD) and Infrared reflection-absorption spectroscopy (IRAS) measurements were carried out to confirm that the formate is successfully synthesized by an energetic CO_2 molecule reacting with a H_a adatom on Cu(111) and Cu(100) surface at a low temperature as 180 K. It was found that the reaction probability of CO_2 to for formate is independent of Cu surface temperatures and Cu surface structures. Both of translational energy and vibrational energy are efficient to convert CO_2 into formate. Specially, the vibrational energy of CO_2 is found to be much preference than translational energy. These experimental results indicate that hot CO_2 molecules directly collide with H_a without passing through an adsorption state of CO_2 on the cold Cu surfacse. That is, formate formation between the hot CO_2 molecules and cool H_a/Cu surfaces proceeds via an Eley-Rideal (ER)-type mechanism in terms of thermal non-equilibrium.

Secondly, I applied angle-resolved analysis for the formate decomposition ($HCOO_a \rightarrow CO_2 + H_2$) on Cu surfaces. It was found that desorbing CO_2 product shows sharp angular distribution along the surface normal direction, indicating that CO_2 obtains a strong repulsion force from the surface towards normal direction. We also found that the translational energy of CO_2 is insensitive to the surface temperature and the angular distributions are independent of the surface structures, which suggest CO_2 molecule, just before desorption or in the region of transition state, should not be contacting with the Cu surface. Based on the principle of micro-reversibility of reaction, these results are corresponding to the suggestion that hot CO_2 directly collides to H_a without via adsorption or precursor state. That is, the process is in an ER-type pathway.

Finally, density functional theory (DFT) calculations were carried out to examine the detailed description of ER-type mechanism for formate synthesis. It was found that in terms of O-C-O bending mode, the vibrational energy of CO_2 is required for the synthesis of formate. By bending the molecular axis of CO_2, the lowest unoccupied molecular orbital (LUMO) of CO_2 decreases in energy level ($\Delta E < 0.50$ eV). Therefore, charge transfer from Cu surface through H_a to CO_2 occurs after the O-C-O bending, which is followed by the formation of the C-H bond with sp^2 configuration.

This newly discovered ER type mechanism for CO_2 conversion under thermal non-equilibrium, which does not require the heating of catalysts, has great potential to open up novel industrial pathways of efficiently converting CO_2 into useful chemicals and fuels.

Contents

Chapter 1 Research background

Chapter 2 Dynamics of gas-surface reactions

Chapter 3 Principles of molecular beam and surface analytical techniques

Chapter 4 Dynamics of formate synthesis from CO_2 hydrogenation on Cu catalysts studied by supersonic molecular beam

Chapter 5 Dynamics of formate decomposition on Cu catalysts studied by angle-resolved analysis of desorbing CO_2 product

Chapter 6 Density functional theory calculations

Chapter 7 Summary and perspective

Appendix

Contents

Nomenclature

ER	Eley-Rideal reaction
LH	Langmuir-Hinshelwood reaction
TPD	Temperature-programmed-desorption
AR-TPD	Angle-resolved temperature-programmed-desorption
AR-SSD	Angle-resolved steady-state desorption
LEED	Low energy electron diffraction
AES	Auger electron spectroscopy
ML	Monolayer
IRAS	Infrared reflection-adsorption spectroscopy
PES	Potential energy surfae
BOA	Born-Oppenheimer Approximation
EHP	Electron-hole pair
TOF	Time-of-flight
UHV	Ultra-high vacuum
SNR	Signal-noise-ratio
TS	Transition state
TST	Transition state theory
IS	Initial state
FS	Final state
GHG	Greenhouse gas
CCS	Carbon capture and sequestration
Gts	Gigatonnes
DFT	Density functional theory
STM	Scanning tunneling microscopy
TEM	Transmission electron microscopy
TOFs	Turn over frequencies
MOFs	Metal-organic frameworks
RWGS	Reverse water gas shift
LUMO	Lowest unoccupied molecular orbital
HOMO	Highest occupied molecular orbital
TPD	Temperature programmed desorption
GGA	Generalized gradient approximation
VASP	Vienna *ab initio* simulation package

Chapter 1

Research background

1.1 The global energy consumption and carbon dioxide emission

We are facing critical social challenges and environmental risks ascribed to the massive emission of carbon dioxide (CO_2) resulting from large anthropogenic energy demands nowadays. Since the past two centuries, fossil fuels such as coal, petroleum and nature gas have been essential for the production of energy and commodity chemicals. From the industry revolution ignited in the 17th century, plenty of novel manufacturing processes have been boosted and deeply advanced the civilization of human society. With the worldwide rapid expansion of population and the development of global economy in past decades, the global energy consumption derived from fossil fuels has significantly increased. For example, around 1, 3000 million tones oil equivalent (Mtoe) energy was demanded in 2015. It is also forecasted that the global energy consumption will grow almost 20% by 2030. Among the global primary energy sources, world demand for coal and natural gas takes up by 5% energy consumption, respectively. More than 90 million barrels per day (Mb/d) of global oil are demanded in 2015 and will increase by 9% higher in 2030 [1]. Certainly, the massive combustion of fossil fuels leads to great amounts of CO_2 emissions. From the viewpoint of CO_2 emissions, the use of these fossil resources is not a sustainable way which will further contribute to global warming.

In recent years, even though many progresses have been made in developing the low-carbon and renewable resources such as hydropower, nuclear, solar and wind et al., we still see the signs that the economic growth is greatly dependent on the fossil fuel energy consumption and carbon emissions. According to the report of the Intergovernmental Panel on Climate Change (IPCC) in 2014 [2], fossil fuels continue to meet more than 80% of total energy demand, and over 90% of energy-related emissions are CO_2, produced by the fossil-fuel combustion. In **Fig. 1.1(a)**, the pie chart shows a breakdown of greenhouse gas production from different source. CO_2 took up around 76% of the overall annual gas emissions in 2010, in which around 68% of these are from the direct fossil fuel combustion, e.g., for the production of heat and electricity [3]. That is, exceeding 14 gigatonnes (Gt) of CO_2 had been generated in 2010 from anthropogenic energy demand and are projected to almost double or even triple by 2050, which are unequivocal ascription of the widespread influence to the physical and biotic environments by the climate change.[2] The total emissions amount of other greenhouse gases such as methane, nitrous oxide and fluoride gas is less than that of CO_2. The present amount of atmospheric CO_2 accounts for 8% of the natural greenhouse effect. The rapid increase in the atmospheric concentration of CO_2 to levels is thus well above those to be expected from natural fluctuations.

Because carbon cycles on the Earth are not able to remove the CO_2 (e. g. by burial in marine sediments) at the same rate as that it is emitted, this gas has accumulated in the atmosphere up to a concentration of 400 ppm to date [4]. As shown by the trends in **Fig. 1.1(b)**, these accumulations of CO_2 are projected to increase further over the next several decades. Due to the induced greenhouse effect, at the same time, the global

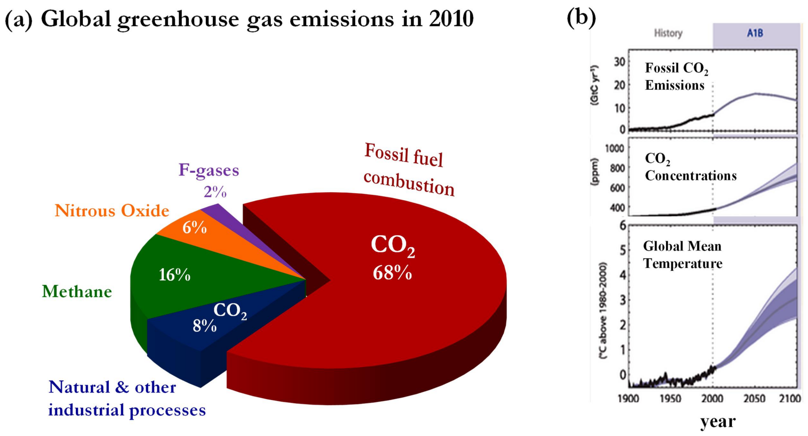

Figure 1.1 (**a**) Global greenhouse gas emissions exceeding 20 gigatonnes (Gt) in 2010 of which approximately 68% are represented by CO_2 emissions. (**b**) The trends of fossil CO_2 emissions, CO_2 concentrations and the global mean temperature in the history (1990 ~ 2000) and prediction in the next few decades till the year of 2100. Details about the sources included in these estimates can be found in the IPCC report (2014) in ref. [2].

mean temperature will increase up to 4 K expected by the year of 2100 with respect to the pre-industrial level. Although the long-term consequences of this global warming can't be fully predicted, most researches have assessed the more widespread negative influences coming to the ecosystem on this blue planet in terms of climate changes [4, 5].

1.2 A crisis derived from carbon dioxide

The climate changes due to massive emission of CO_2 are still in process on this planet and hence are considered as one of the main challenges of humankind at present. A warming above 2 K is predicted to cause serious problems such as life-threatening effects by droughts and extreme weather phenomena [3]. The mean global temperature combined land and ocean surface has a warming of 0.85℃ from the year of 1880 to 2012 [2]. As a result, the global warming has caused series of chain effects occurring on the land and the ocean. For example, on the land, changes are happening in water availability, agricultural productivity, biodiversity, the rise of sea level, the melting of permafrost and the greening of the Sahara et al., and finally it may worse the society stability and the world peace. For the ocean, the ice and glacier in Antarctica and Arctic sea are retreating. Ocean acidification ascribed to the absorption of emitted anthropogenic CO_2 has endangered the living marine organisms [6]. Moreover, the warming climate induces the environment changes underwater that the large quantities of organic carbons stored in ices and frozen soils (permafrost) release the greenhouse gases such as CO_2 and methane (CH_4) [4]. These environmental changes in turn accelerate the global warming.

To reduce the global warming, many countries had submitted their Intended Nationally Determined Contributions (INDCs) for the 21st UN Conference of Parties (COP21, Paris) in December 2015 and made the commitments to cut the GHG emissions and limit global temperature rise to 2°C above pre-industrial levels. To achieve the target of global warming staying below 2℃ without withdraw the economic growth prospects in any region, and to reduce or even finally eliminate the negative effects from climate changes, it is clear that energy use and CO_2 emission need to be decoupled and is emergency to develop new techniques to converse the CO_2 into useful chemicals and fuels such as urea, inorganic carbonates, or methanol (**Figure**

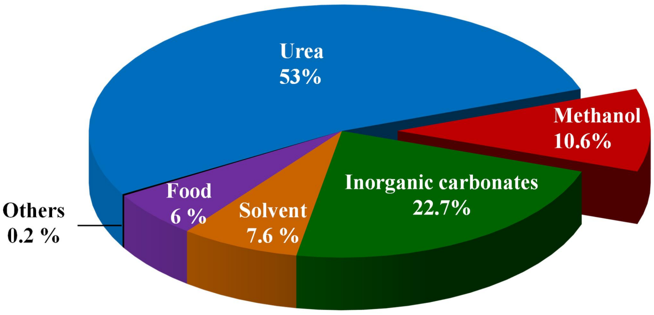

Figure 1.2 Current utilization of CO_2 exceeding 120 megatons (Mt) in industry annually of which methanol accounts for about 10.6% of the annual usage. Data retrieved from ref. [8].

1.2). However, the industry use amounts to only 0.5 % of the total anthropogenic CO_2 emissions, which is exceeding 20 Gt CO_2 annually [3]. Recently the dry reforming of natural gas, methanol (CH_3OH) synthesis and Fischer-Tropsch (FT) synthesis are the three most promising ways to manufacture of syngas, chemicals and fuels from CO_2, in which methanol produced from CO_2 only accounts for about 10.6% of the annual industry usage (**Figure 1.2**) [7]. Therefore, to expand their production capacities by clarifying their reaction mechanisms and developing much more active catalysts may change this critical situation. In turn, the renewable fuels explored actively can be expected to be alternatives to sustain the anthropogenic energy demands in future. Specially, methanol synthesis from CO_2 hydrogenation has gathered a prominent role in the field of CO_2 capture, utilization and storage (CCUS) because this liquid alcohol not only can be utilized as a fuel replacement but also can serve as a feed stock to produce other chemicals while these chemical almost currently obtained from oil and natural gas.

Among all the innovational technologies for CO_2 conversion, the thermal reduction, photo- and electro-chemical reduction are the three main current efforts by developing highly active, selective and environment friendly catalysts. Photo- and electro-chemical reduction of CO_2 would most likely operate on a smaller scale and be more expectable for the production of fine chemicals, while still are far away from practical utilization. But thermal reduction of CO_2 has been maturely applied to produce various useful chemicals [8], in particular, methanol is one of the most desirable and promising products. Because the methanol is not only the building stock for other chemicals, but also is potential sustainable synthetic energy source taking place of fossil fuels, which also is regarded as the foundation of “methanol economy” in the near future [5, 8, 9]. In industry, methanol is synthesized from the gas mixtures ($H_2/CO_2/CO$) at elevated pressures (i.e. 50 ~ 100 bar) and temperatures (i.e. 500 K ~ 600 K) over $Cu/ZnO/Al_2O_3$ catalysts. In this chapter, before further discussion of the mechanism of CO_2 activation on $Cu/ZnO/Al_2O_3$ in gas phase heterogeneous catalytic methanol synthesis, I would like to briefly review on the recent progresses in capture, photo- and electro-chemical conversion of CO_2 by using Cu-based catalysts.

1.3 Innovation in CO_2 -capture and chemical conversion processes

1.3.1 CO_2 capture

In a short term, the implementation of CO_2 capture, utilization and storage (CCUS) technologies is proposed as a means of enabling for CO_2 remove. The main existing CO_2 capture materials such as aqueous alkanolamine solutions and porous solids (i.e. zeolites and activated carbons) perform an important role in the carbon sequestration [10]. On the other hand, metal-organic frameworks (MOFs) have shown great potential applications in gas molecule separations and heterogeneous catalysis owning to their capability of adsorption sites and tunable pore chemistry et al. [11, 12]. As a case study, the $Cu(BTC)_2$ (BTC = benzene-1,3,5-tricarboxylate), namely HKUST-1[13, 14], has shown an excellent property for CO_2 storage, in which the Cu ion is cooperatively working with the adjacent amine behaving as a Lewis base for the adsorption of acid CO_2 molecule [15] .

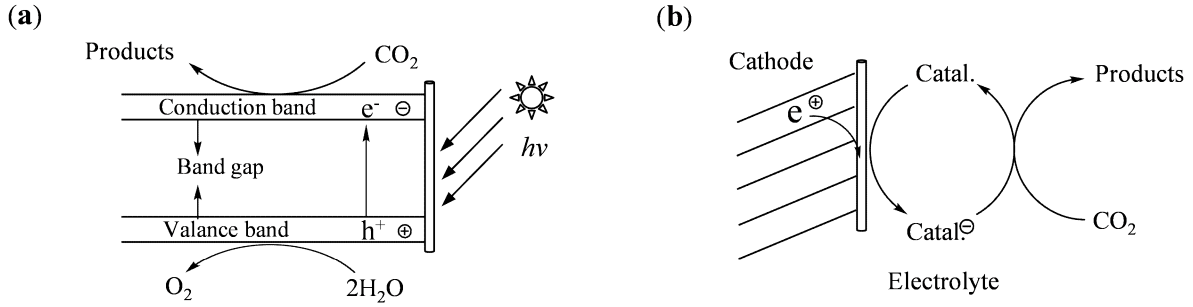

Figure 1.3 (**a**) Schematic representation of the catalyzed electron chemical reduction of CO_2. (**b**) Schematic representation of the mode of action of a photocatalyst for CO_2 reduction and concomitant water splitting.

1.3.2 Photocatalysis

In photocatalysis, it is well known that electron-hole pairs are generated in semiconductor materials excited by light absorption which are then separated and transferred to different sites for redox reactions as schematically shown in **Fig. 1.3(a)**. Here, we still take HKUST-1 as a substrate for example, when HKUST-1 combined with TiO_2 as a hybrid material $Cu(BTC)_2@TiO_2$ in a core-shell structure, electrons can be photo-generated effectively in semiconductor and transfer to CO_2 molecule which is adsorbed on the MOF. The CO_2 thus was activated and converted into CH_4 [16, 17]. Previous studies on Cu/TiO_2 photocatalysts which have shown carbon monoxide, trace amount of methanol and many hydrocarbons such as CH_4, C_2H_4 were produced from CO_2 photo-activations [18]. If ones want to improve the performance of photocatalysts for CO_2 activation, they should know that the quantum efficiency of semiconductor materials is critically based on the two key steps: (1) excellent charge separation, and (2) mild condition for CO_2 molecular adsorption and activation. However, challenges still are there for the photocataltic CO_2 conversion in a mild condition.

1.3.3 Electrocatalysis

Electrochemical reduction of CO_2 requires the use of unreactive metal or carbon electrode and an electric current to produce the required electrons for the formation of CO_2 radical anion as schematically shown in **Fig. 1.3(b)**. Products that can be formed include formic acid, carbon monoxide, methanol, methane and other hydrocarbons. In electrocatalysis, researchers showed that the primary hydrocarbon products on Cu electrodes are CH_4 and C_2H_4 instead of methanol and CO [19]. Interestingly, these electrochemical results conflict with the well-known fact in heterogeneous catalytic methanol synthesis from hydrogenation of CO_2

and CO formation from reverse water-gas-shift (RWGS) over Cu-based catalysts [20, 21]. The possible explanations were conducted that CH_4 and C_2H_4 are formed mainly from the reduction of the CO-H intermediate. After CO_2 is electronically reduced into CO* species on Cu, the aqueous environment promotes CO-H bond formation, and then the applied potential drives the forward reaction into the CH_4 and C_2H_4 production [22].

After all, people would much prefer to produce the fine chemicals by using photochemistry and electrochemistry. But for the industrial utilization of the recycling CO_2, thermal reduction still is a traditional and promising way for the massive chemicals production, like methanol synthesis.

1.4 Methanol synthesis from CO_2 hydrogenation

According to the report released by Information Handling Service (HIS), the global demand of methanol is 60.7 million metric tons (MMT) and is expected to increase significantly to more than 109 MMT in 2023 [23]. However, the annual production of methanol is around 40 MMT and it still is far from to satisfy the demands [24]. Methanol is the simplest and most versatile organic molecule, which is an essential industrial intermediate for the production of a variety of chemicals including formaldehyde, methyl *tert*-butyl ether and acetic acid [24]. Methanol also can be further hydrogenated into alkanes and olefins and performs as a liquid for hydrogen storage and is easy for the energy transportation.

The heterogeneously catalytic reaction of CO_2 and H_2 to produce methanol over Cu-based catalysts thus has been studied extensively. By using $Cu/ZnO/Al_2O_3$ catalysts, methanol is industrially synthesized from the gas mixtures ($H_2/CO_2/CO$) at the high pressures (i.e. 50 ~ 100 bar) and temperatures (i.e. 500 K ~ 600 K). Since the Cu-based catalysts are also catalytically active to the water-gas shift (WGS) reaction, which facilitates the conversion of CO to CO_2. Even though the controversy about the carbon source in the methanol synthesis still is there, most of the researchers agree with that the main carbon source of methanol comes from the CO_2 [25]. In principle, the chemical conversion of CO_2 into methanol can provide renewable, carbon-neutral source for the fuels. Besides of searching new catalysts, the industrial Cu/ZnO-based catalysts are still the hot research topics on the identification of the active sites [26-30].

1.4.1 Active sites of CuZn-based catalysts for methanol synthesis

Even though "methanol-Cu" catalysts have been extensively studied by using different support under various reaction conditions, there are still many controversies concerning the active sites, which are summarized in **Table 1.1**. Based on the previous research, the Cu metal, Cu/ZnO synergy and Cu-Zn alloy may be responsible for the active sites. These supports (such as Al_2O_3, SiO_2 and ZrO_2) generally show high thermal stability under the reaction circumstance of high pressure and high temperature. The role of support may be not limited to dispersing the active metal particles. It may also affect the catalytic performance due to the pore morphology, confinements and chemical effects et al.. However, it is generally accepted that the support highly deconcentrates the active metals and avoids them sintering. For CuZn-based catalysts, it is known that the adsorption of reactants intermediates, transition state and products at step-edge can decrease the energy barriers for the reactions involving transition state with a specific geometry [31-33]. Nano-sizing metal particles would be presented in the reaction conditions which would alter the surface structure and the local density of states for a specific surface site. Therefore, they show much difference in the CO_2 conversion ratio and the methanol catalytic productions. Take the industrial catalysts $Cu/ZnO/Al_2O_3$ for example, the space-time yield of methanol is high up to 7729 $g_{(MeOH)}/Kg_{(cal.\ h)}$. This intrinsic activity of catalysts has been revealed to be related with the stacking fault of the metal particles [26]. On the other hand, the catalytic activity is also determined by the gas pressure, ratio of CO_2 and H_2 in the syngas and the reaction

Table 1.1 Active sites of Cu-based catalysts and the performance for methanol synthesis

catalyst	active site	gas pressure (MPa)	ratio $H_2 : O_2$	reaction temperature (℃)	CO_2 conversion (%)	space-time yield [$g_{(MeOH)}/Kg_{(cal.h)}$]	year [ref.]
$Cu/ZnO/Al_2O_3$	1) Steps of Cu 2) $Zn^{\delta+}$	36	10:1	250	22.7	7729	2012 [34] 2014 [26]
$Cu–ZnO/\gamma$-Al_2O_3	1) Cu surface area 2) Cu–ZnO synergy	3	3:1	250	10.1	76.8	2013 [35]
Cu/ZnO	Cu–ZnO synergy	0.1	9:1	165	-	76.8	1998 [36]
Cu@ZnO (core-shell)	1) Cu–ZnO_x synergy 2) CuZn was inactive	3	3:1	250	2.3	147.2	2015 [37]
Cu/SiO_2	Cu and $Zn^{\delta+}$ synergy	6	3:1	220	5.3	~47.9	1992 [38] 2008 [39] 2009 [40]
Cu/ZrO_2	Encapsulation effect	1.7	3:1	220	4.4	65.3	1997 [41] 2003 [42]
$Cu/ZnO_2/ZrO_2$	Cu^+ on ZnO or/and ZrO	5	3:1	220	9.0	79.6	2004 [43]
$NiGa/SiO_2$	Ni-Ga intermetallic compounds	0.1	3:1	160-260	-	90-125	2014 [44]
Au/ZnO	Au–ZnO synergy	5	3:1	240	1	5.2	2015 [45]

temperature. In the recent research, to decrease the gas pressure and reaction temperature and looking for the mild reaction condition catalysts are the central to the most scientists. To achieve this target, fully understanding of the catalytic mechanism of methanol synthesis is necessary. However, according to recent theoretical paper containing a thorough review of the current state of our understanding shows that the details of mechanism are more complex than previously we thought. For the mechanism topic, we will discuss it in the latter part in this chapter.

On the other hand, the studies of non-Cu-based catalysts also have been explored and are expected to moderate to reaction conditions into ambient pressure and low temperature. The catalytic activities of these non-Cu catalysts are comparable to the Cu catalysts as shown in **Table 1.1.** For example, NiGa catalysts can reduce the CO_2 into methanol at ambient pressure and at the temperature of 160-260 ℃ [24, 25]. The oxide supported Au catalysts, specifically Au/ZnO materials show very low CO product concentration as 1% via the reverse water-gas shift (RWGS) reaction while have little effect on the efficiency of methanol formation [46]. The catalysts which limit the CO production and increase the reaction rate of methanol synthesis would be preferable.

Although $Cu/ZnO/Al_2O_3$ catalysts have excellent performance in the methanol synthesis, the Cu-based catalysis for methanol synthesis is a complicated system. Till now there are still many controversies on the active sites responsible for the reaction activity and the reaction mechanism of methanol synthesis. Here, we make a brief review of the current state of understanding on the active sites of CuZn-based catalysts.

(*i*) Cu performs as an active site

One important key is that the Cu surface has great contribution to the formation rate of methanol synthesis, which has been observed to scale linearly with the activity for sample families with a similar preparation method in several studies (as shown in **Fig. 1.4**). Therefore, it is generally accepted that Cu presents in the metallic state in the catalysts during methanol synthesis reaction conditions and methanol synthesis over Cu-based catalysts is a Cu structure-insensitive reaction. However, K. C. Waugh found that the liner relationship of Cu surface area-activity conflicts the volcano-type dependence of their Cu specific activity on ZnO content (see **Fig. 1.5(a)**) [47]. To solve this problem, he proposed there would be two types of specific activities of Cu. Hadden and co-worker discovered the same effects for the Cu activity with different surface area [48]. Therefore, now it seems that the data in **Fig. 1.4** can be refit better by the green dashed lines to specify the two specific activities. It shows that the Cu-base catalysts set with high Cu surface area, the activity for methanol synthesis is much higher comparing with the catalysts set with low Cu surface area, and the two sets catalysts are not linear. This Cu activity shifting phenomenon may be ascribed to the morphologies of the Cu surface with high area are changing by partly nano-sizing and the appearing strains of Cu surface induced by the reaction condition with high gas pressure.

On the other hand, in the early 35 years ago, Herman et al. studied these catalysts systems and suggested that the active species was a Cu^+ embedded in the support ZnO [46]. Later, Chinchen and Waugh confirmed that both metallic and oxidized copper had great contributions to the formation rate of methanol from the mixture gas ($CO_2/CO/H_2$) [49]. The studies on Cu/ZrO_2 or $Cu/ZnO_2/ZrO_2$ catalysts under the high pressure of mixture gas conditions also suggested the Cu^+ on ZnO or/and ZrO_2 are active sites [50], where Cu metal was encapsulated by the ZrO_2 and then charge transfer occurs from Cu to the oxide supports. Recently, Ahouari et al. attributed the active site to the Cu surface area, but they discovered that the methanol formation rate is not linear with the Cu surface area [44]. This fact conflicts with previous research that the activity of $Cu/ZnO/Al_2O_3$ was a linear function of the Cu metal area as discussed above, excluding poisoning but implicating sintering as the cause of the loss of activities [36]. Cu^+ ion is formed by a Cu atom losing an electron in the outer most electronic orbital $4s^1$. Therefore, Cu^+ would act as a Lewis base and be much easier to denote another electron in the outer most electronic orbital to the CO_2 molecule as Lewis acid.

(*ii*) Morphology effects of Cu-ZnO system

Although ZnO component has negligible catalytic activity on his own and Cu can function alone as a methanol synthesis catalysts, ZnO can substantially boost the activity performance of $Cu/ZnO/Al_2O_3$ by the synergy of Cu-ZnO [26, 51-54]. The Cu-ZnO system is thus considered as a prototype for studying the complex catalytic process for the CO_2 conversion. As shown in **Fig. 1.5(a)**, activity of Cu-ZnO for methanol shows a volcano shape as a function of ZnO content. Some of explanations have been presented by the extensive studies, including:

(1) morphological changes of Cu on ZnO depending on the gas atmosphere [51, 55].

(2) support-induced stain in Cu [56].

(3) ZnO_x species/layers covering part of Cu nanoparticles, which is denoted as a strong metal-support interaction (SMSI) [26, 51, 57].

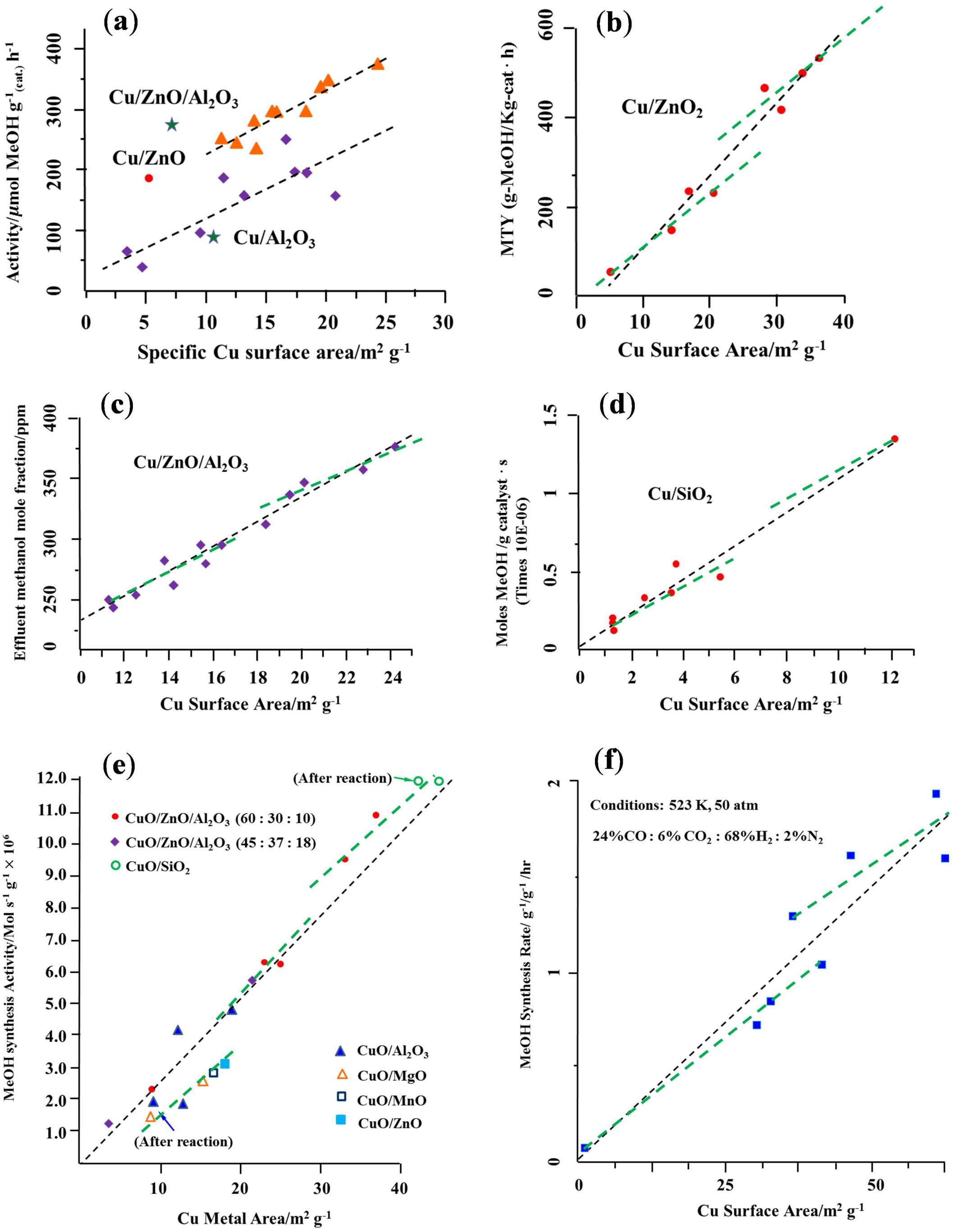

Figure 1.4 Cu Area-activity relationships for various Cu-based catalysts in independent experiments. (**a**) binary (purple rhombus) and ternary (yellow triangle) Cu-based catalysts [58]. (**b**) Cu surface area of Cu/ZnO catalysts [59]. (**c**) Cu surface area of Cu/ZnO/Al$_2$O$_3$ catalysts [60]. [**d**] Cu surface area of Cu/SiO$_2$ catalysts [61]. (**e**) Cu surface area of various Cu-based catalysts [62]. (**f**) Cu surface area of Cu/ZnO catalysts [63]. (a) ~ (f) are redrawn from the references, respectively. The black dashed fitting lines are the original with respect to every reference, while the green dashed fitting lines are proposed in the present thesis.

Table 1.2 summarizes some of the typical studies and the most of the listed catalysts show that catalytic reactions occur under the synergy of Cu and ZnO by changing the morphology of the Cu surface by the wetting on ZnO supports. The presence of defects on the ZnO surface crystallites may have an essential effect on the activity of the Cu/ZnO-based catalysts [64]. Beinik et al. studied the Cu nanoparticles (NPs) on ZnO(0001) as a model to study the interaction between Cu and ZnO [55, 65]. After annealing, the ZnO(0001) surface structure is changed by the surface-directed migration of positively charged subsurface defects. When Cu/Zn(0001) was heated, the sample became to have a fine atomic layer dispersion (wetting) of the initial 3D Cu NPs over the ZnO(0001) surface, that is, the size of Cu NPs becomes smaller, which is differ to the normal observed Cu particles sintering in the high temperature reaction conditions [66]. Although the ZnO in ultrahigh vacuum experiments shows a very low activity toward methanol synthesis [67, 68], in high temperature and high pressure reaction conditions, the oxygen vacancies produced in ZnO serve as active sites for CO_2 dissociation and the following hydrogenations [69].

Table 1.2 Morphology effect

catalysts	reaction condition	catalytic properties
Cu/ZnO [49]	493 K, $H_2/CO_2/CO_2$ 10^3 mbar	Wetting/non-wetting phenomena: smaller Cu particles (10 ~ 15 Å) with low Cu-Cu coordination numbers are formed on ZnO surface.
Cu/ZnO(0001) [66, 70]	0.3 ML Cu on ZnO(0001), 400-575 K	The surface-directed migration of subsurface defects affects the Cu adhesion on polar ZnO(0001).
Cu/ZnO; Cu/SiO_2 [55, 65]	493 K, $H_2/CO/CO_2$, 1.5 mbar	(1) The change in particle morphology is related to a change in the number of oxygen vacancies at the Zn–O–Cu interface. (2) Under similar condition, no morphology effects are observed when Cu is supported on SiO_2.
Cu/ZnO [71]	500 K, CO: H_2 = 1 : 1, 4 bar	(1) A pretreatment with H_2 : CO = 1:1 gives more active Cu nanoparticles than a pretreatment with either pure H_2 or CO. (2) Synergetic effect of the simultaneous presence of CO and H_2 in the pretreatment of the Cu/ZnO-based catalyst.

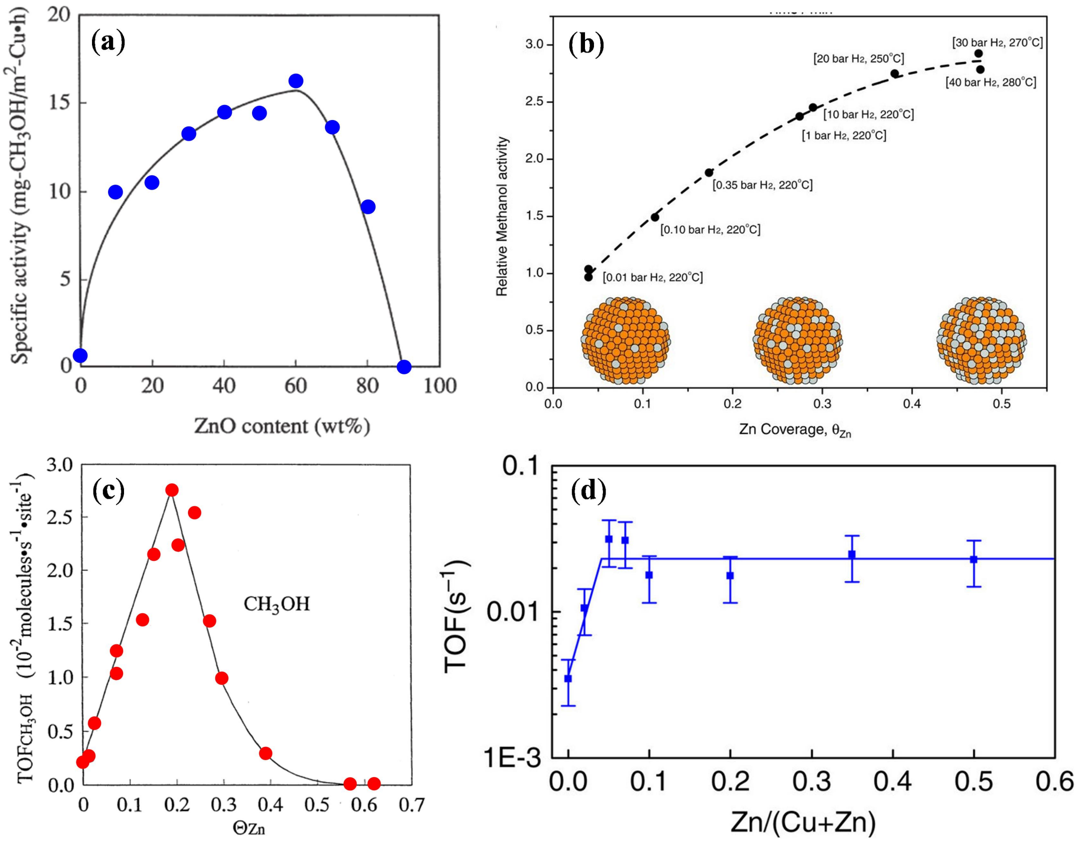

Figure 1.5 The Zn component effects in the CuZn catalysts on the methanol synthesis. (**a**) Specific activity for methanol synthesis as a function of ZnO content in the Cu/ZnO catalyst [59]. (**b**) Relative measured methanol exit concentrations as a function of postreaction values of θ_{Zn} [28]. (**c**) Turnover frequency (TOF) for the methanol formation at 523 K as a function of the θ_{Zn} on the Zn/Cu(111) model catalyst [72]. (**d**) Effect of zinc loading for CuZn/HSAG (high-surface area graphite) on the TOF for methanol formation [73].

(*iii*) Cu-Zn alloy as active sites

Cu-Zn site is found to be responsible for the active site of methanol synthesis from CO_2 and H_2. As shown in **Fig. 1.5(a)** and **Fig. 5(c)**, The TOFs for methanol formation show volcano shape as a function of ZnO content and Zn coverage, respectively. That is, TOF increases linearly with ZnO content below 60wt% for Cu/ZnO catalyst and Zn coverage below $\theta = 0.19$ for Zn/Cu(111) catalyst, respectively. In contrast, the TOF then decreases till the ZnO content drop to 90% and $\theta_{Zn} = 0.5$, respectively. However, **Fig. 1.5(b)** shows different experimental results. That is, the activity increases for θ_{Zn} in the range 0.04 to 0.47. This data indicates that the methanol activity may reach a maximum near $\theta_{Zn} \approx 0.47$. The resean for this difference is not fully understood, but Nakamura et al. has suggested that the loss of activity at higher values of θ_{Zn} resulted from large coverage of ZnO [74]. In **Fig. 5(d)**, the activity increased on increasing Zn loading until the maximum activity was reached at a Zn/(Cu + Zn) atomic ratio of 0.05. A further increase in Zn loading did not change the activity significantly. The author thus explained that the promotion effect for Zn containing catalysts seems to be inherent to the nature and related thermodynamic stability of the Zn phase. Under the real catalytic condition, the CuZn alloy is formed, because some ZnO are reduced by the H_2

gas at 550 °C [27, 41]. However, if the Cu-ZnO is a core-shell structure (Cu@ZnO), the CuZn formed in the reaction condition is not the active site for methanol synthesis anymore. This CuZn alloy can promote hydrogenation of formate to methanol, while the CO_2 is hydrogenated to formate ($HCOO_a$) intermediates of methanol synthesis on metallic Cu surfaces. That is, the Zn in CuZn alloy is not involved in the formate formation by hydrogenation of CO_2 as the initial step for methanol synthesis on Cu-based catalysts.

The above discussion concerning the active site and the role of Cu and ZnO in the $Cu/ZnO/Al_2O_3$ methanol synthesis catalysts can be consistently explained based on the experimental results in the hydrogenations of CO_2. Here we summarize the previous results concerning the role of ZnO and the active site for methanol synthesis from CO_2 hydrogenation based on the surface science model and powder samples, as shown in **Table 1.3**.

Table 1.3 Alloy effect

catalysts	reaction condition	catalytic properties
Zn/Cu(111) [55, 65]	523 K, H_2/CO_2 =0.3, 1.8 MPa	(1) $TOF_{(CH3OH)}$ linearly increased 12 times greater than Cu(111) after Cu(111) was decorated with 19% of Zn. (2) Active state is metallic Zn and Cu as surface alloy. (3) Zn has no promotion effect to the formate synthesis.
Mixture of Cu/SiO_2 and ZnO/SiO_2 (1:3) [75]	523 K, H_2/CO_2 =3, 5 MPa	(1) Migration of Zn from the ZnO particles to the Cu particles. (2) Zn has no promotion effect to the formate synthesis.

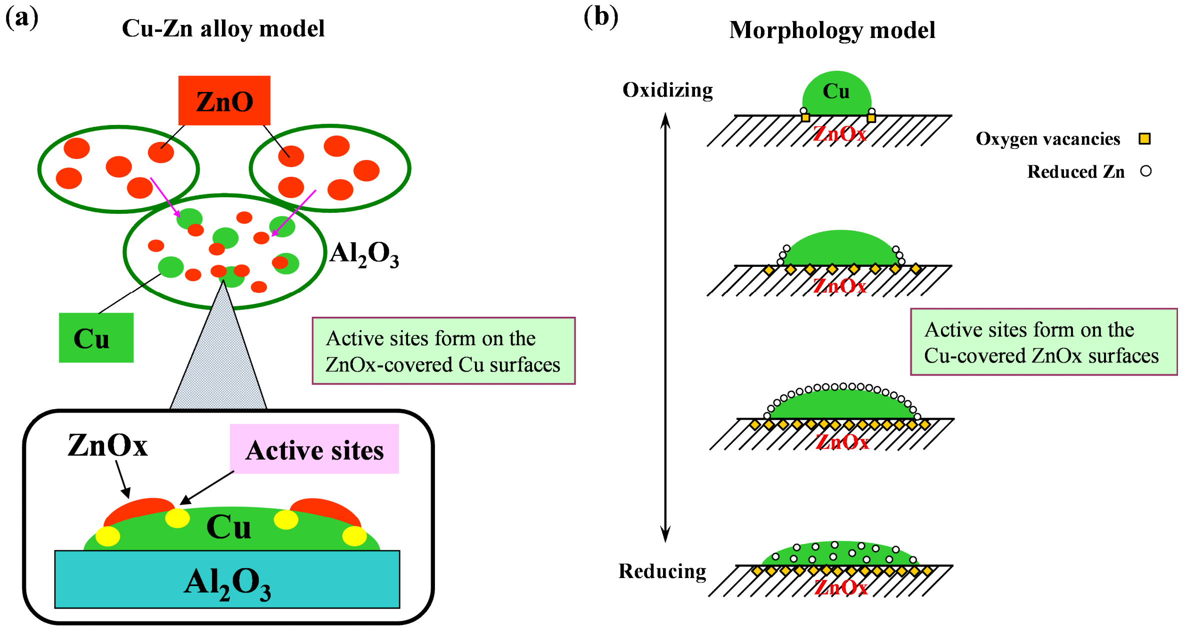

Figure 1.6 (a) Cu-Zn model of active site by Fijitani and Nakamura; The red and green spots represent ZnO and Cu, respectively; **(b)** Morphology model effects by proposed by Topsoe et al.. The yellow squares and white circles stand for oxygen vacancies and reduced Zn, respectively.

Hence, after the above introduction, surface science people would like to say the Cu surfaces have some catalytic activity for methanol synthesis by CO_2 hydrogenation. There are thus two active site models concerning Cu/ZnO-based catalysts which were proposed based on the different experimental research. As shown in **Fig. 1.6(a)**, the mixed system of Cu and ZnO particles is usually comparable to the industrial Cu/ZnO-based catalysts which contain 40% ~ 60% of Cu particles. Under the reaction condition, the ZnO particles climb on Cu surface, the ZnO_x-covered Cu surfaces thus are formed. The boundary of ZnO_x and Cu surface is corresponding to the active site for methanol synthesis, while Cu and ZnO_x are separated in a system, the catalytic activities greatly decreased. On the other hand, researchers also propose morphology model, which is with highly dispersed Cu particles or small Cu clusters on ZnO surface as shown in **Fig. 1.6(b)**. Under the reducing atmosphere such as H_2 and CO gases and high reaction temperature, the oxygen vacancies appear in the near surface of ZnO_x. That is, the oxygen is removed from the surface and the bulk of ZnO_x. The accompany process is the Cu particle is wetting on the ZnO_x and the reduced Zn atoms diffuse onto the Cu particles. The active sites formed on the Cu-covered ZnO_x surface are responsible to catalytic activity of methanol synthesis.

1.4.2 Single crystalline Cu surfaces for methanol synthesis

Actually, the single crystalline Cu surfaces have a little activity on the methanol synthesis without Zn component under the high pressure of mixture gas CO_2/H_2. As summarized in the **Table 1.4**, of course the turnover frequencies (TOFs) of methanol synthesis are different due to the various reaction conditions such as the ratios of CO_2 and H_2 gas, the reaction temperatures et al.. However, the activation energies are comparable in these reactions. Therefore, we proposed that methanol synthesis may be independent on the

Cu surface structure based on the similar TOFs of methanol under the same conditions and the similar activation energy. This may be due to the defects on Cu surfaces which play an active site promoting reactivity of formate ($HCOO_a$) to methoxy (CH_3O_a), and then to the final methanol product.

Table 1.4 Single crystalline Cu surfaces for methanol synthesis

catalyst	reaction conditions	TOF$_{(CH3OH)}$	activation energy	reference
Cu(111)	523 K, CO_2/H_2=1:3, 18 atm	2.1×10^{-3}	74 ± 7 kJ/mol	Nakamura et al.[76]
Cu(110)	a. 530 K, CO_2/H_2=1:11, 5 atm b. 523 K, CO_2/H_2=1:3, 18 atm	a. 8.0×10^{-3} b. 8.0×10^{-3}	a 67 ± 17 kJ/mol b. 80 ± 5 kJ/mol	a. Campbell et al.[75] b. Nakamura et al.[77]
Cu(100)	a. 543 K, CO_2/H_2=1:1, 2 atm b. 523 K, CO_2/H_2=1:3, 18 atm	a. 2.7×10^{-4} b. 3.0×10^{-3}	a. 69 ± 4 kJ/mol b. 77 ± 2 kJ/mol	a. Chorkendorff et al.[78] b. Nakamura et al.[79]
Poly-Cu	510 K, CO_2/H_2=1:11, 5 atm	1.2×10^{-3}	77 ± 10 kJ/mol	Campbell et al.[78]

1.4.3 The mechanism of methanol synthesis over Cu-based catalysts

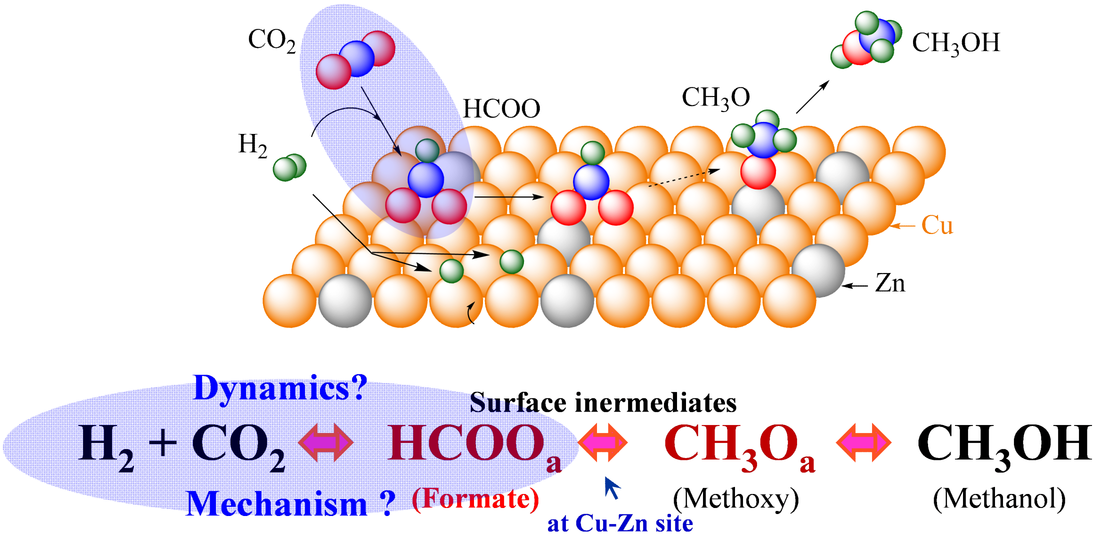

Figure 1.7 The proposed main catalytic mechanism of methanol (CH_3OH) synthesis from CO_2 hydrogenation over CuZn-based catalysts. Formate and methoxy are considered as two important intermediates and other intermediates are between of them. To further hydrogenation of formate, Cu-Zn site is necessary.

Besides controversy of active “methanol copper” for methanol synthesis, the reaction mechanism is far away from the fundamental understanding for the conversion of CO_2. As we mentioned above, CO_2 is the main carbon source for the methanol synthesis. Grabow and Mavrikakis have tried to study a comprehensive catalytic process of methanol synthesis containing a thorough review of our understanding till now by theoretical calculation, which shows that complex details of the mechanism [22]. That is, using a Cu(111) surface as a model for the industrial catalyst $Cu/ZnO/Al_2O_3$, adsorbed formic acid ($HCOOH_a$), which is competitive to the final product formation [80]. adsorbed $HCOOH_a$ intermediate and the hydrogenation of $HCOOH_a$ is proposed in the reaction occurs on the Cu-Zn alloy model as Zn/Cu(111) [22]. The common main elemental steps of the methanol synthesis on Cu(111) surface is reproduced on Cu nanoparticles [26], in which the reaction proceeds through the formation of $HCOO_a$, H_2COO_a (dioxomethylene), H_2CO_a, H_3CO_a (methoxy), and the final product methanol. However, over CeO_2/Cu(111) catalysts, $OCOH_a$ is formed rather than formate, while in the experiment, the observed formate formed from CO_2 hydrogenation was treated as an reaction spectator [81]. After summarizing many previous studies on the mechanism of methanol by using CuZn-based catalysts, **Figure 1.7** schematically presents simply the most possible reaction pathway for the conversion of CO_2 and H_2 to CH_3OH over CuZn-based catalyst. Formate ($HCOO_a$) can be formed firstly on the Cu surface or CuZn alloy. To further hydrogenation of formate, Zn component is necessary. Before obtaining the final product of methanol, methoxy (H_3CO_a) species is formed on the CuZn active site. Normally, the CO_2 molecule doesn’t need to dissociate into CO_a and O_a and can be directly convert to methanol on the Cu-based catalysts. Namely, the whole CO_2 molecule conversion not only increases the carbon conversion to methanol, but also reduces the additional energy to dissociate C=O bond(s) to form CO. From the review on the mechanism of methanol synthesis over CuZn-based catalysts, the formate ($HCOO_a$) is the essential and initial intermediate for the final methanol synthesis.

1.5 CO_2 conversion into formate ($HCOO_a$) On Cu-based catalysts

Formate ($HCOO_a$) is an important intermediate species in methanol synthesis on Cu-based catalysts which is formed by initial hydrogenation of CO_2. The methanol synthesis is normally accompanied by the CO production via the reverse water-gas shift reaction (RWGS: $CO_2 + H_2 \rightarrow CO + H_2O$), which decreases the carbon conversion from CO_2 to methanol. Recent studies have shown that these two competitive reactions don’t share the same intermediate-formate in the initial step of CO_2 hydrogenation on Cu surface [82]. To reduce the CO production and to promote methanol production, the design of highly active catalysts for methanol synthesis is required on the basis of a deep understanding of CO_2 activation on catalysts in terms of kinetics and dynamics.

1.5.1 The role of formate ($HCOO_a$) intermediate in methanol synthesis on Cu/ZnO catalysts

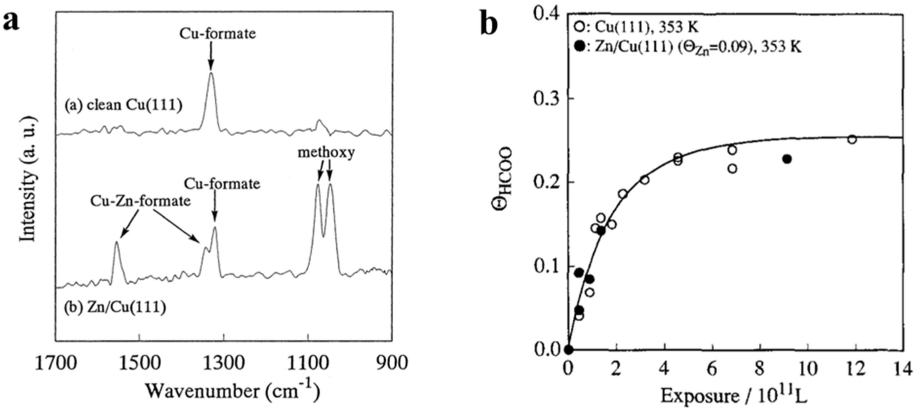

Figure 1.8 (a) In situ IR absorption spectra of formate species and methoxy species on clean Cu(111) and Zn/Cu(111) during CO_2 hydrogenation at 343 K and 760 torr. **(b)** The coverage of surface formate species on Cu(111) and Zn/Cu(111) as a function of exposure at 353 K and 760 torr [83].

As we have discussed above, formate ($HCOO_a$) and methoxy (H_3CO_a) species have been clarified as the two important intermediates for the methanol synthesis on Cu-based catalysts. In particular, the hydrogenation of CO_2 into formate intermediates ($HCOO_a$) is an important reaction step for methanol synthesis insofar as it represents the initial activation process of CO_2 on Cu surfaces; this is because: (1) the reaction probability of the formation of formate is very low (i.e. ~10^{-12}) at 340 K, which is comparable to the reaction probability of methanol synthesis as 3×10^{-12} at 523 K [84]. (2) Cu-formate has been provedto be the active intermediate rather than a spectator for the methanol synthesis over the CuZn-based catalysts [84, 85]. Additionally, our previous studies have shown only Cu has great contribution to the formate formation. The formate species on Cu is migrated onto Cu-Zn site at which the formate is hydrogenated to methoxy species, that is, the role of Zn is to promote the hydrogenation of formate. In this sense, the Zn active species on Cu surface doesn't promote the formation of formate species, which has been confirmed by the studies of (Zn)Cu/SiO_2 [6]. As shown in **Fig 1.8(a)**, methoxy is formed by the formate hydrogenation on Zn deposited Cu(111) surface. **Fig. 1.8(b)**, the formate species are on both of Cu(111) and Zn/Cu(111) surfaces. The identical curves mean that formate is formed on the Cu surface with similar reaction probability (~10^{-12}). Therefore, the study of Cu-formate from CO_2 conversion is essential to the development of the methanol synthesis.

1.6 CO_2 electronic structure and activation chemistry

Before to continue the topic of formate chemistry on Cu catalysts, I turn to summarize and discuss the CO_2 electronic structure and activation chemistry. CO_2 molecule has a closed shell linear system with a $^1\Sigma_g^+$ symmetry in its electronic ground state. The electronic structure of CO_2 may be represented by a Walsh diagram [86]. **Figure 1.9** shows the Walsh diagram and the molecular orbital diagram of CO_2.

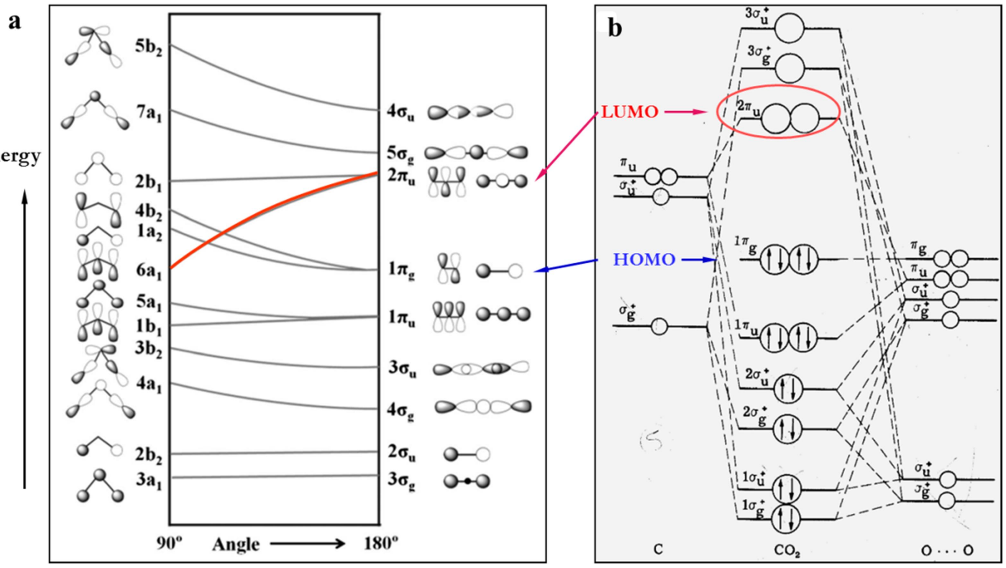

Figure 1.9 (a) Walsh diagram of CO_2 orbital energies in linear and bent geometries (ref. [87], redrawn from ref. [88]). **(b)** Molecular orbital diagram of CO_2.

In **Fig. 1.9(a)**, the right hand side is the schematic drawings of molecular orbitals in an energy sequence. The left hand side reflects the orbital's symmetry properties. **Figure 1.9(b)** depicts the molecular orbitals diagram of CO_2. CO_2 molecule has 22 electrons of which 6 occupy the core 1s orbital, and the rest 16 valence electrons are distributed over four σ-orbitals and two π-orbitals. The highest occupied molecular orbital (HOMO) is assigned as $1\pi_g$ orbital. The lowest unoccupied molecular orbital (LUMO) is the $2\pi_u$orbital. The activation of CO_2 can be judged by the stability of the linear geometry in a qualitative way and the energy positions of the occupied and unoccupied orbitals upon bending the linear geometry (in ground state). We can clearly see that σ-orbital energies a little or almost unchanged from linear to the bent configuration. However, the π orbital energies show pronounced alterations and the degeneracy is split into two components. The splitting for $1\pi_u$ and $1\pi_g$ (HOMO) is not large comparing to $2\pi_u$ orbital (LUMO). The $2\pi_u$ orbital degeneracy splits into two component $2b_1$ and $6a_1$. The $2b_1$ orbital in a plane structure with energy almost unchanged upon bending, whereas the $6a_1$ component (out of plane) decreases sharply in the bending structure and has the similar energy with HOMO. Because the $2\pi_u$ orbital is the only valence orbital, the $2\pi_u - 6a_1$ molecular orbital is very important in determining the bond angle in the activation of CO_2. If the CO_2 activation reaction involves electron transfer from catalyst surface into the CO_2 molecule, the electron would firstly have an occupation of this orbital to form CO_2^-. That is, any excitation makes the electron across the HOMO-LUMO gap in the linear CO_2 molecule will lead to excited states with a preferable bending structure. It is thus considerable to expect that energetically favored reaction will involve the anionic species. On the other hand, if the charge transfer occurs from the CO_2 molecule to the surface, we would have to consider the formation of a CO_2 cation, which is favor of the linear structure.

Figure 1.10 shows a schematic potential energy surface of the electron attachment process [9, 10], the schematic potential energy diagram of CO_2 and CO_2^- being plotted as a function of the C–O distance and the O–C–O bond angle. The ground state of the CO_2 system is shown at R_{co} = 1.15 Å representing the linear system with an enthalpy of formation of -1650 kJ mol^{-1} [11]. The double-well ground state of the CO_2 at R_{co} = 1.24 Å, represents a bent geometry with elongated C–O bonds and an enthalpy of formation -1604 kJ mol^{-1}, i.e. about 0.50 eV higher than linear CO_2 [12]. The CO_2^- ion is metastable with a life time of 60–90 μs [13, 14], indicating that it can be identified by spectroscopy [15]. Elliott et al. reported the CO_2 decomposition on Cu component of a commercial Cu/ZnO/Al_2O_3 catalyst with different activation energies in the temperature range 393–513 K [16]. The value of the activation energy for CO_2 decomposition on Cu component depends on the morphology of the Cu but is not determined by the reaction dynamics, i.e., by the CO_2 being required to be in vibrationally excited state [17]. This phenomenon may be explained by that the CO_2 decomposition on Cu component of Cu/ZnO/Al_2O_3 through a precursor state of carbonate [18]. However, formate synthesis from CO_2 hydrogenation over Cu catalysts is suggested to be a surface structure insensitive reaction via Eley-Rideal type mechanism by both of experimental methods and density functional theory (DFT) calculations [4, 19-21]. Therefore, the formate formation from CO_2 hydrogenation is preferred kinetically and dynamically, and CO formation from CO_2 dissociation is thermodynamically favorable.

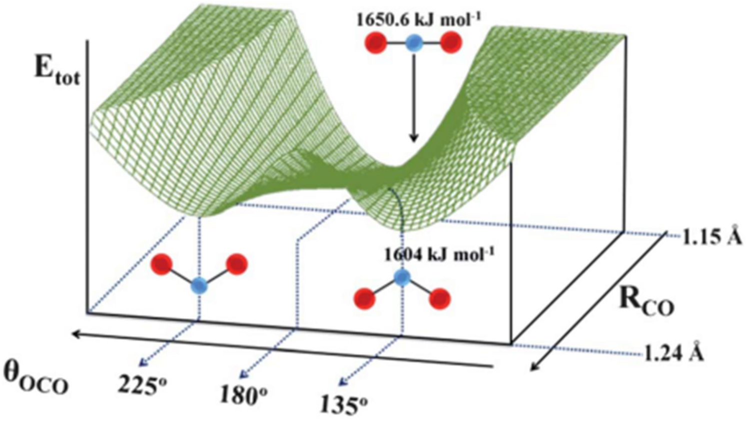

Figure 1.10 Schematic potential energy diagram connecting linear neutral CO_2 with bent anionic CO_2^- (ref.8 and ref.10).

1.7 Suggestion of Eley-Rideal type mechanism for formate synthesis from CO_2 over Cu-based catalysts

This study of formate synthesis via ER type mechanism may be the first report in the context of industrial catalytic reactions, which should have significant importance with respect to industrial catalytic processes of CO_2 conversion. That is because, according to this process, we need not supply energy to the catalyst in the initial elementary step. Instead, we can convert CO_2 to formate on Cu simply by exciting CO_2. Although the methanol is the terminal target product from CO_2 by multi-step hydrogenation, formate is an important intermediated involved in the rate-determined step of methanol synthesis and its formation rate is initial and essential to the development of methanol synthesis. Based on this work, active catalysts and efficient catalytic systems of CO_2 conversion can be developed under thermal non-equilibrium catalytic conditions.

CO_2 chemistry over Cu-based catalysts is of great technological interest due to the fact that Cu/ZnO/Al_2O_3 is still a very active and essential catalyst for industrial methanol synthesis from CO_2 as the main carbon source. In past 20 years, the catalytic synthesis of methanol has been extensively studied in industrial reaction conditions and by the surface science in ultra-high vacuum (UHV) conditions. In particular, we have proposed an Eley-Rideal (ER)-type mechanism for the initial surface conversion of CO_2 on Cu catalysts, thereby suggesting a key method of achieving methanol synthesis. We discuss the ER mechanism in terms of the following two points:

(1) In homogeneous catalytic systems, the ER-type formate synthesis we proposed is analogous to the

insertion of a CO_2 molecule directly into a Cu-H bond in organometallic copper hydride complexes without CO_2 binding with Cu.

(2) In the heterogeneous context of CO_2 hydrogenation to form formate on Cu surfaces, the direct reaction was initially proposed for proceeding via E-R type mechanism by the observed Cu structure-insensitive character.

1.7.1 CO_2 organometallic catalytic reduction chemistry

In homogeneous catalytic systems, copper hydride complexes are versatile reagents with new applications in the CO_2 reductions. Here, we summarized kinds of copper hydride complexes which are studied for the reduction of CO_2 [29-33].

(a) Stryker's reagent: $CuH(Ph_3)_n$ (n = 2, 3)

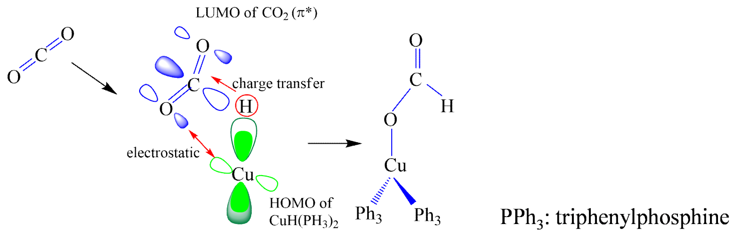

(b) Hexameric copper hydride: $[HCuPPh_3]_6$

$$[HCuPPh_3]_6 + 6PPh_3 \xrightarrow{CO_2} HCOOCu(PPh_3)_2$$

(c) μ-Hydrido Dicopper Cation: $[\{(IDipp)Cu\}_2(\mu\text{-}H)]^+$

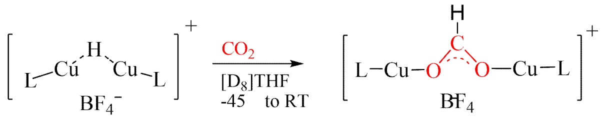

(d) Cu ligated N-heterocyclic carbenes (NHCs): $[(NHC)Cu\text{-}H]_2$

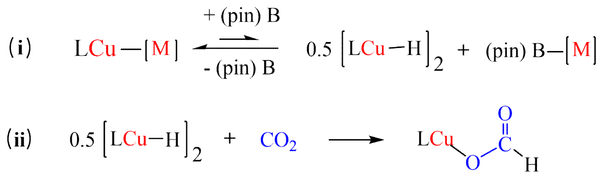

Figure 1.11 Eley-Rideal type formate synthesis we proposed is analogous to the insertion of a CO_2 molecule directly into a Cu-H bond in organometallic copper hydride complexes without CO_2 binding with Cu.

From the homogeneous catalytic systems (a) ~ (d) (see **Fig. 1.11**), Cu–H plays as an active site for the CO_2 reduction by the hydrides complexes. Take the Stryker's reagent $CuH(Ph_3)_2$ complex, as shown in **Fig. 1.11(a)** for example, the CO_2 molecule can directly insert into the Cu–H bond. That is, the charge from highest occupied molecular orbital (HOMO) of $CuH(Ph_3)_2$ to the lowest unoccupied molecular orbital of CO_2 [89].

According to an *ab initio* MO study [32], there is probably an electrostatic repulsion between $Cu^{\delta+}$ and $C^{\delta+}$. It has been reported that the activation barrier was estimated to be small as 0.56 eV, indicating that the insertion of CO_2 into Cu(I)–H bond was facile. For more reaction details, the $CuH(Ph_3)_2$ moiety is slightly distorted, but the CO_2 molecule has significant distortion with a large bending angle (OCO at an angle of 147°), which greatly decrease the CO_2 π^*orbital energy. On the other hand, the H ligand can interact with CO_2 because of the nondirectional 1s valence orbital. As a result, as illustrated in **Fig. 1.12**, CO_2 interacts with the H ligand through the charge-transfer interaction from the occupied orbitals of $CuH(Ph_3)_2$ (The HOMO includes the significant contribution of the H 1s orbital) to π^*orbital of CO_2 molecule and the electronstatic interaction between $Cu^{\delta+}$ and $O^{\delta-}$ atoms. Additionally, the charge-transfer interaction from O to Cu contributes to the Cu–O bond formation in the last stage of the reaction [34].

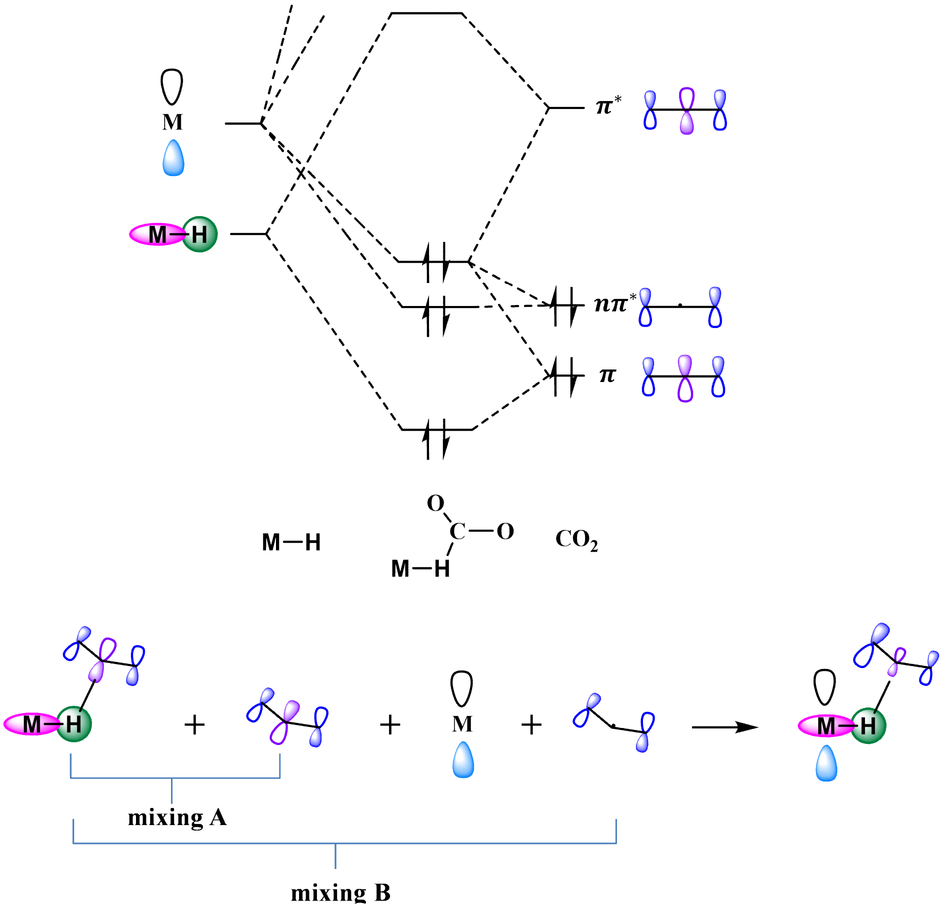

Figure 1.12 The direct reaction of CO_2 molecule with H atom by a insertion of with Cu-H hydride in $CuH(Ph_3)_2$, [90, 91].

Here we proposed the ER-type mechanism is analogous to the formate synthesis by insertion of a CO_2 molecule directly into a Cu(I)-H bond in organometallic copper hydride complexes without CO_2 binding with Cu. In particular, in the μ-hydrido dicopper Cation: $[\{(IDipp)Cu\}_2(\mu\text{-}H)]^+$, the Cu-Cu distance was calculated at 2.509 Å, as shown in **Fig. 1.11(c)**, which is the comparable to the distance of the two nearest neighboring Cu-Cu atoms in the single crystal surface such as Cu(111), Cu(110) and Cu(100).

1.7.2 Formate synthesis from the hydrogenation of CO_2 on Cu catalysts

Besides Vesselli et al. have reported that the fromate synthesis from a coadsorbed CO_2 molecule and a hydrogen adatom via Langmuir-Hishelwood (LH) mechanism on Ni(110) surface [92]. Taylor et al. have also suggested that the formate synthesis on Cu(100) surface proceeds a LH mechanism by kinetic studies [35], based on this suggestion, Nakano et al. first kinetically analyze the data and assuming the following elementary reaction steps [93]:

$$\tfrac{1}{2}H_{2,g} + * \rightleftharpoons H_a \tag{1}$$

$$CO_{2,g} + * \rightleftharpoons CO_{2,a} \tag{2}$$

$$H_a + CO_{2,a} \rightarrow HCOO_a \tag{3}$$

where the $*$ and the subscript a represent a vacant site and an adsorbed state, respectively. The reverse reaction of eq. (3) is considered to be neglected at a low temperature range of 323–363 K. The initial reaction rate of formate formation $r_{0,LH}$ was obtained as:

$$r_{0,LH} = kP_{H_2}^{1/2}P_{CO_2} / (1 + k'P_{H_2}^{1/2})^2 \tag{4}$$

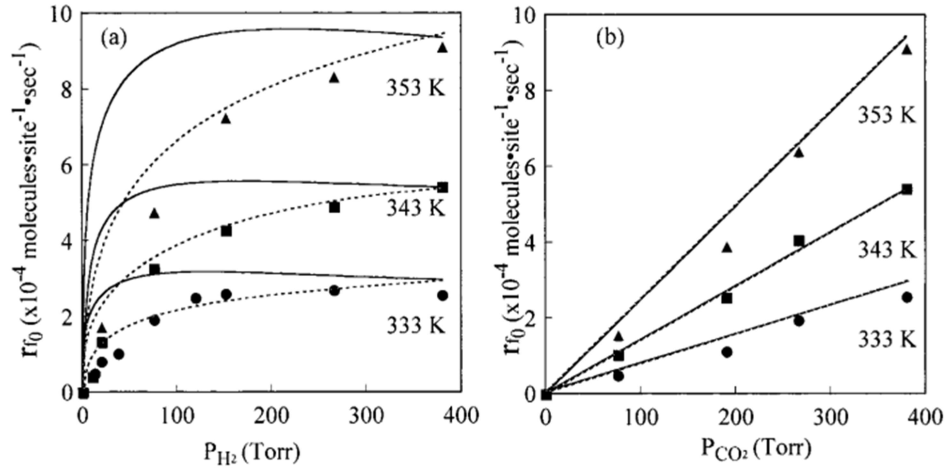

Figure 1.13 Dependence of the initial formation rate of formate on (**a**) H_2 pressure (P_{CO2}= 380 torr constant); (**b**) CO_2 pressure (P_{H2}=380 torr constant). Black spots are the experimental value. Solid lines represent the assuming LH mechanism from calculation, dashed lines represent the assuming ER mechanism [85].

From eq. (4), we see that the initial reaction rate depends on H_2 and CO_2 pressures, in which the reaction rate in the LH mechanism as the function of H_2 and CO_2 pressures was thus calculated as shown in **Fig. 1.13** as solid lines.

On the other hand, we have already proposed that formate is formed from CO_2 via an ER-type mechanism based on the kinetics of pressure dependencies in high-pressure experiments on Cu(111) single-crystal surfaces [94, 95]. That is, CO_2 directly attacks a hydrogen adatom without being trapped on the Cu surface. The reaction is presented by the following equations.

$$\tfrac{1}{2}H_{2,g} + * \rightleftharpoons H_a \tag{5}$$

$$CO_{2,g} + H_a \rightarrow HCOO_a \qquad (6)$$

The unique kinetic feature of this reaction is the H_2 pressure dependence on the initial reaction rate of formate synthesis, $r_{0,ER}$:

$$r_{0,ER} = kP_{H_2}^{1/2}P_{CO_2} / (1 + k'P_{H_2}^{1/2}) \qquad (7)$$

where k and k' are rate constants, and P_{H_2} and P_{CO_2} are the pressures of H_2 and CO_2, respectively [85, 95]. The initial reaction rate in the ER type mechanism was also calculated as dashed lines in **Fig 2.7**. The dashed lines are perfectly fitting to the experimental data. Therefore, Nakano et al. suggested that the formate synthesis from the reaction of H_2 and CO_2 on Cu surface proceeds ER mechanism. That is, the first order in the denominator $(1+k'P_{H_2}^{1/2})^1$ indicates that the adsorbed hydrogen formed as a major adspecies under the steady-state hinders the adsorption of H_2, but does not hinder the adsorption of CO_2. If we assume that the reaction rate is determined by the kinetic or internal energy of CO_2, this direct reaction mechanism can explain the structure-insensitive character in terms of the similar apparent activation energies of 0.58 eV on Cu(111), 0.62 eV on Cu(110), and 0.58 eV on Cu(100), the turnover frequencies (TOFs), and the initial reaction rates for formate formation [85].

Combining the studies on Cu hydride in homogeneous organometallic chemistry and heterogeneous catalysis on Cu surface, ER mechanism may be applicable for the formate synthesis from CO_2 hydrogenation by using Cu-based catalyst. If the suggestion is correct, the initial state of reactant can be controlled by translational energy, and/or vibrational energy of CO_2, which is possible if one uses supersonic molecular beam, this is the motivation of the present studies.

1.8 Summary

We have introduced the serious problem for global warming and climate changes, which are generally considered as the results of massive CO_2 emissions from anthropogenic energy demand. One of the most promising ways to utilize the CO2 is to produce methanol, which is not only the initial building-stock for other useful chemicals, but also is a fuel with high energy intensity. Nowadays, the methanol synthesis in industry is using CO_2/H_2 mixture gas over $Cu/ZnO/Al_2O_3$ catalysts at high pressures and high temperatures. From the viewpoint of economy, the production cost is not cheap due to the maintenance of the high catalysts temperature and high gas pressure. It is thus necessary to study the Cu/ZnO-based catalysts for the active sites and identified the mechanisms. Previous studies had a consensus that formate is an important intermediate for methanol synthesis, which is formed by the initial step of CO2 hydrogenation on the Cu surface. In addition, the methanol synthesis may be independent on the Cu surface structure. Therefore, to study the formate chemistry on Cu surfaces would be great helpful to develop the methanol synthesis techniques.

Cu-formate is an intermediate of methanol synthesis and may not be a spectator. Even though many researchers think that CO_2 is an inert molecule, but here CO_2 may be regarded as a Lewis acid molecule. To activate CO_2 molecule, the electron/charge transfer would be helpful for the reduction of CO_2. In organometallic chemistry of CO_2 hydrogenation, it is suggested that CO_2 is reacted with hydride. It is also suggested that in homogeneous catalysis and heterogeneous catalysis the formate synthesis on Cu catalysts is proceeding via ER-type mechanism. Compared to the common heterogeneous catalytic reactions following LH mechanism, ER-type mechanism for CO_2 hydrogenation would be rare, especially for this kind of heavy molecule in industrial heterogeneously catalytic reaction. Therefore, to clarify the unique property of CO_2

hydrogenation and to explore the dynamics of the formate formation would be significantly important to develop the methanol synthesis.

1.9 Outline of the thesis

This thesis includes seven chapters which try to support the conclusion of Eley-Rideal (ER) type mechanism of CO_2 hydrogenation to formate on Cu catalysts. Firstly, in Chapter 1 we introduce our research background−methanol synthesis from CO_2 multistep hydrogenation. The two controversies concerning methanol synthesis over commercial catalysts of $Cu/ZnO/Al_2O_3$ are there: (1) active sites responsible to the catalytic methanol synthesis; (2) mechanisms of methanol synthesis. However, it is well-known that the formate synthesized by CO_2 hydrogenation on Cu surface is an initial and important intermediate of methanol synthesis. Furthermore, we continue to review the suggested ER-type mechanism of CO_2 conversion into formate over Cu-based catalysts in homogeneously catalytic system and heterogeneously catalytic system. To clarify the reaction mechanism of formate synthesis from CO_2 hydrogenation on Cu catalysts, dynamics studies are necessary. In Chapter 2, we introduce several basic concepts and mechanisms in surface chemical dynamics by illustrating some examples of surface reactions. These basic concepts hopefully help to understand the discussion in the present experimental results. Normally, to clarify the reaction mechanism and the dynamics of formate synthesis, supersonic molecular beam is believed to be an effective tool to control the energy of incident CO_2 molecules. Subsequently, the principles of the molecular beam and the surface analytical techniques are described in Chapter 3. From Chapter 3, we can grasp the related experimental techniques and characterization techniques of surface science. Next, in Chapter 4 we present the objective of this study, the experimental apparatus and methods. Experimental results of molecular beam and discussion are highlighted to prove the formate synthesis on Cu surfaces is a thermal non-equilibrium reaction proceeding via ER type mechanism. Furthermore, from the viewpoint of the principle of micro-reversibility, the angle-resolved analysis of desorbing CO_2 molecules on Cu surfaces from formate decomposition, the reverse reaction of formate synthesis, is carried out by using AR-SSD and AR-TPD techniques in Chapter 5. We try to carry out the angle-resolved analysis to suggest that formate synthesis is ER type mechanism. Chapter 6 shows the theoretical calculation results which support the fact that formate synthesis proceeds via ER-type mechanism. Finally, we summarize the experiments and open up a perspective of methanol synthesis at low temperature in Chapter 7.

❊❊❊ Chapter 1 ❊❊❊

Reference

[1] IEA, World Energy Outlook Special Report 2015: Energy and Climate Change, International Energy Agency, 2015.
[2] IPCC, Climate Change 2014: Mitigation of Climate Change. Working Group III Contribution to the Fifth Assessment Report of the Intergovernmental Panel on Climate Change (Eds.: O. Edenhofer, R. P-Madruga, Y. Sokona, J. C. Minx, E. Farahani, S. Kadner, K. Seyboth, A. Adler, Ina Baum, S. Brunner, P. Eickemeier, B. Kriemann, J. Savolainen, S. Schlömer, C. von Stechow, T. Zwickel), Cambridge University Press, 2014.
[3] IPCC, Special Report on Carbon Dioxide Capture and Storage (Eds.: B. Metz, O. Davidson, H. C. De Coninck, M. Loos and L. A. Meyer), Cambridge University Press, Cambridge, 2005.
[4] J. P. Gattuso, A. Magnan, R. Billé, W. W. L. Cheung, E. L. Howes, F. Joos, Science, 349 (2015).
[5] K. Finlay, R.J. Vogt, M.J. Bogard, B. Wissel, B. M. Tutolo, G. L. Simpson, P. R. Leavitt, Nature, 519 (2015) 215-218.
[6] IPCC, Climate Change 2014: Synthesis Report, 2015.
[7] M. Mikkelsen, M. Jorgensen, F.C. Krebs, Energy Environ. Sci., 3 (2010) 43-81.
[8] M. A. Martinez-Boti, G. L. Foster, T. B. Chalk, E. J. Rohling, P. F. Sexton, D. J. Lunt, R. D. Pancost, M.P. S. Badger, D. N. Schmidt, Nature, 518 (2015) 49-54.
[9] E. A. G. Schuur, A. D. McGuire, C. Schadel, G. Grosse, J. W. Harden, D. J. Hayes, G. Hugelius, C. D. Koven, P. Kuhry, D. M. Lawrence, S. M. Natali, D. Olefeldt, V. E. Romanovsky, K. Schaefer, M. R. Turetsky, C. C. Treat, J. E. Vonk, Nature, 520 (2015) 171-179.
[10] G. A. Olah, A. Goeppert, G. K. S. Prakash, Beyond Oil and Gas: The Methanol Economy, 2 ed., WILEY-VCH, Weinheim, 2009.
[11] G. T. Rochelle, Science, 325 (2009) 1652-1654
[12] J. Cejka, A. Corma, S. Zones, Zeolites and Catalysis. Synthesis, Reactions and Applications. , WILEY-VCH Verlag, Weinheim, Germany, 2010.
[13] J. Jiang, O. M. Yaghi, Chem. Rev., 115 (2015) 6966-6997.
[14] H.-C.J. Zhou, S. Kitagawa, Chem. Soc. Rev., 43 (2014) 5415-5418.
[15] S. S.-Y. Chui, S. M.-F. Lo, J. P. H. Charmant, A. G. Orpen, I. D. Williams, Science, 283 (1999) 1148-1150.
[16] C. Montoro, E. Garcia, S. Calero, M. A. Perez-Fernandez, A. L. Lopez, E. Barea, J. A. R. Navarro, J. Mater. Chem., 22 (2012) 10155-10158.
[17] S. Ye, X. Jiang, L.-W. Ruan, B. Liu, Y.-M. Wang, J.-F. Zhu, L.-G. Qiu, Microporous Mesoporous Mater., 179 (2013) 191-197.
[18] R. Li, J. Hu, M. Deng, H. Wang, X. Wang, Y. Hu, H.-L. Jiang, J. Jiang, Q. Zhang, Y. Xie, Y. Xiong, Adv. Mater., 26 (2014) 4783-4788.
[19] J. L. White, M. F. Baruch, J. E. Pander Iii, Y. Hu, I.C. Fortmeyer, J. E. Park, T. Zhang, K. Liao, J. Gu, Y. Yan, T. W. Shaw, E. Abelev, A.B. Bocarsly, Chem. Rev., 115 (2015) 12888-12935.
[20] K. P. Kuhl, E. R. Cave, D. N. Abram, T. F. Jaramillo, Energy Environmental Sci., 5 (2012) 7050-7059.
[21] R. Reske, H. Mistry, F. Behafarid, B. Roldan Cuenya, P. Strasser, J. Am. Chem. Soc., 136 (2014) 6978-6986.
[22] L. C. Grabow, M. Mavrikakis, ACS Catal., 1 (2011) 365-384.
[23] X. Nie, M. R. Esopi, M. J. Janik, A. Asthagiri, Angew. Chem. Int. Ed., 52 (2013) 2459-2462.
[24] A.G. George A. Olah, G. K. Surya Prakash, J. Org. Chem., 74 (2009) 487-498.
[25] G. C. Chinchen, P. J. Denny, D. G. Parker, M. S. Spencer, D.A. Whan, Appl. Catal., 30 (1987) 333-338.
[26] M. Behrens, F. Studt, I. Kasatkin, S. Kühl, M. Hävecker, F. Abild-Pedersen, S. Zander, F. Girgsdies, P.

Kurr, B.-L. Kniep, M. Tovar, R.W. Fischer, J. K. Nørskov, R. Schlögl, Science, 336 (2012) 893-897.
[27] G. Prieto, J. Zečević, H. Friedrich, K. P. de Jong, P.E. de Jongh, Nat. Mater, 12 (2013) 34-39.
[28] S. Kuld, M. Thorhauge, H. Falsig, C.F. Elkjær, S. Helveg, I. Chorkendorff, J. Sehested, Science, 352 (2016) 969-974.
[29] J.-F. Müller, Z. Liu, V.S. Nguyen, T. Stavrakou, J.N. Harvey, J. Peeters, Nat. Commu., 7 (2016) 13213.
[30] I. Beinik, M. Hellström, T. N. Jensen, P. Broqvist, J. V. Lauritsen, Nat. Commu., 6 (2015) 8845.
[31] F. B. Beatriz Roldan Cuenya, S urf. Sci. Rep., 70 (2015) 135-187.
[32] J. K. Norskov, T. Bligaard, B. Hvolbaek, F. Abild-Pedersen, I. Chorkendorff, C.H. Christensen, Chem. Soc. Rev., 37 (2008) 2163-2171.
[33] R. A.V. Santen, Acc. Chem. Res., 42(1) (2009) 57-66.
[34] I. H. Service, Chemical Economics Handbook - Methanol, 2014.
[35] A. Bansode, A. Urakawa, J. Catal, 309 (2014) 66-70.
[36] H. Ahouari, A. Soualah, A. Le Valant, L. Pinard, P. Magnoux, Y. Pouilloux, Reac Kinet Mech Cat, 110 (2013) 131-145.
[37] S.-i. Fujita, Y. Kanamori, A.M. Satriyo, N. Takezawa, Catal. Today, 45 (1998) 241-244.
[38] A. Le Valant, C. Comminges, C. Tisseraud, C. Canaff, L. Pinard, Y. Pouilloux, J. Catal., 324 (2015) 41-49.
[39] K. S. Jean-Luc Dubois, H. Arakawa, Chem. Lett., 21 (1992) 5-8.
[40] C. A. M. Y. Yang, R. S. Disselkamp, D. Mei, Ja-Hun Kwak, J. Szanyi, C. H. F. Peden, C. T. Campbell, Catal. Lett., 125 (2008) 201-208.
[41] C. A. M. Y. Yang, R. S. Disselkamp, C. H. F. Peden, C. T. Campbell, Top. Catal., 52 (2009) 1440-1447.
[42] M. Kilo, J. Weigel, A. Wokaun, R.A. Koeppel, A. Stoeckli, A. Baiker, J. Mol. Catal. A: Chemical, 126 (1997) 169-184.
[43] G. Wu, Y. Sun, Y.-W. Li, H. Jiao, H.-W. Xiang, Y. Xu, J. Mol. Struct.: THEOCHEM, 626 (2003) 287-293.
[44] J. Słoczyński, R. Grabowski, A. Kozłowska, P. Olszewski, J. Stoch, J. Skrzypek, M. Lachowska, Appl. Catal. A: General, 278 (2004) 11-23.
[45] F. Studt, I. Sharafutdinov, F. Abild-Pedersen, C.F. Elkjær, J.S. Hummelshøj, S. Dahl, I. Chorkendorff, J.K. Nørskov, Nat. Chem., 6 (2014) 320-324.
[46] Y. Hartadi, D. Widmann, R.J. Behm, J. Catal., 333 (2016) 238-250.
[47] K. C. Waugh, Catal. Lett., 58 (1999) 163-165.
[48] R. A. Hadden, P. J. Lambert, C. Ranson, Appl. Catal. A: General, 122 (1995) L1-L4.
[49] R. G. Herman, K. Klier, G. W. Simmons, B. P. Finn, J. B. Bulko, T. P. Kobylinski, J. Catal., 56 (1979) 407-429.
[50] G. C. Chinchen, K. C. Waugh, J. Catal., 97 (1986) 280-283.
[51] J. D. Grunwaldt, A. M. Molenbroek, N.Y. Topsøe, H. Topsøe, B.S. Clausen, J. Catal., 194 (2000) 452-460.
[52] P. E. H. N. J. B. Hansen, Handbook of Heterogeneous Catalysis, 2 ed., Wiley-VCH, Weinheim, Germany, 2008, 2008.
[53] R. Schlögl, Angew. Chem. Int. Ed., 54 (2015) 3465-3520.
[54] S. Kuld, C. Conradsen, P.G. Moses, I. Chorkendorff, J. Sehested, Angew. Chem. Int. Ed., 53 (2014) 5941-5945.
[55] P. L. Hansen, J.B. Wagner, S. Helveg, J.R. Rostrup-Nielsen, B.S. Clausen, H. Topsøe, Science, 295 (2002) 2053-2055.

[56] I. Kasatkin, P. Kurr, B. Kniep, A. Trunschke, R. Schlögl, Angew. Chem., 119 (2007) 7465-7468.
[57] J. Schumann, M. Eichelbaum, T. Lunkenbein, N. Thomas, M.C. Álvarez Galván, R. Schlögl, M. Behrens, ACS Catal., 5 (2015) 3260-3270.
[58] M. Kurtz, N. Bauer, C. Büscher, H. Wilmer, O. Hinrichsen, R. Becker, S. Rabe, K. Merz, M. Driess, R.A. Fischer, M. Muhler, Catal. Lett. 92 (2004) 49-52.
[59] T. Fujitani, J. Nakamura, Catal.Lett. 56 (1998) 119-124.
[60] M. Kurtz, H. Wilmer, T. Genger, O. Hinrichsen, M. Muhler, Catal. Lett., 86 (2003) 77-80.
[61] J. L. Robbins, E. Iglesia, C. P. Kelkar, B. DeRites, Catal. Lett., 10 (1991) 1-10.
[62] G. C. Chinchen, K. C. Waugh, D. A. Whan, Appl. Catal., 25 (1986) 101-107.
[63] W. X. Pan, R. Cao, D. L. Roberts, G. L. Griffin, J. Catal., 114 (1988) 440-446.
[64] G. C. Chinchen, K. C. Waugh, D. A. Whan, Appl. Catal., 25 (1986) 101-107.
[65] C.V. Ovesen, B. S. Clausen, J. Schiøtz, P. Stoltze, H. Topsøe, J.K. Nørskov, J. Catal., 168 (1997) 133-142.
[66] I. Beinik, M. Hellstrom, T.N. Jensen, P. Broqvist, J.V. Lauritsen, Nat. Commun., 6 (2015).
[67] G. Prieto, J. Zečević, H. Friedrich, K.P. de Jong, P.E. de Jongh, Nat. Mater., 12 (2013) 34-39.
[68] H. Yue, Y. Zhao, S. Zhao, B. Wang, X. Ma, J. Gong, Nat. Commun., 4 (2013).
[69] M. Bowker, H. Houghton, K.C. Waugh, J. Chem. Soc., Faraday Trans.1, 77 (1981) 3023-3036.
[70] J. Kiss, J. Frenzel, N.N. Nair, B. Meyer, D. Marx, J. Chem. Phy., 134 (2011) 064710.
[71] P. C. K. Vesborg, I. Chorkendorff, I. Knudsen, O. Balmes, J. Nerlov, A. M. Molenbroek, B. S. Clausen, S. Helveg, J. Catal., 262 (2009) 65-72.
[72] J. Nakamura, Y. Choi, T. Fujitani, Top. Catal., 22 (2003) 277-285.
[73] R. van den Berg, G. Prieto, G. Korpershoek, L.I. van der Wal, A.J. van Bunningen, S. Lægsgaard-Jørgensen, P.E. de Jongh, K.P. de Jong, Nat. Commun., 7 (2016) 13057.
[74] I. N. J. Nakamura, T. Uchijima, T. Watanabe, T. Fujitani, Stud. Surf. Sci. Catal., 101B (1996) 1389-1399.
[75] T. Fujitani, I. Nakamura, T. Uchijima, J. Nakamura, Surf. Sci., 383 (1997) 285-298.
[76] Y. Kanai, T. Watanabe, T. Fujitani, T. Uchijima, J. Nakamura, Catal Lett, 38 (1996) 157-163.
[77] J. Yoshihara, C.T. Campbell, J. Catal., 161 (1996) 776-782.
[78] I. Nakamura, T. Fujitani, T. Uchijima, J. Nakamura, Surf. Sci., 400 (1998) 387-400.
[79] P. B. Rasmussen, M. Kazuta, I. Chorkendorff, Surf. Sci., 318 (1994) 267-280.
[80] J. Yoshihara, S.C. Parker, A. Schafer, C. Campbell, Catal. Lett., 31 (1995) 313-324.
[81] Y. Yang, J. Evans, J.A. Rodriguez, M.G. White, P. Liu, Phys.Chem. Chem. Phys., 12 (2010) 9909-9917.
[82] J. Graciani, K. Mudiyanselage, F. Xu, A.E. Baber, J. Evans, S.D. Senanayake, D.J. Stacchiola, P. Liu, J. Hrbek, J.F. Sanz, J.A. Rodriguez, Science, 345 (2014) 546-550.
[83] E. L. Kunkes, F. Studt, F. Abild-Pedersen, R. Schlögl, M. Behrens, J. Catal., 328 (2015) 43-48.
[84] T. Fujitani, I. Nakamura, S. Ueno, T. Uchijima, J. Nakamura, App. Surf. Sci., 121–122 (1997) 583-586.
[85] H. Nakano, I. Nakamura, T. Fujitani, J. Nakamura, J. Phys. Chem. B, 105 (2001) 1355-1365.
[86] F. Le Peltier, P. Chaumette, J. Saussey, M. M. Bettahar, J. C. Lavalley, J. Mole. Catal. A, 132 (1998) 91-100.
[87] A. D. Walsh, J. Chem. Soc. (Resumed), (1953) 2260-2266.
[88] M. B. Ansari, S.-E. Park, Energy Environmental Sci., 5 (2012) 9419-9437.
[89] H.J. Freund, M.W. Roberts, Surf. Sci. Rep., 25 (1996) 225-273.
[90] S. Sakaki, K. Ohkubo, Inorg. Chem., 27 (1988) 2020-2021.
[91] S. Sakaki, K. Ohkubo, Inorg. Chem., 28 (1989) 2583-2590.

[92] S. Sakaki, Y. Musashi, Int. J. Quantum Chem., 57 (1996) 481-491.
[93] E. Vesselli, L. D. Rogatis, X. Ding, A. Baraldi, L. Savio, L. Vattuone, M. Rocca, P. Fornasiero, M. Peressi, A. Baldereschi, R. Rosei, G. Comelli, J. Am. Chem. Soc., 130 (2008) 11417-11422.
[94] I. Nakamura, H. Nakano, T. Fujitani, T. Uchijima, J. Nakamura, J. Vac. Sci. Technol. A 17(4) (1999) 1592-1595.
[95] G. Wang, Y. Morikawa, T. Matsumoto, J. Nakamura, J. Phys. Chem. B, 110 (2005) 9-11.

Chapter 2

Dynamics of gas-surface reactions

2.1 Introduction

Heterogeneous catalysis takes up an important fraction of the output of the chemical industry nowadays. However, modern catalysis is a rather complex system since industrial products are normally generated by applying an elevated pressure and an elevated temperature, i.e. methanol synthesis, as we mentioned above. Understanding the mechanisms of important catalytic reactions relies on the study of surface reaction dynamics. On the other hand, surface science has to a large extent been driven by catalysis. With the development of a whole arsenal of surface analytical tools, the past 50 years of surf ace science have made a significant progress, although the final target of understanding catalysis at the atomic level is far away to achieve, the main gaps like materials gap, pressure gap and complexity gas are blurring. With the further development of the modern surface sensitive technologies, such as TDS, IRAS, ESR, SFG, STM, X-ray scattering and X-ray absorption, the pressure gap can be narrowed/closed and model catalysts systems with increasing degree of complexity can be explored. Under the ultra-high vacuum (UHV) condition, surface science shows great potential to offer the nature information of the catalysis process occurring on the catalysts surface, specially, for the dynamics studies on surface reaction mechanism, non-adiabatic effects and tunneling effects et al.. In this chapter, we give a brief review of some general concepts and the different mechanisms concerning to the surface reactions, by illustrated some experimental examples of recent development, respectively. These concepts/mechanisms can provide the background to understand the importance of the topic in this thesis. We bias this chapter toward experimental work using molecular beams methods mainly because the molecular beam methods is a powerful tool to study the dynamics of gas-surface reactions.

2.2 Transition-state theory

As we known, an elementary chemical rate process can be clarified with the motion of atomic nuclei along the potential energy surface or surfaces representing the electronic and nuclear-repulsion energy of the system as a function of nuclear coordinates. To calculate the reaction rates for complex systems, Transition-state theory (TST) is a useful method depending upon the validity of the Born-Oppenheimer approximation (BOA). BOA is on the basis of the assumption on the separation of fast motion for electrons and slow motion for nuclei [1]. At thermal conditions, chemical rate processes usually occur along the pathways that lead along the lowest potential energy surface from one stable minimum to another as illustrated in **Fig. 2.1(a)**. Note that the upper adiabatic potential is restricted, and dynamics in this state will not process for chemical rate. If this potential energy surface is well separated from higher potential energy surfaces so that the transitions to the latter surfaces are negligible, an elementary process is called adiabatic. The rates of adiabatic elementary chemical processes can be calculated by using the transition-state theory (TST). Non-adiabatic elementary processes include transitions between different potential energy surfaces. For example, the Lennard-Jones type potential diagram in **Fig. 2.1(b)** for the reaction of N_2 dissociation adsorption on Fe(111) suggests that the reaction processes in non-adiabatic dynamic [2-4]. Normally, this process can occur in the molecular beam experiments, in which the sticking probabilities of product are dependent on the translational energy and vibrational energy of projectile N_2 molecules.

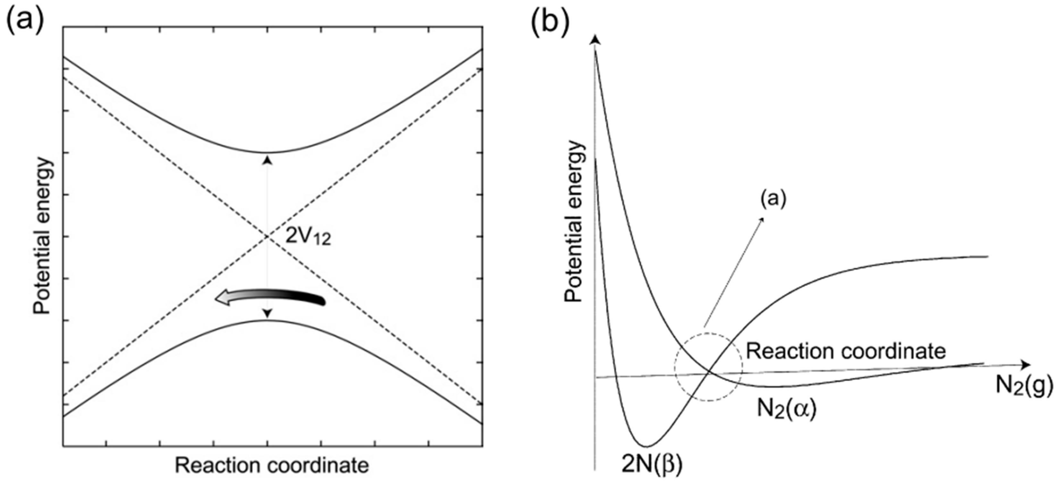

Figure 2.1 (**a**) Potential energy diagram for Landau–Zener model. Adiabatic potentials (solid lines) and non-adiabatic potentials (dashed lines). The arrow illustrates the dynamics on the lower adiabatic (ground state) potential. (**b**) Lennard–Jones type potential energy diagram for the reaction of $N_2(g) + 2* \rightleftharpoons N_2(\alpha) + * \rightarrow 2N(\beta)$. From ref. [4].

According to TST, reaction coordinate is identified as the minimum energy path connecting two stable conformations. The transition state (or activation complex) is associated with the position of maximum energy along the reaction coordinate, representing a saddle point at the potential energy surface. The reaction rate is identified with the reactant flux along the reaction coordinate (the lowest energy path way) across the saddle point in the direction to the final conformation. The TST focuses on the formation and decay of the transition state (or activation complex). By assuming thermodynamic equilibrium between the activated and initial states, a rate constant is usually expressed by the Arrhenius law

$$k_{TST} = \frac{k_B T}{h}\frac{F_A^*}{F_A} exp\left(-\varepsilon_a/k_B T\right) \tag{2.1}$$

where F_A and F_A* are the partition functions of reactants in the initial and activated states,   is the energy difference between these states, and k_B and h are the Boltzmann and Planck constants. For molecular desorption, for example, F_A and F_A* are the partition functions of a molecule in the adsorbed and activated states, respectively. The basic assumptions of TST restricting its applicability are [5]: 1) The initial state and activated complexes in statistical equilibrium; 2) The reaction rate is a classical motion along the reaction path; 3) No connection of the reaction coordinate with other reaction coordinates; 4) Passage through the transition state from reactant to product side is single direction, which is assumed to be "moment of decision" for the reacting system and then will never return to the transition state.

From the assumptions (1) and (4) above, therefore, it is clear that usually there is an upper limit of a rate constant in the TST. The corrected rate constants are customarily represented as

$$k = \kappa k_{\mathrm{TST}} \tag{2.2}$$

where $\kappa \leq 1$ is the so-called transmission coefficient.

TST automatically takes into account thermodynamics and accordingly the TST rate constants for forward and backward processes satisfy the detailed balance principle.

Phenomenologically, a rate constant is usually represented as

$$k = v \, exp\,(-E_a/k_B T) \tag{2.3}$$

where the apparent Arrhenius parameters v and E_a are the pre-exponential factor and the activation energy, respectively.

It is noted that the apparent Arrhenius parameters v and E_a are slightly different from those in Eq. (2.1). In order to solve this problem, the Gibbs free energy of activation (ΔG_0^*) is induced by rewriting Eq. (2.1)

$$k_{TST} = \frac{k_B T}{h} exp\,(-\Delta G_0^*/k_B T) \tag{2.4}$$

Therefore,

$$\Delta G_0^* = \varepsilon_a - k_B T \, ln \frac{F_A^*}{F_A} \tag{2.5}$$

We know that $\Delta G_0^* = \Delta H_0^* - T\Delta S_0^*$, where ΔH_0^* and ΔS_0^* are the enthalpy and entropy of activation.

Therefore, from Eq. 2.3 and Eq. 2.5, one can get

$$E_a = \Delta H_0^* + k_B T, \text{ and } v = e \frac{k_B T}{h} \exp(\Delta S_0^*/k_B) \tag{2.6}$$

So ΔH_0^* can be not considered as the activation energy (E_a). The reaction temperature has contribution to the activation energy. In general, the reactants may own translational, vibrational and rotational degrees of freedom, in which the vibrational mode is efficient to be influenced by the reaction temperature if we ignore the transformation between these degrees of freedom. On the other hand, from the Eq.(2.6), the pre-exponential factor v is identified by the entropy of activation ΔS_0^*. That is, the constant of reaction rate can be enhanced by increasing the value of ΔS_0^*. Therefore, from this dynamical view, in heterogeneous catalysis, to optimize the active site and control the degrees of freedom of reactant would be helpful to increase the reaction rate.

TST governing the kinetics of heterogeneous catalytic reactions are as a rule much more complex due to surface heterogeneity, adsorbate-adsorbate lateral interactions, spontaneous and adsorbate-induced changes in a surface, and/or limited mobility of reactants. Despite all these complicating factors, the kinetics and rate constants of the latter reactions can often also be rationalized by employing TST.

2.3 Tunneling effects

The rate constant predicted by conventional TST is frequently too large, e. g., when the saddle point is not a true point of no return along the path to a particular product. The predicted rate constant also can turn out to be too small, compared to experimental data, when tunneling effect occurs [6]. This is because TST implies classical motion along the reaction coordinate. According to quantum mechanics, reactants may however penetrate via the potential barrier, which is associated with the traditional picture of tunneling. Due to tunneling, the transmission coefficient in Eq. (2.2) may be large, $\kappa \geq 1$, and the apparent Arrhenius parameters defined by Eqs. (2.3) and (2.4) may decrease with decreasing temperature. For realistic potential barriers, these effects may be observed in reactions with participation of hydrogen or deuterium at temperatures below 300 K [7, 8]. Heterogeneous catalytic reactions usually occur at higher temperatures. For this reason, tunneling has not attracted appreciable attention of the heterogeneous catalysis community. In the recent literature, one can however sometimes find the claims that tunneling plays a significant role in practically important catalytic reactions, occurring with participation of relatively heave reactants, provided that a potential barrier is narrow. One of the likely examples seems to be the dissociative adsorption of N_2 on Fe or Ru at thermal energies. Tunneling appears to be significantly influenced by the interplay of the translational and vibrational degrees of freedom [4].

2.4 Non-equilibrium effects

On the basis of an important assumption for TST, the energy distribution of reactants is close to the Boltzmann one. This assumption is often reasonable. Under conditions of slow activation, however, the population of the reactant states with energy exceeding the activation energy and be exhausted due to reaction, and accordingly a rate constant can be lower than the predicted by TST, as it first shown in the seminal paper by Kramers [9].

The Kramers' reaction rate theory is focused on a single irreversible reaction step. In reality, chemical reactions usually occur via multi-steps, and the products of one step are often reactants in another step. Just after reaction events, the energy of reaction products is usually appreciably higher than the thermal energy and in principle this extra energy can be used to accelerate other reaction steps and/or self-acceleration. For example, surface reactions always contain adsorption steps. Just after adsorption, the energy of vibrations of a molecule or atom in the adsorption potential is high, i.e., a molecule or atom is hot, and their energy can be employed to accelerate other steps. This is treated as "hot atom/hot precursor" mechanism, which is the diction between the classical ER mechanism and LH mechanism. The reaction rate is thus higher than one expects.

2.5 Non-adiabatic effects

In adiabatic elementary rate processes, described by TST, the potential energy surface for nuclear motion is well separated from higher potential energy surfaces so that the transitions to the latter surfaces are negligible. Non-adiabatic rate processes include transitions between different potential energy surfaces. Identification and scrutinization of non-adiabatic rate processes on solid surfaces is one of the central goals of the theory of heterogeneous chemical reactions [10]. At present, the situation in this field is far from clear. Although the breakdowns of the Born-Oppenheimer approximation in reactions on metals are often anticipated and the relevant experimental data appears to be abundant, good specific examples illustrating in detail what may happen are still lacking. Among a few advances in this field, it is appropriate to mention, e.g., direct detection of hot electrons and holes excited by adsorption of atomic H and D on ultrathin Ag and Cu films [11, 12]. In many other cases, the interpretation of experimental data is often far from straightforward. One of the reasons of this situation is that the conventional software like the DFT packages does not allow dealing accurately with the excited states.

2.6 Electron-hole pair excitation

The semi-infinite surface of a metal contains a continuum of excitations of the conduction band electrons and it was hypothesized that these could couple to the motion of an atom or molecule for the reaction on or scattering from a metal surface [13]. Excitation of electron-hole pairs can take place with infinitesimally small excitation energies dissipating in the inelastic scattering of molecules and atoms from surface. From chemisorption calculations, it has been shown that as atoms or molecules approach a surface, their sharp electronic states broaden due to interactions with the conduction band states [14]. In addition, they shift in energy with a general rule of thumb being that ionization potentials shit upwards, while affinity levels shift down. For adsorbates that have relatively sharp local densities of states when they are near Fermi level, electronic non-adiabaticity is a significant process, as evidenced by the experimental observation of chemiluminescence [15] and of electron emission after collisions of highly vibrationally excited NO molecules with a low-work-function metal surface [14, 16]. The former as the electronic excitation after highly exothermic chemisorption of adsorbates, the gas-surface reaction should exhibit deep chemisorption wells before the barrier to reaction, whereas the latter process should be important for molecules with high electron affinity [17].

2.7 Phonon excitation

The phonon excitation also is a form of the energy dissipation when a gas atom strikes a surface. The energy loss in terms of the strength of the coupling depends on both the mass of the gas atom and its energy as well as properties originating from the surface such as the mass of a constituent atom, its temperature and the cohesive forces that bind the substrate together. Dissipating energy to phonon subsystem can give rise to the interesting dynamical possibility of trapping into a molecular state at the surface and this continues to be an interesting theme in surface dynamics [18].

The essential aspect of gas-surface reaction is energy transfer, which is distinct from energy transfer in gas-phase collisional encounters. Such an approach might emphasize the unique energy baths characteristic of solids, specifically, phonons and electron-hole pairs (EHPs). Whereas energy transfer between small molecules is reasonable described by quantum dynamics with the Born-Oppenheimer approximation, phonons may often be treated with classical mechanics. The energy exchange to and from EHPs, however, represents a fundamental breakdown of the Born-Oppenheimer approximation.

2.8 Surface reaction mechanism

2.8.1 Precursors, trapping state and hot atom/precursors

The terms of *precursor*, *trapping state* and *hot adatom* are three important and fundamental concepts in the interactions between the adsorbed gas molecules and the surface. Generally speaking, the formation of a stable species may be preceded several surface intermediates, these intermediates are frequently denoted as precursors. For example O_{ad} formation on Pt(111) surface from the dissociated chemisorption of O_2, in which the molecularly adsorbed O_2, still existing in two different states. If this precursor is a physisorbed species formed by energy dissipation of the impinging particle from which a transition into the chemisorbed state occurs, this process is also called *trapping-mediated chemisorption* [19]. This definition is so general that different authors have attributed to precursors very different characteristics (such as localized, dynamic, and thermlized) to explain various behaviors of the sticking probability *S* under different experimental condition dependence, e. g., surface temperature, translational energy and internal energy of the incident molecules, the coverage dependence. The experimental evidence of precursor states has been associated with the existence of adsorbed molecular species or the decrease of the sticking probability with surface temperature and at low adsobate's incident energies. While this is widely accepted for heavy molecules [20-22] much skepticism surrounds the idea of a precursor mediated mechanism in the case of light adsobates (e. g. H_2) because: 1) *S* barely depends on T_s; 2) inefficient molecule-surface energy exchange is assumed due to mass mismatch, 3) the initial decrease of $S(E_\mathrm{i})$ can be theoretically reproduced without molecule surface energy exchange [23-25], and 4) molecularly chemisorbed states had never been observed (except in the particular case of the stepped Ni(510) surface [26].

The intrinsic precursors (adsorption on a clean surface) will lead to a strong dependence of the sticking coefficient on surface temperature. Extrinsic precursors (adsorption in a second layer) yield a characteristic dependence of the sticking coefficient on coverage: over a wide range of coverages the sticking coefficient stays constant. The extrinsic precursor comes into play only at nonzero coverages, but it is in thermal equilibrium with the surface. The term "in trinsic precursor species" denotes particles trapped on the surface before they attain thermal equilibrium. The state is of relevance for various kinetics phenomena in surface reactions and is discussed in the current context [27].

The principle of hot precursors or adatoms had been introduced schematically in G. Ertl's review paper [27]. In the Hot precursor model, the particle impinging on a surface, the coupling is still weak when the particles are at a distance far from the surface, so that the particle hits first the repulsive part of the potential and exchanges its adsorption energy only stepwise. Since the corrugation of the potential parallel to the surface is generally smoother than that perpendicular to it, the particle is expected to travel an appreciable distance across the surface before it comes to rest. On the hasis of these considerations, experiments of CO_2 formation from CO oxidation on Pt(111) illustrates this mechanism, in which hot O adatom thermalized before it hits a neighboring CO molecule, and then CO_2 formation requires a higher activation energy, and hence CO_2 desorbs from the surface only at higher temperature [28]. Quite similar effects are observed in the CO oxidation photochemically by tunneling electrons rather than thermally on Ru(0001) [29]. These results show that the nascent O atoms have comparable energy content in all cases. Although trapping at the surface, adsorbed species is not thermalized by the surface before the reaction taking place.

2.8.2 Langmuir-Hinshelwood (LH) and Eley-Rideal (ER) kinetics

The preceding discussion of reactions involving hot precursors/atoms poses to a key and typical question in the kinetics of heterogeneous catalysis: how to distinguish the kinetics of the reaction of two reagents A + B in adsorption states thermally equilibrated with surface before their reacting with each other (an Langmuir-Hinshelwood (LH) mechanism) and that of one from gas-phase reacting with an adsorbed particle on surface by a direct collision (an Eley-Rideal (ER) mechanism), as schematically shown in **Fig. 2.2**. Clear identification of the limiting case of an ER mechanism has been found be rather difficult and is subject to intense research.

In LH mechanism, two reactant species instantaneously and thermally equilibrate with the catalyst surface when they impinge on the surface (**Fig. 2.2(a)**), followed by the diffusion within long residence time (i.e., exceeding about 10 ps) to form product by the reaction on the surface. The surface acts as a heat bath and provides the energy which allows the adsorbate to overcome a barrier to reaction [30]. . The important point is a complete decoupling of initial reactant adsorption from final product formation: all "memories" of the preadsorption energy and momentum of reactant are lost. Generally, most heterogeneous catalytic reactions are considered to proceed via LH mechanism, where the overall reaction rate generally has a strong dependence on the surface temperature [27]. As mentioned above, the CO_2^- ion is metastable with a life time of 60–90 µs. CO_2^- ion thus has enough time to be formed from CO_2 ionization on catalyst surfaces. One of the examples is demonstrated by the yielding of formate from hydrogenation of CO_2 on Ni(110). Ni-formate formation proceeds via a flip of an H-CO_2 complex which is formed by the reaction of an H adatom with an activated chemisorbed CO_2 molecule (CO_2^-) through increasing the surface temperature [24].

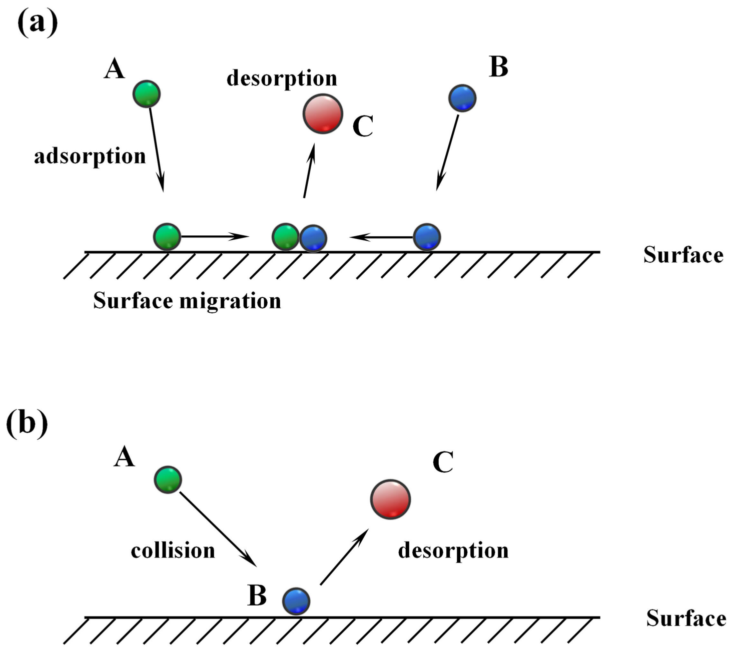

Figure 2.2 Two possible reaction mechanisms in which heterogeneous catalysis proceeds at a catalyst surface: (**a**) a Langmuir-Hinshelwood mechanism and (**b**) an Eley-Rideal mechanism, in which A and B stand for reactants, C stands for product.

The other rare pathway is Eley-Rideal (ER) mechanism, in which a gas phase projectile reacts directly with pre-adsorbed species on surface without passing through local chemisorption or trapping states on the surface (**Fig. 2.2(b)**). The reactive events in the ER pathway occur within the first few picoseconds after collision and the gas-phase reactants are not thermally equilibrated with the surface. The product of the reaction either desorbing or else remaining adsorbed on the surface depending on the particular chemical reaction [25]. The ER-type mechanism can be defined as the direct reaction between a gas-phase reactant with an adspecies to form the product remaining adsorbed on the surface. Molecular beam can be used for precisely control of the initial incident energy and direction of the scattering molecules, combining with the accurate measurement of scattering angular distributions and time-of-flight (TOF). These characters lead itself can be carried out the analysis of scattering angular and TOF distributions depending on the initial conditions. ER reactions can be immediately distinguished from those that follow a LH mechanism. For example, though theoretically proposed in the late 1940s, such ER processes [26], characterized by sub-picosecond reaction times and highly excited products, have only been evidenced experimentally in the 1990s, within the framework of artificial hydrogen reactions on metals. For example, the first demonstration of an ER reaction in the protonation of a very large molecule [$N(C_2H_4)_3N$] (ref.[31]). The properties of these two prototypical mechanisms are summarized in **Table 2.1**.

Table 2.1 Comparison of Langmuir-Hishelwood (LH) mechanism and Eley-Rideal (ER) mechanism

	LH mechanism	**ER mechanism**
Reaction time scale	1) The time lag between adsorption and product formation is much longer (i.e., $\geq \sim 10$ ps) than the relaxation time for reaching thermal equilibrium. 2) Two species attempt to react on the order of 10^{12}-10^{13} times each second.	1) Most reactive events occurred within the first few picoseconds after collision, when the incident atom was in only a weakly held state. 2) The attempt frequency is replaced by the impingement flux, e.g. 1 site^{-1} s^{-1} at 10^{-6} Torr.
Thermal dynamics	Thermal equilibrium	Thermal non-equilibrium
Existent	Common in heterogeneous catalysis	Rare in heterogeneous catalysis
Reaction mode	Either an asymmetric atom-surface stretching frequency or as a frustrated translational frequency of an adsorbed molecule parallel to the surface.	Initial states of the reactant can be selected.

Besides, the hot adsorbed atom mechanisms, as we mentioned above, may be considered as the extreme condition for ER mechanism in terms of non-LH mechanism, in which the gas-phase atom transfers part of its collision energy to one adsorbate and/or the metallic surface upon initial collision and is subsequently deflected towards a motion mostly parallel to the surface. Consequently, such a hot species may react with the adatoms before being thermalized. The projectile does not transfer its kinetic and potential energy to the surface but does enter a quasi-bound state. HA reactions can typically be regarded as close to ER reactions, but may be subdivided into metastable and bound processes. We can thus also consider this process is in a thermal non-equilibrium process.

Most chemical reactions on surfaces proceed according to the LH scheme. So the catalytic reaction may be manipulated by optimizing the reaction temperature, normally the high temperature is favor of the increase of reaction rate. However, as for industrial heterogeneous catalytic reactions, no definitive example has been reported via ER type mechanism. In order to achieve the industrial chemical production reactions proceeding at a low temperature, the ER mechanism as in thermal non-equilibrium character may shed the light on the possibility of low temperature production, in particular, in the field of the methanol synthesis from CO_2 conversion, with lower economic cost. In this thesis, the mechanism of formate synthesis from CO_2 on Cu catalysts was explored in the viewpoints of reaction dynamics.

2.9 Illustrative examples

2.9.1 Vibrational activation scattering

Vibrational excitation of umbrella NH_3 molecule on Au(111) in a direct gas-surface encounter was firstly observed in multi-quantum channels [32]. The vibrational excitation probability is dependent upon the incident molecular–beam kinetic energy linearly and there are clear thresholds of the energy for each vibrational channel, indicating that the scattering molecules leave the surface modes more or less as spectators. Furthermore, these results suggest that a mechanism dominated by direct collision translational to vibrational energy transfer. This mechanism is further supported by the other observation which was that the vibrational excitation probabilities were nearly perfectly independent of surface temperature. It is again consistent with the idea that surface degrees of freedom are spectators to the vibrational excitation process.

While very different behavior is exhibited in the scattering events of NO from Au(111) and Cu(111) [33-35]. In the NO/M(M= Au(111), Ag(111) and Cu(111)) system, the incidence energy dependence showing "zero-energy threshold" clearly indicates that the conversion of translational to vibrational energy is indirect and much less important comparing to the NH_3/Au(111) system. The probability for NO excitation was observed to a strong dependence on surface temperature follows an Arrhenius law with an activation energy equal to the vibrational energy gap in NO. These results support an electronically non-adiabatic interpretation that statistical mechanical population of hot EHP's may excite NO vibration on the basis of the assumption of equal excitation probability for all EHP's. More details of the experimental examples are shown in the **Table 2.2**.

Table 2.2 Vibrational activation scattering examples

system	observations	ref.
NH_3/Au(111)	The vibrational excitation probability of NH_3 scales linearly with the kinetic energy of the incident beam above a threshold energy corresponding to the quanta excited, and is independent of the surface temperature.	[32]
NO/Au(111)	(1) Temperature dependence is non-Arrhenius on Au(111). The large spin–orbit interaction present for Au(111) surface states may be important for vibrational excitation. (2) Nonadiabatic transition rate depends strongly on both the N-O internuclear separation and the molecular orientation. (3) Molecule-surface forces can steer the molecule into strong-coupling configurations	[33] [36]
NO/Ag(111) NO/Cu(111)	Vibrational excitation is found to depend strongly on surface temperature, and relatively weakly on incident kinetic energy.	[34] [35]
H_2/Pt(111)	The comparison for in-plane and out-of-plane scattering and results for dissociative chemisorption in the same system show that for hydrogen-metal systems, reaction and diffractive scattering can be accurately described using the Born-Oppenheimer approximation.	[37]
HCl/Au(111)	(1) The final velocity distributions are largely insensitive to the rotational level and indicate that the energy loss to phonons is small. (2) The incidence energy threshold is strong evidence that translational energy is directly converted to vibrational excitation. (3) The angular distribution of HCl (v = 1) recoiling from Au(111) collapses and shifts to normal recoil at the threshold for vibrational excitation, indicating that near complete consumption of initial translational energy such that only those molecules that happened to depart along the surface normal had the ability to escape the surface.	[38] [39]

2.9.2 Vibrational activation of dissociative chemisorption

The molecule beam can also be used to study the dynamics of trapping as well as adsorption on the surface. In surface science, trapping and adsorption dynamics of gas molecule on surface sheds the light into precursor-mediated dissociation. This mechanism may be the dominant channel to dissociative chemisorption. For instance, N_2 dissociative chemisorption on Fe surface for ammonia synthesis, H_2O and CH_4 dissociative chemisorption on Ni surfaces for water-gas-shift reaction and hydrogen production, respectively [40, 41]. When direct collisional activation may occur with high probability at high incident translational energies, only a small fraction of a Maxwell-Boltzmann gas at room temperature may possess sufficient energy to overcome the barrier for direct dissociation. The dissociative chemisorption may thus represent the rate determining step in many types of catalytic processes.

Accordingly, for example, the dissociation of CH_4 is key step reforming of natural gas for hydrogen production. The dissociative adsorption of CH_4 on Pt(111) [42], Ni(111) [41], Ni(100) [40] and Ru(0001) [43] has attracted substantial attention as it represents a prototype for the vibrational activation of dissociative adsorption. On CH_4/Ni(111) system, both remarkable vibrationally adiabatic picture and vibrationally nonadiabatic picture to properly describe the role of CH_4 vibrational energy to promote the reaction depending on the vibration mode of CH_4. That is, a vibrationally adiabatic trajectory, the reagent translational or the thermal bath of the surface is responsible for the overcome of the reaction barrier of CH_4 at $v = 0$ and $v = 1$. Therefore, there may be each CH_4 vibration diffs in its coupling with lattice motion. Such an effect could translate into differing abilities to transfer energy into or access energy stored in the nickel lattice [44]. On the other hand, a vibrationally nonadiabatic trajectory CH_4 in $v = 1$ start with internal energy and access transition state (TS) whose energy is less than those accessed by $v = 0$ pathway, in which the latter one do not access the minimum TS energy. **Table 2.3** summarizes recent examples of activation of dissociative adsorption.

Table 2.3 Vibrational activation of dissociative adsorption examples

system	observations	ref.
CH_4/Ni(111)	Vibrational excitation of the anti-symmetric C-H stretch activates methane dissociation more efficiently than does translational energy.	[41]
CH_4/Pt(111)	A new phenomenon, thermally assisted tunneling, caused by a coupling of the tunnel barrier to the lattice was proposed for the mechanism of CH_4 dissociation on Pt(111).	[42]
CH_4/Pt(533)	For incident kinetic energies in the range 26 meV < E_i < 1450 meV, the initial dissociation probability of CH_4 on the Pt(533) surface is higher than on Pt(111).	[45]
CD_2H_2/Ni(100)	The reaction probability with two quanta of excitation in one C-H bond was greater than with one quantum in each of two C-H bonds.	[40]
CH_4/Ru(0001)	The measured sticking coefficient of CH_4 is strongly enhanced both by increasing the translational and the vibrational energy of the CH_4 molecule.	[43]
H_2O/Ni(111)	The reaction occurs via a direct pathway, because both the translational and vibrational energies promote the dissociation. The larger increase of the dissociation probability by vibrational excitation than by translation per unit of energy is consistent with a late barrier along the O-D stretch reaction coordinate.	[46]

system	observations	ref.
H_2O/Cu(111)	Excitations in all three vibrational modes (symmetric stretching, bending, and antisymmetric stretching modes) are capable of enhancing reactivity more effectively than increasing translational energy, consistent with the “late” transition state in the reaction path.	[47]
N_2/Fe(111)	The initial dissociative chemisorption probability increases with increasing kinetic energy and with decreasing surface temperature, suggesting that reagent energy provides access to an intermediate state.	[48]

2.9.3 Vibrational and/or translational activation of associative reaction -ER (type) mechanism

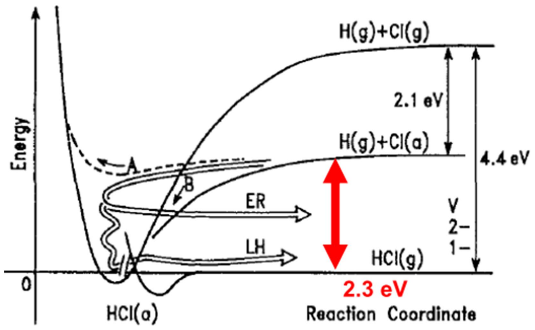

Figure 2.3 Energy diagram for the H + Cl_a → HCl (g) over Au(111) surface proceeding LH mechanism and ER mechanism [49] .

Molecular beam time-of-flight (TOF) is an essential technique to determine angular and velocity distribution of the desorbing products of associative reactions. The resonance-enhanced multi-photon ionization (REMPI) is generally used to determine rotational and vibrational state distributions. To further explain the HA, LH and ER mechanism, here, we give a real reaction in which HA, LH and ER mechanism are exhibited. That is, the reaction of $H_{(g)} + Cl_a \rightarrow$ HCl on Au(111) surface as the example [49, 50]. As shown in **Fig. 2.3**, while LH mechanism proceeding with gas-phase H atom first thermally accommodates to the surface was proved by a near-thermal energy distribution and an angular distribution close to that of a cosine form, for an ER mechanism, a narrow angular distribution and TOF provide clear evidence that the alsorbed Cl atom was directly abstracted by the incident H atom to form a HCl bond. The HCl product leaves the surface with a high kinetic energy in a narrow angular distribution that displays a “memory” of the direction and energy of the incident hydrogen atom. The chemical energy of 2.3 eV is released into product degrees of freedom. The fast TOF component (ER) is found to be mainly composed by two contributions, assigned to HCl product formed in $v = 0$ and $v = 1$. The rotational state distribution for the HCl ($v = 0$) product of the ER mechanism is found to be distinctly non-Boltzmann distribution, with a mean vibrational energy taking up about 5% of the available energy. While for the vibrational energy in $v = 1$, it takes up about 14% of the available energy.

According to the theoretical calculation using quasi-classical trajectories, the available energy in the reaction of $H_{(g)} + Cl_a \rightarrow HCl$ is capable to producing HCl up to $v = 8$ [49], and the large amplitude vibrational motion of HCl ($v = 8$) is highly mechanical and electronical an-harmoic. However, it is still not clear that how the energy partition which would be important to enhance H atom sticking and the vibrational excitation of the desorbing HCl product molecule. More examples of ER mechanism are illustrated in **Table 2.4**.

For a LH mechanism releasing energy from the surface reaction is converted to heat and carried away into the thermal bath of the solid. Therefore, here at least we can treat that the LH reaction is in a thermal equilibrium process, but ER can be a process proceed via a thermal non-equilibrium.

Table 2.4 Dynamics of ER (type) mechanism examples

system	observations	ref.
$Cl_a + H_a/Au(111)$	(1) The direct reaction product leaves the surface with a high kinetic energy in a narrow angular distribution. (2)The indirect reaction product has a near-thermal energy distribution as cosine angular distribution	[51]
	Some reactions occur on essentially a single gas-surface collision by ER mechanism. Others occur between moderated H and Cl_a atoms by LH mechanism.	[49]
$D_a + H/Cu(111)$	Deuterium atoms collide with a H-covered Cu(111) surface, they react to form a HD molecule that leaves the surface with a high degree of vibrational and rotational excitation.	[52]
$D_a\ (H_a) + H_a\ (D_a)/Cu(111)$	(1) The angular distributions are asymmetric. (2)The HD product has a high degree of translational, vibrational and rotational excitation.	[53]
	There is no barrier for the ER reaction pathway, which has a large potential energy release.	[54]
$D_a + CD_{3a}/Cu(111)$	A direct (Eley–Rideal mechanism) gas–surface reaction with a cross section of $\sim 10^{-16}\ cm^2/D$ atom.	[55]
$(N_a + N_2) + N_a/Ag(111)$	The angular distribution of scattered N atoms is very broad. N_2 molecules exhibit a sharp angular distribution.	[56]
$N_a + N_a/Ag(111)$	N_2 yield is mainly due to the relatively long-ranged attractive and barrier-less nature of N-N interaction potential in the presence of the Ag(111)	[57]
$N_2 + N_a/Ag(111)$	Electronic state of the incident atoms is very important in the interaction. Incident N-atoms can removing adsorbed N-atoms in an ER mechanism	[58]
$(N_a + N_2) + O/Ag(111)$	The time dependence of prompt NO formation exhibits an exceptionally fast decay as a consequence of shifting reaction pathways and probabilities over the course of the exposure.	[59]
$N_a + N_a/W(100)$	Ro-vibrational distributions of the N_2 molecules are only slightly affected by the presence of the thermal bath whereas kinetic energy is rather strongly decreased when going from a static surface model to a moving surface one.	[60]
$[N(C_2H_4)_3N] + H_a/Pt(111)$	Molecules are protonated at the surface and leave with kinetic energy which is strongly dependent on the incident energy as a clear demonstration of an ER mechanism.	[31]
$N_2O + Li/Rh(100)$	(1) ER mechanism giving rise to exoelectron and N_2 emission. (2) LH mechanism N_2O molecules are adsorbed on the surface before the reaction takes place.	[61]

system	observations	ref.
$NO + O_2$/Water ice $O_2 + NO$/Water ice $(NO+O_2)$ + Water ice	$NO + O_2$ reaction occurs mainly through the direct ER mechanism to form nitrogen oxides (NO_2, N_2O_3, N_2O_4).	[62]
$N^+ + O_a$/Pd(Poly) $O^+ + O_a$/Pd(Poly) $N^+ + O_a$/Pt(Poly) $O^+ + O_a$/Pt(Poly)	The exit energies of the diatomic molecular products NO and O_2 depend linearly on the incidence energy of the corresponding projectiles.	[63]
$N_2^+ + D_a$/Pd(Poly) $O_2^+ + D_a$/Pd(Poly)	The kinematics of the collisional interaction confirms product formation by an ER reaction mechanism and accounts for inelastic energy losses commensurate with surface re-ionization.	[64]

2.10 Summary

To study the dynamics of gas-surface reactions can help us to understand the mechanisms of the surface reactions in terms of trapping, desorption, diffusion and reactivity. The transition-state theory (TST) governs the kinetics of heterogeneous catalytic reaction such as the rate constants. A rate constant of an elementary reaction step is expressed via the activation energy and apparent Arrhenius parameters. TST is based on an assumption that energy distribution of reactants is follow the Boltzmann one so that it accordingly takes into account thermodynamics and detailed balance principle. Therefore, limitation is there for TST when the tunneling effects and non-adiabatic effects present in the dynamics of surface catalytic reactions. In the gas-surface reaction in thermal non-equilibrium, such as vibrational activation scatter, vibrational activation of dissociative adsorption and vibrational and/or translational activation of associative reactions, precise measurements of the energy transfer still are difficult problems. From the examples we illustrated above, although they are not completely included, the dynamics of CO_2 activation is less attract attentions and is far away studied may be due to CO_2 is a heavy, neutral and inert molecules. As we discussed the relationship between methanol synthesis and CO_2 activation in Chapter 1, to fully understand the mechanism of dynamics of CO_2 activation is helpful to the understanding the processes of methanol synthesis. The molecular beam techniques in ultra-high vacuum (UHV) system have shown very important advantages to investigate the dynamics of the heterogeneous catalysis [41]. Particularly, the CO_2 activation and recycle are relevant with the industrially methanol production and reduction of CO_2 emission.

❊❊❊ Chapter 3 ❊❊❊

Reference

[1] M. Born, R. Oppenheimer, Annal. Phys., 389 (1927) 457-484.
[2] G. Ertl, S.B. Lee, M. Weiss, Surf. Sci., 114 (1982) 515-526.
[3] J.J. Mortensen, L.B. Hansen, B. Hammer, J.K. Nørskov, J. Catal., 182 (1999) 479-488.
[4] N.E. Henriksen, F.Y. Hansen, Phys.Chem. Chem. Phys., 4 (2002) 5995-6000.
[5] V.P. Zhdanov, Chapter 7 Reaction Dynamics and Kinetics: TST, Non-equilibrium and Non-adiabatic Effects, Lateral Interactions, etc, in: E. Hasselbrink, B.I. Lundqvist (Eds.) Handbook of Surface Science, North-Holland, 2008, pp. 231-267.
[6] D.G. Truhlar, B.C. Garrett, S.J. Klippenstein, J. Phys. Chem., 100 (1996) 12771-12800.
[7] W.H. Miller, Acc. Chem. Res., 26 (1993) 174-181.
[8] S. Sato, Chem. Phys., 315 (2005) 65-75.
[9] H.A. Kramers, Physica, 7 (1940) 284-304.
[10] A.M. Wodtke, J.C. Tully, D.J. Auerbach, Int. Rev. Phys. Chem., 23 (2004) 513-539.
[11] H. Nienhaus, H.S. Bergh, B. Gergen, A. Majumdar, W.H. Weinberg, E.W. McFarland, Phys. Rev. Lett., 82 (1999) 446-449.
[12] H. Nienhaus, Surf. Sci. Rep., 45 (2002) 1-78.
[13] E. Muller-Hartmann, T.V. Ramakrishnan, G. Toulouse, Solid State Commun., 9 (1971) 99-101.
[14] B. Kasemo, E. Törnqvist, J.K. Nørskov, B.I. Lundqvist, Surf. Sci., 89 (1979) 554-565.
[15] B. Gergen, H. Nienhaus, W.H. Weinberg, E.W. McFarland, Science, 294 (2001) 2521-2523.
[16] J.D. White, J. Chen, D. Matsiev, D.J. Auerbach, A.M. Wodtke, Nature, 433 (2005) 503-505.
[17] S. Holloway, Surf. Sci., 299–300 (1994) 656-666.
[18] H.J.K. M. Grunze, in: C.T.R. D. J. Auerbach (Ed.) Kinetics of Interface reactions, Springer, Berlin, 1987, pp. PP.125.
[19] H.F. Busnengo, W. Dong, A. Salin, Phys. Rev. Lett., 93 (2004) 236103.
[20] C.T. Rettner, E.K. Schweizer, H. Stein, D.J. Auerbach, Phys. Rev. Lett., 61 (1988) 986-989.
[21] C.T. Rettner, H. Stein, E.K. Schweizer, J. Chem. Phys., 89 (1988) 3337-3341.
[22] M. Beutl, K.D. Rendulic, G.R. Castro, Surf. Sci., 385 (1997) 97-106.
[23] A. Gross, M. Scheffler, Phys. Rev. B, 57 (1998) 2493-2506.
[24] H.F. Busnengo, C. Crespos, W. Dong, J.C. Rayez, A. Salin, J. Chem. Phys., 116 (2002) 9005-9013.
[25] H.F. Busnengo, E. Pijper, M.F. Somers, G.J. Kroes, A. Salin, R.A. Olsen, D. Lemoine, W. Dong, Chem. Phys. Lett., 356 (2002) 515-522.
[26] A.S. Mårtensson, C. Nyberg, S. Andersson, Phys. Rev. Lett., 57 (1986) 2045-2048.
[27] G. Ertl, Dynamics of reactions at surfaces, in: B. C. Gates, H. Knozinger (Eds.) Advances in Catalysis, Academic Press, 2000, pp. 69.
[28] T. Matsushima, Surf. Sci., 127 (1983) 403-423.
[29] H. Öström, H. Öberg, H. Xin, J. LaRue, M. Beye, M. Dell'Angela, J. Gladh, M.L. Ng, J.A. Sellberg, S. Kaya, G. Mercurio, D. Nordlund, M. Hantschmann, F. Hieke, D. Kühn, W.F. Schlotter, G.L. Dakovski, J.J. Turner, M.P. Minitti, A. Mitra, S.P. Moeller, A. Föhlisch, M. Wolf, W. Wurth, M. Persson, J.K. Nørskov, F. Abild-Pedersen, H. Ogasawara, L.G.M. Pettersson, A. Nilsson, Science, (2015).
[30] S.J. Lombardo, A.T. Bell, Surf. Sci. Rep., 13 (1991) 3-72.
[31] E.W. Kuipers, A. Vardi, A. Danon, A. Amirav, Phys. Rev. Lett., 66 (1991) 116-119.
[32] B.D. Kay, T.D. Raymond, M.E. Coltrin, Phys. Rev. Lett., 59 (1987) 2792-2794.
[33] A.M. Wodtke, Y. Huang, D.J. Auerbach, Chem. Phys. Lett., 364 (2002) 231-236.
[34] C.T. Rettner, F. Fabre, J. Kimman, D.J. Auerbach, Phys. Rev. Lett., 55 (1985) 1904-1907.

[35] E.K. Watts, J.L.W. Siders, G.O. Sitz, Surf. Sci., 374 (1997) 191-196.

[36] W.E. Kaden, T. Wu, W.A. Kunkel, S.L. Anderson, Science, 326 (2009) 826-829.

[37] P. Nieto, E. Pijper, D. Barredo, G. Laurent, R.A. Olsen, E.-J. Baerends, G.-J. Kroes, D. Farías, Science, 312 (2006) 86-89.

[38] K.R. Lykke, B.D. Kay, J. Chem. Phys., 92 (1990) 2614-2623.

[39] Q. Ran, D. Matsiev, D.J. Auerbach, A.M. Wodtke, Nucl. Instrum. Methods Phys. Res. B, 258 (2007) 1-6.

[40] R.D. Beck, P. Maroni, D.C. Papageorgopoulos, T.T. Dang, M.P. Schmid, T.R. Rizzo, Science, 302 (2003) 98-100.

[41] R.R. Smith, D.R. Killelea, D.F. DelSesto, A.L. Utz, Science, 304 (2004) 992-995.

[42] J. Harris, J. Simon, A.C. Luntz, C.B. Mullins, C.T. Rettner, Phys. Rev. Lett., 67 (1991) 652-655.

[43] H. Mortensen, L. Diekhöner, A. Baurichter, A.C. Luntz, J. Chem. Phys., 116 (2002) 5781-5794.

[44] R. Milot, A.P.J. Jansen, Phys. Rev. B, 61 (2000) 15657-15660.

[45] A.T. Gee, B.E. Hayden, C. Mormiche, A.W. Kleyn, B. Riedmüller, J. Chem. Phys., 118 (2003) 3334-3341.

[46] P.M. Hundt, B. Jiang, M.E. van Reijzen, H. Guo, R.D. Beck, Science, 344 (2014) 504-507.

[47] B. Jiang, X. Ren, D. Xie, H. Guo, Proc. Natl. Acad. Sci. U.S.A., 109 (2012) 10224-10227.

[48] C.T. Rettner, H. Stein, Phys. Rev. Lett., 59 (1987) 2768-2771.

[49] C.T. Rettner, J. Chem. Phys., 101 (1994) 1529-1546.

[50] K.R. Lykke, B.D. Kay, State-to-state inelastic and reactive molecular beam scattering from surfaces, in *Proc. SPIE* 1208, Laser Photoionization and Desorption Surface Analysis Techniques, 18 (July 1, 1990), 1990, pp. 18-29.

[51] C.T. Rettner, D.J. Auerbach, Science, 263 (1994) 365-367.

[52] C.T. Rettner, D.J. Auerbach, Phys. Rev. Lett., 74 (1995) 4551-4554.

[53] C.T. Rettner, D.J. Auerbach, Surf. Sci., 357–358 (1996) 602-608.

[54] M. Persson, J. Strömquist, L. Bengtsson, B. Jackson, D.V. Shalashilin, B. Hammer, J. Chem. Phys., 110 (1999) 2240-2249.

[55] C.T. Rettner, D.J. Auerbach, J. Lee, J. Chem. Phys., 105 (1996) 10115-10122.

[56] H. Ueta, M.A. Gleeson, A.W. Kleyn, J. Chem. Phys, 135 (2011) 074702.

[57] M. Blanco-Rey, E. Díaz, G.A. Bocan, R. Díez Muiño, M. Alducin, J.I. Juaristi, J. Phys. Chem. Lett., 4 (2013) 3704-3709.

[58] M.A. Gleeson, A.W. Kleyn, Nucl. Instrum. Methods Phys. Res. B, 317, Part A (2013) 109-114.

[59] T. Zaharia, A.W. Kleyn, M.A. Gleeson, Phys. Rev. Lett., 113 (2014) 053201.

[60] E. Quintas-Sánchez, C. Crespos, P. Larrégaray, J.-C. Rayez, L. Martin-Gondre, J. Rubayo-Soneira, J. Chem. Phys., 138 (2013) 024706.

[61] M. Brandt, F. Kuhlmann, T. Greber, N. Böwering, U. Heinzmann, Surf. Sci., 439 (1999) 49-58.

[62] M. Minissale, E. Congiu, S. Baouche, H. Chaabouni, A. Moudens, F. Dulieu, G. Manicó, V. Pirronello, Chem. Phys. Letters, 565 (2013) 52-55.

[63] Y. Yao, K.P. Giapis, Phys. Rev. Lett., 116 (2016) 253202.

[64] Y. Yao, K.P. Giapis, Angew. Chem. Int. Ed., 55 (2016) 11595-11599.

Chapter 3

Principles of molecular beam and surface analytical techniques

3.1 Introduction

A supersonic molecular beam technique has been developed since the first crossed-molecular beam was set up in 1967 by Y. T. Lee (Laureate of Nobel prize in chemistry, 1986) [1]. Till today, because of its unique beam properties:

(1) Large density of gas molecule in the flow;
(2) Sharp velocity distribution;
(3) A well collimated projectile of gas molecules without colliding with each other.

The supersonic molecular beam has become a useful method and has been broadly utilized for the research of chemical reaction dynamics including gas-phase reactions as well as heterogeneous catalytic reactions [2-7]. In this chapter, the principle of the molecular beam and the surface analytical techniques are presented.

3.2 Principles of supersonic molecular beam

3.2.1 Supersonic beam source

A molecular beam is formed from a supersonic jet expansion of gas. **Figure 3.1** presents a schematic diagram of the complicated features of a free-jet expansion under continuum conditions [8]. The shown source is a nozzle with small pin-hole for which the accelerating flow can be approximated as an isentropic flow, with negligible viscous and heat conduction effects. The gas in a high-pressure container (nozzle tube)

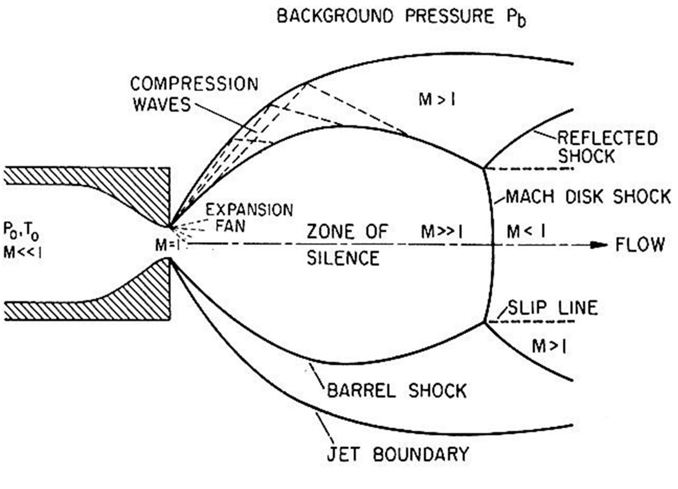

Figure 3.1 Flow structure of a single under-expanded orifice jet in the continuum regimen [8]

starts from a negligibly small velocity. It is called the stagnation state (P_0, T_0) and the gas molecules have a Maxwellian distribution of velocity. With an imposed pressure difference (P_0 - P_b) inside and outside of nozzle, the gas molecules are accelerated, as the cross-sectional area decreases, towards the source exit. The mean velocity of effusing molecules at the slit of nozzle equals to the local speed of sound or Mach number equal to 1 ($M = 1$). The flow may reach sonic speed at the exit of nozzle orifice if the pressure ratio fits [8]:

$$\frac{P_0}{P_b} \geq G \equiv \left(\frac{\gamma+1}{2}\right)^{\frac{\gamma}{\gamma-1}} \tag{1}$$

where γ is the specific-heat ratio C_p/C_v, taken to be 7/5 for CO_2 molecule in the present experiment [9], which is introduced in latter experimental part. The pressure ratio G must less than 2.1 for all gases ($G = 1.89$ for CO_2 gas). If the pressure ratio is less than this critical value, then the flow will exit subsonically, with exit pressure nearly equal to P_b, without any further expansion. As P_0/P_b is beyond the value, M equals 1 at the nozzle orifice, and the exit pressure becomes independent of P_b and equal to P_0/G, approximately half of P_0. The expansion as the flow thus happens after pass through an expansion fan region and attempts to meet the necessary boundary condition imposed by the ambient pressure P_b [8]. The mass flow rate r at the nozzle orifice:

$$r = P_0 \frac{\pi d^2}{4} \sqrt{\frac{\gamma m}{RT_0}} \left(\frac{\gamma+1}{2}\right)^{\frac{\gamma+1}{2(\gamma-1)}} \tag{2}$$

where d is the diameter of nozzle orifice, m is mass number of molecule. The mass flow rate is independent on P_b, but relates to the size of orifice and gas mass number. For more details about the calculations of Mach value in the different zones, please check the theoretical review in ref.[10].

3.2.2 Interaction with background gases

If the background gas density is high ($P_0/P_b < G$), the expansion of the jet gas travels through a shock zone where the molecules are quickly decelerated; if the background gas density is low ($P_0/P_b \geq G$), a molecule in the jet experiences a series of individual scattering events, and the randomization of the velocity distribution occurs over an extended region of space. The volume of the shock zone thus depends on the density of the background gas. As shown in **Fig. 3.1**, two types of shock zones can be developed when a jet has a free expansion into vacuum. A barrel shock forms around the centerline of the expansion, resembling a paraboloid of revolution centered on the jet axis, opening from the expansion orifice. Since the flow at the apes of the expansion fan is turned almost suddenly to move away from the orifice axis, it has to be turned towards the axis to become axial at a downstream distance. This turning is caused by the shock which is essentially an oblique shock. But on either side of the axis for two-dimensional flow and around the axis for axisymmetric flow, the shape of the shock assumes the form of a "barrel" and thus is referred to as a barrel shock. Outside the barrel shock, it is a second shock zone, called Mach disk, which forms a nearly flat terminal shock wave perpendicular to the centerline of the beam. Since the reflection of a wave from a free boundary is unlike, the expansion rays get reflected from the free boundary as compression waves. These compression waves may coalesce to form shock waves that cross each other at axis and meet the barrel shock and reflect back as expansion waves. Depending on the pressure ratios, these structures are well defined and are easily observed through Schlieren photography as shown in the **Fig. 3.2** [11]. That is, the flow downstream of the Mach disk can re-expand and repeat the structure.

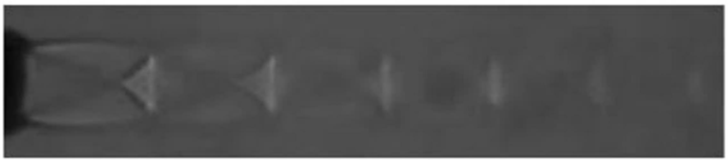

Figure 3.2 Wave patterns in a sonic under-expanded free-jet issuing from a tube run at nozzle pressure ratio $P_0/P_b = 2.73$ (ref. [11]). The barrel shock is clearly visible, as is the terminal shock wave (Mach shock wave). A skimmer can be used to transmit the central portion of the expansion into a second chamber (collimator chamber).

The location of the Mach disk depends only on the ratio of P_0/P_b. Due to the decrease of the collision frequency in the jet of relatively low density, the transition from continuum to free molecular flow occurs and the expansion becomes frozen at a distance from the nozzle much smaller (< 1/10) than the distance:

$$\chi_M = 0.67d(P_0/P_b)^{1/2} \tag{3}$$

at the Mach disk location, measured in the diameter of nozzle orifice d, is remarkably insensitive to γ. This location is very close to that at which a normal shock is able to raise the local pressure to the background pressure, P_b [11]. To generate a well collimated supersonic monotonic beam of gas molecules without colliding with each other, one can place a skimmer aperture to extract the centerline beam inside an isentropic region termed the zone of silence and/or by reducing the background pressure, P_b.

3.2.3 Seeded beams

By adding a small mole fraction of a second species to the gas in terms of gas mixture in the reservoir, one may create a seeded molecular beam. As we discussed above, when the source pressure P_0 is high, the idealized continuum model of gas flow is well generated and the behavior of the supersonic expansion is the same as that for a pure gas with molecular weight and heat capacity taken as the weighted average of the corresponding properties of the gases making up as a mixture. At high source pressures, the effects of gas viscosity and heat transfer may be neglected, and the gas flow may be treated as an adiabatic, isentropic expansion. This assumption leads to the conservation of the sum of the enthalpy and the kinetic energy of directed mass flow as the gas expands into vacuum, therefore, the flow velocity

$$v = \sqrt{\frac{2H(T_0)}{M}} \tag{4}$$

where $H(T_0)$ is the molar enthalpy of the gas at the temperature of the source reservoir, T_0.

Practically, T_0 can be given as nozzle temperature T_n and $H(T_0)$ can be given as C_pT, where C_p is a constant-pressure specific molar heat capacity, which can be considered to be independent of temperature. And Eq. (4) becomes

$$v_{mas} = \sqrt{\frac{2C_pT_n}{M}} \tag{5}$$

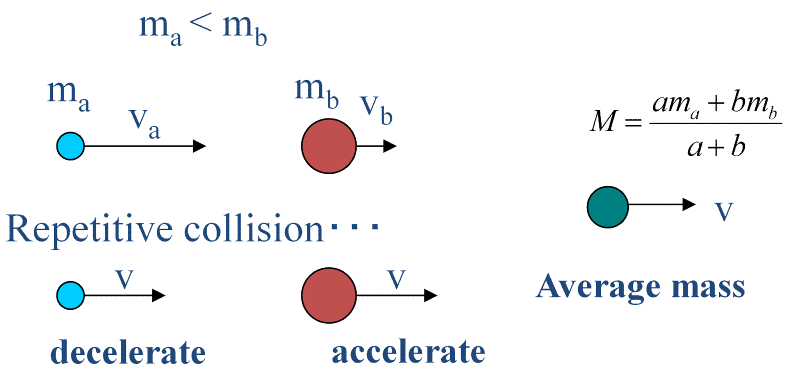

Figure 3.3 Mechanism of seeded beams in supersonic molecular beam techniques. For a gas mixture consisting of a low concentration of a heavy seed gas (m_b) in a light carrier gas (m_a), the flow velocity is dominated by the more abundant-lighter gas. The seed gas can be pushed by the light carrier gas and accelerated to high kinetic energies while the light molecule is slowed down. Eventually they reach the same flow velocity as v.

where M is the average molecular weight (m_a and m_b) for the mixed gas, composed by the light carrier gas (m_a) and heavy seeded gas (m_b),

$$M = \frac{am_a + bm_b}{a+b} \tag{6}$$

As schematically illustrated in **Fig. 3.3**, under the condition of high gas pressure gap between the reservoir and the vacuum and due to 100 ~ 1000 times collisions between molecules in the orifice of the nozzle [12] (orifice diameter Φ = 50 μm, used for this experiment), both component gases: light carrier gas (m_a) and heavy seeded gas (m_b) with different molecular mass respectively reach the same flow velocity and temperature at the same point after repetitive collision in the expansion. the energy transfer occurs as follows:

$$C_p T_n = 1/2\, mv^2 + C_p T \tag{7}$$

where T_n is nozzle temperature, T is the beam itself temperature, $T_n \gg T$. From the Eq. (7), we know that when the nozzle temperature T_n increases (or decreases), the translational energy (E_t) of the molecules in beam increases (decreases). While the rotational temperature is changed from T_n to T after the expansion, which is normally negligible. The vibrational energy is corresponding to the nozzle temperature T_n, this is because the energy difference between each vibrational level is relatively large. The translational energy of beam molecules also can be controlled by mixing the molecule with different mass (this is called a seeding method). For example, if one needs to accelerate the molecule, one just can prepare the mixing gas with atom/molecule with a light mass such as helium to increase the translational energy. Therefore, the translational energy of the beam molecules can be tuned by changing the mole ratio of the heavy molecules and light molecules as well as by controlling the nozzle temperature.

The experimental setup for such a beam is shown schematically in **Fig. 3.4** [13], which is composed by three chambers, (1) Gas container, which connects to the nozzle; (2) skimmer chamber; and (3) test chamber or scattering chamber. In the (1) gas container with high pressure, due to the frequent collisions among the molecules, the energy exchange occurs and finally the system is almost in thermal equilibrium. The energy distribution of the molecules thus shows a broad shape by following Boltzmann distribution. The sharp energy distribution of the beam with close to monotonicity is very useful in the study of scattering and reaction dynamics. According to the Kantrowitz and Grey [10], two factors is expected to affect the beam intensity: (1) the distance between the nozzle and the skimmer. If the distance between the nozzle and the skimmer is increased from small values, the beam intensity decreases. (2) the container pressure P_0. The beam intensity is roughly proportional to the container pressure P_0. However, in practical terms, it is found that the intensity increases in a certain range with increasing the distance, then passes through a maximum, and finally decreases, there is thus a maximum during the adjustment in the beam source preparation. Furthermore, if the apex of skimmer is outside of the silence zone, the intensity depends very little on the P_0 [14].

Besides, molecular beam scattering experiments such as helium scattering investigation has been extensively applied in the study of molecules adsorption on surface, e.g. CO adsorption LiF [15], and on Fe/HOPG (Highly Oriented Pyrolytic Graphite) [15, 16]. The experiments demonstrated the diffraction of He from the LiF surface and thus demonstrated the wave nature of a particle beam. Thus He scattering can be used to study surface structure due to the wavelength of thermal He beam which is on the order of a tenth of a nanometer. The helium scattering is surface extremely surface-sensitive measurement technique. In addition, from the measurement of inelastic scattering of heavy molecules from the surface, the energy transfer process during collision can also be analyzed.

3.3 Techniques of surface analysis combining with supersonic molecular beam

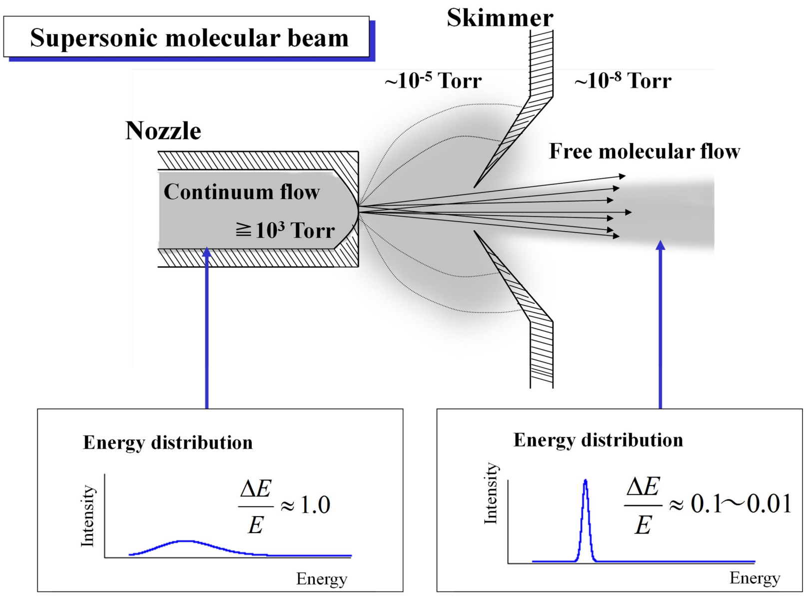

Figure 3.4 Supersonic molecular beam can be generated through free-jet expansion, skimmer and a collimator linearly in a centerline. The nozzle chamber, collimator chamber and test chamber are separately pumped. The energy distribution of gas molecules shows a sharp shape compared to the normal Boltzmann distribution because of the free-jet expansion [13].

3.3.1 Low energy electron diffraction (LEED) and Auger electron spectroscopy (AES)

LEED and AES are very powerful techniques that allow for the characterization of surface structure based on the diffraction of electrons with low kinetic energy [26, 27]. The AES apparatus for measuring the energy of the Auger electrons and LEED setup is the same. It consists of the three grids for AES and a screen presented for LEED, an electron collector is located in the Auger. The electron gun is operated higher energy in the Auger technique but lower energy for LEED. The LEED/AES spectrometer has to be in an ultra-high vacuum (UHV) chamber. Here we briefly introduce the principle of LEED/AES spectrometer and their applicable examples.

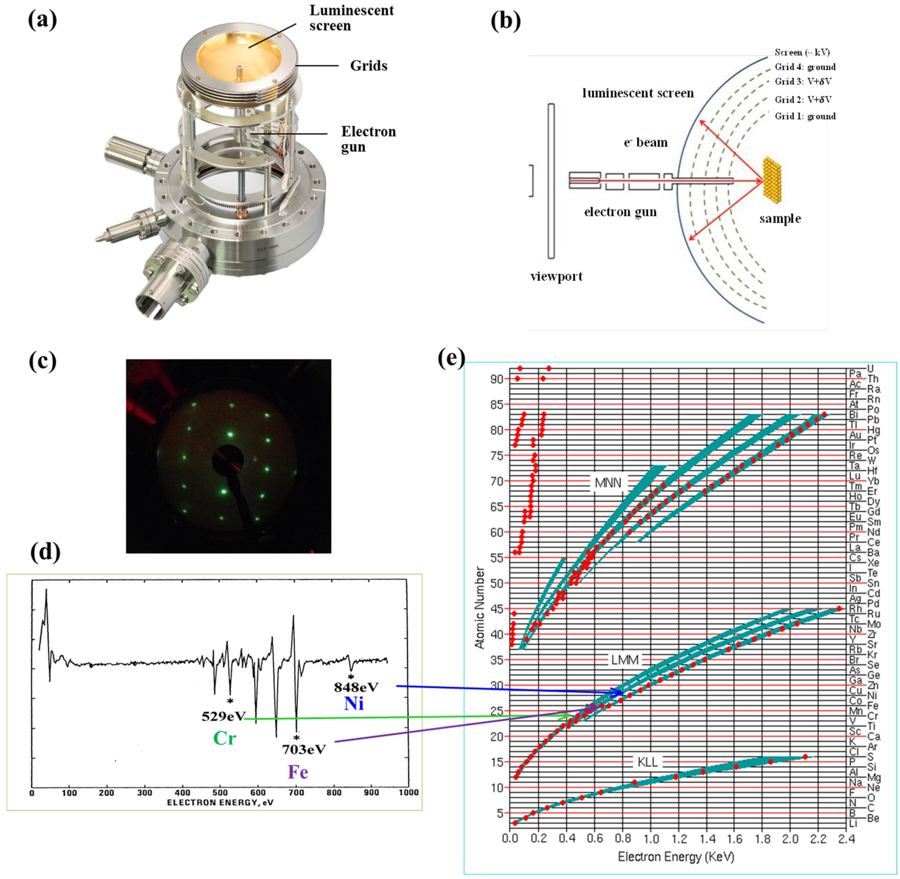

Figure 3.5 The principle of LEED/AES spectrometer and the experimental application examples. (**a**) the physical picture of LEED/AES; (**b**) Schematic diagram of a typical LEED/AES instrument; (**c**) an example of the LEED pattern of Cu(110). (**d**) an AES spectrum: the differential of an secondary electron energy distribution *dN(E)/d(E)* as a function of energy (*E*) emitted electrons. (**e**) Auger transitions lines for different elements. Red dots indicate the most intensity lines. From the differential AES spectrum Ni, Fe and Cr in (d) have been identified.

(1) Principle of LEED

The typical diagram of a LEED system is shown in **Fig. 3.5(a, b)**. The electrons come from an electron gun behind a transparent hemispherical luminescent screen and diffract off the surface of the sample, followed by the heading back towards the electron gun and the grids surrounding it. The electron gun consists of a heated cathode and a set of focusing lenses which send electrons at low energies. The electrons collide with the sample and diffract in different directions depending on the surface. Once diffracted, they are directed to the luminescent screen. Before colliding with the screen, they must pass through four different grids (known as retarding grids), which contain a central hole through which the electron gun is inserted. The first grid is the nearest one to the sample and is connected to earth ground. A negative potential is applied to the second and third grids, which act as suppressor grids, given that they repel all electrons coming from non–elastic diffractions. These grids perform as filters, which only allow the highest–energy electrons to pass through; the electrons with the lowest energies are blocked in order to prevent a bad resolution image. The fourth grid protects the phosphor screen, which possesses positive charge from the negative grids. The remaining electrons collide with the luminescent screen, creating a phosphor glow (see **Fig. 3.5(c)**), where the light intensity depends on the electron intensity.

LEED has high surface sensitivity is due to the use of electrons with incident well-defined low energies from 20 to 200 eV. These electrons have the wavelengths on 2.7 – 0.87 Å, as given by a well-known de Broglie relationship [29]:

$$\lambda = \sqrt{150 / E} \tag{8}$$

where λ is the electron wavelength (Å), E is the electron's energy (eV). These wavelengths are comparable to the atomic spacing. Therefore, the electrons can penetrate the sample for about 10 Å without losing energy and be elastically scattered easily by the atoms in the first few layers of the sample. Such features have made the LEED as one of the most common techniques in surface science for giving the information on the symmetry of the unit cell (qualitative analysis) and the position of the atoms in the crystal surface (quantitative analysis). So electron diffraction is different from X-Ray diffraction. The latter provides information about the structure in bulk of the sample because it has larger mean free path in a scale of micrometer. On the other hand, similar with X-ray diffraction, electron diffraction also follows the Bragg's law. That is, $n\lambda = d\, sin\theta$ for X-ray diffraction, $n\lambda = a\, sin\theta$ for electron diffraction, where λ is the wavelength, a is the atomic spacing, d is the spacing of the crystal layers, θ is the angle between the incident beam and the reflected beam, and n is an integer. As shown in **Fig. 3.6**, the diffracted electrons radiate out from the sample toward a detector. For constructive interference between two waves, the path length difference ($2a\cdot\sin\theta/2d\cdot\sin\theta$) must be an integral multiple of the wavelength. Diffraction of electrons, elastic scattering by the surface, happens when momentum parallel to the surface is conserved between incoming

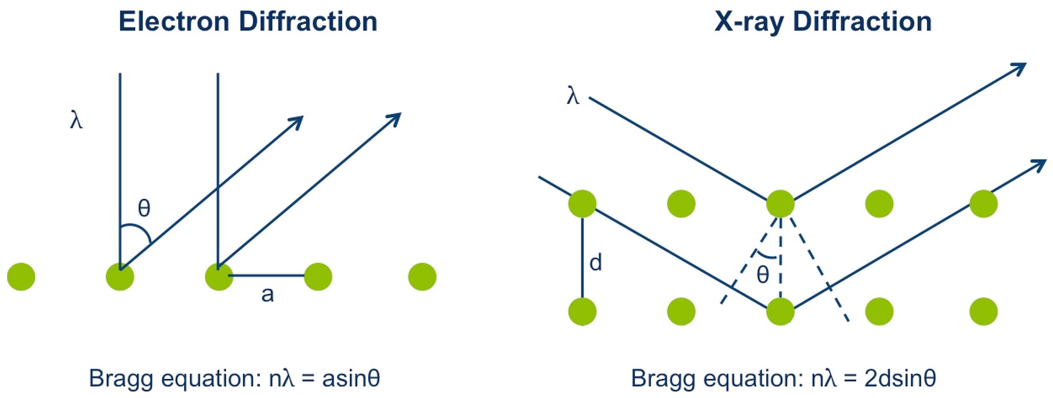

Figure 3.6 Representation of the electron diffraction and X-ray diffraction.

and outgoing beams, up to the addition or subtraction of a reciprocal lattice-vector. These diffracted beams are indexed (*hkl*) by the reciprocal lattice-rod from which they diffract. The outgoing beams are therefore a map of the surface reciprocal-lattice and display its symmetry.

(2) Principle of AES

AES was developed in the late 1960's, deriving its name in honor of Pierre Auger, a French Physicist who first observed the effect in 1925. It is a surface sensitive technique by using the emission of low energy electrons in the Auger process and becomes one of the most commonly employed surface analytical techniques for providing information about the chemical composition of the outmost surface layers of a sample [27,31]. As shown in **Fig. 3.5(d, e)**, the AES can be used to identify the elements information at surface.

The Auger spectroscopy is a method which can be considered as involving three basic steps: (1) atomic ionization by removing of a core electron; (2) electrons at upper level energy falls to a lower level energy; (3) third electron (Auger elections) is excited by the energy given off in step (2) and detected, The atom is left with two vacancies. As shown in **Fig. 3.7**, the principle of Auger operates by allowing a high-energy electron from the beam to eject an electron from its orbit creating an empty hole in the orbit. As this occurs, another electron from a higher orbit moves to fill the empty hole. As the electron changes from an orbital with higher energy to a lower orbit, it releases energy. This energy might eject a third electron in another orbit. By measuring the energy of the emitter electron, called the Auger electron, the atom can be identified. This is because different atoms have different atomic orbits and therefore different Auger energies [32].

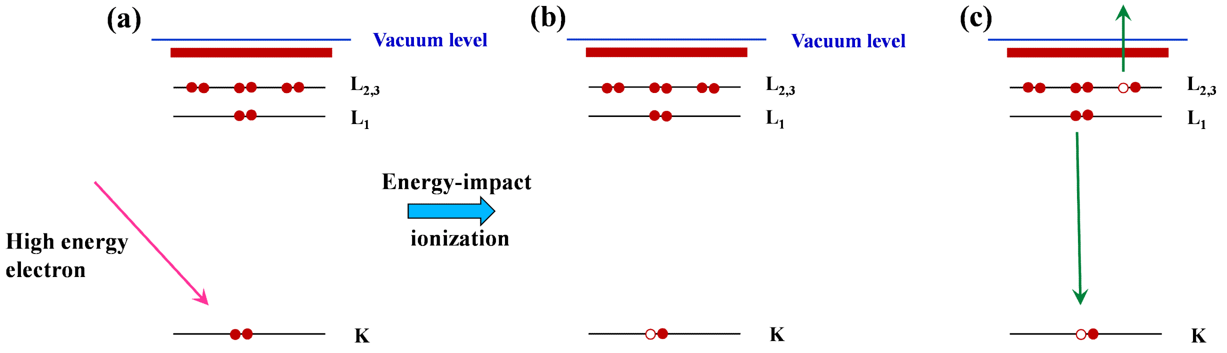

Figure 3.7 The Auger process (**a, b**) ionization occurs through the removal of a K-shell electron by a high energy electron beam. (**c**) one electron falls from a higher level to fill an initial core hole in the K-shell and the energy liberated in this process is simultaneously transferred to a third electron (Auger electron) at the orbital of $L_{2,3}$. The Auger electron emitted from $L_{2,3}$ with an identified kinetic energy.

It should be noted that in the Auger process doesn't exist a real photon intermediating the transition and the Auger electron energy is independent of the excitation energy. In this example as shown in Fig.4.8, we can simply estimate the kinetic energy *KE* of Auger electron from the binding energies of the various orbital energy levels involved:

$$KE = (E_K - E_{L_1}) - E_{L_{2,3}} - \Phi \tag{10}$$

Eq. (3) can be rewritten as

$$KE = E_K - (E_{L_1} + E_{L_{2,3}}) - \Phi \tag{11}$$

where Φ is a parameter related to the electron-electron interaction in the final state and the relaxation energies. However, practically the estimation of KE is much complicated because of the transition probabilities between singly ionized and doubly ionized state of the atom. In general, since the initial ionization is non-selective and the initial hole may therefore be in various shells, there will be many possible Auger transitions for a given element, i.e. some is weak, some is strong in intensity. Auger spectroscopy is based upon the measurement of the kinetic energies of the emitted electrons. As shown in **Fig. 3.5(d, e)**, each element in a sample being studied will give rise to a characteristic spectrum of peaks at various kinetic energies.

3.4 Principles of temperature-programmed-desorption (TPD)

The desorption of adsorbed atoms and molecules is one of the most fundamental elementary surface kinetic processes. The TPD technique can be used for both the quantitative and qualitative (at least in part) characterization of adsorbed molecules on crystal surface in ultra-high vacuum system: (1) the activation energy for desorption; (2) information on the nature and strength of lateral adatom interactions; and (3) the relative surface coverage of adsorbates.

The rate of desorption of a surface species follows Arrhenius-type behavior [33]:

$$R_d = \frac{d\theta_M}{dt} = v(\theta_M) \times \theta_M^n \times exp(\frac{-E_d(\theta_M)}{RT}) \tag{12}$$

where $v(\theta_M)$ is the frequency factor, θ_M is instantaneous coverage, n is kinetic order or desorption order, $E_d(\theta_M)$ is activation energy of desorption and R is gas constant. It is irreversible by increasing surface temperature linearly with time t (s) from initial temperature T_0 to $T(t)$ with a heating rate k (K/s) to induce reaction and desorption occurred on surface.

$$T(t) = T_0 + k \cdot t \tag{13}$$

By combining eq.(5) and eq.(6), the intensity of the desorption signal $I(T)$ is obtained as

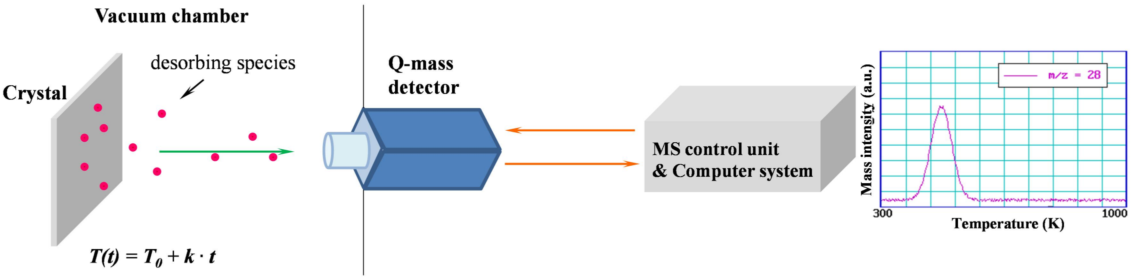

Figure 3.8 Schematic of TPD measurement. The surface is heated up in a heating rate k from T_0 to $T(t)$. Q-mass detector records the intensity of desorbing species. TPD profile thus can be obtained in terms of the mass intensity as a function of surface temperature.

$$I(T) \propto -\frac{d\theta_M}{dt} = \frac{v(\theta_M) \times \theta_M^n}{k} \times exp(\frac{-E_d}{RT}) \tag{14}$$

From eq.(7), we can know that at low T, $E_d > RT$, and little desorption occurs, then the $I(T)$ is vanishingly small ($I(T) \approx 0$); As the temperature T is increased $I(T)$ begins to increase very rapidly when the value of RT approaches that of the activation energy, E_d . When the coverage decrease following desorption of fraction of monolayer, $I(T)$ thus decreases. $I(T)$ decrease to zero again when the surface is heated to high temperature.

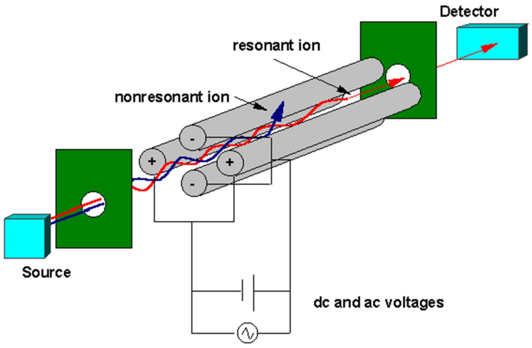

Figure 3.9 Schematic of quadrupole mass spectrometer. It consists of an ion source, ion optics to accelerate and focus the ions through an aperture into the quadrupole filter, the quadrupole filter itself with control voltage supplies, an exit aperture, an ion detector, detection electronics, combining with a high-vacuum system. From online website of NASA: http: //attic.gsfc.nasa.gov/huygensgcms/MS_Analyzer_1.htm.

As shown in **Fig. 3.8**, by temperature- programmed heating of the sample, the adsorbed molecules desorb from the surface into gas-phase. The whole process is programmed by a computer system with quasi-simultaneous monitoring of a large number of possible desorbing products. The intensity of desorption species is characterized by the quadrupole mass spectrometer (Q-mass) which is the most commonly used mass detector in TPD measurements. A quadrupole mass filter consists of four parallel metal rods arranged as shown in **Fig. 3.9**. Two opposite rods have an applied potential of ($U + V \cdot cos(wt)$) and the other two rods have a potential of - ($U + V \cdot cos(wt)$), where U is a DC voltage and $V \cdot cos(wt)$ is an AC voltage. The applied voltages affect the trajectory of ions traveling down the flight path centered between the four rods. For given dc and AC voltages, only ions of a certain mass-to-charge ratio (m/z) pass through the quadrupole filter and all other ions are thrown out of their original path. A mass spectrum is obtained by monitoring the ions passing through the quadrupole filter as the voltages on the rods are varied.

Example shows the TPD profile following adsorption of CO onto a Pd(111) at 300 K (in Fig. 3.8, right side). Peak temperature may be considered as characteristic desorption temperature of CO on Pd(111). The peak area indicates the amount of adsorbed CO on Pd(111). However, to identify a specific adsorption species, surface spectroscopies should be applied to obtain the structural information of surface spices combining with TPD measurements.

3.5 Principles of Infrared reflection-absorption spectroscopy (IRAS)

Infrared spectroscopy with an advantage of high signal-to-noise ratio (SNR) is widely used to characterize molecular adsorption onto single-crystal metal substrates in ultra-high vacuum condition. The dielectric properties of the substrate and adsorbate determine the optimum conditions under which the RAIRS experiment should be carried out. As shown in **Fig. 3.10**, the excitation of vibrational adsorbate modes on metals is governed by a so-called "surface selection rule". In this case, the amplitude and phase of the reflected radiation depend on the direction of the electric field vector, which is composed of one component paralleling with the reflection plane (*p*-polarized), and a second component normal to the reflection plane (*s*-polarized) [17].

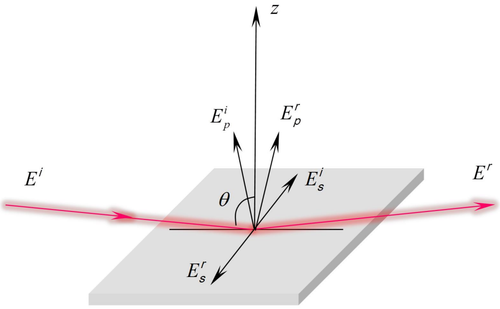

Figure 3.10 The reflection geometry showing the *s* and *p* components of the electric fields (E^i) of incident and reflected (E^r) radiation.

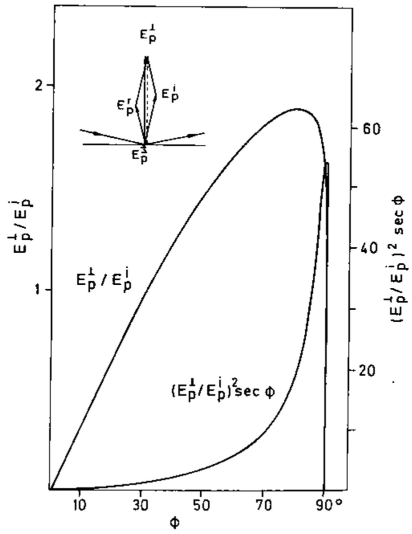

Figure 3.11 The relative amplitude ($E_p^{\perp}/E_p^i$) of the electric field perpendicular to the surface as a function of incident angle, together with the quantity ($E_p^{\perp}/E_p^i$) sec Φ. The inset shows the dominance of the normal component of the field of the surface arising from the component [17].

On considering Fresnel's equations, only the *p*-polarized radiation shows a significantly resultant electromagnetic field close to the metallic surface for high incident angles of radiation near a grazing incidence (at ca. 80°) as shown in **Fig. 3.11**. In contrast, the mean square electric field of radiation polarized in the surface plane is negligible due to the 180° phase shift after reflection at the metallic surface. Hence, only those vibrations with dipole components perpendicular to the surface can be efficiently excited.

IRA spectra contain absorption band structures, related to electronic transitions and vibrations of the bulk, the surface, a film, or adsorbed molecules. In reflectance spectroscopy, the absorbance is usually determined by calculating the $-\log(R_S/R_0)$, where R_S represents the reflectance from the adsorbate-covered substrate, and R_0 is the reflectance from the bare substrate [17].

3.6 Summary

In this chapter, we have introduced the principles of the supersonic molecular beam combining with the surface analytical techniques. By using the supersonic molecule beam, we can effectively control the energy of CO_2. The reaction condition such as the cleanness of Cu surface can be checked by applying LEED/AES, the reaction produces on the surface can be identified by using TPD measurements and RAIRS technique. These techniques thus provide the good conditions to study the dynamics of formate synthesis from CO_2 hydrogenation.

References

[1] Y.T. Lee, Science, 236 (1987) 793-798

[2] Y. Shagam, A. Klein, W. Skomorowski, R. Yun, V. Averbukh, C.P. Koch, E. Narevicius, Nat. Chem., 7 (2015) 921-926.

[3] M. Stei, E. Carrascosa, M.A. Kainz, A.H. Kelkar, J. Meyer, I. Szabó, G. Czakó, R. Wester, Nat. Chem., 8 (2016) 151-156.

[4] E.W. Kuipers, A. Vardi, A. Danon, A. Amirav, Phys. Rev. Lett., 66 (1991) 116-119.

[5] T. Zaharia, A.W. Kleyn, M.A. Gleeson, Phys. Rev. Lett., 113 (2014) 053201.

[6] R.R. Smith, D.R. Killelea, D.F. DelSesto, A.L. Utz, Science, 304 (2004) 992-995.

[7] P.M. Hundt, B. Jiang, M.E. van Reijzen, H. Guo, R.D. Beck, Science, 344 (2014) 504-507.

[8] D.R. Miller, Free Jet Sources, Oxford University Press, New York, Oxford, 1988.

[9] I.F. Silvera, F. Tommasini, Phys. Rev. Lett., 37 (1976) 136-140.

[10] A. Kantrowitz, J. Grey, Rev. Sci. Instrum., 22 (1951) 328-332.

[11] E. Rathakrishnan, Applied Gas Dynamics, 1 ed., Wiley, 2010.

[12] G. Scoles, Atomic and Molecular Beam Methods, in: Atomic and Molecular Beam Methods, Oxford University Press, New York, 1988.

[13] 近藤剛弘, 超音速分子線技術を用いた表面化学反応の制御に関する研究, in: 工学研究科, 筑波大学, 筑波, 2003, pp. 233.

[14] J.P. Valleau, J.M. Deckers, Canad. J. Chem., 43 (1965) 6-17.

[15] T. Kondo, H.S. Kato, T. Yamada, S. Yamamoto, M. Kawai, Eur. Phys. J. D, 38 (2006) 129-138.

[16] J. Oh, T. Kondo, D. Hatake, K. Arakawa, T. Suzuki, D. Sekiba, J. Nakamura, J. Phys. Chem. C, 116 (2012) 7741-7747.

[17] J. John T. Yates, T.E. Madey, Methods of surface characterization, in: Credric J. Powell, Alvin W. Czanderna, David M. Hercules, Theodore E. Madey, J. John T. Yates (Eds.) Vibrational spectroscopy of molecules on surfaces, Plenum press, Newyork and London, 1987.

Chapter 4

Dynamics of formate synthesis from CO_2 hydrogenation on Cu catalysts studied by supersonic molecular beam

4.1 Introduction

Recycling and usage of the CO_2 not only can reduce the global warming deriving from the massive CO_2 emissions because of anthropogenic energy demand, but also are the carbon feedstock for methanol synthesis. Formate synthesis is the initial important reaction step of the methanol synthesis from the direct hydrogenation of CO_2, where the reaction probability of the formate formation (~ 10^{-12}) is comparable with that of the methanol synthesis. We have already proposed that formate is formed via an ER-type mechanism based on the kinetics of pressure dependencies in high-pressure experiments on Cu single-crystal surfaces [1, 2]. If we assume that the reaction rate is determined by the kinetic or internal energy of CO_2, this direct reaction mechanism can explain the structure-insensitive character in terms of the similar apparent activation energies of 0.58 eV on Cu(111), 0.62 eV on Cu(110), and 0.58 eV on Cu(100), the turnover frequencies (TOFs), and the initial reaction rates for formate formation [3-5]. In homogeneous catalytic systems, the direct ER-type formate synthesis we proposed is analogous to the insertion of a CO_2 molecule directly into a Cu-H bond in organometallic copper hydride complexes without CO_2 binding with Cu [6, 7]. We recently questioned whether the thermal non-equilibrium channel exists if the formate formation takes place by a direct reaction between CO_2 and the H_a/Cu surface. To obtain solid experimental evidence of the thermal non-equilibrium activation of CO_2 via the suggested direct ER-type mechanism, we utilized a molecular beam technique in order to control the translational and vibrational energies of incident CO_2 while varying the Cu surface temperature.

The molecular beam has selected as an excellent tool to study the reaction dynamics in surface science. In this work, we present the experimental results about the reaction dynamics of the formate synthesis on Cu catalysts by using supersonic molecular beam. To shed the light on the mechanism of formate synthesis, one needs to study the dynamics of CO_2 catalytic hydrogenation on Cu catalysts. In order to obtain solid experimental evidences of the thermal non-equilibrium activation of CO_2 via the suggested direct ER-type mechanism and clarify the dynamics of formate synthesis, we utilized the molecular beam technique to control the translational and vibrational energies of incident CO_2 while varying the Cu surface temperature. That is, we can supply the energy to CO_2 only, without heating the Cu catalysts.

4.2 Research motivation and objective

The objective of the research is thus to clarify the mechanism and dynamics of formate synthesis from CO_2 hydrogenation on the Cu catalyst surfaces using supersonic molecular beam. The research contents can be classified three categories as follows, which includes:

(i) The dynamics of the formate synthesis from CO_2 and H_2 on Cu surfaces;

(ii) The dynamics of the formate decomposition into CO_2 and H_2 on Cu surfaces;

(iii) The detailed description of forward and reverse reaction by density functional theory (DFT) calculations.

In this work, to examine the reaction mechanism experimentally, we have applied to the supersonic molecular beam technique combining with techniques of surface analysis. From the principle of micro-reversibility, the angle-resolved analysis of the dynamics of CO_2 desorption from the formate decomposition was carried out to supports the dynamics of formate synthesis. The DFT calculations would give us a detailed description of the reaction process between CO_2 with the hydrogen adatom on the Cu catalysts.

4.3 Experimental apparatus and methods

4.3.1 Apparatuses

In this study, we used two supersonic molecular beam apparatuses to confirm that the nature of experimental results (such as the reaction probability of CO_2 to form formate) should be identical and not dependent of apparatus.

(1) Type I: large supersonic molecular beam system (LMB)

The supersonic molecule beam apparatus has been described elsewhere [1, 2]. The experimental apparatus used in the molecular beam work is shown in **Fig. 4.1**, which is schematically depicted in **Fig. 4.2**. In **Fig. 4.1**, the relative locations of CO_2 beam, TPD, FTIR apparatus and scattering detector are illustrated. The rotation of Cu sample can be controlled by the manipulator as the highest part. In this experiment, the beam incident direction is along the normal direction of Cu surface.

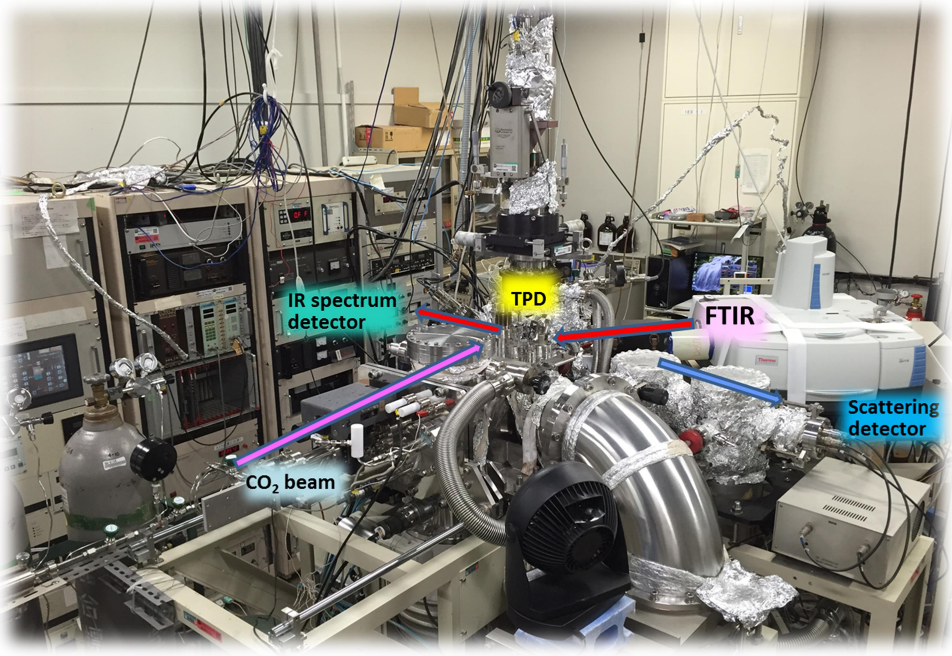

Figure 4.1 Large supersonic molecular beam apparatus as an ultra-high vacuum system. It is equipped by a molecular beam generator and scattering detector, and surface analytic techniques such as IRAS, TPD measurements.

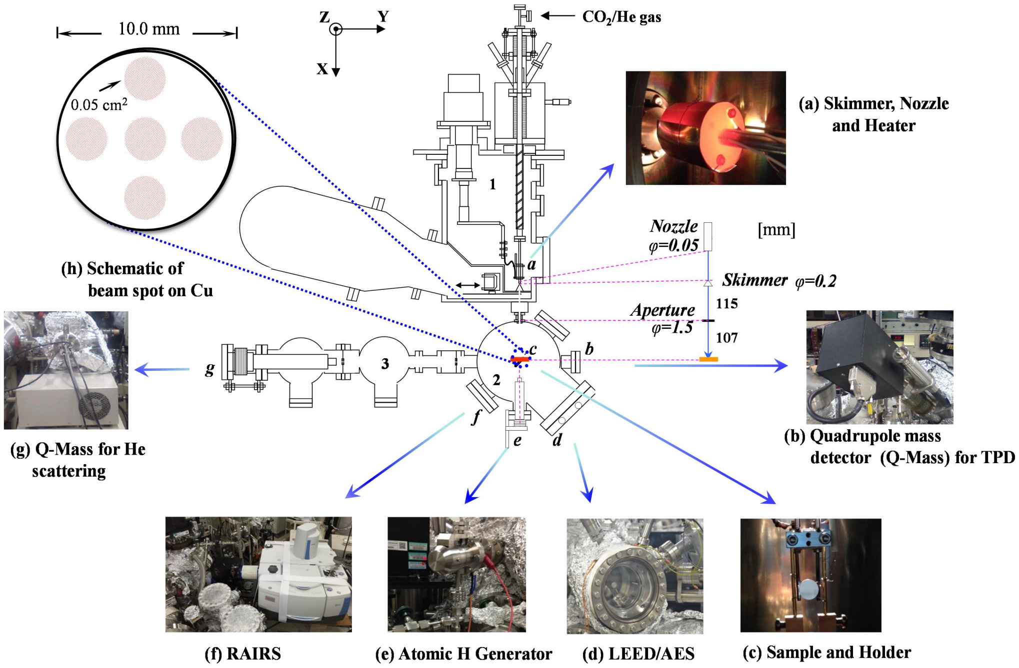

Figure 4.2 Schematic of supersonic molecular beam apparatus (top-view). The apparatus is an ultra-high vacuum system composed of (1) molecular beam source chamber (< 3×10^{-7} torr), (2) reaction chamber (< 3×10^{-10} torr), and (3) He-scattering detector chamber.

After the beam irradiation, the Cu sample surface has to rotate a 45°angle to the IR position or reversely rotate 90° to the Q-mass detector for TPD measurements. As shown in **Fig. 4.2**, the molecular beam apparatus composes three chambers: (1) source chamber, which consists of a beam source, skimmer, nozzle, and heater, is mainly evacuated by a diffusion pump with a pumping rate of 2000 L s^{-1} (for N_2). The background pressure is lower than 3×10^{-7} torr. A supersonic molecular beam is generated by free-jet expansion from the pinhole (diameter ϕ = 50 μm) of a cylindrical nozzle (made from Inconel 601), and skimmed by a conical skimmer into the reaction chamber through a differential pumping chamber. The nozzle temperature for the CO_2/He beam can be precisely controlled from room temperature to 1100 K by a resistive heater (**Fig. 4.2a**) within a temperature fluctuation of ± 2 K. (2) The reaction chamber is equipped with a 6-axis manipulator, which is used for sample alignment in the molecular beam collision and scattering measurement (**Fig. 4.2 b**). The background pressure is lower than 3×10^{-10} torr. The Cu single crystal sample, which has two parallel through-holes, is supported by two tantalum filaments welded to two gold rods. (3) He-scattering detector chamber. The alignment of the molecular beam scattering geometry against the sample was established by the He scattering measurements, where the scattered He beam was detected by the quadrupole mass spectrometer (Q-Mass) in the detector chamber.

Infrared reflection-absorption spectroscopy (IRAS) and TPD measurement

This spectroscopic technique is used to identify adsorbed species under ultra-high vacuum (UHV) conditions. Infrared radiation (IR) is directed onto a well-defined single crystal sample and reflected from a metal surface. The infrared components can be absorbed by the surface adsorbed species, which will produce characteristic features in the IR spectrum.

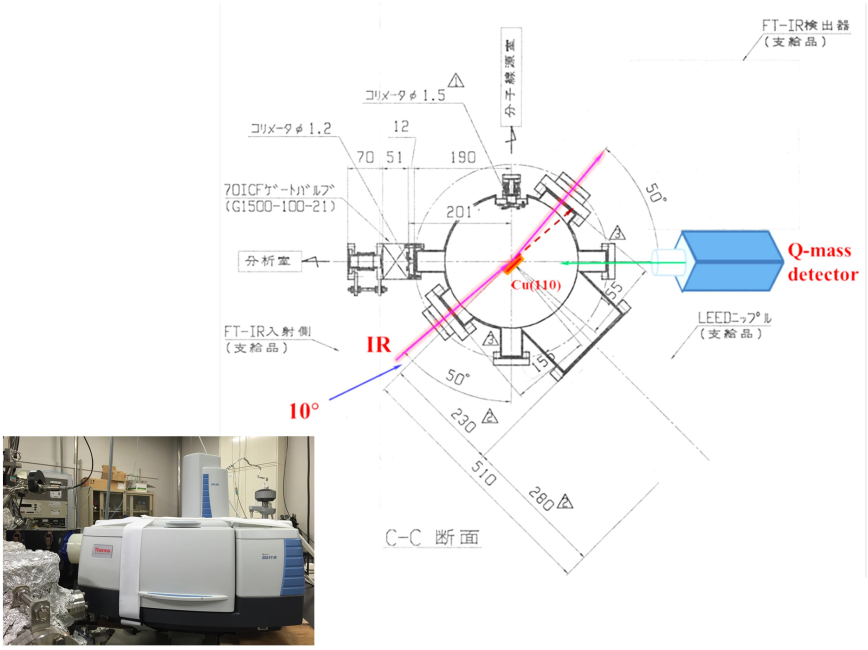

Figure 4.3 Schematic of IRAS equipped with the reaction chamber.

The IRA spectrometer used in this study is a Thermo Scientific Nicolet iS 50 FT-IR with a mid-IR (**Fig. 4.2(f)** and **Fig. 4.3**). The IR detector is made of mercury cadmium telluride (MCT/A, narrow band - 650 cm^{-1} cutoff) with high sensitivity. The IRAS measurements were performed by focusing an IR beam onto a small Cu single crystal (~ 1 cm diameter) at a grazing incidence angle of about 80° from the surface normal via ZnSe windows. The incidence angle of IR beam is important to obtain appreciable intensities for IR bands of molecular adsobates, which should be smaller than 15° between the incident direction and the surface, as we refer the principle of IRAS in Chapter 4. The further description of the IR measurement will be presented in the experimental parts. As shown in **Fig. 4.3**, the Cu sample was located at the center of reaction chamber. During the irradiation of CO_2 beam, the front face was facing to the beam at the surface normal direction. After the irradiation of CO_2 beam, the sample surface was rotated to the IR position by 45° by motor-drove manipulator (**Fig. 4.3**). Before carrying out the IRAS measurements, the MCT/A detector should be cooled down to stabilize the detector by liquid nitrogen for 2 hours. Infrared spectra were then taken in a range of 400-4000 cm^{-1}, with 1200 scans at a resolution of 6 cm^{-1} for both reference (background) and the sample spectra.

The IR measurement procedure was as follows: (1) stopped the CO_2 beam irradiation; (2) sample was rotated to the IR position and the IRAS measurement was carried out as sample spectrum; (3) TPD measurement was performed to remove the formate species; (4) the reference RAIRS was measured after TPD measurements.

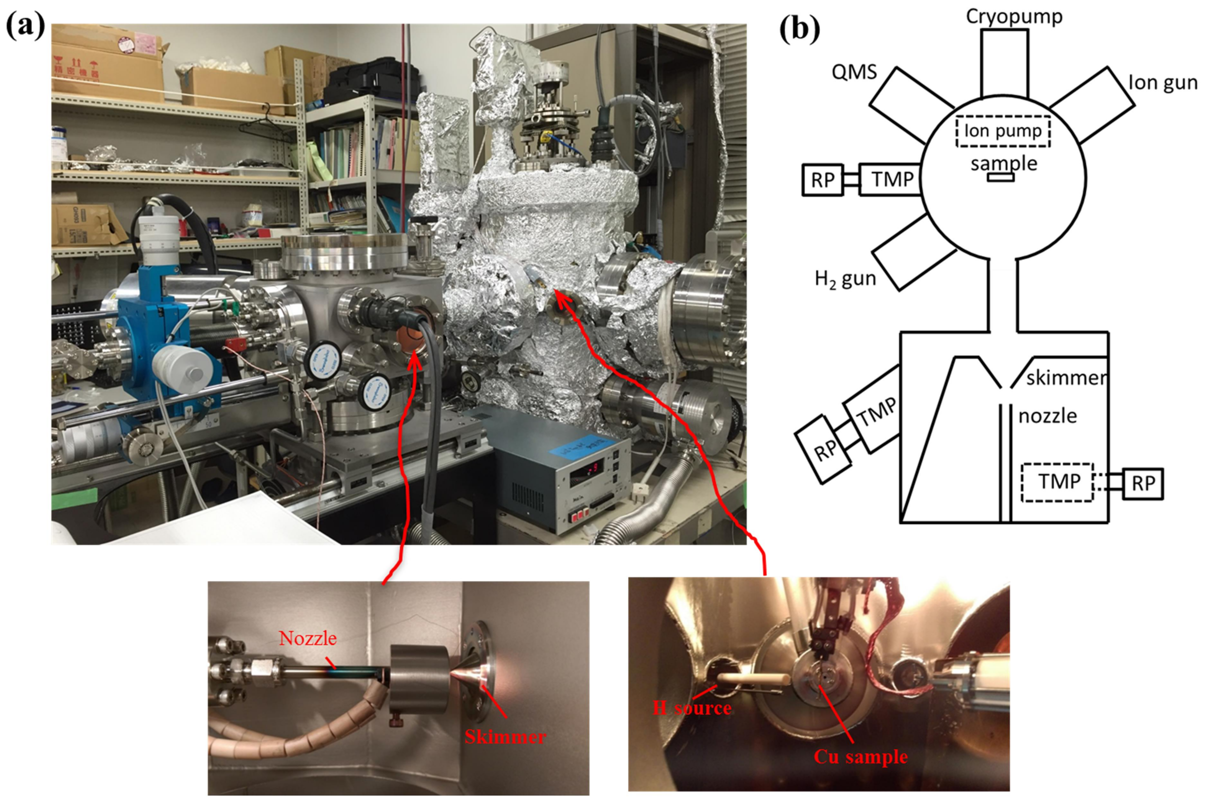

Figure 4.4 Small supersonic molecular beam (SMB) system. (a) Physical photo of SMB apparatus. The insets illustrate the beam source system (composing by nozzle, heater and skimmer) and reaction chamber with atomic hydrogen generator, Cu(100) single crystal. (b) Schematic of SMB apparatus (top-view). The apparatus is an ultra-high vacuum system composed of (1) molecular beam source chamber ($< 5\times10^{-9}$ torr), (2) reaction chamber ($< 3\times10^{-10}$ torr).

(2) Type II: small supersonic molecular beam system (SMB)

As shown in **Figure 4.4,** the small molecular beam (SMB) apparatus composes mainly three chambers: (1) source chamber, which consists of a beam source, skimmer, nozzle, and heater, is mainly evacuated by a TMP with a pumping rate of 520 L s^{-1} (for N_2). The background pressure is lower than 5×10^{-10} torr. A supersonic molecular beam is generated by free-jet expansion from the pinhole (diameter ϕ = 50 μm) of a stainless steel nozzle, and skimmed by a conical skimmer into the reaction chamber through collimator house. The nozzle temperature for the CO_2/He beam can be precisely controlled from room temperature to 1000 K by a resistive heater within a temperature fluctuation of ± 0.1 K (insets of **Figure 1.4(a)**); (2) collimator house. It is differentially pumped by a TMP with a pumping rate of 320 L s^{-1}, in which the pinhole diameter of collimator can be controlled as 0.5 mm, 1.0 mm, 2.0 mm and 5.0 mm; (3) reaction chamber (**Figure 1.4(b)**). It is equipped with a manipulator, which is used for sample alignment in the molecular beam collision measurement. The background pressure is lower than 3×10^{-10} torr. The Cu single crystal sample, which has two parallel through-holes, is supported by two tantalum filaments welded to two gold rods. The

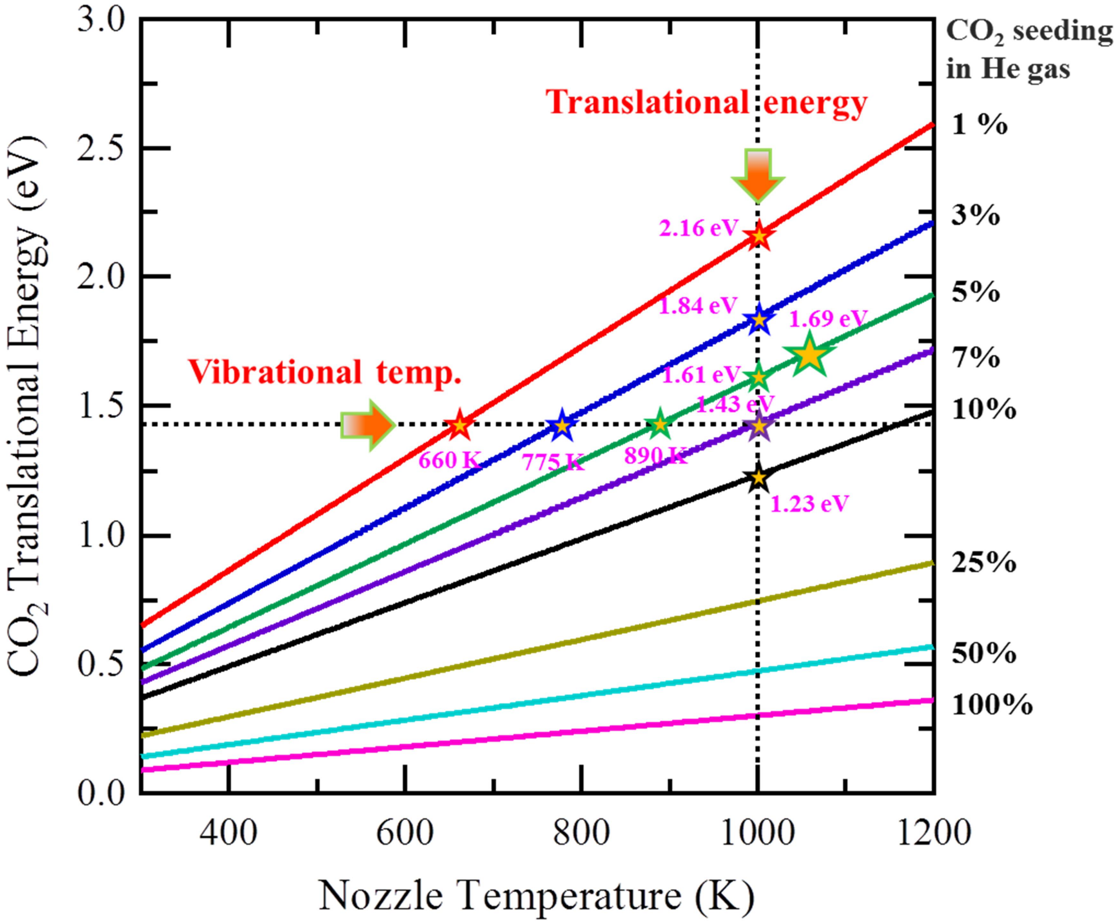

Figure 4.5 The calculated translational energy of incident CO_2 molecules as a function of nozzle temperature. Various contents of CO_2 diluted in He are used to: (1) change the CO_2 translational energy when the vibrational temperature is fixed; (2) change the CO_2 vibrational temperature by vary the nozzle temperature at a fixed translational energy.

tantalum filaments also are used to heat the sample. A cryo-pump was used to cool the sample down to 155 K. For more details, please see the schematic of SMB, Fig.S3.1 in Appendix.

4.3.2 Estimation of the translational energy of CO_2 molecular beam

We estimated the translational energy with a simple calculation that agrees well with the experimentally measured translational energy provided by the time-of-flight technique for polyatomic molecular beams (such as CH_4, CO, and N_2 seeded in He) in our experimental apparatus [8]. For the energy width, we assumed that the ΔE/E value of CO_2 molecules seeded in He is 20–35%, where ΔE is the full width at half maximum (FWHM) of the energy distribution. This is because 20–35% is the typical energy spread for the polyatomic molecular beam seeded in He from a hot nozzle with a diameter of 50 μm in our experimental apparatus [8].

As shown in **Fig. 4.5**, the translational energy is calculated using the following function [8]:

$$E_{calc} = \left(\frac{m_a \sum_i X_i}{\sum_i m_i X_i} \right) \left(\sum_i C_{pi} \right) T_{nozzle} \tag{1}$$

where X is the portion of the gas, C_p is the specific heat of the gas, and T_{nozzle} is the nozzle temperature. Here, the C_p is considered to be independent of T_{nozzle}. In the case of a mixture of two gases (e.g. CO_2 and He), the translational energy (E_T) can be written as follows by assuming that C_p is independent of temperature as $(5/2)k$ and $(7/2)k$ for He and CO_2, respectively, where k is the Boltzmann constant.

$$E_T = \left(\frac{5}{2}a + \frac{7}{2}b \right) kT_n \left(\frac{m_b}{m^*} \right) \tag{2}$$

$$m^* = \frac{am_a + bm_b}{a+b} \tag{3}$$

For example, if the mixture ratio is CO_2 : He = 1: 9, the translational energy of CO_2 can be calculated as:

$$E_T = ((5/2) \times 0.9 + (7/2) \times 0.1) \times kT_n \times (m_b/m^*) / (1.60 \times 10^{-19}) \times 1000 \tag{4}$$

$$m^* = (r_a \times m_a + r_b \times m_b) / (r_a + r_b) \tag{5}$$

where $m_b = 44 \times 1.67 \times 10^{-27}$, $m_a = 4 \times 1.67 \times 10^{-27}$, $k = 1.38 \times 10^{-23}$, $r_b = 10$, and $r_a = 90$. Therefore, $E_T = 1.23 \times T_n$ (meV). For example, when T_n is 1000 K, E_T is about 1.23 eV.

4.3.3 CO_2 molecular beam experimental procedure

Before the irradiation of CO_2 beam onto the surface, we prepare clean Cu surface and atomic hydrogen pre-adsorption. The experimental procedure is illustrated in **Fig. 4.6**. The following is the detailed procedures of steps: (1) surfaces are cleaned by Ar^+ sputtering; (2) atomic hydrogen pre-adsorption on Cu surface by using hydrogen cracker; (3) Heated CO_2 beam irradiation on H_a pre-dosed Cu surfaces; (4) Surface product on Cu surface is characterized by TPD measurements and IRA spectroscopy.

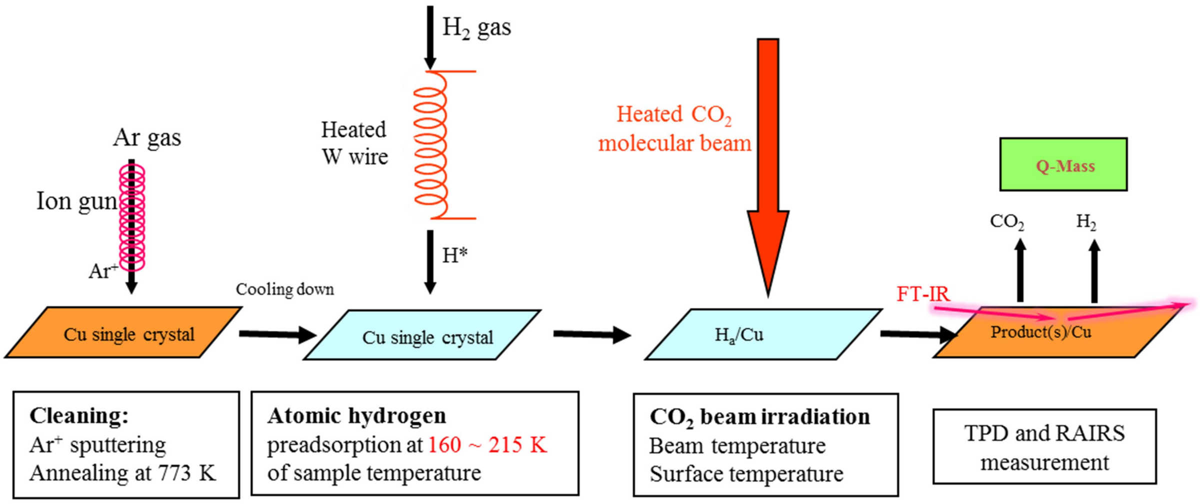

Figure 4.6 Schematic of experimental procedure for the dynamics study of formate synthesis by using molecular beam. Steps are (1) Cu surface cleaning; (2) atomic hydrogen (H_a) preparation; (3) CO_2 beam irradiation on H/Cu surface; (4) Reaction product is checked by TPD and IRAS. Steps (1) and (2) are the experimental preparation methods. Steps of (3) and (4) are for the experimental results.

(1) Surface cleaning

Surface cleaning process is a very important step for this experiment. We used single crystals of Cu(111), Cu(110) and Cu(100) (Surface Preparation Laboratory, Netherlands), which are in a disk-shaped plate (2 mm thick; diameter Φ= 10 mm; 5N purity) with two parallel through-holes. They were mounted to two tantalum filaments for resistive heating, and were cleaned by cycles of Ar^+ sputtering followed by annealing at 773 K. The cleanliness was checked by observing sharp low-energy electron diffraction (LEED) spots and by checking the absence of impurity signals in Auger electron spectroscopy (AES) measurements. The LEED patterns and AES data for Cu(111) are presented by Fig. S2.8 (Appendix) for monitoring the cleaning process. The pressure of Ar gas is 8.0×10^{-5} torr, the beam voltage is 1 kV and the emission current is 10 mA. The LEED patterns of Cu(111) were taken at an electron kinetic energy of ~70 eV. After 5 hours Ar^+ sputtering, the sharp and bright spots with 6-fold symmetry, which is corresponding to the hexagonal lattice symmetry of Cu(111). A typical Auger spectrum for the Cu(111) sample also is shown in Fig. S2.8 in Appendix. Peaks at 60 eV and 105 eV are assigned to Cu, no peaks due to other the heteroatoms such as sulfur, carbon, oxygen appear in the spectrum. Therefore, as described above, the Cu surface can be cleaned by this cleaning process. The cleanness of Cu(110) and Cu(100) samples were also confirmed by LEED/AES in a same way.

(2) Preparation of atomic hydrogen (H_a) on Cu surfaces

The adsorbed atomic hydrogen (H_a) was prepared by splitting H_2 molecules through a heated tungsten filament (diameter Φ= 0.30 mm; heating current I = 3.8 A, see **Fig. 4.6** and **Fig. 4.2(e)**). For more details, please see the schematic drawing of hydrogen cracker in Fig. S2.7. During the dosing of atomic hydrogen, the Cu(111), Cu(110) and Cu(100) were maintained at 200 K, 215 K and 215 K, respectively. The TPD for the recombination of atomic hydrogen ($H_a + H_a \rightarrow H_2$) was measured with different exposures of H_2 gas (see Appendix). On Cu(111), Cu(110) and Cu(100), the peak position shifts to low temperature with the increasing of the atomic hydrogen coverage. Only for the adsorption of hydrogen on Cu(110) an additional small low-temperature satellite peak is observed, the desorbing H_2 peak temperatures shifts to lower temperatures with increasing the exposure of dosed hydrogen gas. The coverage of atomic hydrogen corresponds to the TPD-peak area. The TPD peak areas are integrated as a function of H_2 exposure. For all three copper surfaces, a saturation coverage of 0.5 monolayer (ML) [9] is obtained at the exposure of ~15 L (1 L = 10^{-6} torr s) for Cu(111), ~ 20 L for Cu(110), ~ 15 L for Cu(100).

4.4 Results and discussion

4.4.1 Formate ($HCOO_a$) product confirmation

(1) TPD studies

The experiments were conducted using UHV-LMB equipped with TPD and IRAS as shown in **Fig. 4.1** and **Fig. 4.2**. We examined the formation of formate on Cu(111) via the irradiation of a hot CO_2 molecular beam (5% CO_2 diluted in He) by heating the nozzle at 1050 K (translational energy E_T = 1.69 eV, $\Delta E/E$ = 0.2–0.35) onto a cold atomic-hydrogen pre-dosed Cu(111) (H_a/Cu(111)) surface at 180 K (for the translational energy calculation, see **Figure 4.5**). We set the surface temperature at 180 K in order to avoid the desorption of the pre-dosed atomic hydrogen. After the irradiation of CO_2, temperature-programmed desorption (TPD) measurements of H_2 (m/z = 2), CO_2 (m/z = 44), H_2O (m/z = 18) and CO (m/z = 28) were carried out to confirm the formation of formate species. The detailed calibrations of Q-mass detector and detailed calculation methods of the exposure of CO_2 beam flux can be seen in Appendix.

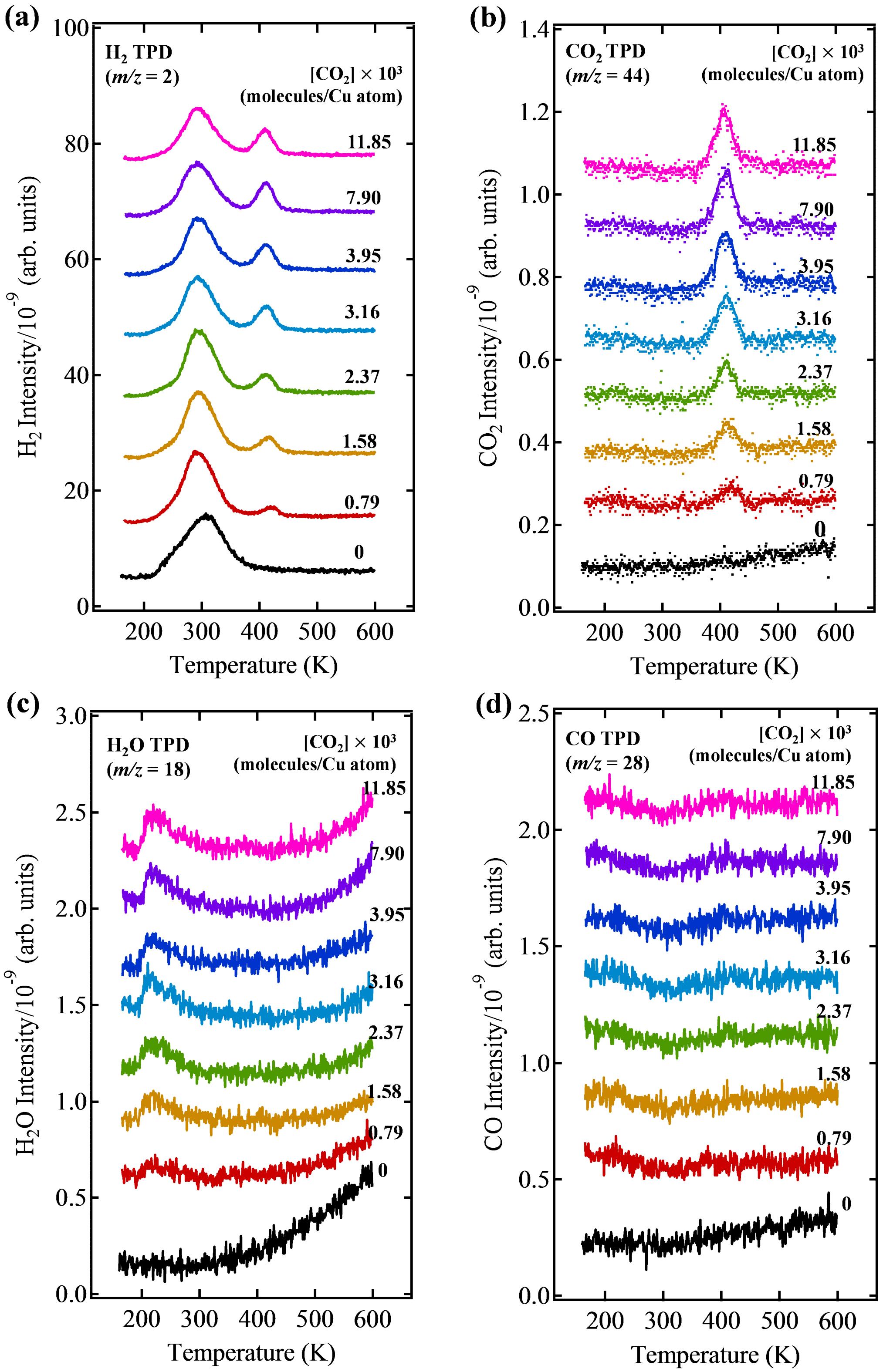

Figure 4.7 Formation of formate on Cu(111) with different CO_2 beam exposures (CO_2 molecules/Cu atom) traced by temperature-programmed-desorption (TPD). The coverage of pre-dosed hydrogen adatoms are the saturated coverage of 0.6 ML. Cu(111) surface is kept at 180 K. The nozzle temperature is 1050 K and the translational energy of CO_2 is 1.69 eV. TPD profiles of (**a**) H_2 (m/z = 2); (**b**) CO_2 (m/z = 44); (**c**) H_2O (m/z = 18); (**d**) CO (m/z=28) after CO_2 beam irradiation to Cu(111) with various exposure of CO_2.

Figure 4.7 shows sets of TPD profiles of H_2 (m/z = 2), CO_2 (m/z = 44), H_2O (m/z = 18) and CO (m/z = 28) to trace the possible products after CO_2 irradiation on the saturated H_a/Cu(111). **Figure 4.7(a, b)** shows series of TPD profiles of H_2 and CO_2 with various exposures of CO_2 (in which 0 means no CO_2 beam irradiation). These two species simultaneously desorb were observed in the range of 390 K – 420 K with TPD peaks at around 408 K on Cu(111), which agrees with the previously reported data [10]. As shown in **Fig. 4.7(a)**, the peak position of H_2 from formate decomposition shifts slightly to lower temperature with increasing the exposure of CO_2. The same phenomenon occurs in the TPD of CO_2 in **Fig. 4.7(b)** with series of single, relatively sharp, symmetric peaks. We note here that the intensity of CO_2 mass signal is relatively quite small than H_2. There are two reasons: 1) CO_2 is a heavy molecule so that cryo-pump in the apparatus has high pumping speed for CO_2; 2) the Q-mass detector has different sensitivities for CO_2 and H_2, leading to the intensity ratio of them is not 2 (according to formate decomposition stoichiometry: $HCOO_a \rightarrow CO_2 + 1/2\ H_2$. The molar ratio of CO_2 and H_2 is 2). Therefore, we used formic acid to prepare formate by dehydrogenation on Cu surface, we calibrated the mass sensitivity of Q-mass detector for CO_2 and H_2, which corresponds to molar ratio as 2 (see Appendix). In **Fig. 4.7(a)**, the sets of first H_2 peaks in the range of 220 K – 360 K with TPD peaks at around 300 K is due to the recombination of pre-dosed atomic hydrogen ($2H_a \rightarrow H_2$.) on Cu(111). The signals of H_2O and CO also were monitored by TPD measurements simultaneously as shown in **Figure 4.7(c, d)**. With increasing the exposure of CO_2 (by increasing the beam irradiation time), the H_2O desorption peaks at around 215 K appear [11]. It indicates that H_2O molecules in background accumulately adsorb on the sample holder when the Cu sample was exposed in the beam irradiation environment. In **Figure 4.7(d)**, no CO peaks appear in the TPD profiles. We can conclude that when the CO_2 beam has the translational energy of 1.69 eV and vibrational temperature of 1050 K, there was no other species such as COOH, HCO species are produced and no dissociation of CO_2 to produce CO happened on the Cu(111) surface.

From Fig. 4.7(a, b), we can observe that the heights of H_2 and CO_2 peaks increase with increasing the exposure of CO_2 irradiation. **Figure 4.8(a)** shows the intensity of H_2 peak in Fig.4.7(a) as a function of CO_2 exposure. The green and blue uptake curve is from the peaks integration of desorption of H_2 from the formate decomposition and atomic hydrogenation respected with different CO_2 exposures, respectively, as shown in **Fig. 4.7(a)**. The purple one is the total hydrogen intensity (formate hydrogen plus recombination hydrogen). For the uptake curve of hydrogen from formate, we can see that when the CO_2 beam exposure is up to 3000 molecules/Cu atom, the formate product is saturated and can't increase even the CO_2 exposure increase. The saturation coverage is about 0.13 monolayer (ML), which is still far away from the normal saturated condition of formate as 0.25 ML [1]. One possible explanation is that the forming formate species at saturation condition block the atomic hydrogen on Cu(111) surface to react with the incident CO_2 molecules. Previous kinetic study reported that the formate decomposition is suggested as a first order desorption kinetics [12]. Assuming a standard frequency factor of $\nu \approx 10^{13}\ s^{-1}$, the activation energy for desorption can be estimated using Redhead equation [13] to be ΔE_{des}^{*} = 101 kJ/mol^{-1}. On the other hand, the total hydrogen coverage decreases and remains constant, comparing with the saturated pre-dosed atomic hydrogen. It can be explained by (1) some the atomic hydrogen desorbed by CO_2/He beam collision; (2) part of the formate species desorbs with taking some of the hydrogen.

(2) IRAS characterization

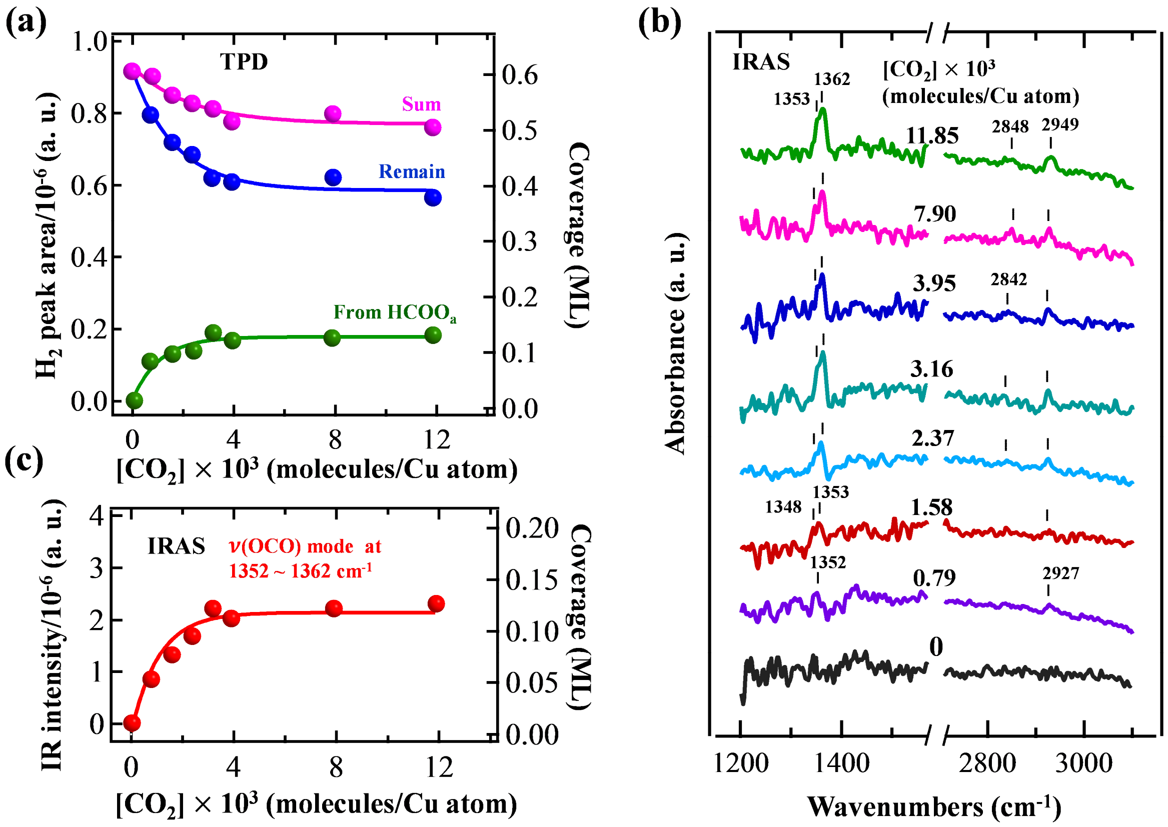

Figure 4.8 Formation of formate on Cu(111) with different CO_2 beam exposures (CO_2 molecules/Cu atom) traced by infrared reflection-adsorption spectroscopy (IRAS). The coverage of pre-dosed hydrogen adatoms are the saturated coverage of 0.6 ML. Cu(111) surface is kept at 180 K. The nozzle temperature is 1050 K and the translational energy of CO_2 is 1.69 eV. (**a**) Integrated areas of hydrogen TPD peaks as a function of the CO_2 exposure. The green and blue dashed curves are the fitting for desorption hydrogen peak at around 300 K and 408 K in Fig.4.7(**a**), respectively. The purple curve is fitting for the sum intensity of hydrogen at around 300 K and 408 K in Fig.4.7 (**a**). (b) IRA spectra after the CO_2 exposure prior to corresponding TPD measurements. (c) IR intensity of ν(OCO) mode of formate at the wavenumbers 1352 ~1362 cm^{-1} in (**b**) as a function of CO_2 exposure.

The reaction product has been further confirmed by Infrared spectroscopy. **Fig. 4.8(b)** shows sets of simple IR spectra of formate product on Cu(111) after the irradiation of 5% CO_2 molecular beam. In the infrared spectrum, the peak at 1362, 2848, and 2949 cm^{-1} is assigned to the symmetric OCO stretching band (ν_s(OCO)), the CH stretching mode ν(CH) and the combination band ($\nu_{comb.}$) of asymmetric OCO stretching and the in-plane CH beading modes, respectively. We also observed that there is a shoulder peak appears at 1353 cm-1 peak, it may be assigned as the stretching band (ν_s(OCO)) of monoformate. These peaks positions were in good agreement with those reported for bridging bidentate formate species on Cu(111) prepared by various methods as summarized by **Table 4.1**. In **Fig. 4.8(b)**, we can observe that the IR adsorbance of peaks increases with the increasing of the exposure of CO_2 beam. That is, the formate product coverage increases when we irradiate the CO_2 beam for a longer time. **Figure 4.8(c)** integrates the IR intensity of stretch mode ν_s(OCO) as a function of CO_2 exposure, the shape uptake curve is the same with the uptake curve (in green) in **Fig. 4.8(a)**. That is, the reaction probabilities are identical from the clarification of TPD and IRAS. More typical IRA spectra of formate synthesized on Cu(111) are shown in **Table 4.1**.

Table 4.1 Vibrational frequencies (cm^{-1}) of the IR peaks for the formate ($HCOO_a$), formic acid (HCOOH), methoxy (CH_3O_a), methanol (CH_3OH_a) species on Cu single crystals

	species	ν_s(OCO)	ν(CH)	$\nu_{comb.}$	ν(OH)	ν(C=O)	preparation	T_{surface}	ref.
Cu(111)	$HCOO_a$	1352-1354	2855	2932	-	-	$CO_2 + H_2$	323-353 K	[5]
		1342-1360	2850	2922	-	-	HCOOH	325-353 K	[1]
Cu(100)	$HCOO_a$	1325	2870	-	-	-	HCOOH	120 K	[14]
		1330	2879	-	-	-	$CO_2 + H_2$	363 K	[3]
Cu(110)	$HCOO_a$	1352-1362	2846-2850	2922-2928	-	1640-1670*	$CO_2 + H_2$	325-353 K	[5]
		1352-1362	2846-2848	-			HCOOH	353 K	[1]
		1360	2920,2960	2922-2928			H_2CO, CH_3CHO	400 K	[15]
		1355	2848	2930			HCOOH	200 K	[16]
		1348-1358	2891-2900	2946-2955			HCOOH	270 K	[17]
	$HCOOH_a$	-	2937	-	3100	1733	HCOOH	85 K	[16]
	CH_3O_a	-	1391, 1337$^\#$	-	-	1016 ν(C-O)	CH_3OH	255 K	[18]
	CH_3OH_a	-	2945, 2985^c	-	3280	3675	CH_3OH	90 K	[15, 18]

Notes: *, from monodentate of $HCOO_a$; #, 1391 cm^{-1} is due to the mode $\delta_a(CH_3)$, 1337 cm^{-1} for the mode of $\delta_s(CH_3)$; **c**, 1391 cm^{-1} is asymmetric stretching $\nu_a(CH_3)$.

In conclusion, from both TPD and IRAS measurements, formate has been successfully synthesis by energetic CO_2 beam molecules colliding with the hydrogen adatoms on a Cu(111) surfaces. In the study, the experimental condition that the CO_2 is heated while the Cu surface was kept at low temperature as 180 K, which is different from precious studies that formate can be synthesized by a high pressure CO_2/H_2 [1]. On the other hand, the H adatoms has no reaction with co-adsorbed CO_2 on Cu(110) surface at around 95 K [12]. The formate coverage shows a saturation condition, in spite of there are hydrogen adatoms left on the surface while the hydrogen has no reaction with the incident CO_2 molecules any more. On the other hand, the produced formate is not further hydrogenated by the co-adsorption H adatoms on Cu(111), indicating that Cu single crystal surface at low temperature doesn’t support the hydrogenation of formate to produce other species. Therefore, the fact that formate is the only product from the energetic CO_2 molecules with hydrogen adatom on Cu surface which can provide a novel model to study the dynamics of CO_2 activation on Cu surfaces.

4.4.2 Effects on the reaction probability of CO_2 to form formate ($HCOO_a$)

4.4.2.1 Cu surface temperature effect and Cu surface structure effect

Generally, most of the heterogeneous catalysis proceeds via Langmuir-Hinshelwood mechanism. Both surface temperature and surface structure thus have great contribution on the reaction rate. In this study, the formate synthesis example gives us a good model to study these properties.

We thus investigate the effects of Cu surface temperature on the reaction probability of CO_2 to form formate. **Figure 4.9 – Figure 4.13** show the sets of TPD profiles of H_2 (m/z = 2), CO_2 (m/z = 44) (for the respective TPD profiles of H_2O (m/z = 18) and CO (m/z = 28), please see Appendix) from formate decomposition after CO_2 irradiation on the saturated H_a/Cu(111) with different surface temperature at 120 K, 140 K, 160 K, 180 K and 200 K, respectively. In these experiments, the nozzle temperature is the same as 1000 K and the translational energy of CO_2 is 2.16 eV. We see that the intensities of CO_2 and H_2 from the decomposition of surface formate increase with increasing the exposure of CO_2 beam at various surface temperatures. In **Figure 4.9(b)**, the first large and sharp CO_2 TPD peaks come from the background CO_2 desorbed from the sample holder due to the Cu sample is keeping at 120 K. The intensities of sets of CO_2 peaks decrease with the surface temperature increasing and disappear up to 160 K.

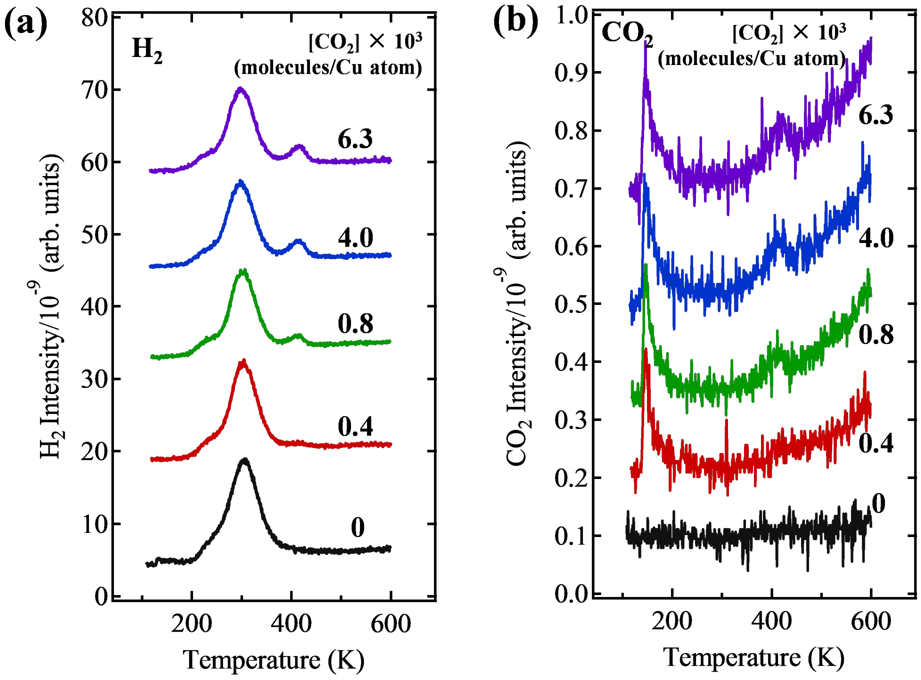

Figure 4.9 Formation of formate on Cu(111) with different CO_2 beam exposures (CO_2 molecules/Cu atom) traced by temperature-programmed-desorption (TPD). Cu(111) surface is kept at 120 K. The coverage of pre-dosed hydrogen adatoms are the saturated coverage of 0.6 ML. The nozzle temperature is 1000 K and the translational energy of CO_2 is 2.16 eV. TPD profiles of (**a**) H_2 ($m/z = 2$); (**b**) CO_2 ($m/z = 44$);

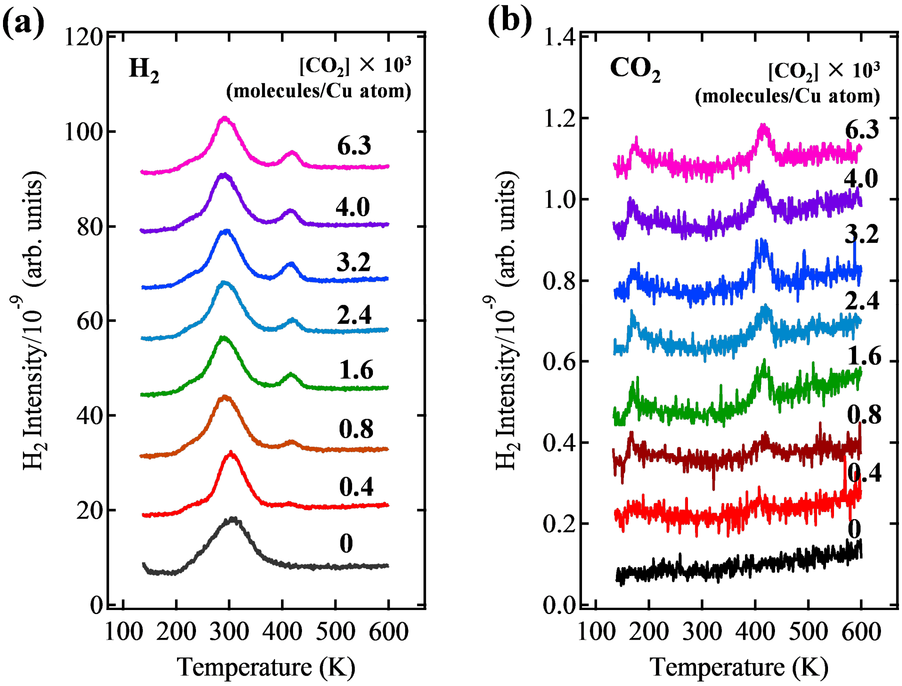

Figure 4.10 Formation of formate on Cu(111) with different CO_2 beam exposures (CO_2 molecules/Cu atom) traced by temperature-programmed-desorption (TPD). Cu(111) surface is kept at 140 K. The coverage of pre-dosed hydrogen adatoms are the saturated coverage of 0.6 ML. The nozzle temperature is 1000 K and the translational energy of CO_2 is 2.16 eV. TPD profiles of (**a**) H_2 ($m/z = 2$); (**b**) CO_2 ($m/z = 44$);

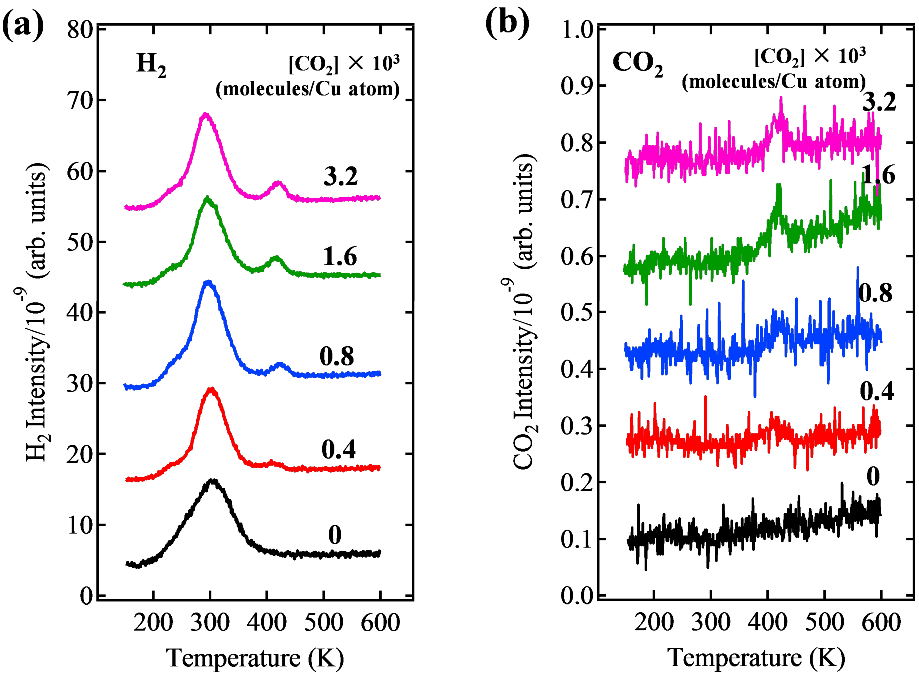

Figure 4.11 Formation of formate on Cu(111) with different CO_2 beam exposures (CO_2 molecules/Cu atom) traced by temperature-programmed-desorption (TPD). Cu(111) surface is kept at 160 K. The coverage of pre-dosed hydrogen adatoms are the saturated coverage of 0.6 ML. The nozzle temperature is 1000 K and the translational energy of CO_2 is 2.16 eV. TPD profiles of (**a**) H_2 ($m/z = 2$); (**b**) CO_2 ($m/z = 44$);

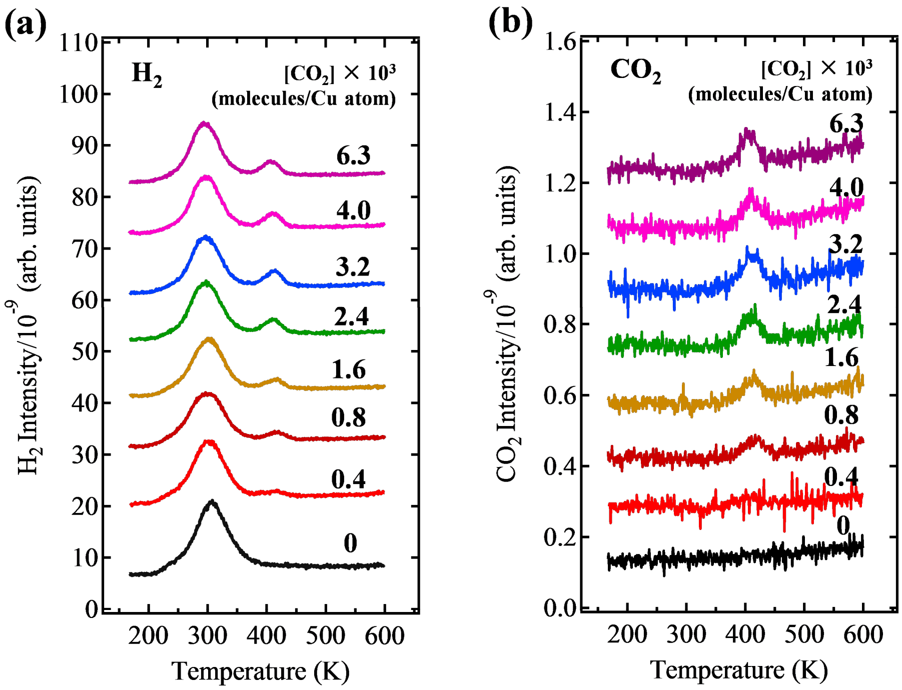

Figure 4.12 Formation of formate on Cu(111) with different CO_2 beam exposures (CO_2 molecules/Cu atom) traced by temperature-programmed-desorption (TPD). Cu(111) surface is kept at 180 K. The coverage of pre-dosed hydrogen adatoms are the saturated coverage of 0.6 ML. The nozzle temperature is 1000 K and the translational energy of CO_2 is 2.16 eV. TPD profiles of (**a**) H_2 (*m/z* = 2); (**b**) CO_2 (*m/z* = 44);

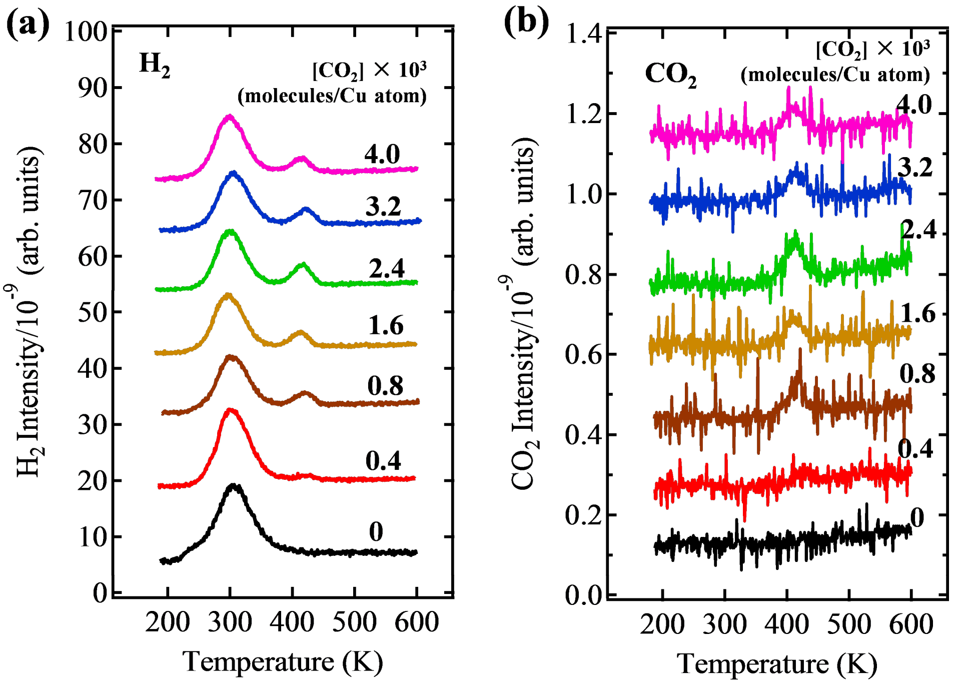

Figure 4.13 Formation of formate on Cu(111) with different CO_2 beam exposures (CO_2 molecules/Cu atom) traced by temperature-programmed-desorption (TPD). Cu(111) surface is kept at 200 K. The coverage of pre-dosed hydrogen adatoms are the saturated coverage of 0.6 ML. The nozzle temperature is 1000 K and the translational energy of CO_2 is 2.16 eV. TPD profiles of (**a**) H_2 (*m/z* = 2); (**b**) CO_2 (*m/z* = 44);

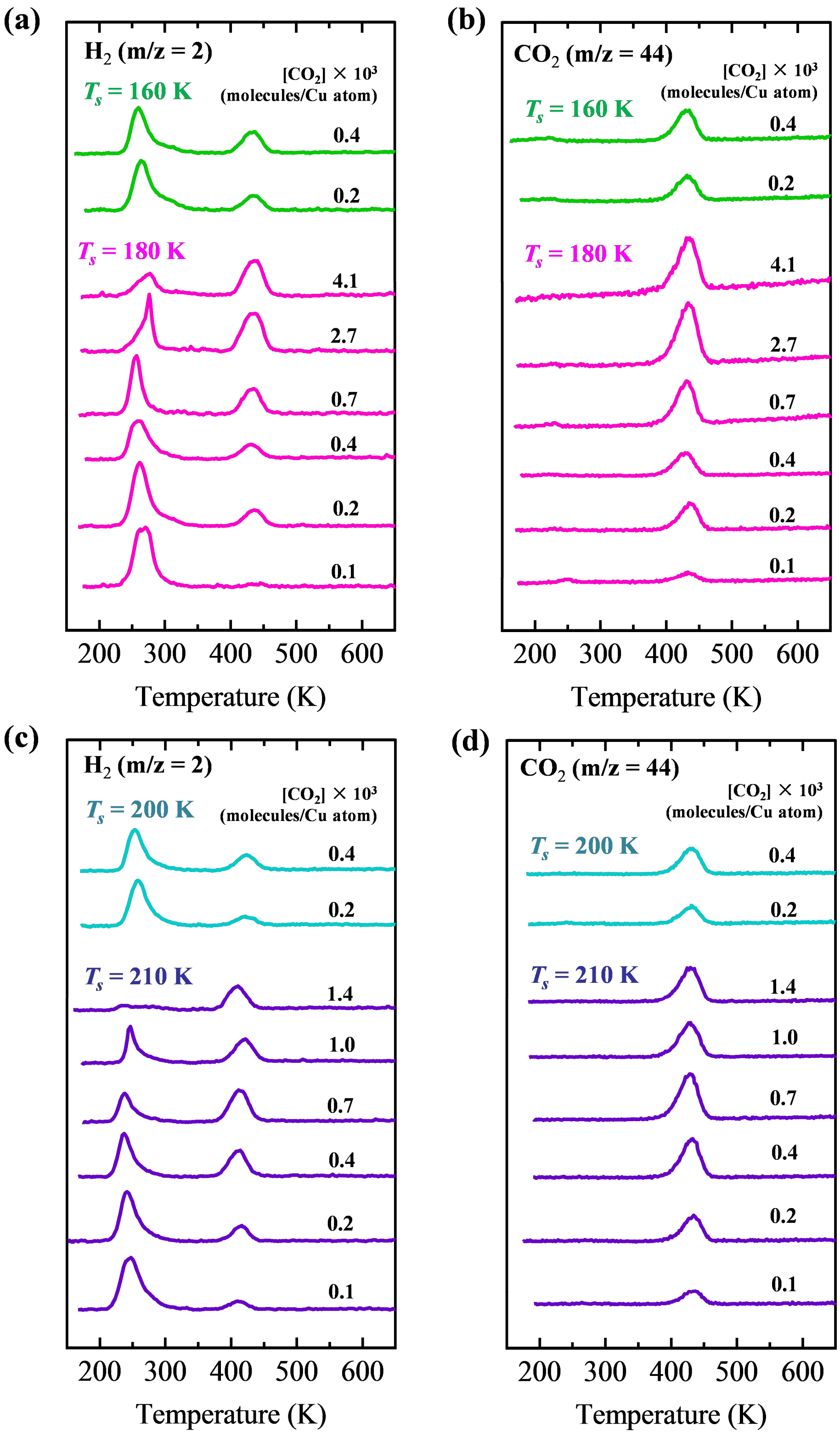

Figure 4.14 Formation of formate on Cu(100) with different CO_2 beam exposures (CO_2 molecules/Cu atom) traced by temperature-programmed-desorption (TPD). Cu(100) surface is kept at 160 K, 180 K, 200 K and 210 K, respectively. The coverage of pre-dosed hydrogen adatoms are the saturated coverage of 0.6 ML. The nozzle temperature is 1000 K and the translational energy of CO_2 is 2.16 eV. TPD profiles of (**a, c**) H_2 ($m/z = 2$); (**b, c**) CO_2 ($m/z = 44$);

Similarly, surface temperature effects also were investigated on a Cu(100) single crystal surface. **Figure 4.14** shows the sets of TPD profiles of H_2 (m/z = 2), CO_2 (m/z = 44) from formate decomposition after CO_2 irradiation on the saturated H_a/Cu(100) with different surface temperature at 160 K, 180 K, 200 K and 210 K, respectively. In these TPD files, the asymmetry of first H_2 peaks may be due to the anisotropy of Cu(100) after CO_2 beam irradiation.

Figure 4.15 show the hydrogen intensities from formate decomposition as a function of total exposure of CO_2 on Cu surfaces, which is derived from the TPD data of formate-H_2 in Fig. 4.9(a) - Fig.4.13(a) on Cu(111) and Fig. 4.14(a, c) on Cu(100). The CO_2 translational energy was fixed at 2.16 eV and a constant vibrational temperature of 1000 K (T_{nozzle} = 1000 K) by using 1% CO_2/He mixture gas as an incident beam. They can be regarded as buildup curves because the intensity of TPD hydrogen is known to be proportional to the formate coverage on Cu surfaces. As shown in **Fig. 4.15(a)**, the saturated coverage was identical regardless of the Cu(111) surface temperature in the range of 120 K – 200 K. From the initial slope of the uptake curve, the reaction probability is estimated to be ~ 1.2×10^{-3}, which is much higher than that of high-pressure formate synthesis (~ 2.0×10^{-12}) at 380 torr CO_2/380 torr H_2 and 340 K [3]. For more details about the calculation of reaction probability of CO_2, please see Appendix.

Similarly, the coverage of formate product is dependence on the CO_2 beam exposure but regardless to the surface temperature either in the range of 160 K – 210 K. The saturating behavior seen in **Figure 4.15(b)** is probably due to the coverage formate product, inhibiting surface reactions between the CO_2 and atomic hydrogen. We thus estimated the equilibrium coverage formate product as 0.22 ML, which is comparable with reported saturation condition of formate on Cu surfaces as 0.25 ML.

Figure 4.16 shows the surfaces temperature dependence surface structure dependence of the reaction probability of CO_2 to form formate. The reaction probabilities are obtained from the initial formation rate of formate derived from the results in Fig. 4.15. We can see that the reaction probabilities for Cu(111) and Cu(100) are in the same order of magnitude. That is, the initial reaction probability of CO_2 with a constant kinetic energy (E_T = 2.16 eV, T_v = 1000 K) is independence on both surface temperature (T_s) and surface structure. These results suggest that the CO_2 molecule react directly with the hydrogen atom adsorbed on Cu surface. That is, the reaction proceeds via Eley-Rideal (ER) type mechanism which doesn't process the intermediate trapping or hot precursor state. Therefore, the reaction proceeds via a direction chanel so the reaction probability of CO_2 is independence of surface structure. On the other hand, this mode is different from the well-known example of CO_2 hydrogenation on Ni surfaces to form formate. In latter study, CO_2 is negatively charged by Ni surface via carbon chemically bonded. With the temperature is increased and H approaches, formate is yielded through Langmuir-Hinshelwood mechanism [19, 20].

According to previous report, the reaction activation barrier of formate synthesis from CO_2 hydrogenation is estimated as 0.7 eV on Cu(110) and Cu(111) surface [2]. The reaction occurs on Cu(111) and Cu(100), obviously such a barrier exists, which can't overcome by the co-adsorbed CO_2 and atomic hydrogen at 95 K by coupling to the heat bath of the Cu surface [12], but instead requires accumulation of energy to a certain degree of freedom of the impinging CO_2 molecule. That is, the adsorbed hydrogen atom and Cu surface can't activate OCO bending mode of CO_2 which is required for the accomplishment of the reaction. Therefore, the reaction probability of CO_2 is independence of surface temperature. Few of gas-surface reactions illustrate such characters, to the best of our knowledge, except for the dissociative chemisorption of H_2 on Ni surfaces is insensitive with surface temperature, but is sensitive to the surface structure [21].

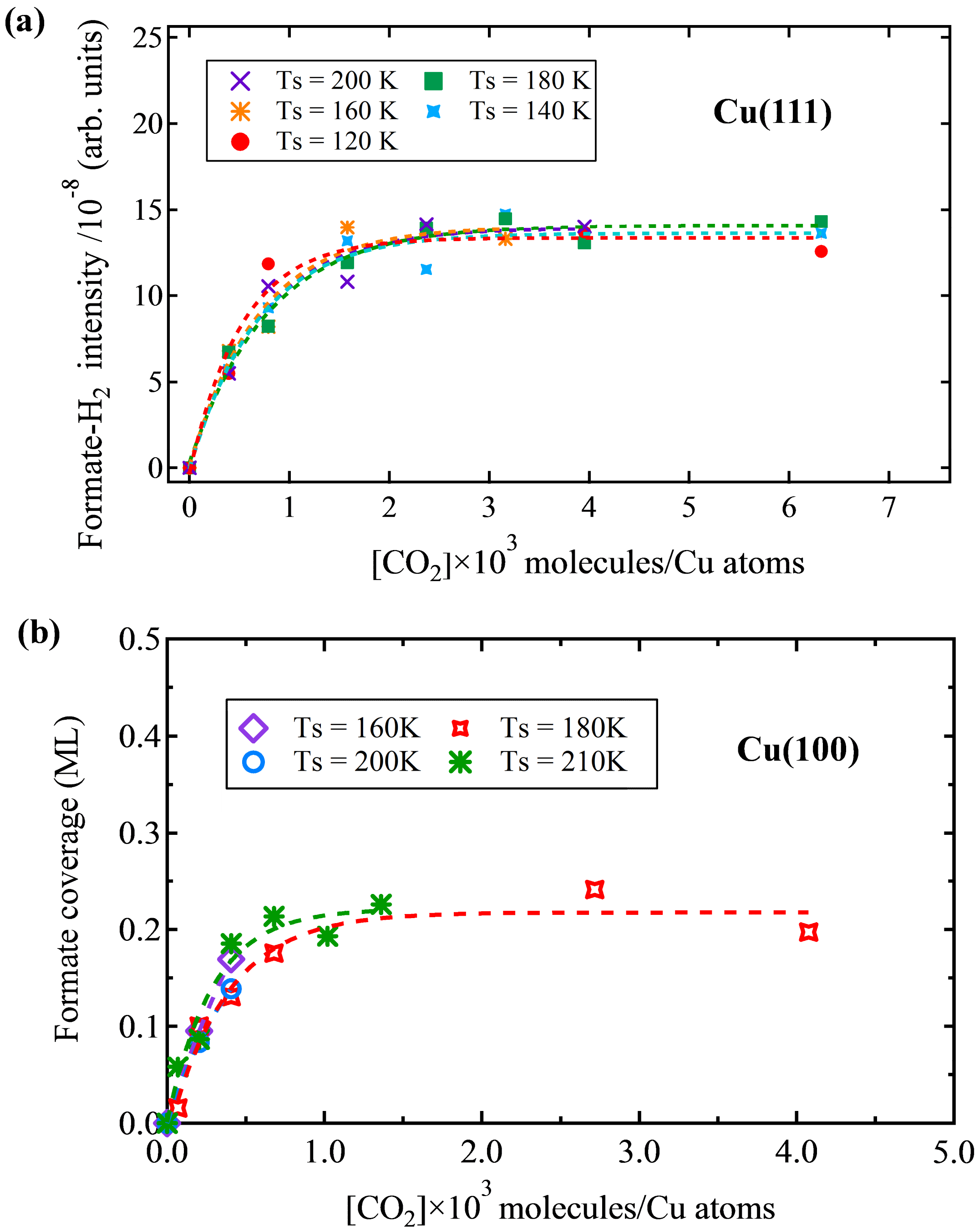

Figure 4.15 The dependencies of the yielding formate amounts on T_{surface} and CO_2 exposure in CO_2 molecular beam experiments on (a) Cu(111) surface; (b) Cu(100) surface. (**a**) Peak area intensity of TPD-H_2 from the product $HCOO_a$ decomposition as a function of CO_2 beam exposure on a saturated H_a/Cu(111) with different surface temperatures derived from Fig. 4.9(a) - Fig.4.13(a). (**b**) Similar the coverage of formate formate dependence on the exposure of CO_2 beam at a saturated pre-dosed H_a on Cu(100) with different surface temperatures derived from Fig. 4.14(a, c).

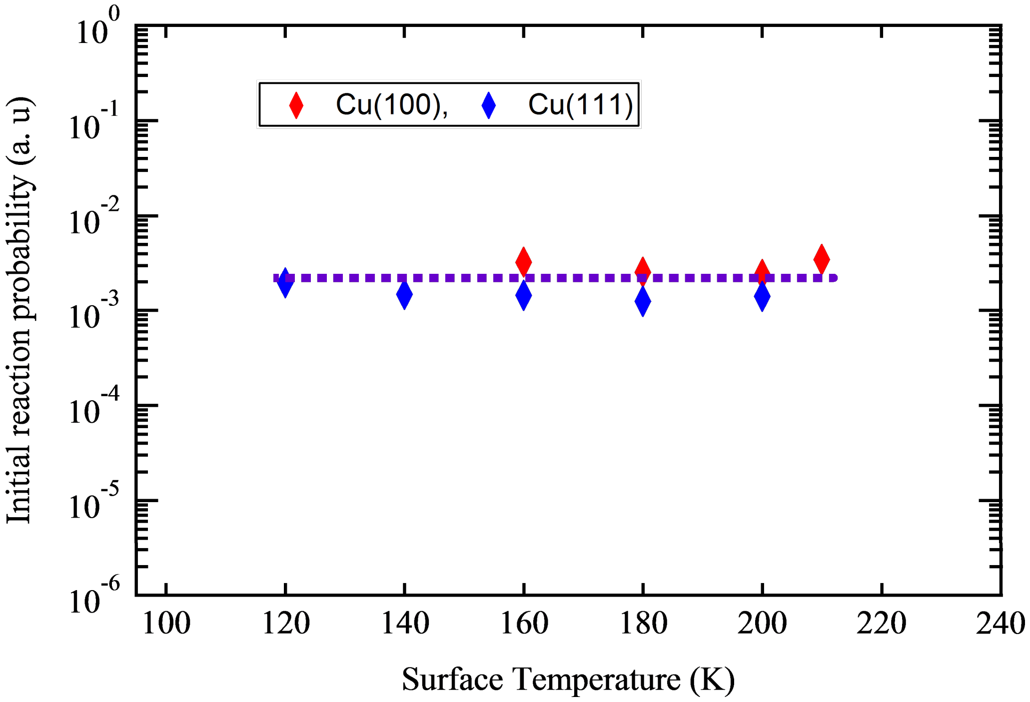

Figure 4.16 The initial reaction probability for CO_2 hydrogenation to form formate on Cu(111) and Cu(100) surfaces as a function of surface temperature. The data are derived from Fig. 4.15 under a fixed translational energy and vibrational temperature of incident CO_2 beam molecules.

4.4.2.2 Translational energy and vibrational energy effects

We have known that the surface temperature and surface structure have no effects on the initial reaction probability of CO_2 transformation into formate on Cu single crystal surfaces. Direct reaction between gas-phase CO_2 with hydrogen adatoms occurs on Cu surfaces. Therefore, increasing both translational energy and vibrational energy would promote the reaction.

Figure 4.17 shows the dependencies of the yielding formate amounts on the translational energy of CO_2 beam molecules on both Cu(111) and Cu(100) surfaces. As shown in Fig. 4.5, the translational energies can be varied from 1.23 eV to 2.16 eV by changing the ratios of CO_2 in helium mixture gas, while the nozzle temperature was keeping at 1000 K to fix the vibrational energy of CO_2 (E_{vib} = 66 meV) and surface temperature was maintained at 180 K. We found that total amounts of hydrogen (amounts of unreacted hydrogen plus formate hydrogen) decrease after CO_2 beam irradiation, while keep constant when the formate is saturated on Cu(111) (see purple uptake curve in Fig. 4.8 (a)). Maybe this is because the formate species stabilizes the atomic hydrogen on Cu surface through hydrogen bonds. On the other hand, the loss of hydrogen increases with the increasing of the translational energy of CO_2 on Cu(100) (see Fig.S 3.1 in Appendix). This is probably due to some of the hydrogen adatoms are kidded out from surface by the beam irradiations.

Similarly, **Figure 4.18** shows the dependencies of the yielding formate amounts on the vibrational energy of CO_2 beam molecules on both Cu(111) and Cu(100) surfaces. In **Fig. 4.18 (a)**, no formate was formed when

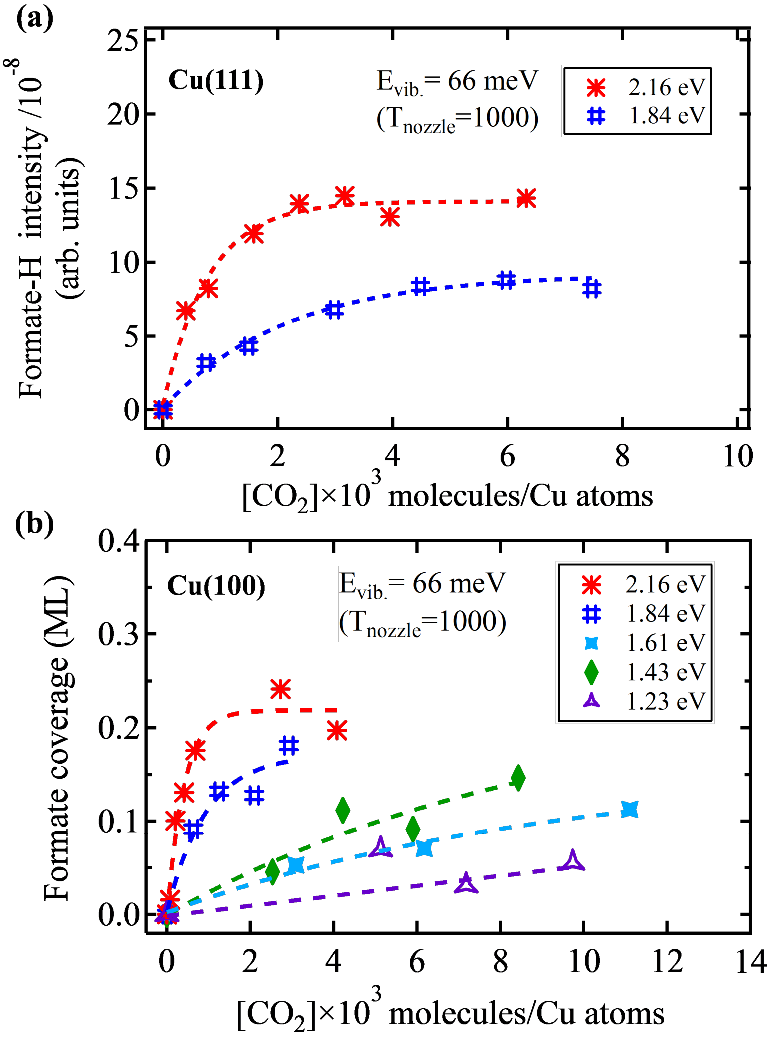

Figure 4.17 The dependencies of yielding formate amounts on translational energy of CO_2 (E_{trans}) at a constant vibrational temperature as 1000 K (E_{vib} = 66 meV) of CO_2. (a) Cu(111) surface; (b) Cu(100) surface. Peak area intensities of TPD-H_2 from the product $HCOO_a$ decomposition were plotted as a function of CO_2 beam exposure. Pre-dosed H_a is at a saturated coverage as 0.6 ML on both Cu(111) and Cu(100) at 180 K.

the vibrational temperature of CO_2 was as lower as 660 K even though the translational energy was as large as 1.4 eV. Therefore, there should be a threshold of vibrational energy to activate a CO_2 molecule and a limitation of the transformation of translational energy into vibrational energy for a CO_2 molecule.

We plot the reaction probabilities of CO_2 to form formate as a function of E_{trans} and E_{vib} of CO_2 molecules in **Figure 4.19**. The translation energies were calculated from Figure 4.5 by changing the ratios of CO_2 in CO_2/He beam mixtures at a constant nozzle temperature as 1000 K. The vibrational energy was obtained by varying the nozzle temperature while keeping the translational energy at 1.4 eV. Series experiments thus were carried out at the same surface temperature as 180 K. The data in **Figure 4.19** show that the reaction probabilities are exponentially increase significantly at all E_{trans} and E_{vib} studied. On the other hand, the reaction probabilities are almost same for both Cu(111) and Cu(100) surfaces if the reaction conditions are corresponding. It indicates again that the reaction probability has no surface structure dependence.

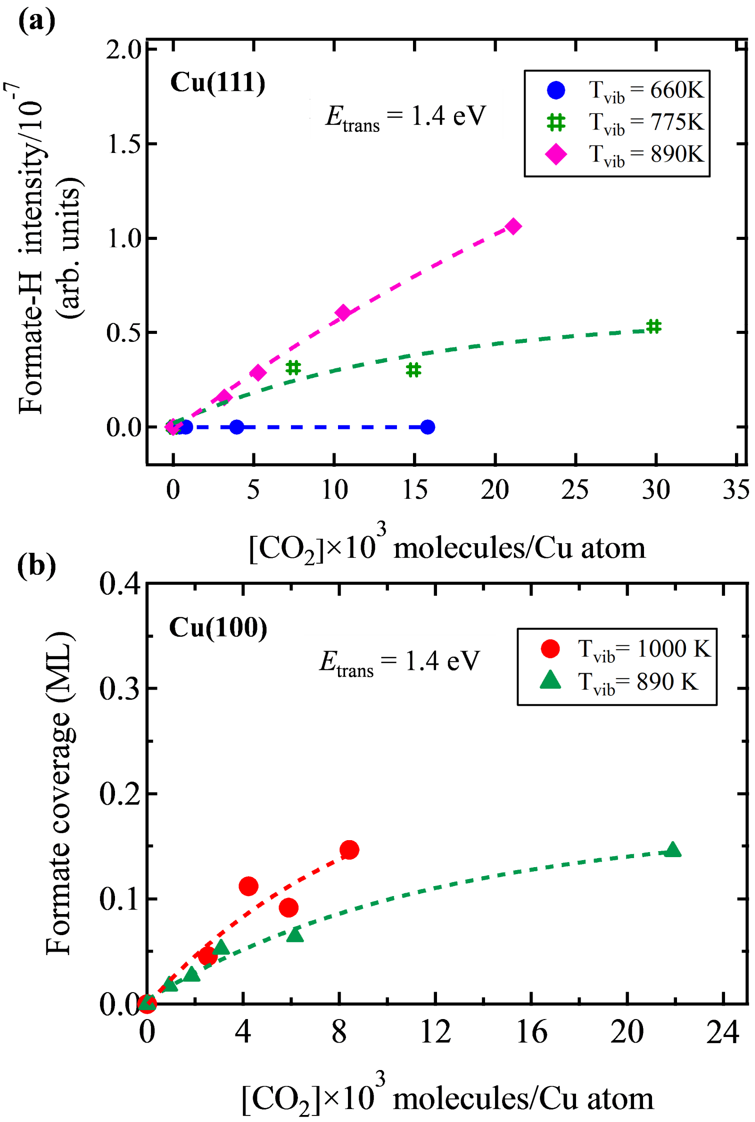

Figure 4.18 The dependencies of yielding formate amounts on vibrational energy of CO_2 (E_{vib}) at a constant translational temperature as 1000 K (E_{trans} = 1.4 eV) of CO_2. (a) Cu(111) surface; (b) Cu(100) surface. Peak area intensities of TPD-H_2 from the product $HCOO_a$ decomposition were plotted as a function of CO_2 beam exposure. Pre-dosed H_a is at a saturated coverage as 0.6 ML on both Cu(111) and Cu(100) at 180 K.

In **Figure 4.19(a)**, the translational energy of CO_2 beam molecules is large (1.23 eV – 2.16 eV) comparing with the DFT calculation for the reaction barrier (~ 0.71 eV). In contract, the calculated average vibrational energies are as low as 0.053 eV – 0.066 eV in **Figure 4.19(b)**, while the E_{trans} is as high as 1.4 eV, leading to the yielding of formate species. Therefore, beside of part of the high translational energy of CO_2 may use to overcome the Pauli repulsion to approach to H adatom, part of them may use to induce the phonon excitation (mainly) and electron-hole excitation when the molecule collides to the surface. On one hand, differ from H_a, due to its light mass, its scattering or chemisorption on a metal surface makes the translational energy transfer is inefficient [22]. For the CO_2 molecules with heavy mass (m/z = 44), energy and momentum losses are ascribed to the transfer of CO_2 translational energy to heavy Cu surface atoms (m/z = 64) is efficient.

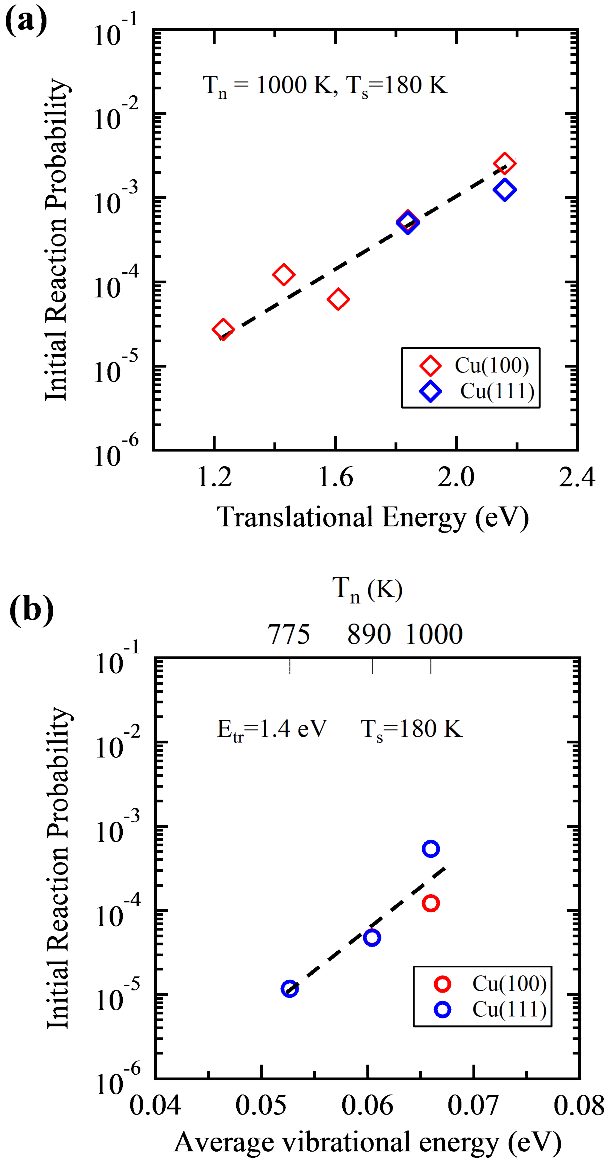

Figure 4.19 The initial reaction probability of CO_2 hydrogenation to form formate on Cu(111) and Cu(100) surfaces: (**a**) as a function of translational energy of incident CO_2 molecules along surface normal direction; (**b**) as a function of average vibrational energy of incident CO_2 molecules along surface normal direction. The Cu surfaces are maintained at 180 K.

How much translational energy CO_2 molecule loses in the collision at surface can be estimated by building up two models of Hard Cube model and Smooth Surface model [23]. On the other hand, in the reaction event, part of E_{trans} would convert into E_{vib} resulting from the interaction between CO_2 molecule and Cu surface in terms of the synergy of Pauli repulsion (see Appendix) and Van der Waals force. This may be because the charge distribution in the CO_2 molecules with a bending mode is uneven. That is, carbon atom is much positive charged while oxygen would be negative charged. The carbon atom and two oxygen atoms would obtain different repulsive force from the surface. Therefore, the vibrational energy of CO_2 would increase.

As we mentioned in Chapter 3, supersonic molecular beam system can generate CO_2 molecules with sharp distribution of translational energy, while the vibrational energy of CO_2 molecules is still in a Maxwell-Boltzmann distribution. In **Fig. 4.19**, the reaction probabilities exponentially increase with increasing the vibrational energies, which thus can be fitted as an Arrhenius form. For the translational energy dependence, part of translational energy transforms into vibrational energy. Upon collision of tilted CO_2 molecules with Cu surface near the hydrogen atoms, the translational energies may be distributed to vibrational, rotational, and translational energies of CO_2 accompanied with energy dissipations into the Cu surface. For example, the translation energy of 1.4 eV may be converted to vibrational energies with a Boltzmann distribution and some parts of CO_2 will gain vibrational energy above 0.4 eV.

From the difference of the slops of two linear fitting line, we calculation the efficiency for reaction probability as $\rho_{Trans} = \Delta \ln P_{re}/\Delta E_{Trans} = 5$, which is much smaller than the calculated vibrational energy efficiency as 41. Therefore, we concluded that the vibrational energy of CO_2 is much preference than the translational energy in the formate synthesis.

4.4.2.3 Coverage of pre-dosed atomic hydrogen effects

The initial reaction probability of thermal CO_2 and H_2 gas on Cu surface is known to be as low as ~ 10^{-12}. Kinetics study on formate synthesis indicates that the formate formation rate has no H2 gas pressure dependence, suggesting that the hydrogen adatoms dissociated from H_2 molecules blocked the reaction between CO_2 and H_a due to the that H adatoms occupy the bare Cu surface atoms. In the molecular beam experiment, we also investigated the effect of hydrogen pre-dosed coverage on the reaction probability of

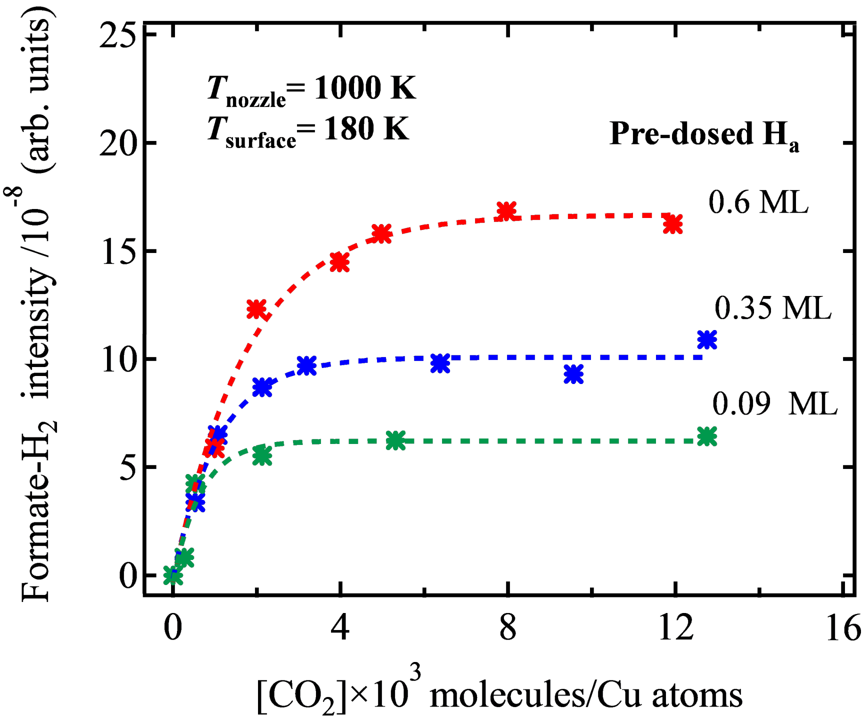

Figure 4.20 Dependence of the initial reaction probability of CO_2 hydrogenation to form formate on the pre-dosed atomic hydrogen coverage on Cu(111). The translational energy and vibrational temperature were fixed at 1.4 eV and 1000 K, respectively. The surface temperature was 180 K. The pre-dosed hydrogen coverages were prepared as 0.6 monolayer (ML), 3.5ML and 0.09 ML on Cu(111).

CO_2. The incident energy of CO_2 (E_T = 1.43 eV, $T_{vib.}$ = 1000 K) was fixed and the surface temperature was maintaining at 180 K. Three different coverages as 0.6 ML (saturated), 0.35 ML and 0.09 ML of pre-dosed atomic hydrogen were used. **Figure 4.20** shows the results about the dependence of the initial reaction probability of CO_2 hydrogenation to form formate on the pre-dosed atomic hydrogen coverages on Cu(111). Here, we monitored the hydrogen decomposition from formate decomposition which can be considered the intensity of formate on Cu(111).

First, the formate saturation condition is corresponding to the coverage of pre-dosed hydrogen. However, we still can observe the unreactive atomic hydrogen associative desorption from the surface during the TPD measurements. It is thus an open question that why there are unreactive hydrogen atoms which do not react with incident CO_2 molecules while the formate still is not in normal saturation condition (0.25 ML). Second, the reaction probability of CO_2 to synthesize formate is independence of the coverages of pre-dosed atomic hydrogen. It probable can be explained the cross-section of the CO_2 molecular beam should be the same when the CO_2 molecules attack hydrogen adatoms on the Cu(111) surface.

4.4.2.4 Tunneling effects

Transition-state-theory (TST) guides that the classical reaction motion should be along the reaction coordinate. However, according to quantum mechanics, tunneling effect may exist in hydrogen-involved

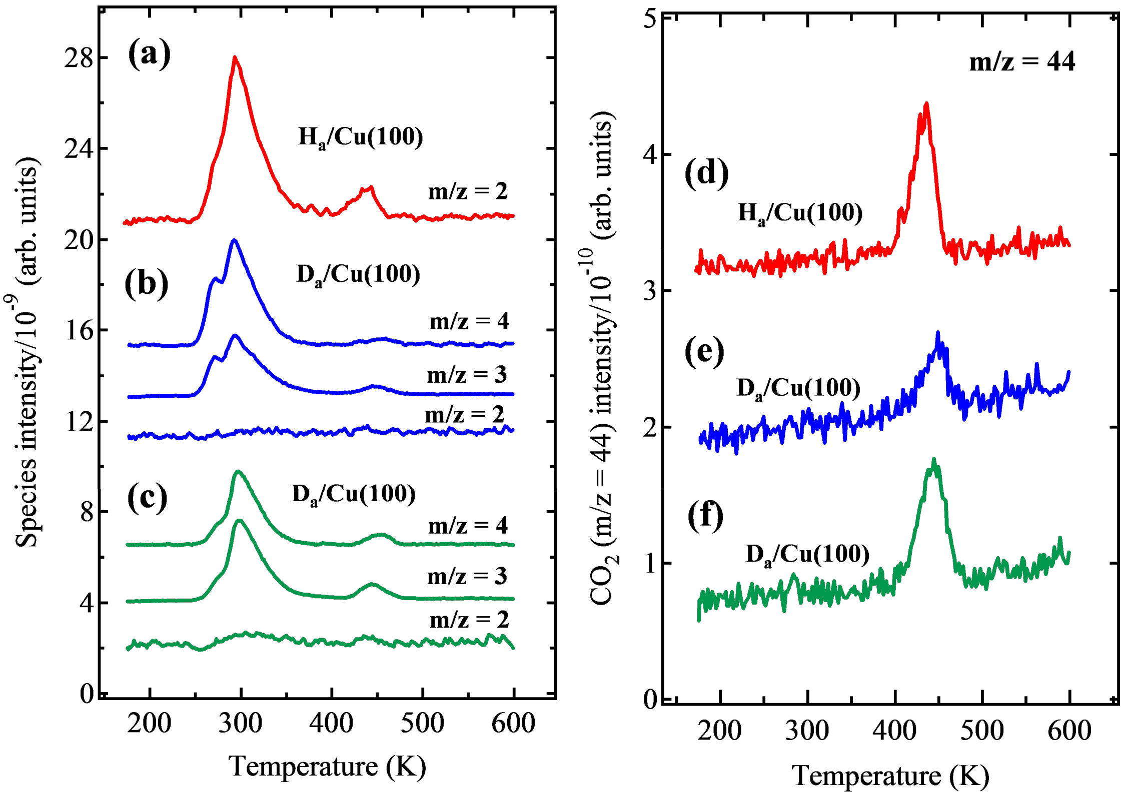

Figure 4.21 The dependencies of formate formation on hydrogen isotope effect and CO_2 exposure in CO_2 molecular beam experiments on Cu(100) traced by TPD (T_{nozzle} = 1000 K, E_{trans} = 1.23 eV. T_s = 215 K, heating rate 2.0 K/s). (**a, d**) H_a predosed on Cu(100) (CO_2: 1.4×10^4 L). (**a**) H_2 (m/z=2) and (**d**) CO_2 (m/z = 44) TPD signal. (**b, e**) D_a predosed on Cu(100) (CO_2: 1.4×10^4 L).(**b**) D_2 (m/z=4), HD (m/z=3), H_2 (m/z=2) and (**e**) CO_2 (m/z = 44) TPD signals. (**c, f**) D_a predosed on Cu(100) (CO_2: 2.8×10^4 L). (**c**) D_2 (m/z=4), HD (m/z=3), H_2 (m/z=2) and (**f**) CO_2 (m/z = 44) TPD signals.

reactions that hydrogen atom tunnels through the potential barrier [24, 25]. V. P. Zhdanov theoretically suggested that the apparent Arrhenius parameters (pre-exponential factor and activation energy) may decrease with decreasing reaction temperature because of tunneling effect [26]. However, since the heterogeneous catalytic reactions usually occur at higher temperatures, the tunneling effects are always neglected in the heterogeneous catalytic process. In order to clarify the ER mechanism for formate synthesis, we thus investigate whether the tunneling effects exist in the CO_2 hydrogenation on Cu catalysts.

Similar molecular beam experiments were carried out on Cu(100) by using D_2 as well as H_2 to investigate the isotope effect on the reaction. As shown in **Figure 4.21**, the simultaneous desorption of CO_2 and D_2 were observed at 450 K in TPD after the irradiation of CO_2 with T_{nozzle} at 1000 K on Cu(100) at 215 K. This shows the formation of DCOO on the Cu(100) surface by the molecular beam CO_2 irradiation. From the comparison of the TPD results between on H/Cu(100) and D/Cu(100), it is found that the production yield is about 2.6 times larger for H/Cu(100) compared to D/Cu(100). The small difference in the production yield clearly indicates that no significant tunneling effect in the formate synthesis. That is, formate formation is required for CO_2 directly attacks hydrogen adatom on Cu surface.

4.4.3 Vibrational state population fraction of CO_2

The number of vibrational modes (different types of vibrations) in a CO_2 molecule is $3N$-5 = 4, where N = 3 is the number of atoms. These vibrational modes, shown in **Figure 4.22(a)**, are responsible for the heat excitation by the heating of nozzle. The arrows indicate the directions of motion, Vibrations labeled ν_1 and

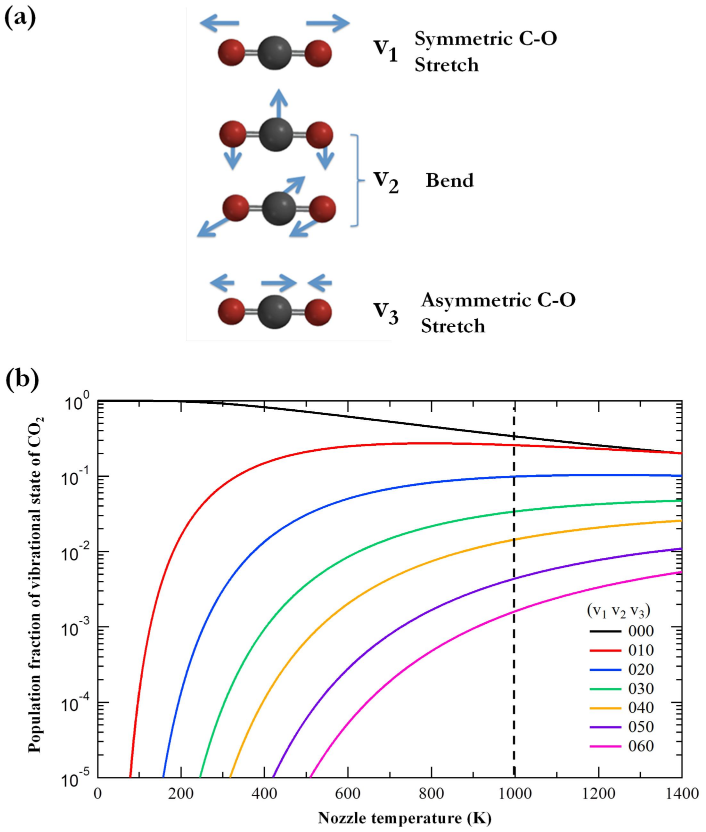

Figure 4.22 (a) The vibrational modes of a CO_2 molecule, ν_1 is symmetric C-O stretch, ν_2 is the bend mode and ν_3 is as asymmetric C-O stretch. **(b)** The dependence of population fraction of vibrational state (ν_2) of CO_2 molecule dependence on nozzle temperature (T_{nozzle}).

ν_3 represent the stretching of the chemical bonds, one in a symmetric mode (ν_1), in which both C=O bonds lengthen and contract together (in-phase), and the other in an asymmetric mode (ν_3), in which one bond shortens while the other lengthens. The other two equal-energy bending vibrations in CO_2 are identical to be a ν_2 mode, except that one bending mode is in the plane of the paper, and one is out of the plane of paper. Since the bending excitation is important to the conversion of linear CO_2 molecule to the Cu-formate, we estimated the population fraction of vibrational state of CO_2 only for ν_2 mode and didn't consider the symmetric mode ($\nu_1 = 0$) and symmetric mode ($\nu_3 = 0$).

During the free jet expansion, binary collisions among the molecules occur about 100 ~ 1000 times [27], resulting in internal energy relaxation and to energy transfer from the rotational modes to kinetic energy in the direction of jet expansion. However, the vibrational degrees of freedom generally almost remain during supersonic expansion, since for thousands of collisions may be required for energy conversion into translational energy [27]. Therefore, we may estimate the relative population in the *i*-th vibration state by the Boltzmann distribution:

$$P_{v=i} = exp(-E_{v=i} / k_B T_n) / Z_v \tag{1}$$

where $E_{v=i}$ is the energy of the *i*-th vibrational state, k_B is Boltzmann's constant, T_n is the nozzle temperature and Z_v is the vibrational contribution of the partition function [28]. The vibrational state population fraction of CO_2 can be thus expressed as:

$$P_{v=i} = \frac{g_{v_i} exp(-E_{v=i} / k_B T_n)}{\sum_i g_{v_i} exp(-E_{v=i} / k_B T_n)} \tag{2}$$

For example, the ratio between the population of $\nu_2 = 1$ and $\nu_2 = 0$ vibrational states population fraction is 0.919 (~91.87%) for T_n = 300 K [29-31]. **Figure 4.22(b)** shows the CO_2 population fraction of vibrational state as a function of nozzle temperature based on our calculations. When the nozzle is at room temperature (~300 K), the majority of the vibrational modes are at low energy levels such as $\nu(000)$, $\nu(010)$ and $\nu(020)$. In the 10% CO_2 beam experiments, we found that no formate was formed when the nozzle temperature is below 950 K. Therefore, the activation of CO_2 vibrational mode to form the formate requires high nozzle temperature up to 1000 K, that is, it requires the increase of the population fractions of CO_2 molecule with high energy levels of the bending modes. On the other hand, the nozzle temperature can decrease to 775 K in the experiment of 1% CO_2 (**Figure 4.18(a)**) to form formate, indicating that the translational energy of CO_2 has also a great promotion to active the CO_2 molecule even at lower vibrational energy level.

4.5 Summary and conclusion

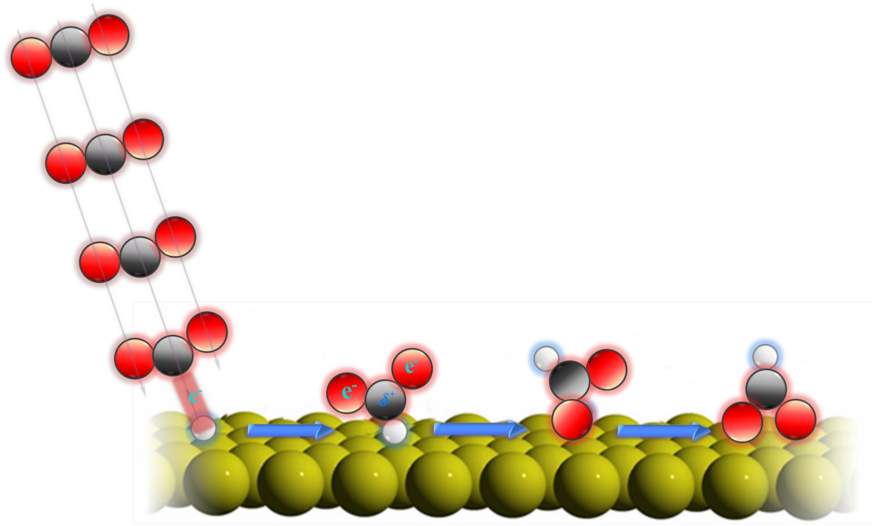

Figure 4.23 Schematics illustration of formate synthesis proceeding via Eley-Rideal (ER)-type mechanism on Cu surfaces.

We experimentally show the evidences to prove that formate synthesis from CO_2 hydrogenation on Cu catalysts proceeds via an ER-type mechanism, as schematically shown in **Fig. 4.23**. That is, the CO_2 molecule directly attacks the hydrogen adatom on the Cu surfaces, because both translational energy and vibrational energies promote the reaction. The reaction mechanism is consistent with the suggestions by kinetic analysis mentioned in Chapter 1. We consider the Eley-Rideal type mechanism includes many important dynamics concepts such as non-Born-Oppenheimer approximation (BOA), non-adiabatic process and thermal non-equilibrium process, which are introduced in Chapter 2. The important evidences are summarized as follows:

(1) The surface-insensitive reaction

We have successfully synthesize the formate on Cu(111) and Cu(100) by using molecular beam. The reaction may be not sensitive to the surface structure. According to the definition of ER-type mechanism, the surface-insensitivity is a significant property for the direct gas-surface reaction.

(2) The independence on the Cu surface temperature

Usually, the rates of heterogeneously catalytic reactions on surfaces are dependent on catalysts' temperature. However, we found the formate synthesis seems to be insensitive to the Cu surface temperature, that is, this should be a direct reaction between CO_2 and hydrogen where the CO_2 is without passing through a trapping or precursor state before the reaction.

(3) Minor tunneling effects

Our isotope experiments on Cu(100) surface further shows that the tunneling effect in the formate synthesis is minor or even negligible because CO_2 still reacts with the heavy deuterium atoms on the surface.

(4) Translational energy and/or vibrational effects

We showed that both translational energy and vibrational energy are required for the formate synthesis. The translational energy of CO_2 may transform into the vibrational energy. The vibrational energy is much preference for CO_2 than translational energy to the formate synthesis on Cu surfaces.

It is worth noting that no reaction of CO_2 adsorbed species ($CO_{2,\ a}$) with co-adsorbed H_a occurs on Cu(110) at 98 K under thermal equilibrium [12]. To the best of our knowledge, the formation of formate species on Cu surfaces is the first example of an ER-type mechanism among industrial catalytic reactions.

References

[1] H. Nakano, I. Nakamura, T. Fujitani, J. Nakamura, J. Phys. Chem. B 105 (2001) 1355-1365.

[2] G. Wang, Y. Morikawa, T. Matsumoto, J. Nakamura, J. Phys. Chem. B 110 (2005) 9-11.

[3] P.A. Taylor, P.B. Rasmussen, C.V. Ovesen, P. Stoltze, I. Chorkendorff, Surf. Sci. 261 (1992) 191-206.

[4] J. Nakamura, Y. Kushida, Y. Choi, T. Uchijima, T. Fujitani, J. Vac. Sci. Technol. A 15 (1997) 1568-1571.

[5] I. Nakamura, H. Nakano, T. Fujitani, T. Uchijima, J. Nakamura, J. Vac. Sci. Technol. A 17(4) (1999) 1592-1595.

[6] S. Bagherzadeh, N.P. Mankad, J. Am. Chem. Soc. 137 (2015) 10898-10901.

[7] C.M. Zall, J.C. Linehan, A.M. Appel, J. Am. Chem. Soc. 138 (2016) 9968-9977.

[8] T. Kondo, H.S. Kato, T. Yamada, S. Yamamoto, M. Kawai, Eur. Phys. J. D 38 (2006) 129-138.

[9] G. Anger, A. Winkler, K.D. Rendulic, Surf. Sci.220 (1989) 1-17.

[10] H. Nishimura, T. Yatsu, T. Fujitani, T. Uchijima, J. Nakamura, J. Mole. Catal. A 155 (2000) 3-11.

[11] B.J. Hinch, L.H. Dubois, Stable and metastable phases of water adsorbed on Cu(111), J. Chem. Phys. 96 (1992) 3262-3268.

[12] K.H. Ernst, D. Schlatterbeck, K. Christmann, Phys. Chem. Chem. Phys. 1 (1999) 4105-4112.

[13] L.G.L. Y. B. Kagan, E. V. Slivinskii, S. M. Loktev, G. I. Lin, A. Y. Rozovskii, and A. N. Bashkirov,, Dokl. Akad. Nauk SSSR 221 (1975).

[14] L.H. Dubois, T.H. Ellis, B.R. Zegarski, S.D. Kevan, Surf. Sci. 172 (1986) 385-397.

[15] B.A. Sexton, A.E. Hughes, N.R. Avery, Surf. Sci. 155 (1985) 366-386.

[16] M. Bowker, S. Haq, R. Holroyd, P.M. Parlett, S. Poulston, N. Richardson, J. Chem. Soc., Faraday Trans. 92 (1996) 4683-4686.

[17] B.E. Hayden, K. Prince, D.P. Woodruff, A.M. Bradshaw, Surf. Sci. 133 (1983) 589-604.

[18] A. Peremans, F. Maseri, J. Darville, J.M. Gilles, J. Vac. Sci. Tech. A 8 (1990) 3224-3228.

[19] E. Vesselli, L.D. Rogatis, X. Ding, A. Baraldi, L. Savio, L. Vattuone, M. Rocca, P. Fornasiero, M. Peressi, A. Baldereschi, R. Rosei, G. Comelli, Carbon Dioxide Hydrogenation on Ni(110), J. Am. Chem. Soc. 130 (2008) 11417-11422.

[20] G. Peng, S.J. Sibener, G.C. Schatz, S.T. Ceyer, M. Mavrikakis, J. Phys. Chem. C 116 (2011) 3001-3006.

[21] H.J. Robota, W. Vielhaber, M.C. Lin, J. Segner, G. Ertl , Surf. Sci. 155 (1985) 101-120.

[22] O. Bünermann, H. Jiang, Y. Dorenkamp, A. Kandratsenka, S. Janke, D.J. Auerbach, A.M. Wodtke, Science 350 (2015) 1346-1349.

[23] J. Oh, T. Kondo, K. Arakawa, Y. Saito, W.W. Hayes, J.R. Manson, J. Nakamura, J. Phys. Chem. A 115 (2011) 7089-7095.

[24] S. Sato, Tunneling in bimolecular reactions, Chem. Phys. 315 (2005) 65-75.

[25] W.H. Miller, Beyond transition-state theory: a rigorous quantum theory of chemical reaction rates, Acc. Chem. Res. 26 (1993) 174-181.

[26] B.I.L. E. Hasselbrink, Handbook of Surface Science, in: V.P. Zhdanov (Ed.) Reaction dynamics and kinetices: TST, non-equilibrium and non-adiabatic effects, lateral interacitons, etc., ELSEVIER, Amsterdam, 2008.

[27] G. Scoles, Atomic and Molecular Beam Methods, Atomic and Molecular Beam Methods, Oxford University Press, New York, 1988.

[28] O. Michio, J. Phys.: Condens. Matter 22 (2010) 263003.

[29] H. Romanowski, R.B. Gerber, M.A. Ratner, J. Chem. Phys. 88 (1988) 6757-6767.

[30] A. Chedin, J. Mol. Spectrosc. 76 (1979) 430-491.

[31] D. Bailly, R. Farrenq, G. Guelachvili, C. Rossetti, J. Mol. Spectrosc. 90 (1981) 74-105.

Chapter 5

Dynamics of formate decomposition on Cu catalysts studied by angle-resolved analysis of desorbing CO_2 product

5.1 Introduction

Energy transfer and bond rupture/formation are two important events in a chemical reaction [1, 2]. Consequently, the reaction mechanism must be examined with both aspects in mind. For gas-phase bimolecular reactions, energy transfer processes have been extensively examined by applying crossed molecular beam techniques, where detailed dynamical parameters such as total momentum, energy, and angular momentum, before and after the collision events, can describe the partitioning of energy into each available mode of the products [3, 4]. On the other hand, to study how the energy released in the gas-surface reaction is disposed in the products is one of the promising approaches to investigate the reaction dynamics [5-7]. However, characterizing the energy transfer processes in gas-surface chemical reactions is challenging because of the large number of degrees of freedom available to the surface atoms. In chapter 5, we have shown the thermal non-equilibrium character for the formate synthesis from CO_2 via ER-type mechanism by using supersonic molecular beam technique. As the comprehensive study, the dynamics of formate synthesis can be inferred by the reverse process as the CO_2 desorption measurements from formate decomposition on the basis of mircro-reversibility principle.

The measurement of angular distributions of desorbing species after having been supplied to the surface by a molecular beam have been extensively studied since 1960s [8]. Many researchers had discussed that thermal equilibrium between desorbing species and the surface is in favor of a cosine or Maxwellian distribution of desorbing species on the basis of second low of the thermodynamics [9-11]. However, Comsa argued that the species leaving from the surface are including the elastically and inelastically scattered ones, the cosine/maxwillian distributions are the behavior of sum of these species [12]. So the desorbing species would show a non-cosine distribution if the scattering is abstracted because force exerting the molecule from the surface may be not isotropic. One of the well-known experiments by van Willigen in surface physics is that the permeated hydrogen associated desorbing from Fe, Pd and Ni showed strongly sharp angular distribution along the surface normal direction. It was found that the energy distribution of the hydrogen molecules desorbing over the barrier had to exhibit a mean particle energy which is larger than the $2kT$ expected from Maxwellian distribution [13]. That is, the associatively desorbing atomic hydrogen obtained a repulsive force from the surface. Similar behavior has also been observed in the thermal recombination desorption of nitrogen on Cu(111) surface [14].

The energy released from the surface reaction mainly depends on the location of the transition state and the surface structure. For example, the partitioning of energy between translational energy and vibrational excitation reveals information about the repulsion between the molecule and the surface and how the vibrational coordinate changes as the molecule desorbing from the transition state into vacuum. On the basis of the principle of detailed balance, the thermal non-equilibrium dynamics observed for formate synthesis on Cu surfaces should reflect the dynamics of the reverse reaction, i.e. the decomposition of formate into CO_2

and H_a ($HCOO_a \rightarrow CO_2 + H_a$). The forward and backward reaction should share the same transition state structure. More specifically, the potential energy difference of formate decomposition between the transition state (TS) and the final state of $CO_2 + H_a$ should be converted to the translational and/or vibrational energy of product CO_2 molecules rather than the dissipation of heat onto the Cu surface. Such hyper-thermal molecules would receive repulsive force from surfaces and show sharp angular distributions that deviate from the cosine law [15], which can be measured by angle-resolved steady-state desorption (AR-SSD) and angle-resolved temperature programmed desorption (AR-TPD) [16-18]. To analyze a gas-surface chemical reaction, angle-resolved (AR) analysis of the desorbed products from the surface is one of the direct methods used because it relates to the transition state (TS) structure of the reaction. In this Chapter, we present the angle-resolved dynamical analysis of formate decomposition on Cu catalysts through carrying out two experiments: a thermal formate decomposition experiment for AR-TPD and a steady-state reaction of HCOOH and O_2 for AR-SSD.

5.2 CO_2 desorption from thermal decomposition of adsorbed formate ($HCOO_a \rightarrow CO_2 + H_a$)

We have successfully synthesized formate by using CO_2 beam and shown that the reaction follows ER-type mechanism. If there is an active state (like hot precursor/atom) on the surface just before formate synthesis or/and just before desorption in the thermal decomposition, the CO_2 may be scattered by co-adsorbed species on its trajectory, it would yield a CO_2 desorption at the deviated angle from the normal direction of surface in a certain reaction condition. Angle-resolved (AR) product desorption analysis has provided a method to directly assign active surface species from desorbing products [16]. It is in contrast to structural analysis with surface spectroscopy such as vibrational spectroscopy and diffraction methods, which are based on the signal from surface species after energy dissipation. In this study, we examined this kind of desorption dynamics by applying AR-TPD to measure the intensity distributions of CO_2 desorbing from thermal decomposition of formate on three low index surfaces: Cu(111), Cu(110) and Cu(100), and investigated the sensitivity of the desorption dynamics on the surface structure.

5.2.1 Experimental apparatus

The AR-TPD has been described elsewhere for the surface reaction studies [16, 19]. Here, the details also are introduced. As shown in **Figure 5.1**, the apparatus is an ultra-high vacuum system composed of three chambers that are separately pumped. The reaction chamber was equipped with an Ar^+ ion gun, sample manipulator and LEED system. The slit chamber consists of two slits; the two slits can yield reliable AR signals because they effectively separate the CO_2 molecules that arrive directly through surface reactions from those that are emitted into the reaction chamber and scattered from the chamber wall. The analyser chamber has a quadrupole mass (Q-mass) spectrometer for AR-TPD. The AR signals were calibrated by considering area factors (see Appendix). Upon temperature programmed heating, formate decomposition was observed by the angle-resolved mass spectrum signals of product $^{13}CO_2$ and H_2 in TPD measurements.

5.2.2 Experimental methods

The sample surfaces of the single crystals Cu(111), Cu(110) and Cu(111) (all sample with: 2 mm thick, diameter ∅ = 10 mm, 5N purity. Surface Preparation Laboratory, Netherlands) were suspended by two tantalum wires through two parallel holes in the sample for their experiments, repectively. The tantalum wires were also used as a filament for the resistive heating of the sample. The Cu(111), Cu(110), and Cu(100) surfaces were cleaned by the same method as molecular beam experiments. That is, the samples were cleaned by cycles of Ar^+ sputtering followed by annealing at 773 K. The sample cleanliness was checked by

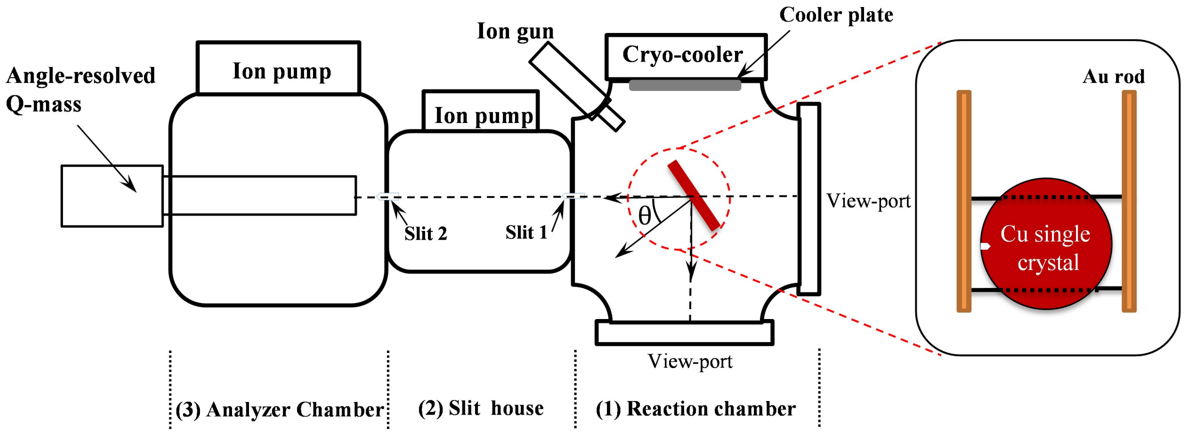

Figure 5.1 Schematic top view of angle-resolved temperature-programmed desorption (AR-TPD). (1) In the reaction chamber ($< 5\times10^{-10}$ Torr), two view-ports are used for the alignment of the Cu sample to the two slits, which is aimed along the line of the two slits and the analyser. (2) In the slit house, the first slit (slit 1) locates at 45.0 mm away from the Cu sample. The second slit (slit 2) locates at 55.0 mm away from the slit1. The diameters of the first and second slit are 2.7 mm and 4.0 mm, respectively. (3) In the analyser chamber, the signals are detected by Q-mass. The detected signals are collected by a computer system simultaneously with the signals of the programmed surface temperature, and then AR-TPD profiles are obtained.

observing sharp diffraction spots in LEED pattern and Auger electron spectroscopy.

The ^{13}C-formic acid (H^{13}COOH) (Aldrich, purity $\geq$ 98%, 99% of ^{13}C) liquid sample was purified by freeze-pump-thaw cycles in order to remove any dissolved gases. The surface adsorbed formate (H^{13}COO) species was prepared as follows. (i) On clean Cu(110) and Cu(100) surfaces, we directly introduced ^{13}C-formic acid (H^{13}COOH) (Aldrich, purity $\geq$ 98%, 99% of ^{13}C). (ii) On the clean Cu(111) surface, we pre-deposited surface oxygen atoms (^{18}O) by dosing labelled oxygen ($^{18}O_2$, purity $\geq$ 98%), and then introduced ^{13}C-formic acid. We have characterized the formate species on the Cu(110) through introducing formic acid by using FTIR spectra. The presence of surface oxygen enhances the Brønsted basicity of the surface, thereby contributing to the formation of formate on Cu(111). In the absence of oxygen on Cu(111), no formation of formate was observed [20].

5.2.3 Results and discussion

Figure 5.2 presents the IRAS confirmation of the prepared formate from dehydrogenated formic acid on a clean Cu(110) surface. The peaks at 1340 cm^{-1} are assigned to the symmetric OCO stretching band (ν_S(O^{13}CO)) of formate, which is comparable with the formate produced in molecular beam experiments (**Figure 4.10(b)**) and previous reported results (**Table 4.1**). The broad peaks at around 1680 cm^{-1} probably due to the little amount of water or the water noise in IRAS system. We can see that the formate was saturated after the Cu(110) was exposed 215 L H^{13}COOH due to the adsorbance intensity of symmetric OCO stretching band (ν_S(O^{13}CO)) didn't increase any more. After the surface was heated to 360 K, and then back to 215 K, the formate remained on the Cu(110) surface (black curve). Accordingly, the adsorption structure of formate on Cu surface also has been well characterized experimentally by near-edge X-ray adsorption

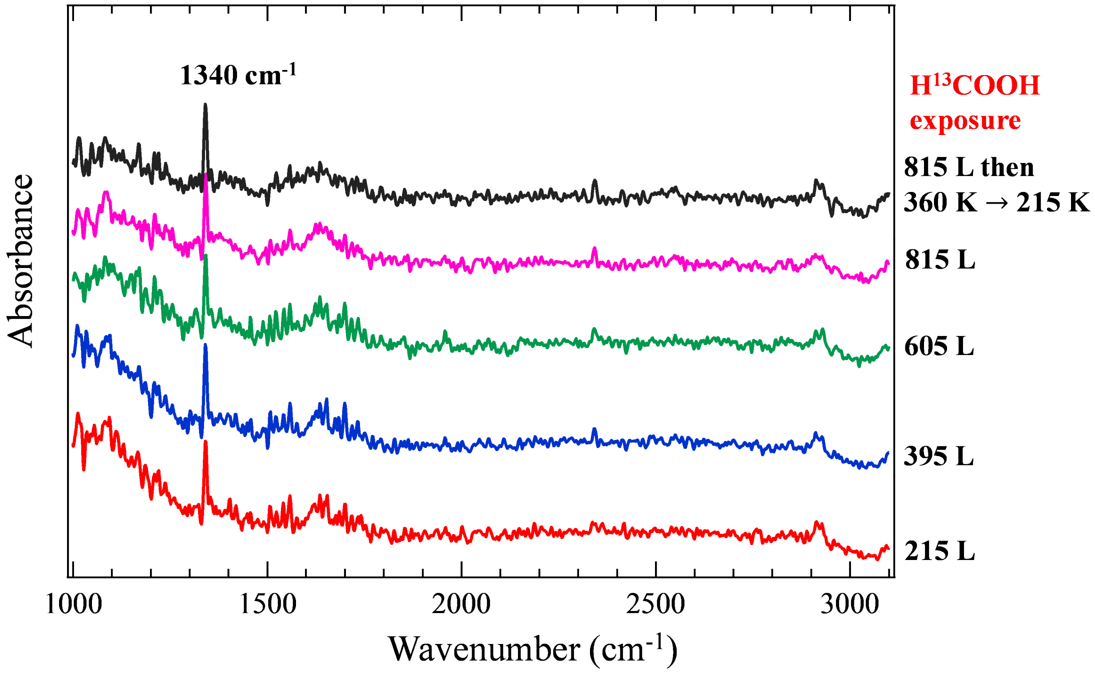

Figure 5.2 The IRA spectra collected after clean Cu(110) was exposed by different exposures of ^{13}C-labeled formic acid (H^{13}COOH) at 215 K.

spectroscopy (NEXAFS), surface extended X-ray adsorption fine structure (SEXAFS) [21-23], photo-electron diffraction (PhD) [22], normal incidence X-ray standing wave-field adsorption (NIXSW) [24] and scanning tunnelling microscope (STM) [25, 26]. Hence, we can conclude that in this experiment, formate is a bidentate structure adsorbed on two neighboring Cu surface atoms along $[1\bar{1}0]$ direction.

Therefore, to understand the formate adsorption structure is helpful to study the formate decomposition dynamics on Cu surfaces. We introduced formic acid at room temperature (298 K) to produce Cu surface formate. In the subsequent heating, CO_2 was desorbed 350 K ~ 460 K on Cu surfaces. The formate coverage, θ_{HCOO}, was determined from the HCOOH exposure relative to the production of formate with the value of a monolayer (~ 0.25 ML). As shown by **Figure 5.3,** the AR-TPD results of $^{13}CO_2$ with 0.25 monolayer (ML) formate coverage, where TPD peaks of $^{13}CO_2$ were measured along the azimuth of the $[2\bar{1}\bar{1}]$ direction on Cu(111) (**Figure 5.3(a)**), the [001] and $[1\bar{1}0]$ directions on Cu(110) (**Figure 5.3(b)**), and the [011] direction on Cu(100) (**Figure (5.3(c)**). The desorption temperatures of $^{13}CO_2$ agree well with the previously reported data [27, 28]. The intensities of the $^{13}CO_2$ peaks were plotted against polar angles. The resultant peak height had about 10% uncertainty at low formate coverage. It was found that the angular distributions all take on the shape of $\cos^8\theta$ on the Cu(110), Cu(111), and Cu(100) surfaces, sharply collimating to the surface normal direction ($\theta = 0°$) independently of the structure of Cu surfaces and the azimuthal directions.

In addition, the formate coverage dependence has also been investigated as shown in **Figure 5.4**. The sharp distributions of $^{13}CO_2$ clearly indicate that the desorbing CO_2 from the decomposition of formate obtains a repulsive force from the Cu surface with high translational energy. We believe that, just before desorption in the process of TS → $^{13}CO_{2,\,g}$ + H_a, nascent $^{13}CO_2$ molecules receive the repulsive force (Pauli

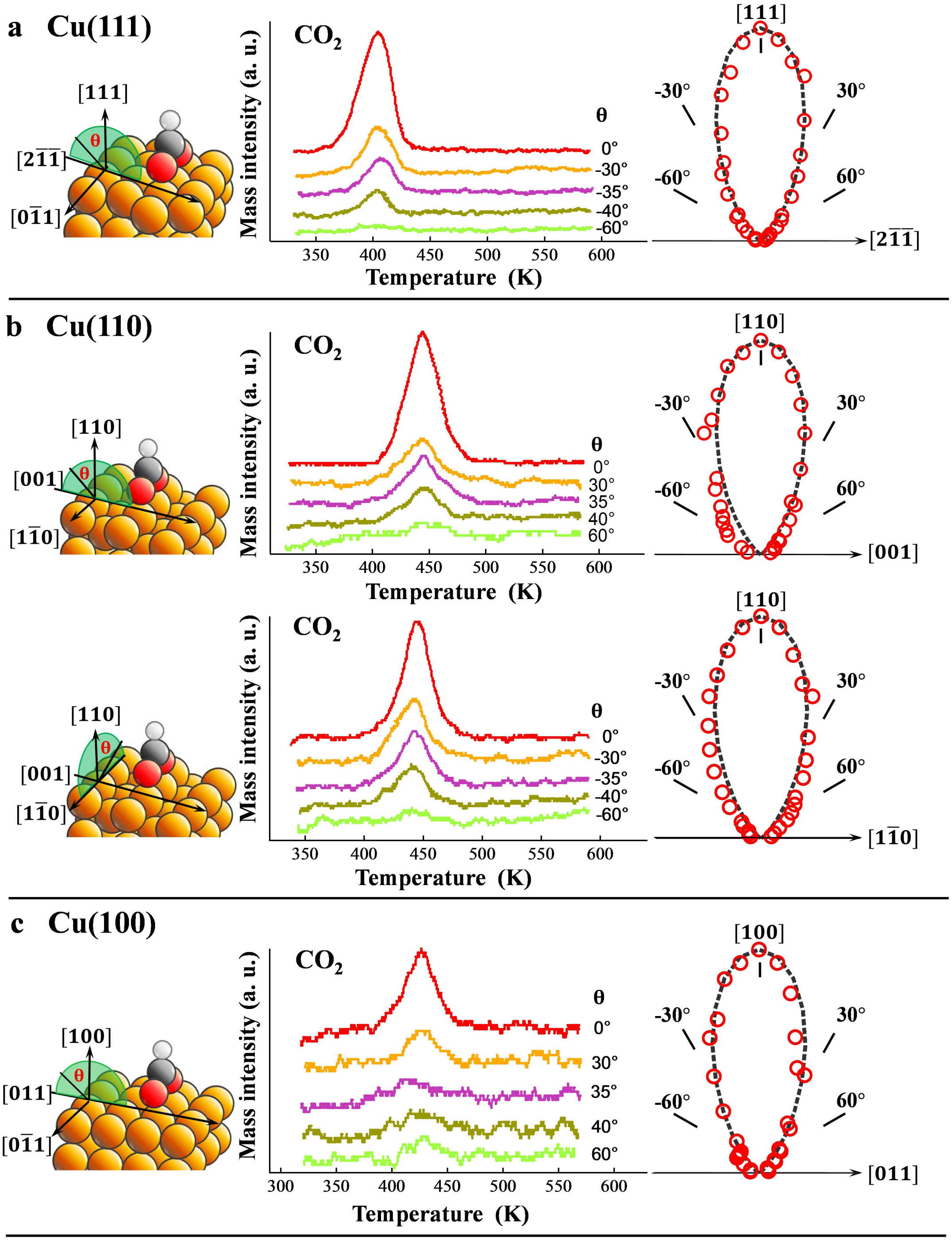

Figure 5.3 AR-TPD of $^{13}CO_2$ formed by the decomposition of $H^{13}COO_a$ on Cu(111), Cu(110), and Cu(100). $H^{13}COO_a$ was prepared by the dehydrogenation of $H^{13}COOH$ with a same coverage of 0.25 monolayer (ML). In each panel, the schematic of the Cu surface structure, AR-TPD results, and the polar graph of desorption intensity at peak temperature (408 K, 447 K, and 423 K for Cu(111), Cu(110), and Cu(100), respectively) are shown. (**a**) Cu(111) along the polar angle θ in [2$\bar{1}\bar{1}$]. (**b**) Cu(110) along θ in [001], and Cu(110) along e θ in [1$\bar{1}$0]. (**c**) Cu(100) along θ in [011]. The intensity distributions of $^{13}CO_2$ all take on the shape of $\cos^8\theta$ (black dashed curves in polar graphs) to the desorbing polar angles, where θ indicates the desorbing angle away from the surface normal direction ($\theta = 0°$). Here, the data on Cu(111) and Cu(110) are from the master's thesis (Jiamei Quan- Dissertation for Master Degree in Engineering, Univ. of Tsukuba, 2013).

(a) Desorbing polar angle in plane of [$2\bar{1}\bar{1}$] and [111] over Cu(111)

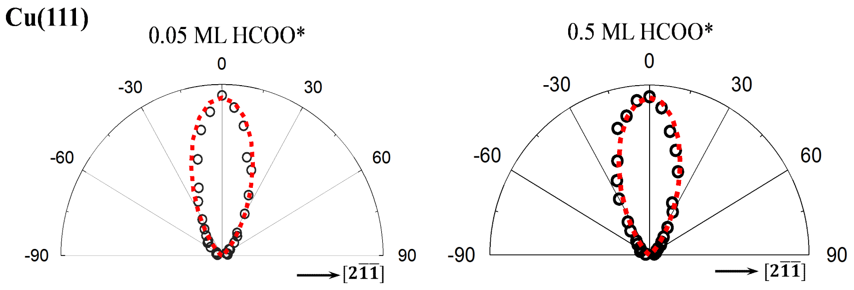

(b) Desorbing polar angle in plane of [001] and [110] over Cu(110)

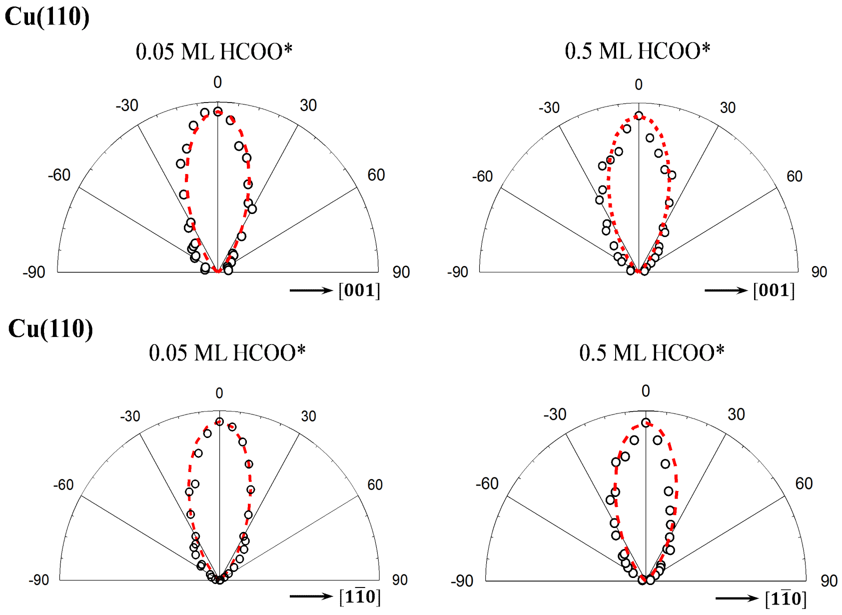

(c) Desorbing polar angle in plane of [011] and [100] over Cu(100)

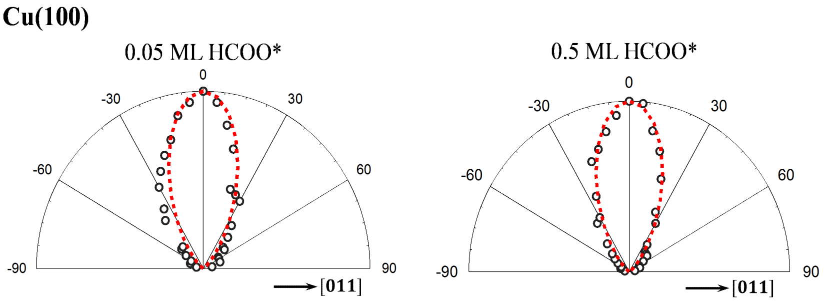

Figure 5.4 Angular distribution of desorbing CO_2 from Cu single crystal surfaces. (**a**) Cu(111): polar ngle θ in the plane of [$2\bar{1}\bar{1}$] and [111], 0.05 ML and 0.5 ML $HCOO_a$, (**b**) Cu(110): polar angle θ in the plane of [001] and [110], 0.05 ML and 0.5 ML formate ($HCOO_a$); and polar angle θ in the plane of [$1\bar{1}0$] and [110], 0.05 ML and 0.5 ML $HCOO_a$; (**c**) Cu(100): polar angle θ in the plane of [011] and [100], 0.05 ML and 0.5 ML $HCOO_a$.

repulsion) from the Cu surface along the surface normal direction. We therefore conclude that the temperature of desorbing $^{13}CO_2$ molecules is higher than that of the Cu surface, in the viewpoint of detailed balance, which is consistent with the results of molecular beam experiments. The identical angular distributions of $^{13}CO_2$ on Cu(110), Cu(100), and Cu(111) in **Fig. 5.3** and **Fig. 5.4**, suggesting an identical TS irrespective of the surface structure [29]. Moreover, the structure insensitivity observed for formate decomposition agrees with that observed for formate formation with regard to the activation energies, turnover frequencies, and initial reaction rates [30-32].

5.2.4 Conclusion

The angle-resolved distributions of CO_2 desorbing from thermal decomposition of formate on Cu surfaces show the properties:

(1) The distribution shapes are identical as a form of $\cos^n\theta$ ($n = 8$) along surface normal direction;

(2) The distribution shape is independence of surface structures and surface azimuths;

(3) The distribution shape is independence of formate coverages.

The results indicate that the CO_2 molecules just before desorption obtain the repulsive force from surface toward the surface normal direction. The neighbour formate and Cu surface atom would have negligible effects on the desorption dynamics of CO_2. That is, the CO_2 desorption from formate decomposition on Cu surfaces is a thermal non-equilibrium process. It suggests that the CO_2 directly desorb after C-H bond braking without trapping on the Cu surface. Therefore, the results from AR-TPD experiments, in turn, support the fact that the CO_2 molecule needs high translational energy to overcome the repulsion from the Cu to form formate by colliding with H_a adatom.

5.3 CO_2 desorption under the steady-state HCOOH oxidation on Cu(110)

5.3.1 Experimental apparatus

The experimental apparatus and procedures for measurements under steady-state reaction conditions have been described previously in details [16, 18]. Briefly, the apparatus consists of three separately pumped chambers for controlling the reaction conditions, as shown in **Fig. 5.5**. These three chambers are separately pumped. The reaction chamber is an ordinary UHV vessel with high pumping rate. Either the chopper house or the analyser chamber must be evacuated with a large pumping rate ~ 7 m3/s, respectively by two cooled copper plates which are connected with a mini-cryopump. Such a large pumping rate is required for the angle-resolved measurement. The chopper house is equipped with a cross-correlation chopper blade for time-of-flight (TOF) measurements and has two narrow slit facing the reaction chamber and detector chamber. The angle-resolved (AR) mass signals were obtained by a differentially pumped quadrupole mass spectrometer (QMS). The translational energy distribution of the desorbed molecules was measured by the time-of-flight (TOF) technique, where the desorbed molecules are detected by the QMS after passing through the slit, cross-correlation chopper, and the drift tube. The flight path between the chopper blade and the ionizer is 377 mm. The chopper, with pseudo-randomly positioned 255 slits of equal width, was rotated at 196.1 Hz, where a time resolution of 20 μs is obtained. The detected signal was recorded by a multichannel analyzer with 20 μs × 255 channels with a high transmission of molecules (50%) [18].. The start signal for the TOF measurement was provided by a photo-coupler, which is triggered by the trigger hole of the chopper. The trigger position of the chopper was determined from curve fitting to the velocity distribution of an effusive Ar beam. A deviation of time in the TOF due to the experimental setup was evaluated to be 8.935 μs in the case of $^{13}CO_2$ molecules and it provided a correction to the measured TOF spectra.

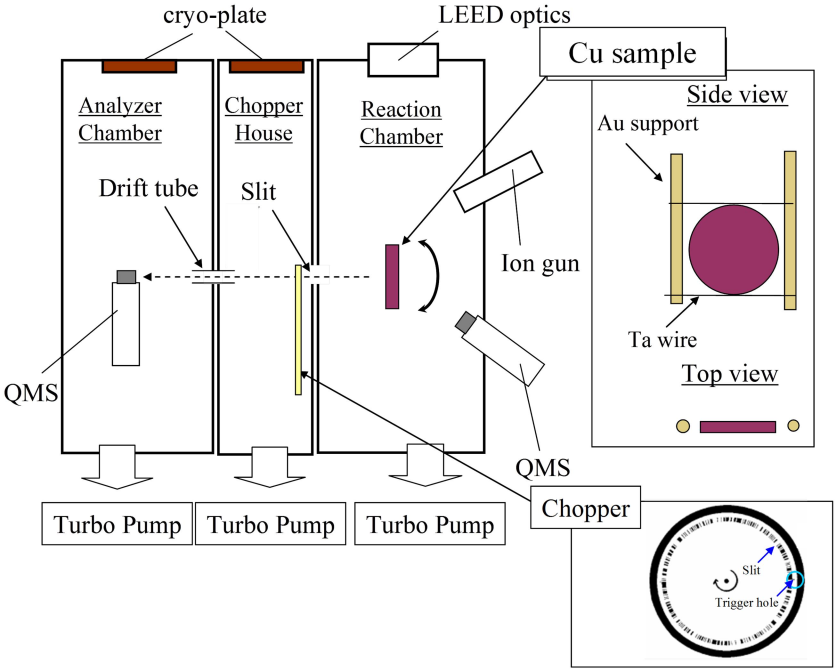

Figure 5.5 Schematic diagram of angle-resolved steady-state desorption (AR-SSD) incorporating time-of-flight (TOF) techniques. (1) The reaction chamber is equipped with an ion gun, LEED optics and a QMS detector for TPD measurement; (2) The chopper house has a pseudo-random chopper blade for cross-correlation time-of-flight techniques, which is used for analyzing the energy of the desorbing molecules through the two narrow slits from reaction chamber. (3) Analyzer chamber has a QMS detector with high sensitivity to obtain the angle-resolved mass signal.

A sample surface of the single crystal Cu(110) (2 mm thick, diameter Ø = 10 mm, 5N purity, Surface Preparation Laboratory, Netherlands) was suspended by two tantalum wires through two parallel holes in the sample. The tantalum wires were also used as a filament for the resistive heating of the sample. The sample was cleaned by cycles of Ar^+ sputtering followed by annealing at 773 K. The sample cleanliness was checked by observing sharp diffraction spots in LEED pattern. The ^{13}C-formic acid ($H^{13}COOH$) (Aldrich, purity $\geqslant$ 98%, 99% of ^{13}C) was purified by freeze-pump-thaw cycles in order to remove any dissolved gases. The $H^{13}COOH$ was introduced through a doser facing with Cu(110) surface, while O_2 was backfilled.

5.3.2 Results and discussion

The formation of $^{13}CO_2$ during the steady-state reaction of $H^{13}COOH$ with O_2 on Cu(110) was monitored by angle-resolved intensity measurements using a mass spectrometer. $H^{13}COOH$ and O_2 were continuously introduced and maintained at $P(H^{13}COOH) = 0.7\times10^{-7}$ Torr and $P(O_2) = 1.15\times10^{-7}$ Torr, respectively. **Figure 5.6(a)** shows the surface temperature dependence of the AR $^{13}CO_2$ mass signals (m/z = 45) at $\theta = 0°$with heating and cooling of the Cu(110) sample. The production of $^{13}CO_2$ was negligible below 400 K; however, it started to rise significantly above 400 K and reached the maximum level at 452 K, after which it started decreasing gradually. In both heating and cooling modes, the CO_2 signals were observed to be almost identical indicating that the reaction of formic acid with oxygen has reached the steady state.

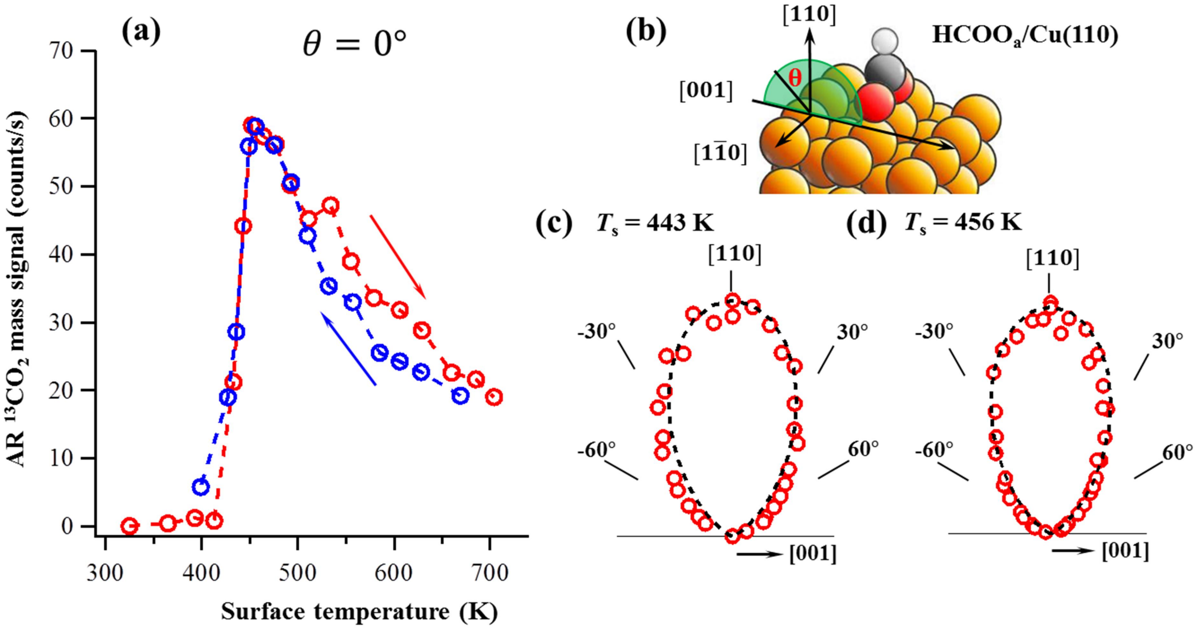

Figure 5.6 (**a**) AR $^{13}CO_2$ signal, as a function of surface temperature, along the direction normal (θ = 0°) to the Cu(110) surface under steady-state reaction conditions. The pressures of $H^{13}COOH$ and O_2 are 0.7×10^{-7} Torr and 1.15×10^{-7} Torr, respectively. The surface temperature was first increased from 325 K to 704 K (red circles) and then decreased to 400 K (blue circles) as indicted by arrows. (**b**) Schematic of bidentate formate species on Cu(110). AR distribution of $^{13}CO_2$ with polar angle along the [001] direction of Cu(110) under steady-state reaction conditions. (**c, d**) $^{13}CO_2$ AR distributions at surface temperatures of 443 K and 456 K, respectively. Black dashed-curves represent the distributions of $\cos^n \theta$ (n = 6) obtained by fitting analysis.

The kinetics of formate decomposition on Cu surfaces have been studied extensively, and it is well known that this decomposition takes place at 410–450 K to form CO_2 and H_2 [27, 28]. The formation of CO_2 above 400 K in **Fig. 5.6(a)** is thus attributed to the decomposition of formate. As shown in **Fig. 5.6(b)**, the adsorbed formate structure is in a bidentate form, i.e., two O atoms are bound to the two nearest neighboring surface Cu atoms; this has clearly been identified previously [33]. It is also known that formic acid reacts readily with adsorbed oxygen to form formate and water, even at room temperature [25, 28, 32, 34]. The signals corresponding to the masses of $^{13}C^{16}O$ (m/z = 29) and $^{13}C^{16}O^{16}OH$ (m/z = 46) are negligible. The elemental steps for the overall reaction of formic acid with oxygen in Fig. 2a are therefore regarded to be as follows [25]:

$$O_2 \rightarrow 2O_a \tag{1}$$

$$H^{13}COOH + O_a \rightarrow H^{13}COO_a + OH_a \tag{2}$$

$$2OH_a \rightarrow H_2O + O_a \tag{3}$$

$$H^{13}COOH + OH_a \rightarrow H^{13}COO_a + H_2O \tag{4}$$

$$H^{13}COO_a \rightarrow {}^{13}CO_2 + H_a \quad (5)$$

$$2H_a \rightarrow H_2 \quad (6)$$

Steady-state coverage of intermediates on Cu(110) is determined by the kinetics of elementary steps (1) ~ (6). The elementary steps of (1) ~ (3) and (6) are fast at room temperature while the reaction (5) is slow as the rate-determining step taking place above 400 K [25]. Although the kinetics of step (4) has not been measured so far, one can regard that the major intermediate is formate in the steady-state reaction above 400 K based on the kinetic balance. The steady state coverage of O_a, OH_a, and H_a should be small. We consider in the present reaction conditions that formate decomposition proceeds on adsorbate (O_a, OH_a, H_a)-free Cu(110) surfaces.

Note that the decomposition of formate in eq. (5) is the reverse reaction of formate synthesis by the hydrogenation of CO_2. On the basis of microreversibility, the dynamics of formate decomposition is interesting, especially in relation to the proposed ER-type mechanism for formate synthesis on Cu catalysts.[35] Hence, we examined the reaction dynamics of formate decomposition by measuring the angular intensity and translational energy distributions of CO_2 as functions of desorption angle and surface temperature. **Figures 5.6(c)** and **5.6(d)** show the AR-measured distributions of ${}^{13}CO_2$ along the [001] direction of Cu(110) at 443 K and 456 K, and $P(H^{13}COOH) = P(O_2) = 0.7\times10^{-7}$ Torr. The angular distributions of desorbing ${}^{13}CO_2$ at both temperatures show a sharp collimation with $\cos^n\theta$ ($n = 6$) along the surface normal direction. These sharp distributions indicate that the desorption of ${}^{13}CO_2$ molecules by the thermal decomposition of formate is a thermal non-equilibrium process. This is contrast to the desorption of fully thermally accommodated adsorbed species on the surface, which shows a cosine distribution [36, 37]. Between 443 K and 456 K, the AR distribution was observed to be independent of surface temperature, suggesting that the CO_2 just before desorption at the TS for formate decomposition, is not energetically coupled with the Cu(110) surface. The origin of the observed sharp distribution perpendicular to the surface can be explained by the Pauli repulsion between CO_2 and the Cu surface with sp-band character at the Fermi level [38], as suggested by the present DFT calculations [29]. If the CO_2 is energetically coupled with the surface, the AR distribution should be broader at higher surface temperatures.

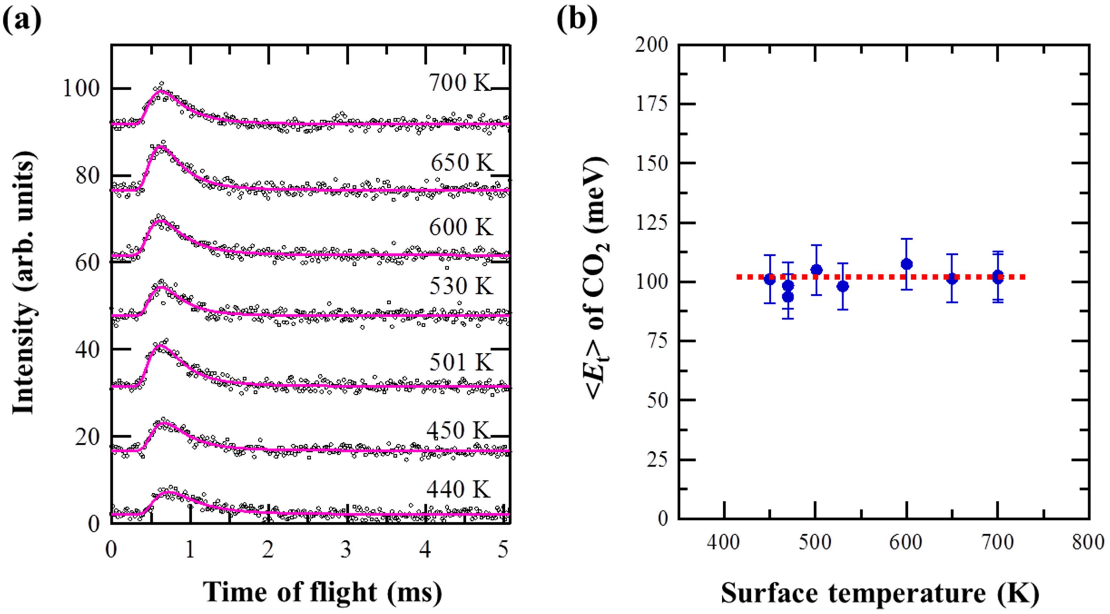

Figure 5.7 (**a**) Deconvoluted TOF spectra of $^{13}CO_2$ (circles) and least squares fits (lines) along the surface normal (θ = 0°) direction of Cu(110) under steady-state reaction condition for varying surface temperatures. The pressure of $H^{13}COOH$ is 1×10^{-7} Torr and O_2 is 1×10^{-7} Torr. (**b**) The mean translational energy $<E_t>$ of $^{13}CO_2$ derived from the TOF spectra in (**a**).

Figure 5.7(a) shows a series of time of fright (TOF) data for $^{13}CO_2$ measured during the steady state reactions of $H^{13}COOH$ with O_2 at various reaction temperatures. As shown in **Fig. 5.7(b)**, mean translational energies $<E_t>$ of $^{13}CO_2$ (see Supporting Information) are found to be as low as 100 meV independent of reaction temperature between 450 K and 700 K. The $<E_t>$ of 100 meV corresponds to the CO_2 temperature T of 580 K by assuming as $<E_t> = 2kT$ (k: Boltzmann constant), which is lower than the surface temperature of 700 K in Fig.3. This indicates the presence of cooling mechanism near the TS. As described in Fig.1, the Cu-O and C-H bonds of formate are cleaved near the TS while the energy was used for climbing the decomposition reaction barrier or breaking the bonds. The endothermic process should cool the TS. The nascent CO_2 at the TS is thus cold, which then experiences the Pauli repulsion from H_a/Cu. The product CO_2 consequently desorbs from the surface with translational energy only acquired as a result of the energy released from the TS, which is independent of surface temperature as shown by **Fig. 5.7(b)**. We note here that the mean translational energy of 100 meV is much smaller than the DFT-calculated 0.71 eV energy difference between the TS and the FS. Thus, this 0.71 eV energy can be considered to be distributed to the vibrational energy and the rotational energy too, as described in the discussion of DFT-calculations in Chapter 6.

The measured thermal non-equilibrium results clearly indicate that nascent CO_2 desorbs without trapping its adsorption state after passing through the TS during the decomposition of formate. That is, no significant energy transfer takes place between CO_2 and the surface around the TS for formate decomposition. From the viewpoint of energy transfer, this is in contrast to what has been observed in associative desorption reactions at surfaces reported in the literatures. For example, the translational energy of CO_2 formed by the oxidation of CO on Pd(133) increases linearly with increasing surface temperature under steady-state reaction conditions and follows the relationship: $<E_t> = 0.24\text{ eV} + 2kT_s$ (ref. [39]). The difference in T_s-dependence of $<E_t>$ between the present study and the literatures is probably caused by the

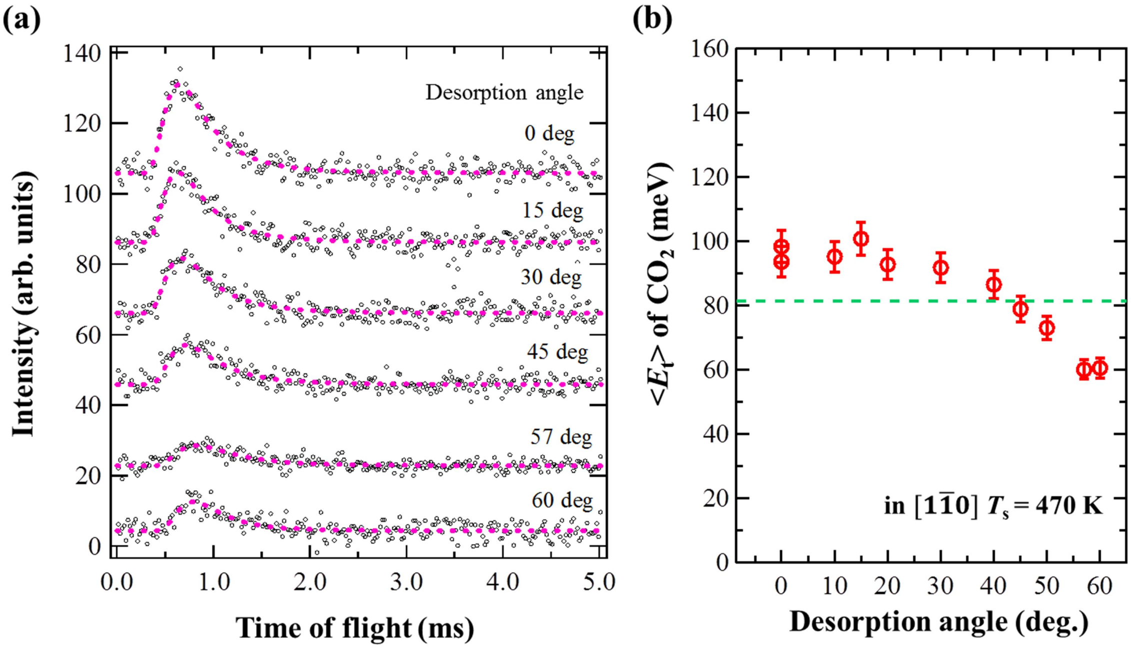

Figure 5.8 (**a**) Deconvoluted TOF spectra of $^{13}CO_2$ (circles) and least squares fits (dashed lines) along the [1$\bar{1}$0] direction of Cu(110) at 470 K under steady-state reaction conditions as a function of desorption polar angle θ. The pressure of $H^{13}COOH$ is 1 × 10^{-7} Torr and O_2 is 1 × 10^{-7} Torr. (**b**) The mean translational energy <E_t> of $^{13}CO_2$ derived from the TOF spectra in (a).

difference of their TS structures. In the present formate decomposition case, CO_2 at the TS has no bonding with the Cu surface. That is considered to be the origin of the thermal non-equilibrium dynamics of formate decomposition.

Finally, the polar angle dependence, from the surface, of TOF was measured for desorbed $^{13}CO_2$ for the steady-state reaction of $H^{13}COOH$ with O_2. **Figure 5.8(a)** shows the TOF results for angles of 0°, 15°, 30°, 45°, 57°, and 60° at a reaction temperature of 470 K. The <E_t> of $^{13}CO_2$ was then plotted as a function of the polar angle of CO_2 desorption along the [1$\bar{1}$0] direction, as shown in **Fig. 5.8(b)**. It was found that <E_t> decreases with increasing polar angle and is independent of reaction temperature. Decreases in mean translational energy at higher polar angles have also been reported for CO_2 desorption during CO oxidation reactions on Rh(111)[30-32] and Pt(111).[33] This decrease in <E_t> cannot be explained by the one- dimensional van Willigen model.[32-35] However, the angle dependence can be explained by considering Pauli repulsion and van der Waals interactions. With increasing desorption polar angle, CO_2 should interact with the Cu surface for longer times through Pauli repulsion and then by exerting van der Waals forces. These synergistic forces result in the transformation of the translational energy of CO_2 into internal energy because unequal electron densities distributed around carbon and two oxygen atoms in the molecular orbitals interact differently with the surface via Pauli repulsion and Van der Waals interactions. The importance of Van der Waals interactions in the final energy states of CO_2 desorbed from formate decomposition on Cu(110) was also shown by recent molecular dynamics simulations methods [40].

In summary, we found that $^{13}CO_2$ desorption during formate decomposition in the steady-state reaction of $H^{13}COOH$ with O_2 on Cu(110) is a thermal non-equilibrium process, in which the translational energy (as low as ~ 100 meV) of $^{13}CO_2$ is independent of surface temperature. DFT calculations of formate decomposition on Cu(110) reveal that CO_2 has been formed at the TS after cleavages of the Cu-O and C-H bonds of adsorbed formate. This suggests that the TS is cooled down because of the endothermic bond ruptures and that CO_2 and H_a/Cu(110) are thermally decoupled at the TS. The energy difference between TS and FS is thus expected to be converted to the internal energy (vibration, rotation and translation) of desorbing CO_2. It is also suggested that the internal energy conversion of desorbing CO_2 takes place via Pauli repulsion and Van der Waals forces [40]. These thermal non-equilibrium features support the proposed ER type mechanism of formate synthesis by Cu catalysts, which is an important elemental step in the synthesis of methanol by the hydrogenation of CO_2.

5.3.3 Conclusion

Under a steady-state reaction condition, even though the resident time of formate intermediate on the surface is quite short, angular distributions of CO_2 formed by the decomposition of formate from the oxidation of formic acid show sharp shapes, indicating that the CO_2 molecules receive strong repulsive forces along the surface normal direction. We also found that the translational temperature of desorbing molecules is independent on the surface temperature. It thus suggests that the desorbing CO_2 molecule is in thermal non-equilibrium with the surface temperature.

5.4 Summary

We thus summarized the results as following:

(1) By applying the AR-SSD measurement of the desorbing CO_2 from the steady-state reaction of $H^{13}COOH + O_2$ on Cu surfaces, we found that the angular distribution of desorbing CO_2 is along surface normal direction and is independent of surface temperature. In addition, by using TOF technique, we found that the translational energy of CO_2 is insensitive to the surface temperature. The translational temperature of CO_2 molecule decreases with the increasing of polar angle.

(2) By carrying out AR-TPD experiments of desorbing CO_2 from thermal decomposition of formate on Cu(111), Cu(110) and Cu(100) surfaces, we found that the shape of angular distributions are the same and sharp. These distributions are also along surface normal direction and insensitive to the Cu surface structure and the formate coverage.

On the basis of these results of AR-SSD and AR-TPD, we thus conclusively propose that the CO_2 molecule directly leaves H_a after C-H bond breaking in the formate decomposition with large translational energy toward surface normal direction due to the Pauli repulsion. The repulsive force would convert into the translational energy which at least the translational temperature of CO_2 has non-equilibrium with surface temperature. That is, CO_2 does not take adsorption, trapping or precursor states on the Cu surface during the reaction, which is supported by the identical and sharp angular distributions which are insensitive to the surface structure and surface temperature. From the view point of micro-reversibility of reaction, the conclusion, in turn, supports the ER-type mechanism for formate synthesis from the reaction between CO_2 molecule and hydrogen adatom on Cu surfaces proved by the molecular beam experiment.

Reference

[1] G. Ertl, Dynamics of reactions at surfaces, in: B. C. Gates, H. Knozinger (Eds.) Advances in Catalysis, Academic Press, 2000, pp. 69.
[2] A.M. Wodtke, D. Matsiev, D.J. Auerbach, Prog. Surf. Sci., 83 (2008) 167-214.
[3] J.C. Polanyi, Acc. Chem. Res., 5 (1972) 161-168.
[4] Y.T. Lee, Angew. Chem. Int. Ed., 26 (1987) 939-951.
[5] C.T. Rettner, D.J. Auerbach, J.C. Tully, A.W. Kleyn, J. Phys. Chem., 100 (1996) 13021-13033.
[6] M. C. Lin, G. Ertl, Annu. Rev. Phys. Chem., 37 (1996) 587-615.
[7] K.D. Rendulic, A. Winkler, Surf. Sci., 299–300 (1994) 261-276.
[8] J.N. Smith, W.L. Fite, J. Chem. Phys., 37 (1962) 898-904.
[9] J.C. Maxwell, Phil. Trans., 170 (1897) 231-256.
[10] I. Langmuir, Phys. Rev., 8 (1916) 149-176.
[11] P. Clausing, Annal. Phys., 396 (1930) 533-566.
[12] G. Comsa, J. Chem. Phys, 48 (1968) 3235-3240.
[13] W. Van Willigen, Phys. Lett. A, 28 (1968) 80-81.
[14] M.J. Murphy, J.F. Skelly, A. Hodgson, J. Chem. Phys, 109 (1998) 3619-3628.
[15] G. Comsa, R. David, Surf. Sci. Rep., 5 (1985) 145-198.
[16] T. Matsushima, Surf. Sci. Rep., 52 (2003) 1-62.
[17] T. Matsushima, K. Shobatake, J. Mole. Catal. A, 315 (2010) 135-147.
[18] T. Matsushima, Prog. Surf. Sci., 82 (2007) 435-477.
[19] T. Matsushima, Phys. Chem. Chem. Phys., 9 (2007) 3031-3042.
[20] H. Nishimura, T. Yatsu, T. Fujitani, T. Uchijima, J. Nakamura, J. Mole. Catal. A, 155 (2000) 3-11.
[21] M.D. Crapper, C.E. Riley, D.P. Woodruff, A. Puschmann, J. Haase, Surf. Sci., 171 (1986) 1-12.
[22] D.P. Woodruff, C.F. McConville, A.L.D. Kilcoyne, T. Lindner, J. Somers, M. Surman, G. Paolucci, A.M. Bradshaw, Surf. Sci., 201 (1988) 228-244.
[23] J. Somers, A.W. Robinson, T. Lindner, D. Ricken, A.M. Bradshaw, Phys. Rev. B, 40 (1989) 2053-2059.
[24] A. Sotiropoulos, P.K. Milligan, B.C.C. Cowie, M. Kadodwala, Surf. Sci., 444 (2000) 52-60.
[25] M. Bowker, E. Rowbotham, F.M. Leibsle, S. Haq, Surf. Sci., 349 (1996) 97-110.
[26] T. Fujitani, Y. Choi, M. Sano, Y. Kushida, J. Nakamura, J. Phys. Chem. B, 104 (2000) 1235-1240.
[27] D.H.S. Ying, J.M. Robert, J. Catal., 61 (1980) 48-56.
[28] Y. Yao, F. Zaera, Surf. Sci., 646 (2016) 37-44.
[29] G. Wang, Y. Morikawa, T. Matsumoto, J. Nakamura, J. Phys. Chem. B, 110 (2005) 9-11.
[30] P.A. Taylor, P.B. Rasmussen, C.V. Ovesen, P. Stoltze, I. Chorkendorff, Surf. Sci., 261 (1992) 191-206.
[31] J. Nakamura, Y. Kushida, Y. Choi, T. Uchijima, T. Fujitani, J. Vac. Sci. Technol. A, 15 (1997) 1568-1571.
[32] I. Nakamura, H. Nakano, T. Fujitani, T. Uchijima, J. Nakamura, J. Vac. Sci. Technol. A 17(4) (1999) 1592-1595.
[33] D. Kreikemeyer-Lorenzo, W. Unterberger, D.A. Duncan, M.K. Bradley, T.J. Lerotholi, J. Robinson, D.P. Woodruff, Phys. Rev. Lett., 107 (2011) 046102.
[34] F.C. Henn, J.A. Rodriguez, C.T. Campbell, Surf. Sci., 236 (1990) 282-312.
[35] H. Nakano, I. Nakamura, T. Fujitani, J. Nakamura, J. Phys. Chem. B, 105 (2001) 1355-1365.
[36] H.J. Robota, W. Vielhaber, M.C. Lin, J. Segner, G. Ertl, Surf. Sci., 155 (1985) 101-120.
[37] H. Horino, I. Rzeźnicka, A. Kokalj, I. Kobal, Y. Ohno, A. Hiratsuka, T. Matsushima, J. Vac. Sci. Technol.

A, 20 (2002) 1592-1596.
[38] T. Schiros, K.J. Andersson, L.G.M. Pettersson, A. Nilsson, H. Ogasawara, J. Electron Spectrosc. Relat. Phenom., 177 (2010) 85-98.
[39] Y. Seimiya, G. Cao, Y. Ohno, T. Yamanaka, T. Matsushima, K. Jacobi, Surf. Sci., 415 (1998) L988-L992.
[40] Y.H. F. Muttaqien, H. Oshima, I. Hamada, and Y. Morikawa, in preparation, (2017) 2016, Osaka University.

Chapter 6

Density functional theory calculations

6.1 Introduction

This experimental work of supersonic molecular beam and angle-resolved analysis illustrate the mechanism and dynamics of formate synthesis on Cu surfaces. The kinetics studies of formate synthesis on Cu catalysts have also provided some kinetic parameters such as activation barriers, turn over frequencies (TOF) and tried to elucidate the reaction process and mechanism as mentioned in Chapter 1 and Chapter 2. We also have proposed that the local structure is same at different Cu surfaces in the formate synthesis and formate decomposition based on the feature we had observed of surface structure insensitivity. Complementary density functional theory (DFT) calculations of formate synthesis on Cu surface should be performed and expected to support these proposals.

On the other hand, the complement of the theoretical calculations also has been conducted to investigate the reactivity of formate on Cu catalysts, as summarized in **Table 6.1**. Even though most of these calculations are related to methanol synthesis, the formate formation by the direct reaction between the gas phase CO_2 and H adatom has been proposed to proceed via ER-type mechanism. However, there are still lacks of detailed descriptions for the reaction process of formate synthesis.

In this chapter, to examine the details of the ER-type mechanism for the formation of formate on Cu surfaces, we carried out density functional theory (DFT) calculations and show the details to the reaction process of formate formation and formate decomposition on Cu surface.

$$HCOO_a \rightleftharpoons CO_2 + H_a$$

It is well-known that there are two types of formate on Cu surfaces: monodentate formate and bidentate formate [1-4]. In the molecular beam experiments, results support the conclusion that the vibrational energy of CO_2 molecule is much preference than the translational energy to form formate on Cu surfaces. That is, bending structure of CO_2 is quite essential to form formate because the protrude carbon atom in CO_2 molecule binds with H adatom processes through lowest energy pathway on the potential energy surface of the surface reaction. Therefore, the C-H bond formation should be the first step of the reaction. The angle-resolve analysis also supports to this assumption and the formate decomposition proceeds via a thermal non-equilibrium. Before bidentate formate is finally stabilized, monodentate formate should be an intermediate which can be treated as the direct formate product as the result from ER type reaction process.

We have reported the energy diagram for formate synthesis from CO_2 and H_2, in which CO_2 is converted to bidentate formate via monodentate formate [5]. The adsorption energies of bidentate formate and monodentate formate on Cu(110) were calculated as -1.10 eV and -0.32 eV with respect to the energy for $CO_2 + H_a$, respectively. That is, bidentate formate is much more stable compared to monodentate formate. The energy diagram well explained the experimentally measured activation energies and the structure dependence for formate synthesis/decomposition so that we believe the decomposition mechanism that bidentate formate is once transformed into monodentate formate followed by the decomposition into CO_2 and H_a. We thus consider that monodentate formate is an important intermediate to determine the dynamics of formate decomposition. Firstly, therefore, we shed light on the structural changes near the transition state (TS) of monodentate formate decomposition on Cu(110) calculated by density functional theory (DFT).

Table 6.1 Summary of DFT calculation methods for formate synthesis from CO_2 hydrogenation over Cu catalysts ($CO_{2,g} + H_a \rightarrow HCOO_a$) via ER-type mechanism

researcher	surface	mono-formate E_a (eV)	bi-formate E_a (eV)	method	year/ref.
Wang et al.	Cu(110)	0.18	1.20	DFT-GGA[a]	2006/[1]
	Cu(100)	0.16	0.93		
	Cu(111)	0.14	0.69		
Mavrikakis et al.	Cu(111)	0.28	1.02	DFT-GGA	2008/[2]
Mei et al.	Cu(111)	0.19	0.57	DFT-DSPM[b]	2008/[3]
Yang et al.	Cu nanoparticles (Cu_{29})	-	1.23	DFT-(DMol code)	2010/[4]
Mei et al.	Cu(111)	0.62	0.70	DFT-GGA	2011/[5]
Guo et al.	Cu(111)	0.60	1.15	DFT-VASP[c]	2011/[6]

[a]**GGA**: Generalized gradient approximation; [b]**DSPM**: Dimer saddle point search method;
[c]**VASP**: Vienna *ab initio* simulation package.

6.2 Calculation modes and methods

All the calculations were performed using the plane-wave DFT (VASP code) [6, 7]. The exchange-correlation energy and potential are described by the generalized gradient approximation (PW91) [8]. The electron-ion interaction is described by the projector-augmented wave (PAW) scheme [9, 10], and the electronic wave functions are expanded by plane waves up to a kinetic energy of 400 eV. A periodical three-layer slab is used with a ~ 10 Å vacuum region between slabs. The calculated models are chosen as 3×2 unit cells with the corresponding coverage of 1/6 ML. During the calculation, the first layer and the adsorbed species were allowed to relax. The surface Brillouin zone was sampled using a 4×4×1 Monkhorst-Pack mesh [11]. The minimization of the reaction pathways and the search for the TSs were performed with the climbing-image nudged elastic band method (CI-NEB) [12, 13]. During the calculation, the first layer and the adsorbed species were allowed to relax until the force acted on each atom was smaller than 0.03 eV/Å.

6.3 Results and discussions

Figure 6.1(a) shows the energy diagram of a relative energy change starting from monodentate formate to the product of CO_2 and H_a/Cu(110) surface as a function of the reaction coordinate. The energy diagram profile starts from a monodentate-formate/Cu(110) surface as an initial state (IS). The barrier for the

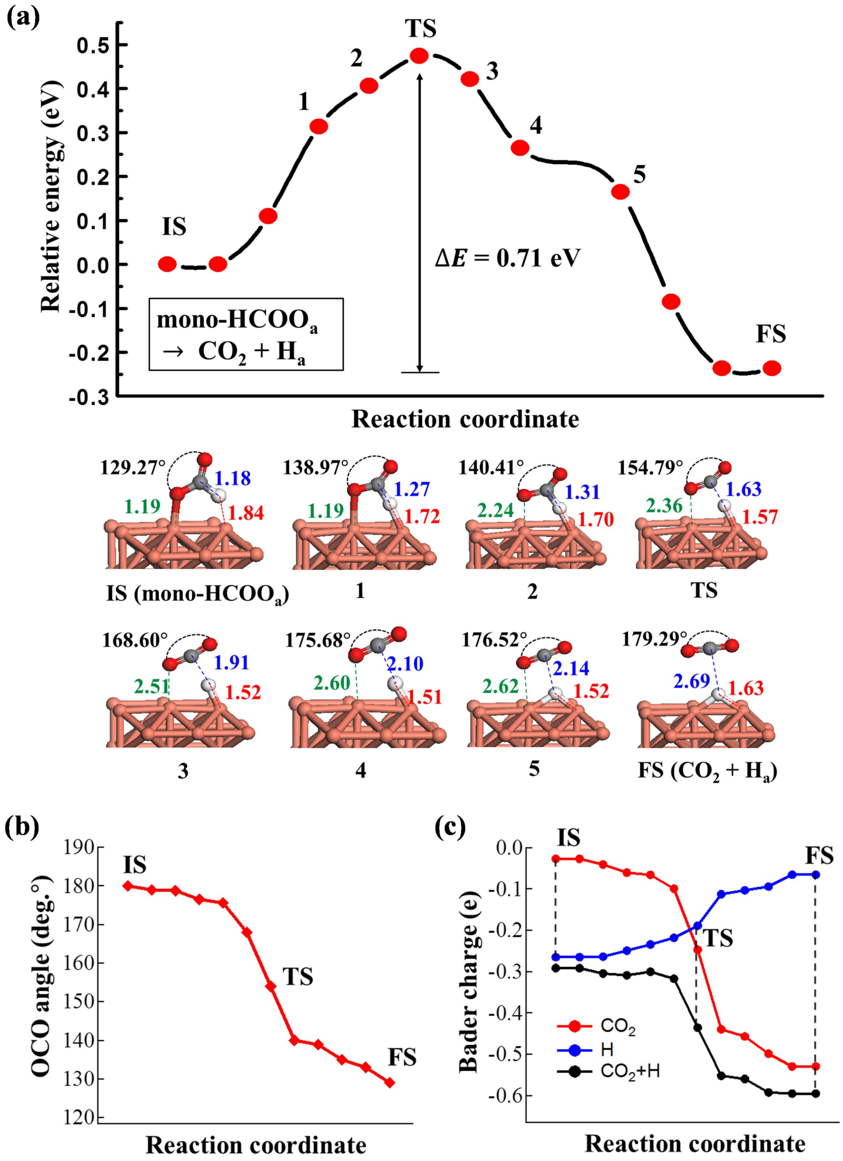

Figure 6.1 The conversion process of CO_2 to formate on Cu(110) calculated by density functional theory (DFT). (**a**) Relative energy as a function of the reaction coordinate for formate synthesis upon CO_2 approaching an adsorbed H atom on Cu(110). The insets provide side views of the system with the bond length (Å) and the O-C-O angle (deg°.). The reference zero of the energy scale corresponds to the energy of CO2 and atomic H adsorption state on Cu(110). (**b**) The O-C-O angle (deg°.) as a function of the reaction coordinate. (**c**) Bader charge analysis. IS, TS, and FS denote the initial state, transition state, and final state, respectively.

decomposition of formate is calculated to be 0.5 eV, during which the monodentate formate is rotated to form a Cu-H bond and is followed by the successive cleavage of the Cu-O and C-H bonds of the formate. The unique point is that nascent CO_2 has already been formed at the TS after the cleavage of two bonds. The structural changes (TS → 3 → 4 → 5 → FS) in insets of **Fig. 6.1** provide useful information to discuss the dynamics of formate decomposition. From the TS to the FS, the O-C-O angle changes as 154.79° → 168.60° → 175.68° → 176.52° → 179.29°. The angle of 154.79° corresponds to a highly excited bending mode, which is 0.44 eV higher than CO_2 with the angle of 180°[14]. The angle changes thus suggest that the energy gain of 0.71 eV from the TS to the FS in Fig. 1 is mainly transformed into the vibrational energy of CO_2. It is also noted that the distance between CO_2 and the Cu surface changes as 2.10 Å → 2.14 Å → 2.69 Å for the structures 4 → 5 → FS without significant changes in CO_2 and H_a/Cu, while the energy difference between 4 and FS is 0.5 eV. This energy difference is thus partly ascribed to the Pauli repulsion between CO_2 and the Cu surface. It is suggested that the desorbing CO_2 molecule receives some repulsive forces, leading to an increase in translational energy and/or rotational energy of CO_2. Accordingly, the structural changes from the TS to the FS suggest that the energy gain of 0.71 eV is converted to the internal energy (vibration, rotation and translation) of CO_2.

From the viewpoint of formate synthesis, the energetic diagram also clearly shows that CO_2 directly attacks a surface hydrogen adatom, thereby forming formate via the ER-type mechanism. Upon the approach of CO_2 to the H_a/Cu(110) surface, the relative energy increases by 0.4–0.5 eV without any significant bending of the O-C-O angle (176.5°). This can be ascribed to the Pauli repulsion between CO_2 and the surface (the concept of Pauli repulsion is explained in the Appendix). The repulsion can be overcome by the translational energy of CO_2. The O-C-O bond angle then starts to bend from 180° to 155° before the TS (**Fig. 6.1(b)**). This suggests that, in terms of the O-C-O bending mode, the vibrational energy is also required for the synthesis of formate. By bending the O-C-O structure, the lowest unoccupied molecular orbital (LUMO) of CO_2 molecule decreases in energy level ($\Delta E < 0.5$eV) [15]. Therefore, charge transfer from H_a/Cu(110) to CO_2 occurs after the O-C-O bending (**Fig. 6.1(c)**), which is followed by the formation of the C-H bond with sp^2 configuration. The activation barrier of the formate synthesis is calculated to be 0.71 eV, which is comparable to that measured by high-pressure experiments of formate synthesis from CO_2 and H_2 on Cu(110) (i.e. 0.62 eV) [16]. The translational energy (E_T) of CO_2 used in molecular beam experiments are much larger than 0.71 eV, which is probably due to the loss of energy by the excitation of phonons and electron-hole pairs during the collision of CO_2 with the surface; in this way, the energy that remains available to the reaction becomes smaller.

6.4 Conclusion

According to the calculation results, the CO_2 directly attacks the hydrogen adatom to form formate without trapping on the surface. This is regarded as an ER-type mechanism. The reaction barrier is comparable to the experimental results as 0.73 eV. The translational energy and vibrational energy are required to overcome Pauli repulsion in terms of reaction barrier. In the formate decomposition, the reaction energy released from the reaction may transfer into the CO_2 molecules, and also obtain translational energy in terms of Pauli repulsion. These calculation results are consistent with the experimental results.

These thermal non-equilibrium features support the proposed ER type mechanism of formate synthesis by Cu catalysts, which is an important elemental step in the synthesis of methanol by the hydrogenation of CO_2.

❊❊❊ Chapter 6 ❊❊❊

References

[1] C.A.M. Yong Yang, R.S.Disselkamp, Ja-Hun Kwak, C.H.F. Peden, C.T.Campbell, J. Phys. Chem. C, , 114 (2010) 17205-17211.

[2] G.J. Millar, C.H. Rochester, K.C. Waugh, J. Chem. Soc. Faraday Trans., 87 (1991) 1491-1496.

[3] M. Bowker, S. Haq, R. Holroyd, P.M. Parlett, S. Poulston, N. Richardson, J. Chem. Soc., Faraday Trans., 92 (1996) 4683-4686.

[4] E. Iglesia, J. Phys. Chem., 90 (1986) 5272-5274.

[5] G. Wang, Y. Morikawa, T. Matsumoto, J. Nakamura, J. Phys. Chem. B, 110 (2006) 9-11.

[6] G. Kresse, J. Furthmüller, Comput. Mater. Sci., 6 (1996) 15-50.

[7] G. Kresse, J. Hafner, Phys. Rev. B, 49 (1994) 14251-14269.

[8] J.P. Perdew, J.A. Chevary, S.H. Vosko, K.A. Jackson, M.R. Pederson, D.J. Singh, C. Fiolhais, Phys. Rev. B, 46 (1992) 6671-6687.

[9] P.E. Blöchl, Phys. Rev. B, 50 (1994) 17953-17979.

[10] G. Kresse, D. Joubert, Phys.Rev. B, 59 (1999) 1758-1775.

[11] H.J. Monkhorst, J.D. Pack, Phys. Rev. B, 13 (1976) 5188-5192.

[12] G. Henkelman, H. Jónsson, J. Chem. Phys., 113 (2000) 9978-9985.

[13] G. Henkelman, B.P. Uberuaga, H. Jónsson, J. Chem. Phys., 113 (2000) 9901-9904.

[14] B. Mondal, J. Song, F. Neese, S. Ye, Curr. Opin. Chem. Biol., 25 (2015) 103-109.

[15] H.J. Freund, M.W. Roberts, Surf. Sci. Rep., 25 (1996) 225-273.

[16] H. Nakano, I. Nakamura, T. Fujitani, J. Nakamura, J. Phys. Chem. B, 105 (2001) 1355-1365.

Chapter 7

Summary and perspective

7.1 Summary

A combination of experimental and theoretical studies has been carried out to investigate the mechanism and dynamics of formate synthesis from CO_2 hydrogenation on Cu catalysts. We have discovered that a CO_2 molecule may directly react with hydrogen on Cu catalysts via an ER-type mechanism under thermal non-equilibrium. **Figure 7.1** schematically illustrates the conversion process between CO_2 and formate on Cu surfaces.

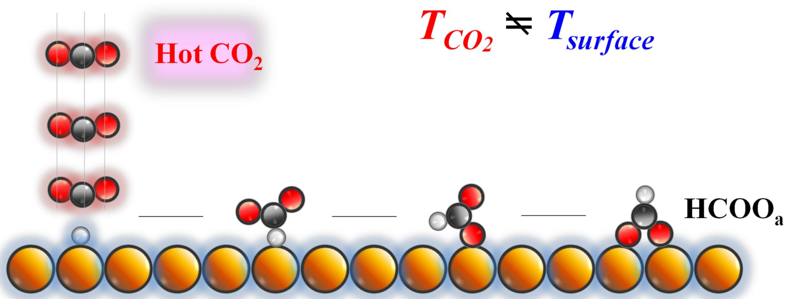

Figure 7.1 Schematic of reaction conversion between CO_2 and formate ($HCOO_a$) on Cu surfaces

(1) Dynamics of formate synthesis on Cu catalysts studied by supersonic molecular beam

In the real catalytic reaction conditions, high pressures of reactant gases (CO_2/H_2) mixture and elevated catalyst temperatures are necessary for formate synthesis on Cu surfaces [1, 2]. In addition, it has been reported that no reaction occurs between the CO_2 molecules and H_2 molecules co-adsorb on the Cu surface at ~95 K [3]. In our study on the dynamics of formate synthesis, the translational energy and vibrational energy of CO_2 should be the prerequisites for the formate formation on Cu catalysts. We proposed that the translational energy of CO_2 is used to overcome the Pauli repulsion (to increase the potential energy) to approach to the H_a adatom on Cu, while vibrational energy is used to change the *sp* linear molecule structure to the sp^2 structure. Therefore, a threshold nozzle temperature ($T_{vib.}$) as ~ 770 K for CO_2 was measured and the translational energy of 1.23 eV is comparable to the reaction barrier as 0.75 ~ 1.05 eV [4, 5]. Moreover, the formation rate of formate is independent on the surface structure and surface temperature. The results clearly indicate that CO_2 should directly react with the H_a adatom without trapping or via precursor state on the surface. Therefore, the formate synthesis from CO_2 hydrogenation is in a thermal non-equilibrium process.

(2) Dynamics of formate decomposition on Cu catalysts studied by angle-resolved analysis

From the analysis of dynamics of the reverse reaction-formate decomposition, it was suggested that the desorbing CO_2 molecule from formate decomposition receives a repulsive force exerted from Cu surface and CO_2 thus has high translational temperature independent of surface temperature. On the basis of micro-reversibility of reaction, the desorbing product of CO_2 from formate decomposition should be hyper-thermal and be in non-equilibrium with surface. Firstly, we observe the identical sharp angular distributions of the desorbing CO_2 product along surface normal direction, indicating that the CO_2 obtains strong repulsive force from surface. This repulsion is needed for CO_2, in turn, to overcome to form formate on the surface in the formate synthesis. Secondly, we found that the translational temperature of CO_2 is independent of the surface temperature and the angular distributions are insensitive to the surface structure, which indicates that the CO_2 molecule, just before desorption or in the region of transition state, should have no contact with Cu surfaces. That is, the bidentate formate ($HCOO_a$) flips over the H moiety through monodentate formate followed by the CO_2 desorption after C-H breaking. For the formate synthesis, as a reverse process, it was suggested the CO_2 directly react with H atom to form C-H through mono-dentate followed by a more stable bidentate structure of formate, that is, the process is in an ER-type pathway.

(3) Density functional theory calculations

The theoretical calculations further give the detailed description for the ER-type reaction process. When the CO_2 molecule is close to the hydrogen (~1.91 Å), charge transfers from the H_a/Cu surface to CO_2 molecule. After the LUMO orbital of CO_2 accepts the charges and then the energy level decreases, leading to the formation of an active bending structure of CO_2. As a result, the formate is formed through the active molecule binding with H atom on the surface.

7.2 Perspective

As we mentioned above, the formate synthesis is an initial and essential step for the methanol synthesis. We have shown that the formate can be synthesized by increasing energy of CO_2, which is in thermal non-equilibrium with the Cu catalysts. Therefore, this reaction channel may be applicable to the methanol synthesis on Cu/ZnO-based catalysts at low temperatures (i.e. room temperature) by using the molecular beam system of CO_2. For example, the large amounts of hydrogen adatoms can be prepared by the H_2 dissociative adsorption on Pd doped Cu surface [6].

As schematically shown in **Fig. 7.2**, we proposed a Cu-Zn alloy catalytic model which is comparable to the industrial catalysts as we discussed in Chapter 1. For example, the real Cu/ZnO catalysts were found to have steps, terraces and Cu-Zn alloy as the active sites [7]. CO_2 may be converted into methanol by multistep hydrogenation under the catalytic synergy of Cu and ZnO as follows:

$$H_a + H_a \rightarrow H_2 \tag{1}$$

$$CO_2 + H_a \rightarrow HCOO_a \tag{2}$$

$$(Cu\text{-}Cu)\text{-}HCOO_a \rightarrow (Cu\text{-}Zn)\text{-}HCOO_a \tag{3}$$

$$HCOO_a + H_a \rightarrow H_2CO_{2,a} \tag{4}$$

$$H_2CO_{2,a} + H_a \rightarrow H_2COOH_a \tag{5}$$

$$H_2CO_{2,a} + 2H_a \rightarrow H_2CO_a + H_2O \tag{6}$$

$$H_2CO_a + H_a \rightarrow H_3CO_a \tag{7}$$

$$H_3CO_a + H_a \rightarrow H_3COH \tag{8}$$

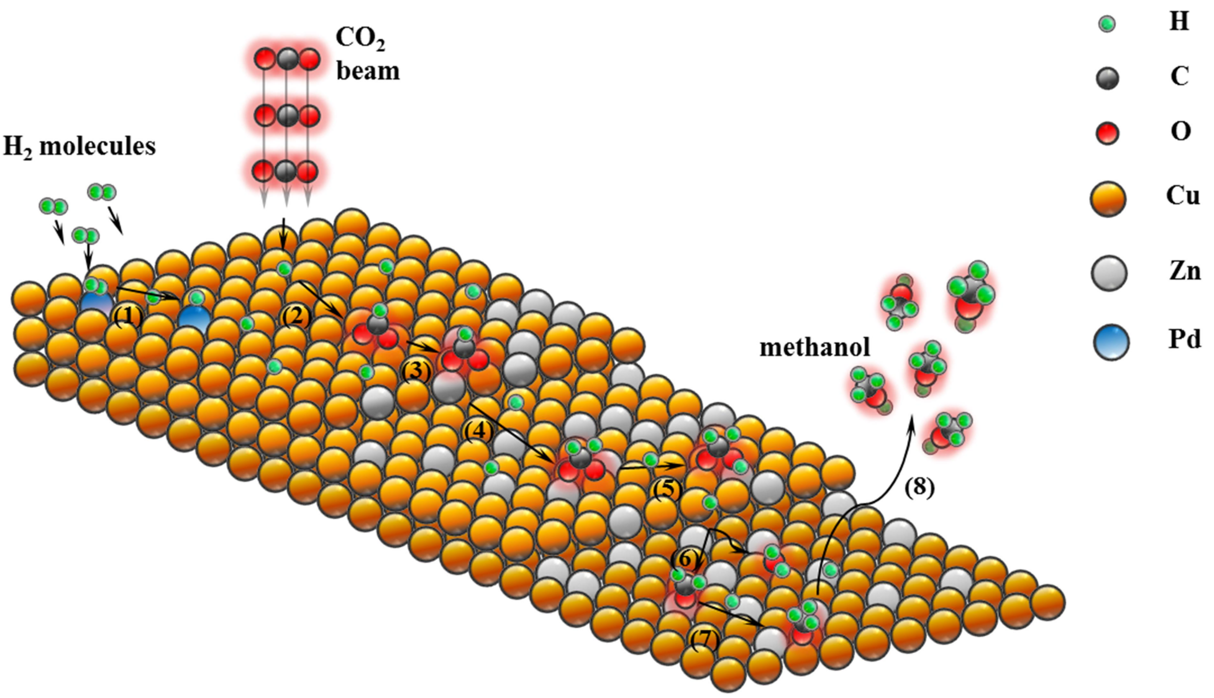

Figure 7.2 Schematic proposal of methanol (CH_3OH) synthesis over Palladium-doped CuZn-based catalyst by using molecular-beams system of CO_2 and H_2. This proposal is expected to activate CO_2 to synthesize methanol (CH_3OH) at room temperature.

where subscript *a* represents adsorption. Firstly, it has been found that the atomic palladium doped in Cu surface is very active for the dissociation of H_2 molecules [6], as shown in Step (1). Step (2) is formate synthesis on Cu catalysts by a hot CO_2 molecule colliding with hydrogen adatom via ER type mechanism, as reported in this thesis; step (3) is migration of formate from Cu site to Cu-Zn alloy site, where the migration is possible because the Cu-Zn-formate is much stable than the Cu-formate [8]. That is, the Cu-Zn bidentate formate binds to a Cu atom and neighboring Zn atom with two O atoms, respectively; step (4) to step (7) are the further hydrogenation of formate to methoxy (H_3CO_a) via the intermediates dioxymethylene ($H_2CO_{2,a}$), formaldehyde ($H_2CO_{2,a}$) et al. [9, 10]. However, the only observable intermediates are formate and methoxy on Cu/ZnO-based catalyst, except for ZrO_2-supported Cu catalysts [11]. The step (5) and step (6) should be the fast reactions with low reaction barriers. Step (8) is the methanol formation from the direct hydrogenation of methoxy [12, 13].

In the methanol synthesis from hydrogenation of CO_2, on the other hand, all the hydrogen sources in the reaction steps also could be supplied from atomic hydrogen beam or/and hydrogen molecular beam. The atomic hydrogen beam may hydrogenate the intermediates to form methanol. In the hydrogen molecular beam, there is no clear evidence but it may be expected that hot hydrogen atoms produced on Cu catalyst through splitting H_2 molecules using molecular beam technique [14]. These hot hydrogen atoms would diffuse over the surface of Cu/ZnO-based catalyst and encounter the adsorbed intermediates to continue the reaction process. Both of the hydrogen beams may supply the kinetic energy to hydrogen to overcome the reaction barrier, and accomplish the multistep of hydrogenation to form the final methanol product. On the other hand, the Cu/ZnO-based catalysts could be maintained at a low temperature, such as at room temperature. At least, the methanol production was found to be promoted by the excited CO_2 molecules [15].

On the other hand, the Haber-Bosch (HB) process for ammonia synthesis from N_2 reacting with hydrogen over Fe-based catalysts [16-18] and the Fischer-Tropsch (FT) process for CO hydrogenation [19, 20] on the transitional metal catalysts are greatly dependent of catalysts temperature. It is thus large energy is required to maintain the high temperature of catalysts for the reactions. Contrastively, for methanol synthesis, CO_2 molecules could be excited by the microwave with optimized energy and terrestrial heat. The hydrogen source could be recycled from by-products of the oil company and from the catalytic splitting of water by solar energy. Therefore, this discovered channel in CO_2 hydrogenation, which does not require the heating of catalysts, is expected to open up novel industrial pathways of effective converting CO_2 into useful chemicals and fuels, such as methanol.

Reference

[1] H. Nishimura, T. Yatsu, T. Fujitani, T. Uchijima, J. Nakamura, J. Mole. Catal. A, 155 (2000) 3-11.

[2] H. Nakano, I. Nakamura, T. Fujitani, J. Nakamura, J. Phys. Chem. B, 105 (2001) 1355-1365.

[3] K.H. Ernst, D. Schlatterbeck, K. Christmann, Phys. Chem. Chem. Phys., 1 (1999) 4105-4112.

[4] Y. Yang, J. Evans, J.A. Rodriguez, M.G. White, P. Liu, Phys.Chem. Chem. Phys., 12 (2010) 9909-9917.

[5] G. Wang, Y. Morikawa, T. Matsumoto, J. Nakamura, J. Phys. Chem. B, 110 (2005) 9-11.

[6] G. Kyriakou, M.B. Boucher, A.D. Jewell, E.A. Lewis, T.J. Lawton, A.E. Baber, H.L. Tierney, M. Flytzani-Stephanopoulos, E.C.H. Sykes, Science, 335 (2012) 1209-1212.

[7] M. Behrens, F. Studt, I. Kasatkin, S. Kühl, M. Hävecker, F. Abild-Pedersen, S. Zander, F. Girgsdies, P. Kurr, B.-L. Kniep, M. Tovar, R.W. Fischer, J.K. Nørskov, R. Schlögl, Science, 336 (2012) 893-897.

[8] T. Fujitani, T. Matsuda, Y. Kushida, S. Ogihara, T. Uchijima, J. Nakamura, Catal Lett, 49 (1997) 175-179.

[9] G.C. Chinchen, K.C. Waugh, J. Catal., 97 (1986) 280-283.

[10] G.C. Chinchen, K.C. Waugh, D.A. Whan, Appl. Catal., 25 (1986) 101-107.

[11] I.A. Fisher, A.T. Bell, J. Catal., 172 (1997) 222-237.

[12] J. Nakamura, Y. Choi, T. Fujitani, Top. Catal., 22 (2003) 277-285.

[13] L.C. Grabow, M. Mavrikakis, ACS Catal., 1 (2011) 365-384.

[14] C.T. Rettner, D.J. Auerbach, Phys. Rev. Lett., 74 (1995) 4551-4554.

[15] G.C. Chinchen, P.J. Denny, D.G. Parker, M.S. Spencer, D.A. Whan, Appl. Catal., 30 (1987) 333-338.

[16] F. Bozso, G. Ertl, M. Grunze, M. Weiss, J. Catal., 49 (1977) 18-41.

[17] F. Bozso, G. Ertl, M. Weiss, J. Catal., 50 (1977) 519-529.

[18] M. Kitano, S. Kanbara, Y. Inoue, N. Kuganathan, P.V. Sushko, T. Yokoyama, M. Hara, H. Hosono, Nat. Commun., 6 (2015).

[19] X.C. Guo, D.A. King, Chapter 4 - Coadsorption of Carbon Monoxide and Hydrogen on Metal Surfaces, in: K. D.A, W. D.P (Eds.) Chem. Phys. Solid Surf., Elsevier, 1993, pp. 113-155.

[20] W.-Y. Yu, G.M. Mullen, C.B. Mullins, J. Phys. Chem. C, 118 (2014) 2129-2137.

Appendix

Contents

⁂ Appendix ⁂

1. Supplementary text

Pauli repulsion

The Pauli principle states that only one electron can occupy each fully-specified quantum orbital. Generally, when a molecule first approaches a metal surface, in the long distance there is an attractive interaction ascribed from Van der Waals dispersion force. After at a distance about 3 Å the molecule may interact with the surface chemically. When the electronic wave functions of the molecule and surface begin to overlap, they must orthogonalize to each other to prevent more than two electrons being in the same energy level. For filled levels, this introduces an energy cost, giving a repulsive force in terms of Pauli repulsion. As shown in **Fig. S1**, the classic picture used to illustrate the possible adsorbate-surface interactions that govern chemisorption on a metal to unoccupied metal surface orbitals, the back donation of electrons from the metal into the lowest energy anti-bonding orbital of the adsorbate, and the Pauli repulsion due to the interaction between filled metal surface orbitals at the top of the valence band and the filled molecular orbitals of the adsorbate.

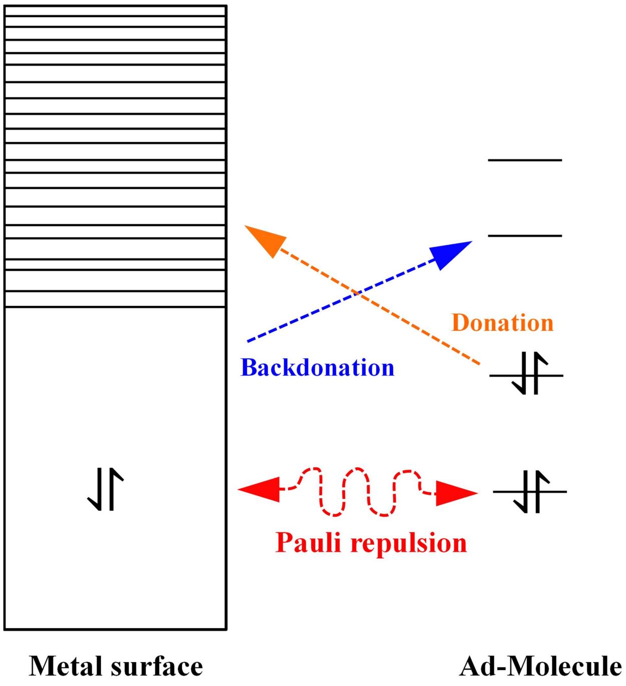

Figure S1.1 Fundamental interactions between the frontier orbitals of an adsorbate and a metal surface band structure that occur upon chemisorption. Redraw from ref. 1.

The Pauli repulsion is dependent on the electronic structure of molecule and surface. For example, we may propose that when a CO_2 molecule approaches a H_a/Cu surface, the interaction between the delocalized metal s-states that spill out into the vacuum region and the molecular π_u orbitals gives Pauli repulsion, which is only overcome when CO_2 molecule own enough translational energy to binding with a H adatom. This gives a barrier about 0.73 eV to the formation of formate [2]. In contrast, for metals with partially filled d-bands, like Nickel, the Pauli repulsion would be reduced, resulting in lower reaction barrier to formate formation reaction barrier as 0.43 eV [3]. On the other hand, Researches had taken the H_2 interacts with metal surface for example to investigate the function of d-states in Pauli repulsion. Considering the role of the d-states either in terms of direct hybridization between the molecular states and the *d*-states, or as providing an outlet for s-electrons, which can transfer at no energy cost into the more localized d-states, thus removing their contributions to the Pauli repulsion [4-6].

The Pauli repulsive principle forbids that the charge clouds of two electrons showing the same quantum numbers can have some significant overlap. On the other hand, an overlap of the charge clouds of electrons can cause an insufficient screening of the nuclear charge, leading to an ionic repulsive force in terms of Coulomb repulsion. Normally this electrostatic force existing in interatoms or internuclears are yielded at a distance shorter than typical bond length [7]. Based on this, we can propose that the Coulomb repulsion thus plays a minor role in the interaction between the CO_2 and Cu surface. More specific details should be clarified by theoretical calculations.

2. Large supersonic molecular beam (LMB) experiments

2.1 methods

2.1.1 CO_2 Beam spot area calculation

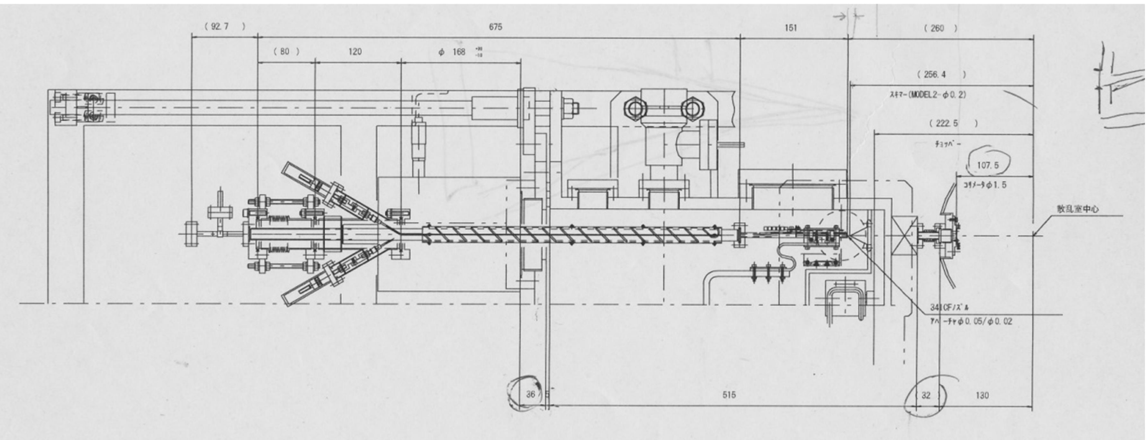

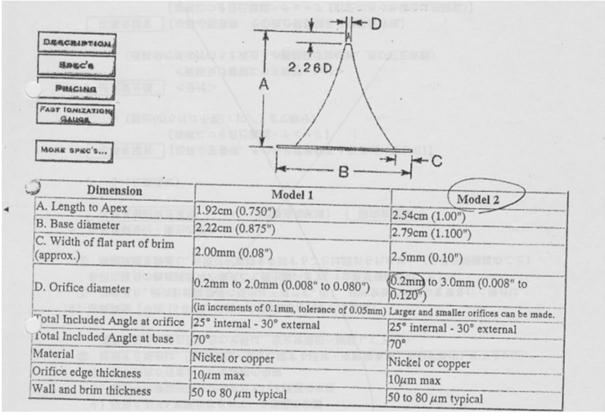

Dimension	Model 1	Model 2
A. Length to Apex	1.92cm (0.750")	2.54cm (1.00")
B. Base diameter	2.22cm (0.875")	2.79cm (1.100")
C. Width of flat part of brim (approx.)	2.00mm (0.08")	2.5mm (0.10")
D. Orifice diameter	0.2mm to 2.0mm (0.008" to 0.080")	0.2mm to 3.0mm (0.008" to 0.120")
	(in increments of 0.1mm, tolerance of 0.05mm)	Larger and smaller orifices can be made.
Total Included Angle at orifice	25° internal - 30° external	25° internal - 30° external
Total Included Angle at base	70°	70°
Material	Nickel or copper	Nickel or copper
Orifice edge thickness	10μm max	10μm max
Wall and brim thickness	50 to 80 μm typical	50 to 80 μm typical

Figure S2.1 Original parameters of apparatus of the apparatus and skimmers used for the calculation of beam spot area on Cu single crystal surface.

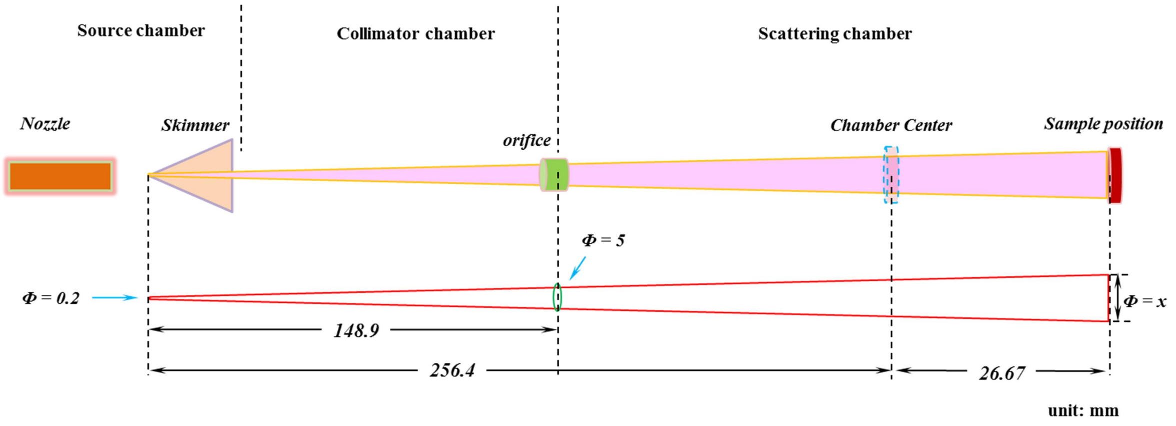

Figure S2.2 Schematic of beam spot area calculation

From the schematic, the diameter of beam spot x :

$$\frac{(5-0.2)}{148.9}=\frac{(x-0.2)/2}{(256.4+26.67)}$$

$$x = 9.5\,mm$$

The diameter of Cu sample is 10 mm, the ratio factor of two areas thus is considered as:

$$\frac{S_{beam}}{S_{sample}}=\frac{\pi(9.5/2)^2}{\pi(10/2)^2}=0.9$$

2.1.2 Calculation of Cryo-pump pumping speed

(1) Cryo-pump off

Background pressure $P_{sc0} = 2.64\times10^{-9}$ torr,
10% CO_2 (in He) beam irradiation at $T_{nozzle} = 1000$ K, then
$P_{so} = 7.82\times10^{-3}$ Pa, $P_{pipe} = 0.091$ MP, $P_{sc} = 1.60\times10^{-8}$ torr
So,

$$\Delta P_{off} = 1.60\times10^{-8}\text{ torr} - 2.64\times10^{-9}\text{ torr} = 1.336\times10^{-8}\text{ torr}$$

$$\Delta P_{off} = f_{CO_2}\Delta P_{CO_2} + f_{He}\Delta P_{He}$$

$$= 1.42\times\frac{Q_{CO_2}}{480\text{dm}^3/\text{sec}} + 0.18\times\frac{Q_{He}}{520\text{dm}^3/\text{sec}}$$

$$= 1.42\times\frac{Q_{CO_2}}{480\text{dm}^3/\text{sec}} + 0.18\times\frac{9Q_{CO_2}}{520\text{dm}^3/\text{sec}}$$

$$\therefore\ Q_{CO_2} = \Delta P(\text{torr})\times165\ (\text{dm}^3/\text{sec})$$

$$= 1.336\times10^{-8}\text{ torr}\times165\ (\text{dm}^3/\text{sec}) = 2.204\times10^{-6}\text{ torr dm}^3/\text{sec}$$

(2) Cryo-pump on

Background pressure $P_{sc0} = 3.23\times10^{-10}$ torr.
10% CO_2 (in He) beam irradiation at $T_{nozzle} = 1000$ K,
$P_{so} = 7.89\times10^{-3}$ Pa, $P_{pipe} = 0.091$ MP, $P_{sc} = 3.80\times10^{-9}$ torr
So

$$\Delta P_{on} = 3.80\times10^{-9}\text{ torr} - 3.23\times10^{-10}\text{ torr} = 3.477\times10^{-9}\text{ torr}$$

If the cryo-pump pumping speed is x, then

$$\Delta P = \Delta P_{off} - \Delta P_{on} = 1.336\times10^{-8}\text{ torr} - 3.477\times10^{-9}\text{ torr} = 9.98\times10^{-9}\text{ torr}$$

$$= 1.42\times\frac{Q_{CO_2}}{(480+x)\text{dm}^3/\text{sec}} + 0.18\times\frac{9Q_{CO_2}}{520\text{dm}^3/\text{sec}}$$

$$\because\ Q_{CO_2} = 2.204\times10^{-6}\text{ torr dm}^3/\text{sec}$$

$$\therefore\ x = 525\text{ dm}^3/\text{sec}$$

❊❊❊ Appendix ❊❊❊

2.1.3 CO_2 beam (diluted in He) flux calculation

The balance gas pressure in reaction chamber ΔP (torr),

$$\Delta P = Q/S \qquad (1)$$

where S (dm^3/sec) is pumping speed, and Q (torr·dm^3/sec) is the beam flux.
Therefore, the partial pressure of He and CO_2,

$$\Delta P_{CO_2} = \frac{Q_{CO_2}}{(480+525)dm^3/sec} = \frac{Q_{CO_2}}{1005dm^3/sec}, \quad \Delta P_{He} = \frac{Q_{He}}{520dm^3/sec} \qquad (2)$$

respectively, where pumping speed of CO_2 is 1005 dm^3/sec, He is 520 dm^3/sec.

The ionization factor of B.A gauge for CO_2 and He molecules $f_{CO_2} = 1.42$, and $f_{He} = 0.18$, thus

$$\Delta P = f_{CO_2}\Delta P_{CO_2} + f_{He}\Delta P_{He} = 1.42\times\frac{Q_{CO_2}}{1005dm^3/sec} + 0.18\times\frac{Q_{He}}{520dm^3/sec}$$

For 1% CO_2 (in He) beam, $Q_{He} = (99/1)Q_{CO2}$

$$Q_{CO_2} = \Delta P / (1.42/1005+0.18\times(99/1)/520)$$

$$= \Delta P /(0.001413 + 0.03427) = \Delta P /0.03568$$

$$Q_{CO_2} = 28.0\times \Delta P \text{ (torr·dm}^3\text{/sec)}$$

For example, 1% CO_2 (in He) beam irradiation at $T_{nozzle} = 1000$ K,
Background pressure $P_{sc0} = 3.2\times10^{-10}$ torr.

So $\Delta P = 3.0\times10^{-7}$ torr – 3.2×10^{-10} torr = 3×10^{-7} Torr
Therefore,

$$Q_{CO_2} = 28\times10^{-3}\ (m^3/sec.)\ \times3\times10^{-7}\ (Torr)\ \times133.3(N/m^2\bullet Torr)\times6.02\times10^{23}\ (mol^{-1})$$

$$/(8.31(N\ m/mol\ K)\ \times\ 300(K))$$

$$= 2.7\ \times\ 10^{14}$$

It is notable that 300 K is the CO_2 gas temperature in reaction chamber.
Cu(111) is 1.76×10^{15} /cm^2, the diameter of Cu sample is 10 mm,

Beam spot area on Cu(111) surface is $0.9\times \pi(1/2)^2 = 0.7$ cm^2.

So on Cu(111), Cu atoms are 1.76×10^{15} /cm^2 × 0.7 cm^2 = 1.23×10^{15}
Therefore, the CO_2 beam flux:
$2.7\times10^{14}/(1.23\times10^{15})$= 0.2195 CO_2 molecules/(Cu atom · s)

❊❊❊ Appendix ❊❊❊

For 5% CO_2 (in He) beam, $Q_{He} = (95/5)Q_{CO2}$

$$Q_{CO_2} = \Delta P / (1.42/1005+0.18\times(95/5)/520) = \Delta P /(0.001413+0.006577)$$

$$= \Delta P /0.008$$

$$Q_{CO_2} = 125 \times \Delta P \text{ (torr dm}^3\text{/sec)}$$

For example, 5% CO_2 (in He) beam irradiation at $T_{nozzle} = 1050$ K,
Background pressure $P_{sc0} = 3.2\times10^{-10}$ torr.

So $\Delta P = 9.0\times10^{-8}$ torr – 3.2×10^{-10} torr = 8.97×10^{-8} torr

Therefore, $Q_{CO_2} = 125\times10^{-3}$ (m^3/sec.) $\times 8.97\times10^{-8}$ (Torr) $\times 133.3$(N/m^2 Torr) $\times 6.02\times10^{23}$ (mol^{-1})/(8.31(N m/mol K) $\times 300$(K)) = 3.6×10^{14}

It is notable that 300 K is the CO_2 gas temperature in reaction chamber.
Cu(111) is 1.76×10^{15} /cm^2, the diameter of Cu sample is 10 mm,

Beam spot area on Cu(111) surface is $0.9\times \pi(1/2)^2 = 0.7$ cm^2.

So on Cu(111), Cu atoms are 1.76×10^{15} /cm^2 $\times$ 0.7 $cm^2 = 1.23\times10^{15}$
So, the CO_2 beam flux:
$3.61\times10^{14}/(1.23\times10^{15}) = 0.2935$ molecules/(Cu atom · s)

For 7% CO_2 (in He) beam, $Q_{He} = (93/7)Q_{CO2}$

$$Q_{CO_2} = \Delta P / (1.42/1005+0.18\times(93/7)/520) = \Delta P /(0.001413+0.0046) = \Delta P /0.006$$

$$Q_{CO_2} = 166.67\times \Delta P \text{ (torr dm}^3\text{/sec)}$$

For example, 7% CO_2 (in He) beam irradiation at $T_{nozzle} = 1000$ K,
Background pressure $P_{sc0} = 3.2\times10^{-10}$ torr.

So $\Delta P = 6.8\times10^{-8}$ torr – 3.2×10^{-10} torr = 6.78×10^{-8} torr
Therefore,

$Q_{CO_2} = 166.7\times10^{-3}$ (m^3/sec.) $\times 6.78\times10^{-8}$ (Torr) $\times 133.3$(N/m^2·Torr) $\times 6.02\times10^{23}$ (mol^{-1})/(8.31(N m/mol K) $\times 300$(K)) = 3.64×10^{14}

It is notable that 300 K is the CO_2 gas temperature in reaction chamber.
Cu(111) is 1.76×10^{15} /cm^2, the diameter of Cu sample is 10 mm,

Beam spot area on Cu(111) surface is $0.9\times \pi(1/2)^2 = 0.7$ cm^2.

So on Cu(111), Cu atoms are 1.76×10^{15} /cm^2 $\times$ 0.7 $cm^2 = 1.23\times10^{15}$
So, the CO_2 beam flux:

$3.63\times10^{14}/(1.23\times10^{15}) = 0.2951$ CO_2 molecules/(Cu atom · s)

✻✻✻ Appendix ✻✻✻

For 3% CO_2 (in He) beam, $Q_{He} = (97/3)Q_{CO2}$

$$Q_{CO_2} = \Delta P / (1.42/1005+0.18\times(97/3)/520)$$

$$= \Delta P /(0.001413 + 0.0112) \quad = \Delta P /0.0126$$

$$Q_{CO_2} = 79.4 \times \Delta P \text{ (torr dm}^3\text{/sec)}$$

For example, 3% CO_2 (in He) beam irradiation at T_{nozzle} = 1000 K,
Background pressure $P_{sc0} = 3.2\times10^{-10}$ torr.

So $\Delta P = 2.0\times10^{-7}$ torr – 3.2×10^{-10} torr = 2×10^{-7} Torr
Therefore,

$$Q_{CO_2} = 79.4\times10\text{^}(-3)\ (m^3/sec.)\ \times2\times10\text{^}(-7)\ (Torr)\ \times133.3(N/m^2\ Torr)\ \times6.02\times10\text{^}(23)(mol^{-1})$$

$$/(8.31(N\ m/mol\ K)\ \times300(K))$$
$$= 5.1\ \times\ 10^{14}$$

It is notable that 300 K is the CO_2 gas temperature in reaction chamber.
Cu(111) is 1.76×10^{15} /cm², the diameter of Cu sample is 10 mm,

Beam spot area on Cu(111) surface is $0.9\times\pi(1/2)^2 = 0.7$ cm².

So on Cu(111), Cu atoms are 1.76×10^{15} /cm² × 0.7 cm² = 1.23×10^{15}
Therefore, the CO_2 beam flux:
$5.1\times10^{14}/(1.23\times10^{15})$= 0.4146 CO_2 molecules/(Cu atom · s)

2.1.4 Calculation of the reaction probability of CO_2 to convert into formate

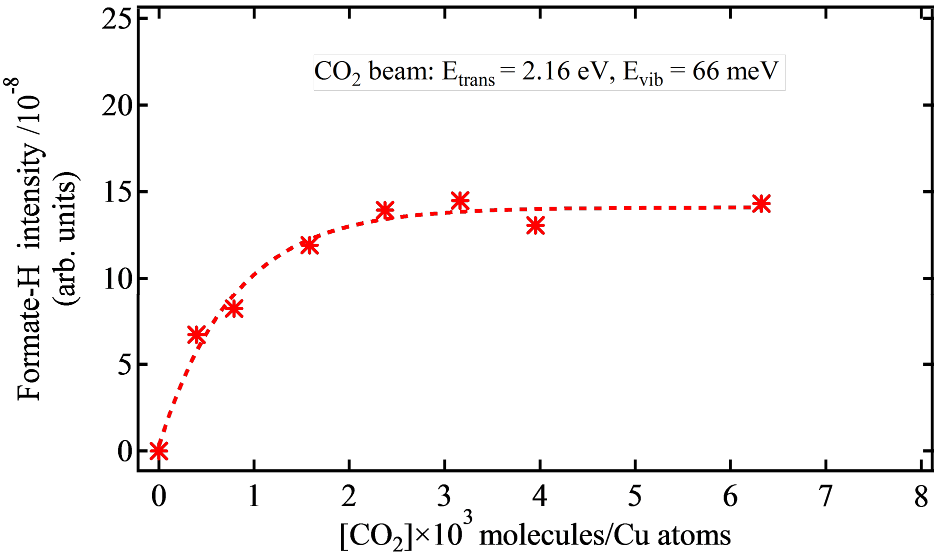

Figure S2.3 Example of uptake curve for the calculation of reaction probability

From the data in the figure, the fitting curve (dashed line) can be expressed as

$$y = y_0 + A\exp\left\{\frac{-x}{\tau}\right\}$$

The slop function thus can be

$$\frac{dy}{dx} = -\frac{A}{\tau}\exp\left\{\frac{-x}{\tau}\right\}$$

Therefore, the initial reaction probability of CO_2 ($x = 0$) is

$$P = -\frac{A}{\tau y_0}\times10^{-3}$$

From the fitting parameters by using software (IGOR PRO 6.031, WaveMetrics, Inc.), we can obtain: $y_0 = 14.09$, $A = -13.81$ and $\tau = 0.785$, so the reaction probability of CO_2:

$$P = 1.24\times10^{-3}$$

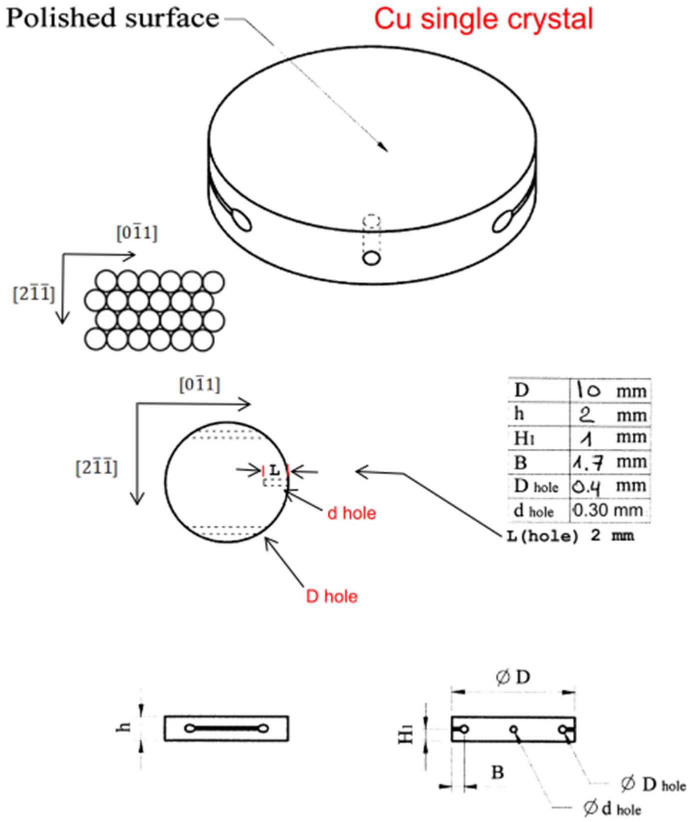

Figure S2.4 Schematic of Cu single crystal sample with various parameters

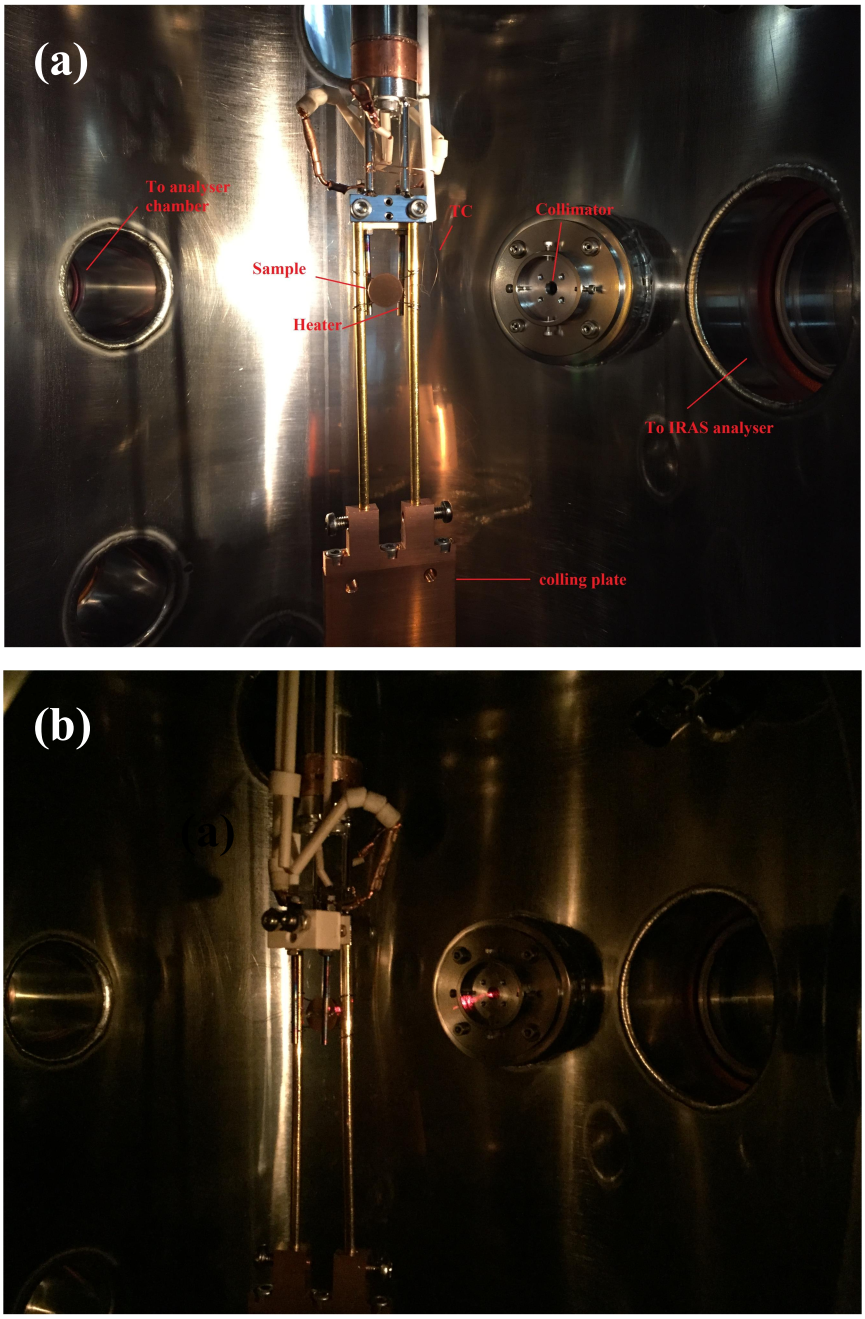

Figure S2.5 (a) The reaction chamber with a Cu sample, sample holder, collimator hole for molecular beam, cooling plate connecting a cryo-pump. (b) The sample position is collimated with the beam hole using a laser.

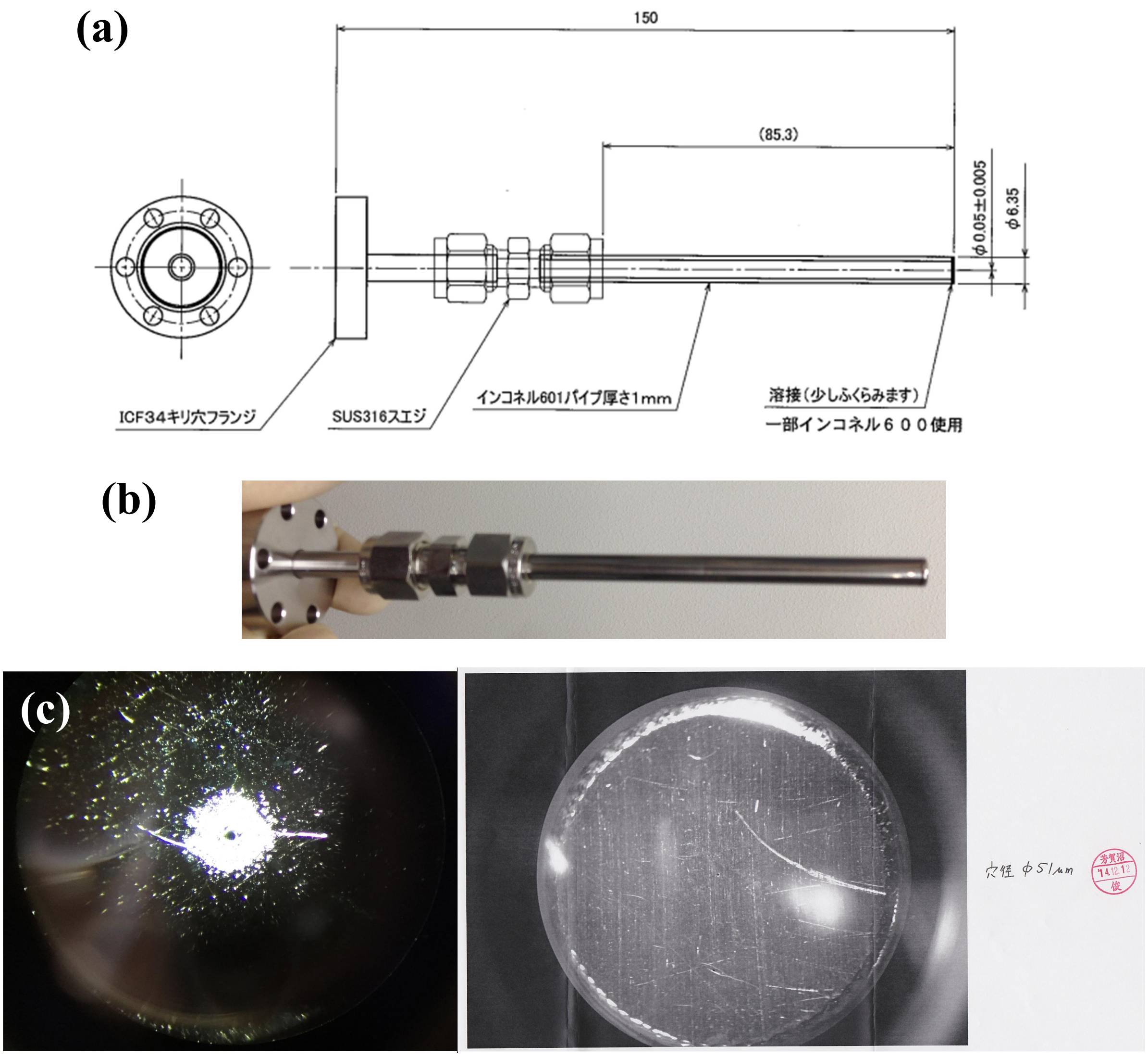

Figure S2.6 (a) Schematic of nozzle structure. (b) The photo of nozzle (Made from Omegatron (株式会社オメガトロン)). (c) Pinhole of nozzle with a diameter as 51µm.

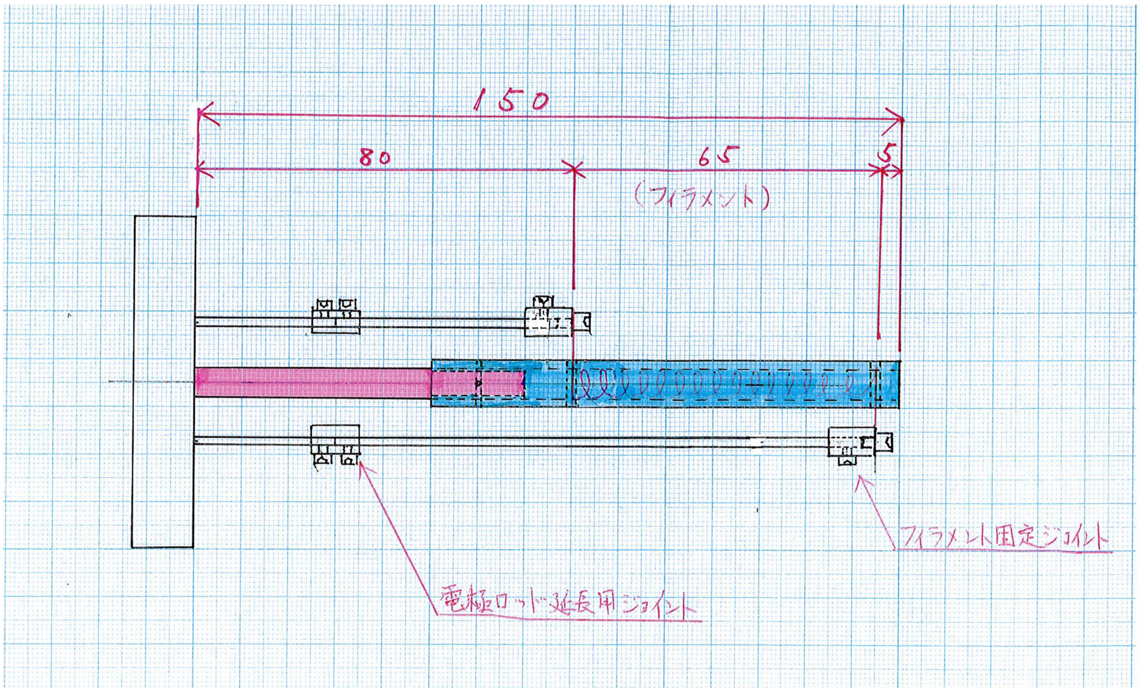

Figure S2.7 Schematic of atomic hydrogen generator

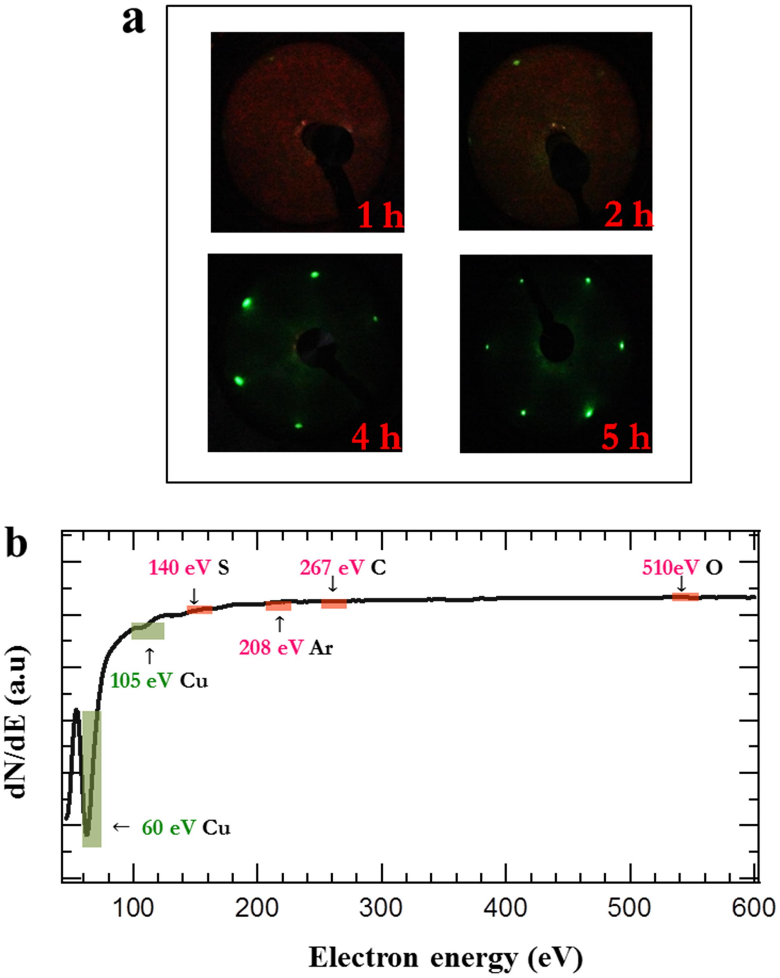

Figure S2.8 Cleanness of Cu(111) after cycles sputtering confirmed by LEE/AES (a) Low-energy electron diffraction (LEED) (70 eV) patterns and (**b**) Auger electron spectroscopy (AES) spectra of clean Cu(111) surfaces measured at room temperature.

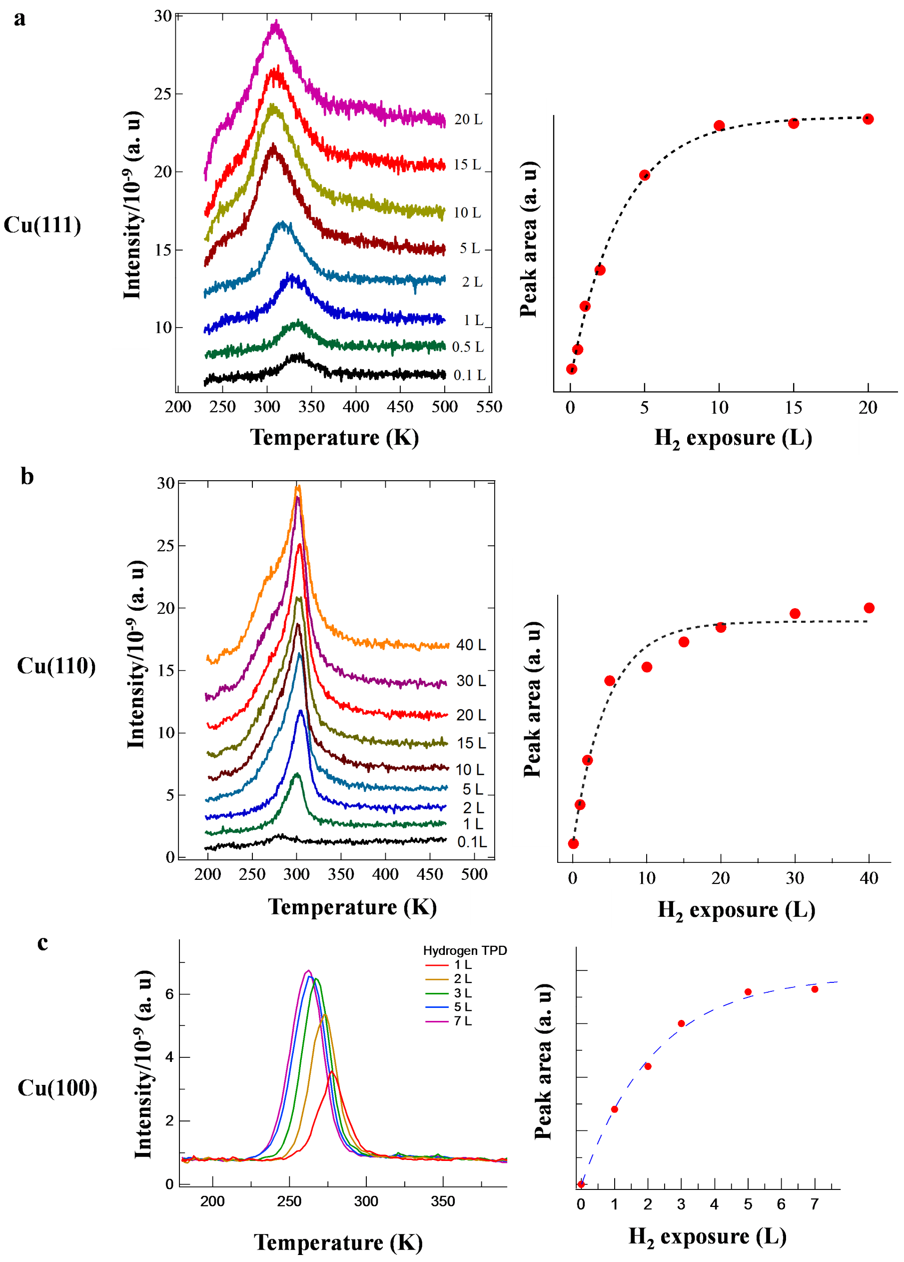

Figure S2.10 Temperature programmed desorption (TPD) profiles of H_2 on Cu(111), Cu(110) and Cu(100). TPD spectra of H_2 were measured after various H_2 exposure through a hot-tungsten filament. The associatively desorbed (recombination desorption of) hydrogen ($H_a + H_a \rightarrow H_2$) were detected. (**a**) Cu(111), (**b**) Cu(110) and (**c**) Cu(100). Heating rate is 2.0 K/s.

2.1.5 Calibration of the quadrupole mass (Q-Mass) detector signals for the ratio of CO_2 and H_2 in TPD measurements

Because the Q-Mass detector has different sensitivities for the desorbing CO_2 and H_2, careful calibration is required. We calibrated the signals using the TPD profiles of desorbing CO_2 and H_2 from the decomposition of formate ($HCOO_a \rightarrow CO_2 + 1/2\ H_2$). The formate for the calibration measurement is prepared by the dehydrogenation of formic acid (HCOOH).

As shown in **Fig. S2.11**, the average measured intensity ratio of CO_2 and H_2 is about 0.17 (left vertical axis) for the Cu(111) experiment, which is calibrated to the stoichiometric ratio of 2 (the ratio of CO_2 and H_2 formed by the formate decomposition, right vertical axis). The intensity ratio of CO_2 and H_2 measured in the molecular beam experiment lies close to the calibrated ratio of 2.0. The same method is applied to the calibration of signals for the Cu(110) surface experiment.

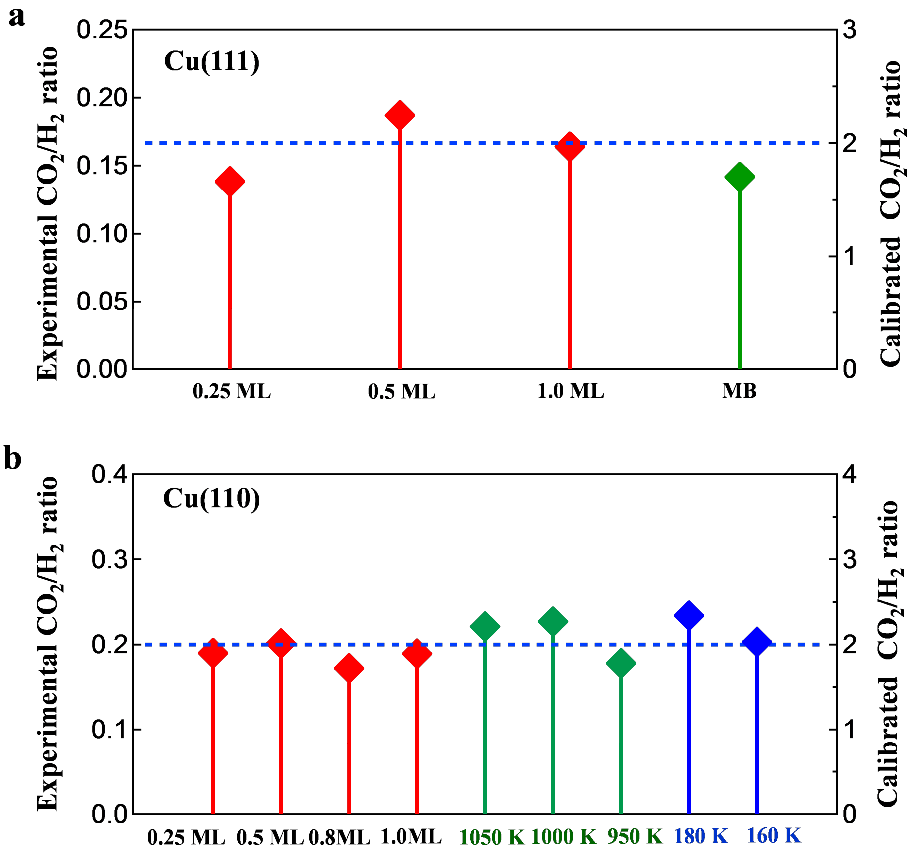

Figure S2.11 The calibration of CO_2 and H_2 signal intensity ratio measured by Q-mass. We have calibrated Q-mass signals by using TPD results of HCOO/Cu(111) and HCOO/Cu(100) prepared by the dehydration of formic acid as the standard TPD-signals with CO_2:H_2 = 2:1. (a) The CO_2/H_2 signal ratio measured from Cu(111): The red squares are the TPD peak area ratios of CO_2 and H_2 from the decomposition of formate with various coverages prepared by direct dehydrogenation of formic acid (HCOOH).

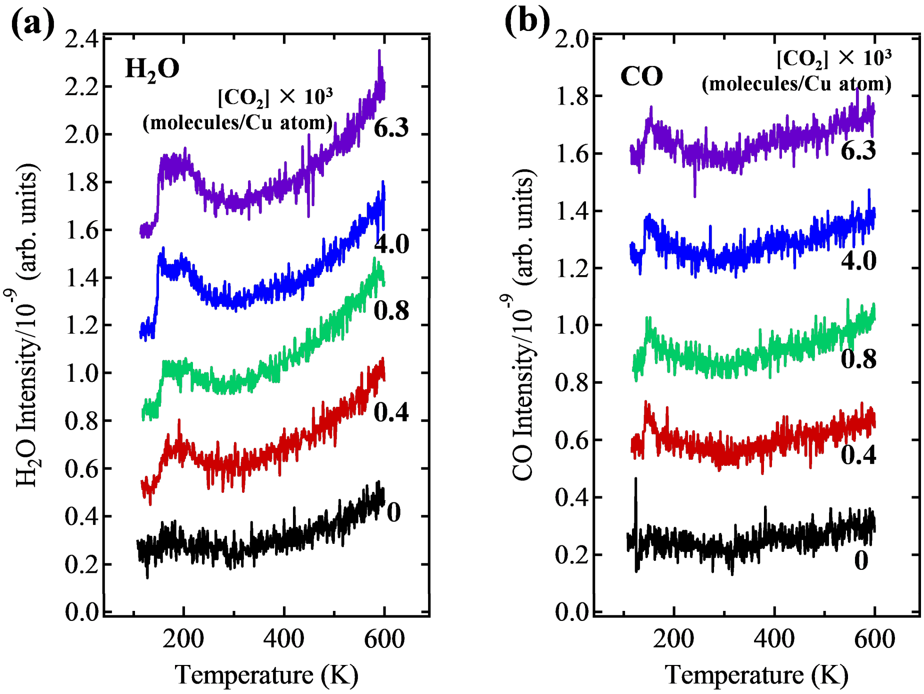

Figure S2.12 Formation of formate on Cu(111) with different CO_2 beam exposures (CO_2 molecules/Cu atom) traced by temperature-programmed-desorption (TPD). Cu(111) surface is kept at 120 K. The coverage of pre-dosed hydrogen adatoms are the saturated coverage of 0.6 ML. The nozzle temperature is 1000 K and the translational energy of CO_2 is 2.16 eV. TPD profiles of (**a**) H_2O (*m/z* = 18); (**b**) CO (*m/z* = 28);

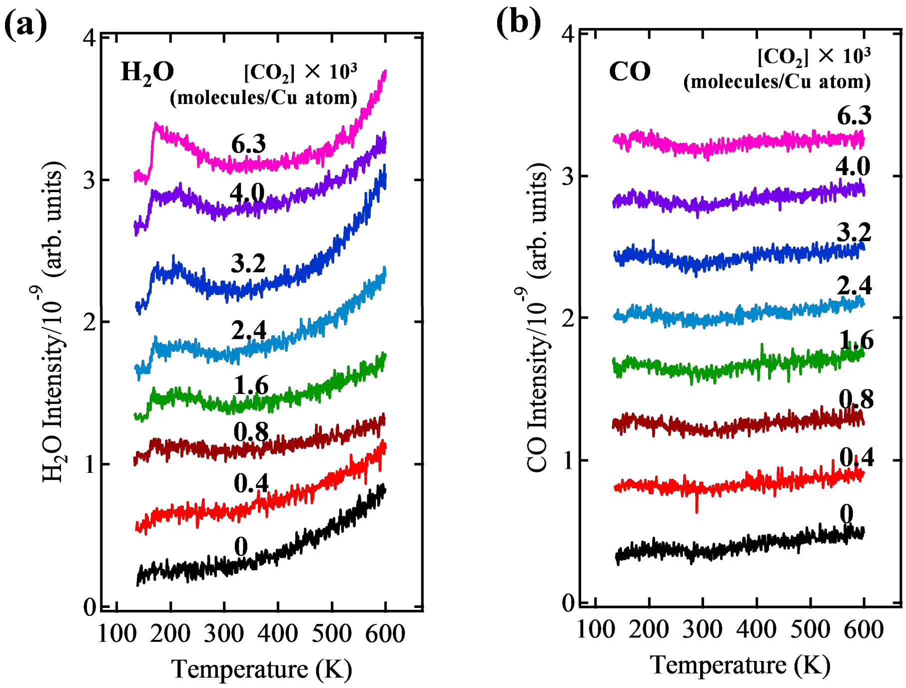

Figure S2.13 Formation of formate on Cu(111) with different CO_2 beam exposures (CO_2 molecules/Cu atom) traced by temperature-programmed-desorption (TPD). Cu(111) surface is kept at 140 K. The coverage of pre-dosed hydrogen adatoms are the saturated coverage of 0.6 ML. The nozzle temperature is 1000 K and the translational energy of CO_2 is 2.16 eV. TPD profiles of (**a**) H_2O (*m/z* = 18); (**b**) CO (*m/z* = 28);

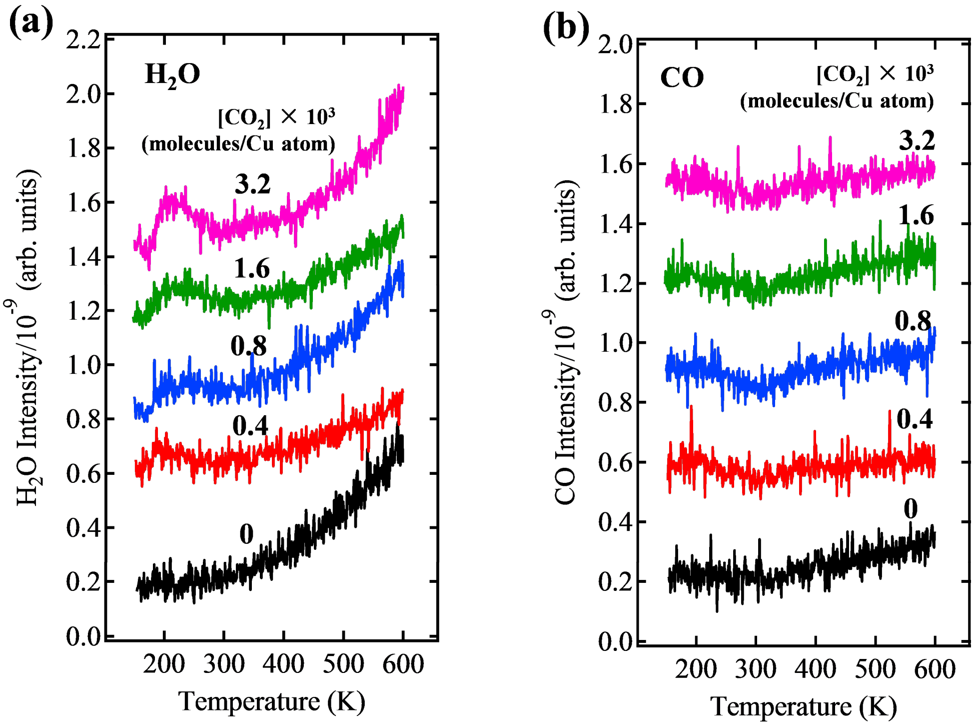

Figure S2.14 Formation of formate on Cu(111) with different CO_2 beam exposures (CO_2 molecules/Cu atom) traced by temperature-programmed-desorption (TPD). Cu(111) surface is kept at 160 K. The coverage of pre-dosed hydrogen adatoms are the saturated coverage of 0.6 ML. The nozzle temperature is 1000 K and the translational energy of CO_2 is 2.16 eV. TPD profiles of (**a**) H_2O ($m/z = 18$); (**b**) CO ($m/z = 28$);

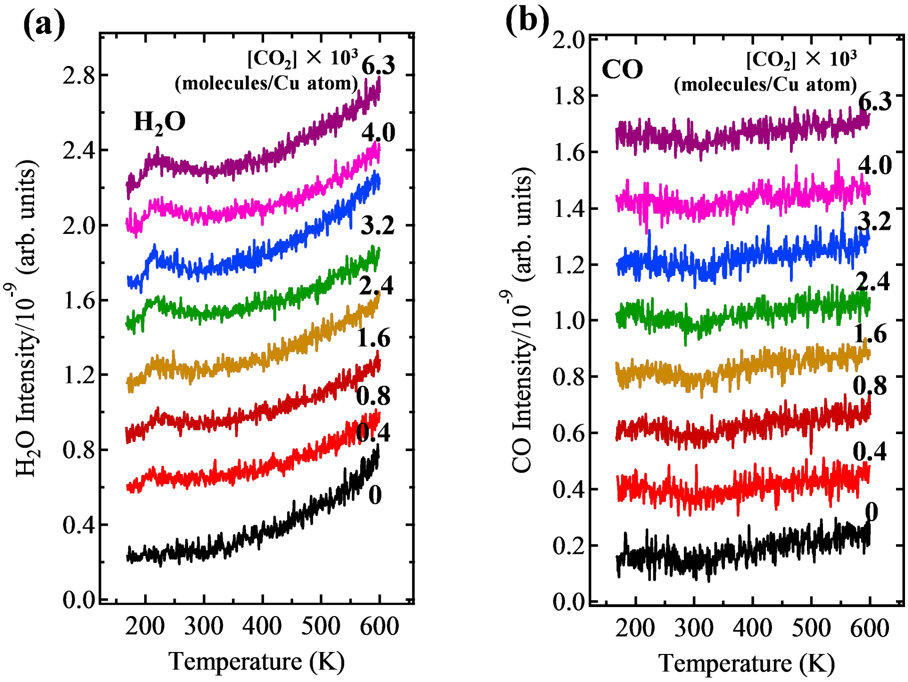

Figure S2.15 Formation of formate on Cu(111) with different CO_2 beam exposures (CO_2 molecules/Cu atom) traced by temperature-programmed-desorption (TPD). Cu(111) surface is kept at 180 K. The coverage of pre-dosed hydrogen adatoms are the saturated coverage of 0.6 ML. The nozzle temperature is 1000 K and the translational energy of CO_2 is 2.16 eV. TPD profiles of (**a**) H_2O ($m/z = 18$); (**b**) CO ($m/z = 28$);

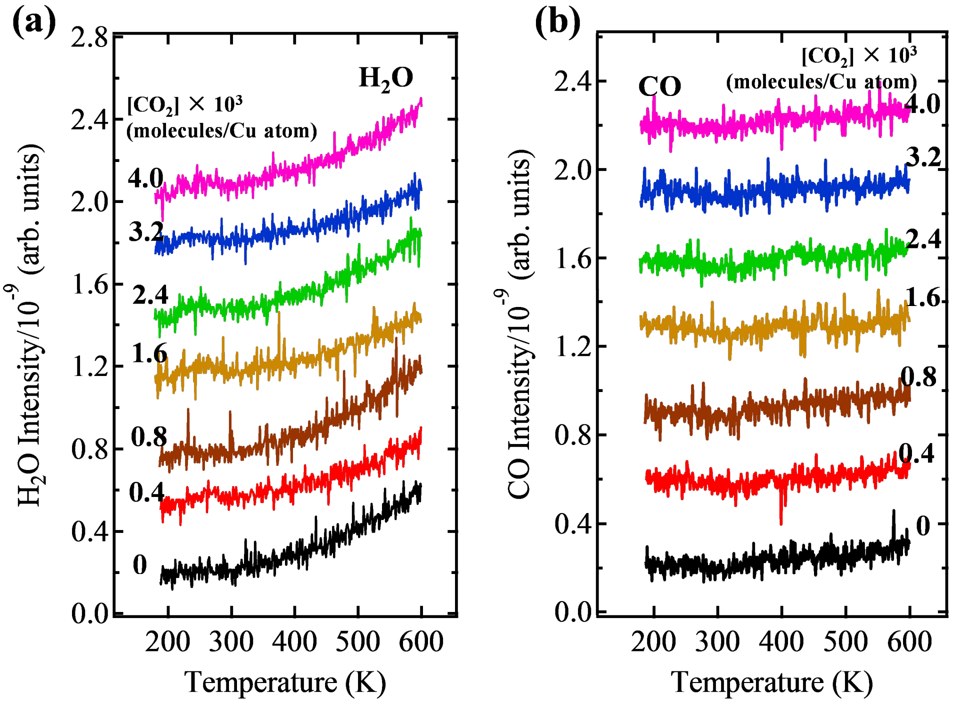

Figure S2.16 Formation of formate on Cu(111) with different CO_2 beam exposures (CO_2 molecules/Cu atom) traced by temperature-programmed-desorption (TPD). Cu(111) surface is kept at 200 K. The coverage of pre-dosed hydrogen adatoms are the saturated coverage of 0.6 ML. The nozzle temperature is 1000 K and the translational energy of CO_2 is 2.16 eV. TPD profiles of (**a**) H_2O ($m/z = 18$); (**b**) CO ($m/z = 28$);

3. Small supersonic molecular beam (SMB) experiments

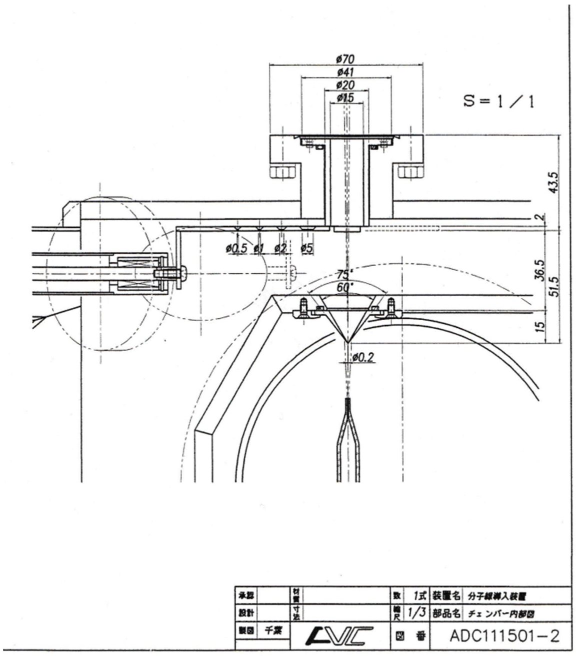

Figure S3.1 Schematic of source chamber of small molecular beam apparatus

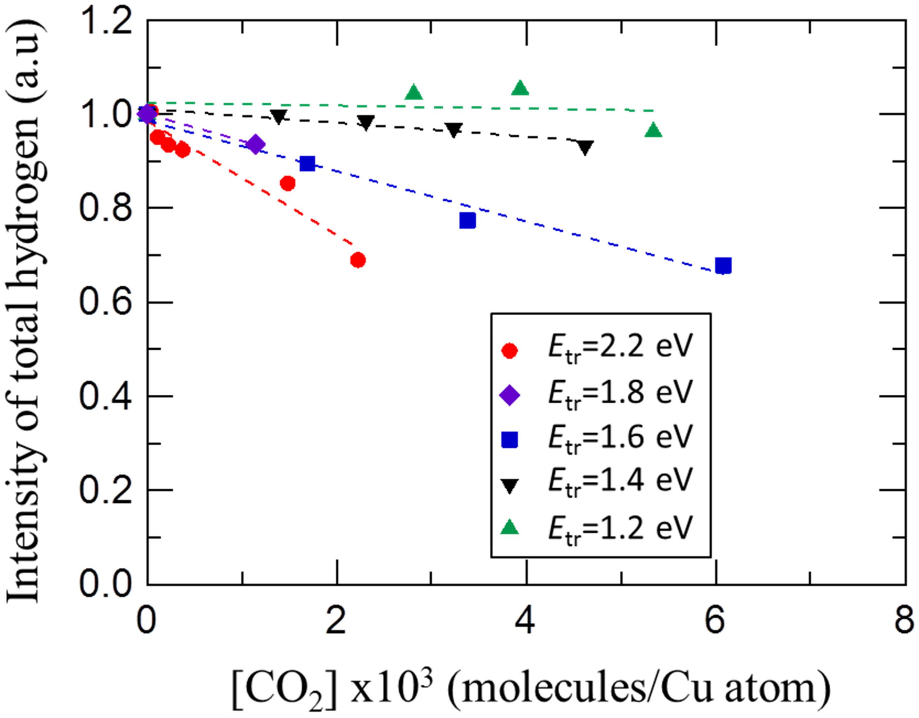

Figure S3.1 The total amounts of hydrogen (unreacted hydrogen plus formate hydrogen) decrease with increasing translation energy of CO$_2$ beam. Experiments are carried out by small molecular beam apparatus.

4. Angle-resolved analysis of formate decomposition experiments

(i) Angle-resolved temperature-programmed desorption (AR-TPD)

Collimation of molecular total flux desorbing from the Cu surface

The flux of the desorbing CO_2 has to be collimated due to the slits spot on surface are different when the sample is changing the polar angle (**Fig. S4.1**).

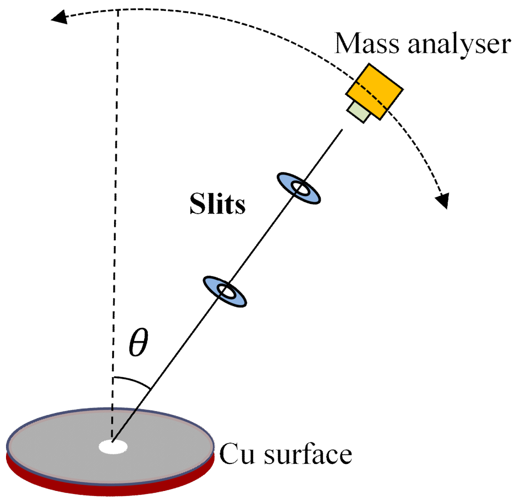

θ (°)	*f* (area factor)
0 ~ 35	cos θ
40	1.260
45	1.288
50	1.307
55	1.321
60	1.331
70	1.345
80	1.352

Figure S4.1 Schematic diagram of the collimation of molecular total flux desorbing from the Cu surface [8]. The front surface area of the copper surface to the apertures of the collimator increases as the polar angle θ increases, resulting in the increase of the integrated amount of formate species. As a result, the intensity of desorbing CO_2 from the formate decomposition at the angle θ is larger than that on the area of the Cu surface facing normal to the collimator. Hence, the collimation of the CO_2 desorbing flux (I_{cal}) can be written as follows: $I_{cal} = I_{dec} / f$, where I_{dec} is the detected intensity of CO_2 and f is the area factor corresponding the polar angle. All AR signals used in this work were calibrated by considering this area factors.

(ii) Angle-resolved steady-state desorption (AR-SSD)

4.1 How to obtain the time-of-flight (TOF) spectrum

In the TOF measurements, the desorbed molecules from the surface were detected by the QMS after passing through the slit, cross-correlation chopper, and drift tube. The chopper, with pseudorandomly positioned 255 slits of equal width, was rotated at 196.1 Hz, where a time resolution of 20 μs is obtained. The detected signal was then recorded by a multichannel analyzer with 20 μs × 255 channels.

The measured TOF data, $s(t)$, were then cross-correlated with the pseudorandom chopper array function $g(t)$ to derive the deconvoluted TOF spectrum $f(t)$ by using software (IGOR PRO 6.031, WaveMetrics, Inc.), as shown in **Fig. S4.2**, where $f(t)$ can be represented as $f(t) = \int_{-\infty}^{\infty} s(t+\pi)g(\pi)d\pi$, from ref. [9, 10].

4.2 Correction of time

There are mainly two uncertain factors that inevitably cause the deviation of time in TOF due to the experimental setup. The deviation of time originates from the "start signal deviation, Δt_a" and the "finite detection time, Δt_b"; Δt_a is the difference between the time of molecule chopping at the chopper and the trigger signal provided by the photocoupler due to slight geometrical deviations of the photocoupler at the chopper from the ideal position. To correct the deviation of Δt_a, a white light signal was measured by the photomultiplier. The peak position difference between the TOF spectrum of white light and the pseudorandom chopper arrays corresponds to Δt_a, while the difference in the width mainly originates from the chopper gate function. From the difference in peak position, Δt_a was corrected as shown in **Fig. 4.3**. The resultant trigger position was found to shift by 20 μs, which is different from our previous work[45] because we have rotated the chopper to the opposite direction from that in the previous work.

The other deviation, Δt_b, is the time of flight of the molecules in the detector after ionization at the top of QMS. After entering the ionization part, the ionized molecules fly a quadrupole distance, taking about a few dozen microseconds depending on the intended mass. Then, Δt_b was corrected by estimating the corresponding flight time as -38.935 μs, as reported previously [11, 12].

In addition to corrections to Δt_a and Δt_b, we have corrected the position of each data point such that it corresponds to the center of the chopper array width (20 μs). For example, the data point obtained at the time between 0 and 20 μs, is not plotted at 0 μs, but plotted at 10 μs.

4.3 How to estimate the average energy

To estimate the average energy from the TOF spectrum, the TOF spectrum was firstly fit by using the following flux-type modified Maxwell-Boltzmann distribution function, $h(t)$, where $(1/v)$ was multiplied to the distribution to include the ionization sensitivity in QMS.

$$h(t) = C_1 + \frac{C_2}{t^4} exp\left(-\frac{m(L/t - v_0)^2}{2kT}\right) dt$$

Here, C_1, C_2, v_0, and T are the fitting parameters. L is the flight pass of 377 mm, m is the mass of $^{13}CO_2$ (m/z = 45), and k is the Boltzmann constant. As an example, a fitting result is shown by the pink curve in Fig. S2(c). The TOF was then converted to a velocity distribution $f(v)$ by using the fitting result of $h(t)$, as shown in **Fig. S4.4**. Finally, we have calculated the average energy $\langle E \rangle$ by using the obtained $f(v)$ and the following equation:

❉❉❉ Appendix ❉❉❉

$$\langle E \rangle = \frac{1}{2} M \frac{\int_0^\infty v^2 f(v) dv}{\int_0^\infty f(v) dv}$$

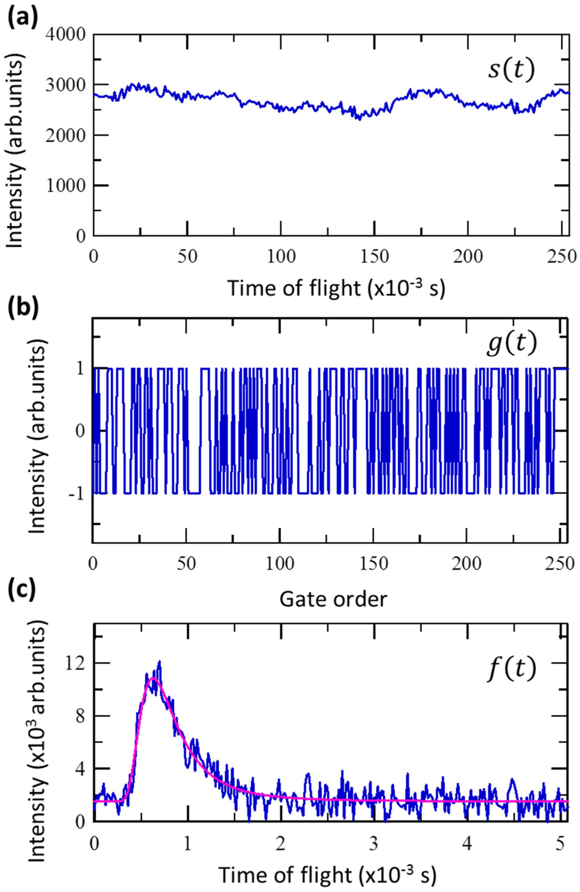

Figure S4.2 Determination of TOF spectra. (a) Typical example of the measured TOF data, $s(t)$. (b) Function of the pseudorandom chopper array $g(t)$ is shown. (c) The obtained TOF spectrum $f(t)$ after the cross-correlation of $s(t)$ with $g(t)$. The pink curve shows the fitting results (see Section IV).

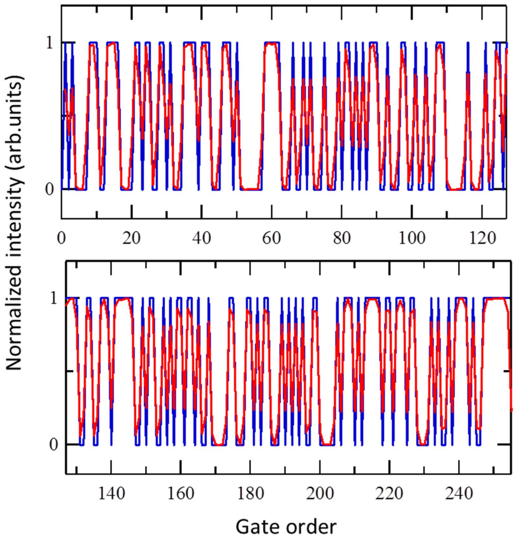

Figure S4.3 Pseudorandom chopper array (blue curves) and time of flight of white light (red curves). Here, Δt_a was calibrated to accord the peak position between the chopper array and the time of flight.

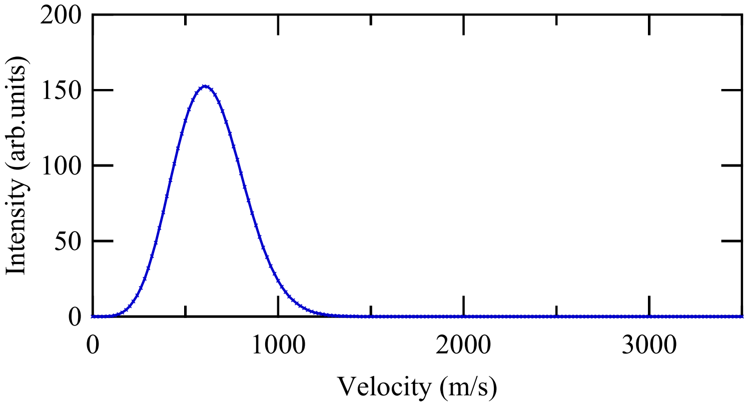

Figure S4.4. Velocity distribution converted from a time-of-flight spectrum

❊❊❊ Appendix ❊❊❊

References

[1] M. Neurock, Catalytic surfac ereaction pathways and energetics from first principles, in: K.C.W. G.F. Froment (Ed.) Dynamics of Surfaces and Reaction Kinetics in Heterogeneous Catalysis, ELSEVIER, Netherlands, 1997.

[2] G. Wang, Y. Morikawa, T. Matsumoto, J. Nakamura, J. Phys. Chem. B, 110 (2005) 9-11.

[3] E. Vesselli, L.D. Rogatis, X. Ding, A. Baraldi, L. Savio, L. Vattuone, M. Rocca, P. Fornasiero, M. Peressi, A. Baldereschi, R. Rosei, G. Comelli, J. Am. Chem. Soc., 130 (2008) 11417-11422.

[4] B. Hammer, J.K. Nørskov, Surface Science, 343 (1995) 211-220.

[5] J. Harris, S. Andersson, Phys. Rev.Lett., 55 (1985) 1583-1586.

[6] B.I.L. E. Hasselbrink, Handbook of Surface Science, in: S. Holloway, N.V. Richardson (Eds.) Intra-molecular Energy Flow in Gas–Surface Collisions, ELSEVIER, Amsterdam, 2008.

[7] H. Fuchs, Nanotechnology, in: H. Fuchs (Ed.) Nanoprobes, John Wiley & Sons, 2009.

[8] T. Matsushima, *Surf. Sci. Rep.* **2003**, 52, 1-62.

[9] G. Scoles, in Atomic and Molecular Beam Methods, Vol. 2, Oxford University Press, New York, 1992.

[10] G. Comsa, R. David, B. J. Schumacher, Rev. Sci. Instrum. 1981, 52, 789-796.

[11] T. Kondo, M. Sakurai, T. Matsushima, J. Nakamura, J. Chem. Phys. 2010, 132, 134704 (1-9).

[12] T. Matsushima, Y. Ma, O. Nakagoe, e-J. Surf. Sci. and Nanotechnol. 2006, 4, 593-601.

❋❋❋ Appendix ❋❋❋

List of Publications

1. ○<u>Jiamei Quan</u>, Takahiro Kondo, Guichang Wang, Junji Nakamura, Energy Transfer Dynamics of Formate Decomposition on Cu(110), *Angew. Chem. Int. Ed.* (DOI: 10.1002/anie.201611342), Selected as **hot paper**, selected as **Front cover** --- (Chapter 5)
2. ○<u>Jiamei Quan</u>, Takahiro Kondo, Junji Nakamura, Eley-Rideal type activation of CO_2 on Cu catalysts, *in preparation* --- (Chapter 4)

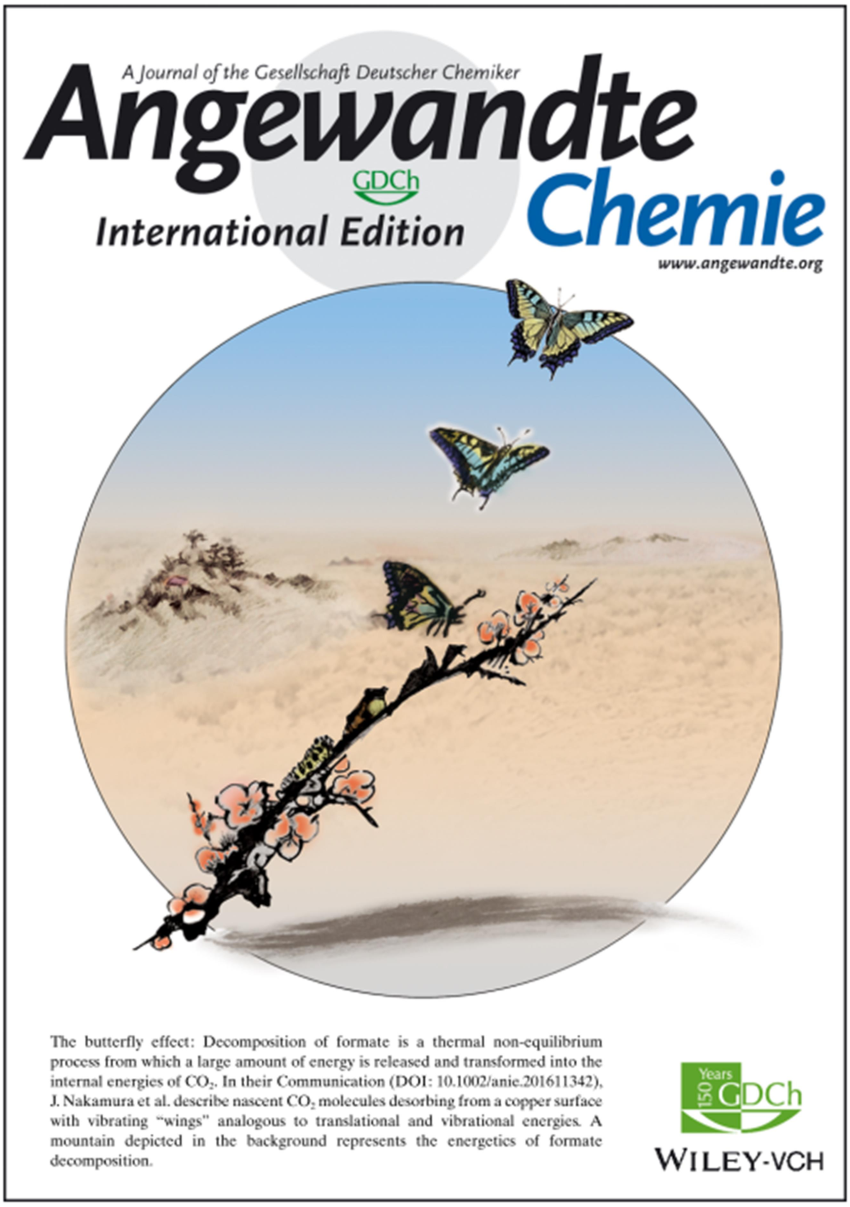

A Journal of the Gesellschaft Deutscher Chemiker
Angewandte Chemie
GDCh
International Edition
www.angewandte.org

The butterfly effect: Decomposition of formate is a thermal non-equilibrium process from which a large amount of energy is released and transformed into the internal energies of CO_2. In their Communication (DOI: 10.1002/anie.201611342), J. Nakamura et al. describe nascent CO_2 molecules desorbing from a copper surface with vibrating "wings" analogous to translational and vibrational energies. A mountain depicted in the background represents the energetics of formate decomposition.

150 Years GDCh
WILEY-VCH

Honors and Awards

1. オナーズプログラム（筑波大学大学院教育プログラム・文部科学省特別経費）
   (Honors Graduate Program Student at University of Tsukuba) July 2013 ~ March 2014
2. 文部科学省外国人留学生学習奨励費
   (Monbukagakusho Honor Scholarship) Oct. 2013 ~ March 2014
3. スーパーグローバル大学創成支援事業による国費外国人留学生（国内採用）
   (Monbukagakusho (MEXT) scholarship (Top Global University)) Oct. 2015 ~ March 2016
4. Best poster award, Dynamics of normal-emission of CO_2 formed by thermal decomposition of formate on Cu surfaces, P076, *NIMS Conference 2013*, Tsukuba, Japan. July. 2013,
5. The travel (Young) award, Direct evidence for Eley-Rideal mechanism of CO_2 hydrogenation on Cu surfaces, *The 7th International Symposium on Surface Science (ISSS7)*, Shimane, Japan Nov. 2014

List of Presentations

3. International conference

(1) ○J. Quan, M. Sakurai, T. Kondo and J. Nakamura, Dynamics of Normal-emission of CO_2 Formed by Thermal Decomposition of Formate on Cu surfaces, NIMS Conference 2013, Tsukuba, Japan, July. **2013**, Poster presentation (P-076).

(2) ○J. Quan, M. Sakurai, T. Kondo and J. Nakamura, Thermal non-equilibrium Decomposition of Formate on Cu Surfaces, AVS 60th International Symposium & Exhibition, Long Beach, CA, USA, Oct. **2013**. Oral presentation (SS2-ThA2).

(3) ○J. Quan, T. Ogawa, T. Kondo and J. Nakamura, Dynamics of CO_2 Activation on Cu Surfaces, 30th European Conference on Surface Science, Antalya, Turkey, Aug-Sep. **2014**, Oral presentation (Tu-C15-518).

(4) ○J. Quan, T. Ogawa, T. Kondo and J. Nakamura, Direct Evidence for Eley-Rideal Mechanism of CO_2 Hydrogenation on Cu surface, The 7th International Symposium on Surface Science (ISSS-7), Shimane, Japan, Nov. **2014**, Oral presentation (4pB2-1(Travel award)).

(5) ○J. Quan, T. Kondon, Guichang Wang, T. Ogawa and J. Nakamura, Eley-Rideal type Mechanism for Formate Synthesis from Carbon dioxide Hydrogenation on Cu surfaces, Gordon Research Conference (Dynamics at Surfaces), Newport, Rhode Island, Aug. **2015**, Poster presentation (Mo-We: 42)

4. Domestic conference (Japan)

(1) ○J. Quan, M. Sakurai, T. Kondo and J. Nakamura, Angular Distribution of Desorbing CO_2 in Decomposition of Formate on Cu(111) and Cu(110), 草津市, 日本化学会第93春季年会, March **2013**. Oral presentation (1G6-45).

(2) ○J. Quan, T. Kondo, G. Wang, T. Ogawa and J. Nakamura, Dynamics of CO_2 Hydrogenation on Cu surfaces at low temperature, 第34回表面科学学術講演会, 島根県, Nov. **2014**, Oral presentation (8Ca01).

(3) ○J. Quan, T. Kondo, G. Wang, T. Ogawa and J. Nakamura, Eley-Rideal Type Mechanism for Formate synthesis from CO_2 Hydrogenation on Cu surfaces, 表面・界面スペクトロスコピー2014, 京都市, Nov. **2014**, Oral presentation (No.4).

(4) ○J. Quan, T. Kondo, G. Wang, T. Ogawa and J. Nakamura, Thermal Non-equilibrium Activation of Carbon Dioxide on Cu catalysts, 第35回真空・表面科学合同講演会, つくば市, Dec. **2015**, Oral presentation (1Ea03S).

(5) ○J. Quan, T. Kondo, G. Wang, T. Ogawa and J. Nakamura, Thermal non-equilibrium in formate synthesis and formate decomposition on Cu surface, 表面・界面スペクトロスコピー2015, 埼玉県, Nov. **2015**, Poster presentation (P-26S).

Acknowledgements

During these three years of doctoral course, there are many people to whom I am thankful for their great support and sincere encouragement during my doctoral course. It is them that help me overcome many difficulties in the experimental work and graduate student's life.

First of all, I would like to express my deep gratitude to my supervisor, Prof. Junji Nakamura, for his patience, his guidance, his invaluable advice and comments, understanding shown during many fruitful and creative discussions, sharing selflessly his academic experience and idea with me, and the friendly co-operative atmosphere all along this time, and I would never forget his continuous support and encouragement, it is him, who have open the amazing academic door of surface science to me, since my mater course.

Then I would like to specially thank Associate Professor Takahiro Kondo for his kind instruction and trustful support, his many important suggestions and constructive ideas during our discussion, particularly concerning the preparation of experimental sample and data processing. Without his great help, I couldn't complete this thesis and learn so much experimental skills and details.

My warm thanks also are expressed to Professor Yasuhiro Horrike, who is not only one of my PhD. committees, also is my Honors Program's coordinator. He shows his warm heart to my experiment and the discussions. And thanks to Professor Masahiro Kitajima, who offers many advices to me for my experiments. Also my appreciation is expressed to Professor Tatsuo Matsushima (Hokkaido University) for giving me the possibility to carry out AR-TPD work, whenever I have questions and meet the problems, he would show his kindness and guide me about the solution, methods and mechanism of experiments.

I am also thankful to my PhD. committees from University of Tsukuba, Professor Kazuya Saito, Professor Masahiro Sasaki and Professor Susumu Okada, for their fruitful comments and suggestions, which have been exceedingly helpful to my PhD. thesis writing and to my work in the degree committee.

Earnest thanks are offered to molecular beam team in Nakamura & Kondo's group, Miss Yuka Amaha, Mr. Tetsuya Ogawa, Mr. Taijun Kozarashi, Mr. Tomoyasu Mogi. Due to their hard working and positive attitudes, I receive many positive comments and suggestions from them. I also would like to extend my deep appreciation to other Nakamura & Kondo Laboratory members, for their great continuous help since the first day I joined the excellent group, for their valuable discussions, cooperation and pleasurable experience in my laboratory life. And I would like to appreciate all those who have helped me to get here and are not named on this page but will always be remembered with affection.

And last but not least my sincere thanks to my family, particularly, to my dear parents, for their selfless support and love.

February 2017
Graduate School of Pure and Applied Sciences
University of Tsukuba

Jiamei Quan